


Fall 2013

Design and Assembly of Nanostructured Complex Metal Oxide Materials for the Construction of Batteries and Thermoelectric Devices

Gautam Ganapati Yadav
Purdue University

Follow this and additional works at: https://docs.lib.purdue.edu/open_access_dissertations

 Part of the [Chemical Engineering Commons](#), [Mechanics of Materials Commons](#), and the [Physics Commons](#)

Recommended Citation

Yadav, Gautam Ganapati, "Design and Assembly of Nanostructured Complex Metal Oxide Materials for the Construction of Batteries and Thermoelectric Devices" (2013). *Open Access Dissertations*. 35.
https://docs.lib.purdue.edu/open_access_dissertations/35

This document has been made available through Purdue e-Pubs, a service of the Purdue University Libraries. Please contact epubs@purdue.edu for additional information.

PURDUE UNIVERSITY
GRADUATE SCHOOL
Thesis/Dissertation Acceptance

This is to certify that the thesis/dissertation prepared

By Gautam Yadav

Entitled

Design and Assembly of Nanostructured Complex Metal Oxide Materials for the Construction of Batteries and Thermoelectric Devices

For the degree of Doctor of Philosophy

Is approved by the final examining committee:

Yue Wu

Chair

You Yeon Won

Xiulin Ruan

Arvind Varma

To the best of my knowledge and as understood by the student in the *Research Integrity and Copyright Disclaimer (Graduate School Form 20)*, this thesis/dissertation adheres to the provisions of Purdue University's "Policy on Integrity in Research" and the use of copyrighted material.

Approved by Major Professor(s): Yue Wu

Approved by: Michael Harris

Head of the Graduate Program

09/30/2013

Date

DESIGN AND ASSEMBLY OF NANOSTRUCTURED COMPLEX METAL OXIDES
MATERIALS FOR THE CONSTRUCTION OF BATTERIES AND
THERMOELECTRIC DEVICES

A Dissertation

Submitted to the Faculty

of

Purdue University

by

Gautam Ganapati Yadav

In Partial Fulfillment of the

Requirements for the Degree

of

Doctor of Philosophy

December 2013

Purdue University

West Lafayette, Indiana

To my parents, Vikram & Manali!

ACKNOWLEDGEMENTS

“You will never succeed in life”

-My 8th Grade Teacher

“You can do whatever you want...Don't let anyone ever tell you what can and can't do”

-My Mother

I am forever in debt to my mother for helping me realize that nothing was impossible and things were always within my grasp if I tried hard enough and worked hard towards my goals. She pushed me forward even when certain factors in my life tried to pull me back, and now here I stand, in sight of my doctoral degree. My father, the ever humble and brilliant man, has been a guiding light that has helped me to get through dark passages of my life. His love, guidance, and belief in my abilities, empowered me with the strength to endure any hardship and challenge any obstacle. My brother, Vikram, has been my best friend, my mentor and the greatest ally that anyone could ever ask for in one's life. His brotherly love is the stuff of legend, and is something that I take great pride in bragging about to other people. My sister-in law, Manali's affable nature has taught me to enjoy and cherish life and

be happy with the small things in life. This thesis is for my family, their vital bond – love - has strengthened and honed me to reach this stage of my life. I am ever-so-blessed to have them.

This thesis would not have been possible without my guru – Professor Yue Wu. I take pride in being his very first student to graduate from his group. It was his passion and dedication for science, and the determination to be the best and succeed that made me chose him as my advisor. He pushed me to settle for nothing but the best and strive hard to achieve my goals. It is because of his teaching that today I feel very confident in my abilities to do excellent and independent research. I am also very grateful to him to allow me to pursue my passion for teaching. The best teaching award that I received would not be possible if it wasn't for his patience and understanding. I hope the teacher-student bond that we have developed over these past four years last forever.

I would also like to thank Professors Arvind Varma, You-Yeon Won and Xiulin Ruan for participating as my committee members and lending their guidance. Their helpful insights taught me to look deeper into the science and take pleasure in understanding the physical principles that govern the experimental process. Professor Xiulin Ruan and his student, Dr. Bo Qiu, have played a much bigger role by collaborating with us and the fruits of this endeavor have resulted in the form of a publication. I am very thankful to both of them.

I would also like to thank Professor Caruthers for providing the important equipment's that made the battery work successful. I would like to thank Anand David and Huazhang(Victor) Zhu for their help in making coin cells.

I would also like to thank Professors Mike Harris and Osman Basaran for being great mentors when I was their teaching assistant for their respective courses. I learned a lot of the subject matter from the masters themselves, and about the philosophy of teaching. They gave me the freedom to experiment my own teaching methods for which I will be always grateful. It is because of them as well that I won the best teaching award.

One final note about the best teaching award, it would really not have been possible without the votes of the students that I taught for two-semesters. I cherish the moments and have made life-long friends. I consider the one year of teaching as being one of the most pivotal moments of my graduate life. Thank you for being awesome! I would also like to thank my undergraduate teaching assistants - Nathan Davis, Jiang Guo, Kimberly Ohn, Thomas Osbourne and Joel Roche - who turned to be really close friends at the end of our stint.

I would like to thank my former and current group members – Dr. Genqiang Zhang, Joseph Susoreny, Haoran Yang, Haiyu Fang, Scott Finefrock, Daxin Liang, Kelly Rickey and Jaewon Lee. They were always there in the time of need and never gave second thought to lend help whenever required. They have been great friends and I believe that it is the camaraderie between us that has made the Wu group successful and strong.

I was also lucky to meet certain individuals in the safety committee. I consider them as my mentors and well-wishers and thank them for inculcating me with strong ethics and teaching me the value of safety. Thank you Linda Davis, Gabriela Nagy and Yury Zvinevich.

I would like to thank Neramith Khamvongsa for being a really awesome friend. Her birthday cards every year and her funny stories made me realize that I was lucky to have some really amazing friends.

I would also like to thank some of my Canadian friends – Victoria Bentley, Ryan Alexander, Dianne Murray and Nicole Fernandes - who have kept in touch with me since my undergraduate days.

I was lucky to stumble upon a gem in my office in Forney Hall of Chemical Engineering. I would like to thank Daniela Marongiu for helping me understand the abstruse world of solid-state physics and being a guide through the maze of nanotechnology, and most importantly, her help in breaking my stereotypical view of physicists being unkempt individuals. She, however, corroborated my view of physicists being extremely nerdy individuals and their crazy passion for science.

I would like to thank the custodians Linda Wesley and Skyler for being great friends and having many thought-provoking discussions on a wide variety of topics. Wisdom does not need to necessarily flow from one tap!

I would like to thank Dianne Swindle, Joseph Dorroll, Janet Shaw, Brian Lydy, Rebecca Hughes and Kiley Dickman for the many free coffee and bagels. Your kindness has humbled me and made me even more appreciative of its positive impact on the lives of people.

I would also like to thank my guitar teacher, Jim Klaverenga. Jim's patience and kindness has shown me the other side of being a great teacher. He has not only made a better guitar player, but he has also made me a better human being.

Finally, I would like to thank my really awesome friends whose companionship that I have enjoyed over these years and made my graduate life memorable – Jack Hyunh, Hye Yeon Park, Ranjita Ghose, Anuradha Bhat, Tej Choksi, Allison Ustonyski, Ryan Culpepper, Eric King, Steven Illes, Kapil Banakar, Margaret Hwang, Ian Smith, Tina Lu, Eumin Lee, Greg Muller, Ahmad Al-Kukhun, Vinod Kumar Venkatakrisnan, Rong Zhang, Lei Ling, Silei Xiong, Danni Gao, Andy Koswara, Dhairya Mehta, Dharik Sanchan, Jeha Lee, Sooha Lee, Brad Messmer and countless more. I apologize if some of the names are not there, you will always be there in my heart and mind, and I appreciate the friendship we have had over these years.

My graduate life has involved interactions with people from different walks of life. This has made my graduate experience very diverse and richer; I feel that I am a new man and for this, I would finally like to thank Purdue University – Boiler Up! If I had to mention my graduate experience as a metaphor, it would be like a sailor’s journey through various stages serving on the ship to finally become the captain of the ship! I would like to end this with the last few lines from the poem *Invictus* that aptly describes my feeling at the end of my PhD – *I am the master of my fate, I am the captain of my soul!*

TABLE OF CONTENTS

		Page
LIST OF TABLES.....		xiv
LIST OF FIGURES		xv
ABSTRACT.....		xxvi
CHAPTER 1. INTRODUCTION		1
1.1 Thermoelectrics.....		5
1.2 Lithium-ion Batteries.....		10
1.3 Thesis Objective and Structure		16
1.4 Conclusion		18
1.5 References		19
CHAPTER 2. PHYSICAL PRINCIPLES BEHIND THERMOELECTRICS		22
2.1 Deriving the thermoelectric figure of merit (ZT), and efficiency of a device for power generation (η)		22
2.2 Electrical Conductivity		31
2.3 Thermal Conductivity.....		42
2.4 Seebeck Coefficient		44

2.5	The Challenge in Thermoelectrics	53
2.6	Advent of Nanotechnology: Nanostructuring of Thermoelectric Materials	55
2.6.1	Nanostructuring and its impact on intrinsic properties	56
2.6.2	Nanostructured Bulk Thermoelectrics	64
2.7	Conclusions	67
2.8	References	69
CHAPTER 3.	LITHIUM-ION BATTERIES: AN OVERVIEW	71
3.1	Mechanism of Lithium-ion Batteries.....	72
3.2	Overview of requirements and crystal structure of cathode electrodes.....	76
3.3	Overview of requirements and crystal structure of anode electrodes.....	83
3.4	Origin of voltage in transition metal oxides	87
3.5	Brief overview of requirements of electrolyte	100
3.6	References	104
CHAPTER 4.	OXIDE THERMOELECTRICS	106
4.1	General introduction	106
4.2	Seebeck coefficient in oxides	111
4.3	Electrical conductivity in oxides	119

4.4	Summary	122
4.5	References	123
CHAPTER 5. FEASIBILITY AND SUSTAINABILITY OF OXIDES FOR THERMOELECTRICS.....		125
5.1	Introduction	126
5.2	Methods	128
5.3	Results & discussion	132
5.3.1	Price	133
5.3.2	Sustainability	135
5.3.3	Efficiency ratio	140
5.3.4	Toxicity	141
5.4	Conclusions	142
5.5	References	145
5.6	Web references	150
CHAPTER 6. ULTRATHIN NANOWIRES OF STRONTIUM TITANATE		152
6.1	Motivation and need	153
6.2	Synthesis method	154
6.2.1	Formation of potassium titanate nanowires	154
6.2.2	Preparation of strontium precursor	155

6.3	Results.....	156	
6.4	Thermal conductivity: measurement.....	158	
6.4.1	Analyzing the thermal conductivity.....	158	
6.5	Generality of the synthesis method.....	163	
6.6	Conclusions.....	164	
6.7	References.....	166	
CHAPTER 7. POROUS NANOWIRES OF NEW PHASE OF CALCIUM COBALT OXIDE FOR THERMOELECTRIC AND LITHIUM-ION BATTERY APPLICATIONS.....			168
7.1	Introduction.....	169	
7.2	Synthesis of porous nanowires.....	172	
7.3	Material characterization techniques.....	173	
7.4	Results.....	174	
7.5	Spark plasma sintering & thermoelectric property measurements.....	181	
7.6	Discussion of thermoelectric properties.....	182	
7.7	Electrode fabrication procedure.....	188	
7.8	Electrochemical evaluation.....	189	
7.9	Conclusions.....	194	
7.10	References.....	196	

CHAPTER 8.	LITHIUM COBALT OXIDE: A STUDY OF DIFFERENT NANOSTRUCTURE'S RELATIONSHIP TO ELECTROCHEMICAL PROPERTIES.....	200
8.1	Introduction.....	200
8.2	Experimental.....	203
8.2.1	Microemulsion-based synthesis procedure.....	203
8.2.2	Post-Annealing Procedure.....	203
8.2.3	Electrochemical Characterization.....	204
8.3	Results.....	205
8.4	Electrochemical tests.....	212
8.5	Conclusion.....	221
8.6	References.....	222
CHAPTER 9.	CONCLUSION AND FUTURE OUTLOOK.....	226
APPENDICES		
	Appendix A: Spark Plasma Sintering.....	229
	A.1. References.....	230
	Appendix B: Coin Cell Assembly.....	231
	Appendix C: Doping of Strontium Titanate with Lanthanum: Tweaking of Hydrothermal Method to Produce New Nanowire Morphology.....	232
	C.1. Formation of Sodium Titanate Nanowires.....	233

C.2. Formation of Hydrogen Titanate Nanowires.....	233
C.3. Formation of Strontium Titanate Nanowires	233
C.4. Results	234
C.5. Doping Reactions with Lanthanum precursors	236
C.6. Results	236
C.7. Conclusion.....	239
Appendix D: Synthesizing of Microplates of Calcium Cobalt Oxide ($\text{Ca}_3\text{Co}_4\text{O}_9$) by Molten Salt Method.....	240
Appendix E: Growth of Vertically Aligned Cobalt Oxide Nanowires.....	243
VITA	247

LIST OF TABLES

Table	Page
Table 4.1. Various Conditions for the ratio of degeneracies, g_3 and g_4 . [Koshibae, Tsutsui & Maekawa, 2000]	117
Table 5.1. Materials allocated with a reference number for convenient representation in ensuing figures. The materials have been arranged from low to high temperature. Please note that these ZT values are approximate values obtained experimentally. [Yadav et al., 2011]	128
Table 5.2. Table of limiting elements for various thermoelectric materials by calculating the mole fraction/unit of different elements in the materials and the reserve availability. [Yadav et al., 2011]	137
Table C.1. Relationship between doping reactant amounts and final product formation....	237
Table D.1. Annealing ramp rates	240

LIST OF FIGURES

Figure	Page
Figure 1.1. Energy flow chart in the United States for the year 2012. [Lawrence Livermore National Laboratory, 2012].....	2
Figure 1.2. Carbon dioxide emission from the various sources shown in Figure 1.1. [Lawrence Livermore National Laboratory (Carbon Flow), 2012].....	3
Figure 1.3. Schematic representation of a power generation thermoelectric device. (Illustration by Gautam G. Yadav)	6
Figure 1.4. ZT improvement of various materials over the last 60 years. The improvements shown are all laboratory-based results and were some form of nanostructured-based materials. [Vineis, Shakouri, Majumdar & Kanatzidis, 2010].....	9
Figure 1.5. Energy density of various battery systems based on weight and size. [Tarascon & Armand, 2001]	11
Figure 1.6. The potential ranges and the respective capacities of various cathode and anode materials used in lithium-ion batteries. [Tarascon & Armand, 2001]	14
Figure 2.1. Thermoelectric power generation device. (Illustration by Gautam G. Yadav)	23

Figure	Page
Figure 2.2. Plot of efficiency, η_{\max} versus temperature. Temperature of the cold side was taken to be 300K.	28
Figure 2.3. Geometric parameters of thermoelectric leg.(Illustration by Gautam G. Yadav)	29
Figure 2.4. The Fermi-Dirac distribution function dependence on temperature. (Illustration by Gautam G. Yadav, Adapted from Huang, 2012)	34
Figure 2.5. Density of states representation for three dimension sphere. (Illustration by Gautam G. Yadav)	36
Figure 2.6. Illustration of concentration of charge carriers in bulk semiconductor through using density of states and Fermi-Dirac distribution. (Illustration by Gautam G. Yadav)	38
Figure 2.7. Explanation of Seebeck effect with the use of a conductor.(Illustration by Gautam G. Yadav, Adapted from Kasap, 1997)	45
Figure 2.8. Explanation of Peltier effect with the use of a conductor.(Illustration by Gautam G. Yadav, Adapted from Chaikin, 1990)	49
Figure 2.9. The inter relationships of various parameters and their ultimate effect on ZT. (Illustration by Gautam G. Yadav)	54
Figure 2.10. Density of States in Two Dimensions.(Illustration by Gautam G. Yadav)	57
Figure 2.11. Density of States versus Energy for different dimensions.(Illustration by Gautam G. Yadav)	62

Figure	Page
Figure 2.12. Illustration of nanostructuring methods to reduce the lattice thermal conductivity.(Illustration by Gautam G. Yadav)	67
Figure 3.1. Mechanism of lithium-ion batteries. (Illustration by Gautam G. Yadav)	73
Figure 3.2. The change in potential in the cathode and anode associated with the charging step.	74
Figure 3.3. Periodic table with a red box highlighting the elements that could be useful in lithium-ion batteries. [Adapted from UC DAVIS, 2010]	77
Figure 3.4. Crystal structure of layered lithium transition metal(M) oxides, LiMO_2 . (Illustration by Gautam G. Yadav, Adapted from Park, 2012)	79
Figure 3.5. Spinel phase of LiMn_2O_4 (Illustration by Gautam G. Yadav, Adapted from Gateshki, 2006)	81
Figure 3.6. Olivine structure of Lithium Iron Phosphate (LiFePO_4). (Illustration by Gautam G. Yadav, Adapted from Park, 2012).....	82
Figure 3.7. Structure of Graphite in its delithiated and lithiated phase.(Illustration by Gautam G. Yadav, Adapted from Park, 2012).....	86
Figure 3.8. Anode and Cathode band levels in terms of an energy diagram.	89
Figure 3.9. Electronic configurations of different transition elements. (Illustration by Gautam G. Yadav, Adapted from Wood & Chu, 2010)	91

Figure	Page
Figure 3.10. Voltage dependence on oxidation state.(Illustration by Gautam G. Yadav, Adapted from Johannes, 2010)	92
Figure 3.11. Graphical illustration of bonding between transition metal and oxygen. (Illustration by Gautam G. Yadav, Adapted from Aydinol, Kohan, Ceder, et al., 1997; Johannes, 2010)	94
Figure 3.12. (a) Trend of voltage with increasing atomic weight of transition metals. [Adapted from Aydinol, Kohan, Ceder, Cho & Joannopoulous, 1997] (b) Explanation for the drop in voltage at Nickle. (Illustration by Gautam G. Yadav, Adapted from Aydinol, Kohan, Ceder, et al., 1997; Johannes, 2010)	95
Figure 3.13. (a) Voltage trend with respect to anion in LiCoX_2 . (Adapted from Aydinol, Kohan, Ceder, Cho & Joannopoulous, 1997) (b) Explanation for drop in voltage for sulfur. (Adapted from Johannes, 2010) (c) Density of States explanation for drop in voltage for sulfur. (Adapted from Nazri & Pistoia, 2004) (a,b & c illustrations are done by Gautam G. Yadav)	98
Figure 3.14. Illustration of crystal structure bonding influence on voltage. (Illustration by Gautam G. Yadav, Adapted from Johannes, 2010)	99
Figure 3.15. Illustration of the ideal scenario for an electrolyte (top diagram); and SEI layer formation (bottom diagram). (Illustration by Gautam G. Yadav, Adapted from Goodenough & Kim, 2010)	102

Figure	Page
Figure 4.1. (a) Illustration of Sodium Cobalt Oxide (Na_xCoO_2). (b) Illustration of Calcium Cobalt Oxide ($\text{Ca}_3\text{Co}_4\text{O}_9$). (c) Illustration of Strontium Titanate (SrTiO_3). (Illustrations by Gautam G. Yadav)	108
Figure 4.2. (a) Illustration of CoO_6 octahedron and the splitting of its band due to crystal field splitting. (b) Illustration of edge sharing in CoO_2 layer. (Illustrations by Gautam G. Yadav)	112
Figure 4.3. Illustration of the electronic configurations of cobalt ions, Co^{3+} and Co^{4+} . (Illustration by Gautam G. Yadav)	116
Figure 4.4. Illustration of charge conduction in layered cobaltates. (Illustration by Gautam G. Yadav)	118
Figure 4.5. Illustration of small polaron hopping mechanism. (Illustration by Gautam G. Yadav)	120
Figure 5.1. A plot of maximum ZT value of different materials versus temperature (K) labeled by the corresponding material numbers. [Yadav et al., 2011]	133
Figure 5.2. A logarithmic-scale plot of price in dollars per mole for different materials. The material numbers correspond to the respective thermoelectric materials mentioned in Table 5.1. [Yadav et al., 2011]	134
Figure 5.3. A logarithmic-scale plot of the abundance of different elements existing in various thermoelectric materials. [Yadav et al., 2011]	136

Figure	Page
Figure 5.4. A plot of efficiency ratio for various materials. Material numbers correspond to the respective thermoelectric materials as mentioned in Table 5.1. [Yadav et al., 2011].....	141
Figure 6.1. General synthesis method for SrTiO ₃ nanowires. (Illustration by Gautam G. Yadav).....	155
Figure 6.2. (a) XRD patterns of SrTiO ₃ , K ₂ Ti ₈ O ₁₇ and TiO ₂ nanopowder Aldrich, respectively. (b) TEM image of TiO ₂ nanopowder Aldrich (scale bar, 50nm). (c) TEM image of K ₂ Ti ₈ O ₁₇ nanowires (scale bar, 100 nm), inset at the top corner is a HRTEM image of a K ₂ Ti ₈ O ₁₇ (scale bar, 2nm). (d) TEM image of SrTiO ₃ nanowires (scale bar, 100nm), inset at the top corner is a HRTEM image of SrTiO ₃ nanowire (scale bar, 2 nm). [Yadav et al., 2011].....	157
Figure 6.3. Illustration showing the phonon transport in the SrTiO ₃ nanostructured bulk pellet and its approximation as a continuous porous medium. (Illustration by Gautam G. Yadav).....	159
Figure 6.4. Comparison of thermal conductivity plot between bulk crystal data, empirical model and experimental measurements of SrTiO ₃ nanowires. Also presented are the effective phonon mean free paths in bulk crystal and SrTiO ₃ individual nanowires. [Yadav et al. 2011].....	162

Figure	Page
Figure 6.5. (a) TEM image of BaTiO ₃ nanowires (scale bar, 0.2μm), inset at the top corner is the HRTEM image of BaTiO ₃ nanowire (scale bar, 5nm). (b) TEM image of PbTiO ₃ nanowires (scale bar, 100nm), inset at the top corner is the HRTEM image of PbTiO ₃ nanowire (scale bar, 2nm). [Yadav et al., 2011].....	164
Figure 7.1. (a) Schematic representation of the microemulsion synthesis of porous Ca ₉ Co ₁₂ O ₂₈ nanowires. (b) XRD pattern of the precipitate and final Ca ₉ Co ₁₂ O ₂₈ nanowires. [Yadav et al., 2013].....	175
Figure 7.2. (a) FTIR spectrum of the precipitate precursor. (b) TGA analysis on the precipitate precursor.(The blue line corresponds to the heat generated(exothermic) or heat imparted(endothermic) in the annealing process; the red line corresponds to the temperature ramp rate in the annealing process; the green line corresponds to the weight loss in the annealing process) [Yadav et al., 2013].....	176
Figure 7.3. (a) SEM overview of the precipitate nanowires (scale bar is 5μm). (b) SEM of individual precipitate nanowire (scale bar is 500nm). (c) TEM image of precipitate nanowires (scale bar is 0.2μm). (d) EDX of the precipitate nanowires (unidentified peak is from the chamber). [Yadav et al., 2013]	178
Figure 7.4. Illustration of the role of CTAB in the precipitate nanowire formation. (Illustration by Gautam G. Yadav)	180

Figure	Page
Figure 7.5. (a)SEM overview of the $\text{Ca}_9\text{Co}_{12}\text{O}_{28}$ nanowires (scale bar is $5\mu\text{m}$). (b)SEM of individual $\text{Ca}_9\text{Co}_{12}\text{O}_{28}$ nanowire (scale bar is 300nm). (c) TEM image of $\text{Ca}_9\text{Co}_{12}\text{O}_{28}$ nanowires (scale bar is $0.5\mu\text{m}$). (d) TEM image of the individual particles making the $\text{Ca}_9\text{Co}_{12}\text{O}_{28}$ nanowire(scale bar is 5nm), inset showing the high resolution TEM image of $\text{Ca}_9\text{Co}_{12}\text{O}_{28}$ (scale bar is 5nm) [Yadav et al., 2013]	180
Figure 7.6. (a)Thermal conductivity of the SPS $\text{Ca}_9\text{Co}_{12}\text{O}_{28}$ nanowires and the respective phonon and electrical contributions. (b) Electrical conductivity of the SPS $\text{Ca}_9\text{Co}_{12}\text{O}_{28}$ nanowires. (c) Plot of $\ln(\sigma T)$ versus $1000/T$ with linear fit and respective equation shown. (d) Seebeck coefficient of the SPS $\text{Ca}_9\text{Co}_{12}\text{O}_{28}$ nanowires. (e) Power Factor of the SPS $\text{Ca}_9\text{Co}_{12}\text{O}_{28}$ nanowires. (f) Figure of Merit, ZT, of the SPS $\text{Ca}_9\text{Co}_{12}\text{O}_{28}$ nanowires. [Yadav et al., 2013].....	187
Figure 7.7. (a)Charging-discharging curves of $\text{Ca}_9\text{Co}_{12}\text{O}_{28}/\text{Li}$ half-cell cycled at 100mA/g (0.1C). (b)Discharge capacity of $\text{Ca}_9\text{Co}_{12}\text{O}_{28}/\text{Li}$ half-cell cycled at $100(0.1\text{C})$ and $1000(1\text{C})\text{mA/g}$. (c) Coulombic efficiency of $\text{Ca}_9\text{Co}_{12}\text{O}_{28}/\text{Li}$ half-cell cycled at $100(0.1\text{C})$ and $1000(1\text{C})\text{mA/g}$. (d)Retention of discharge capacity of $\text{Ca}_9\text{Co}_{12}\text{O}_{28}/\text{Li}$ half-cell at different charge rates. [Yadav et al., 2013].....	192
Figure 8.1. (a) Schematic representation of the LiCoO_2 synthesis method.(b) XRD spectrum for the different annealing conditions used to synthesize LiCoO_2 (* indicates Cobalt Oxide impurity).(c) TGA curve of the precursor mimicking the 700°C , 3hour annealing run.	206

Figure	Page
Figure 8.2. Raman shift of all the different annealing conditions of LiCoO_2 . The Raman shift for the 600°C 1.5 hour sample was done at 100x magnification.....	207
Figure 8.3. (a) Overview SEM image of the precursor (scale bar 20 μm). (b) Magnified SEM image of a single nanowire precursor(scale bar 500nm). (c) SEM image of LiCoO_2 nanowires synthesized at 600°C for 1.5h (scale bar 500nm). (d) SEM image of LiCoO_2 nanoparticles synthesized at 600°C for 3h (scale bar 3 μm). (e) SEM image of LiCoO_2 nanoparticles synthesized at 700°C for 1.5h (scale bar 5 μm), inset showing HRTEM image of LiCoO_2 nanoparticle (scale bar 2nm). (f) SEM image of LiCoO_2 nanoparticles synthesized at 700°C for 3h (scale bar 5 μm). (g) EDX spectrum of LiCoO_2 synthesized at 700°C for 1.5h.	210
Figure 8.4. (a) Size analysis chart for 600°C, 1.5 hours annealing condition. (b) Size analysis chart for 600°C, 3 hours annealing condition. (c) Size analysis chart for 700°C, 1.5 hours annealing condition. (d) Size analysis chart for 700°C, 3 hours annealing condition.....	211
Figure 8.5. (a) Discharge fade plot of the LiCoO_2 coin cells at 0.1C. (b) Coulombic efficiency plot of the LiCoO_2 coin cells at 0.1C. (c) Differential capacity plot of the LiCoO_2 coin cells for the first cycle at 0.1C, inset is a magnification of the discharge sequence [the colors represent the same conditions as shown in (a) and (b)]. (d) Differential capacity plot of the LiCoO_2 coin cells for the twentieth cycle at 0.1C, inset is a magnification of the charge sequence [the colors represent the same conditions as shown in (a) and (b)]. (e) Differential capacity plot of the nanowire (Sample 1) LiCoO_2 coin cell showing the shift in voltage from first to twentieth cycle at 0.1C. (f) Discharge fade plot of the nanowire (Sample 1) LiCoO_2 coin cells at 0.1C showing the comparison between 80 and 96 weight % LiCoO_2	213

Figure	Page
Figure 8.6. (a) Discharge fade plot of the LiCoO ₂ batteries at 1C. (b) Coulombic efficiency plot of the LiCoO ₂ batteries at 1C. (c) Discharge fade plot of the LiCoO ₂ batteries at 5C. (d) Coulombic efficiency plot of the LiCoO ₂ batteries at 5C. (e) Different rate tests conducted on the LiCoO ₂ batteries. (f) Coulombic efficiency plot of the different rate tests conducted on the LiCoO ₂ batteries.....	220
Figure A.1. Spark Plasma Sintering Process (Illustration by Gautam G. Yadav).....	230
Figure B.1. Coin Cell Assembly Diagram. (Illustration by Gautam G. Yadav)	231
Figure C.1. (a) XRD patterns of SrTiO ₃ , hydrogen titanate and sodium titanate nanowires, respectively. (b) TEM image of sodium titanate (scale bar, 0.2μm). (c) TEM image of hydrogen titanate nanowires (scale bar, 0.5μm). (d) TEM image of SrTiO ₃ nanowires (scale bar, 0.1μm), inset at the top corner is a FFT image of a SrTiO ₃ nanowire.	235
Figure C.2. XRD Spectrum of Case 1 where La _{0.6} Sr _{0.4} TiO ₃ is formed.	237
Figure C.3. XRD Spectrum of Case 2 where it is proved that La _{0.1} Sr _{0.9} TiO ₃ is formed. Magnified images of the respective angles are shown below the main XRD spectrum.	238
Figure D.1. Scanning electron image (SEM) of Calcium Cobalt Oxide (Ca ₃ Co ₄ O ₉).....	241
Figure D.2. X-ray Diffraction spectrum of Calcium Cobalt Oxide(Ca ₃ Co ₄ O ₉).	242

Figure	Page
Figure E.1. (Top and Middle Image) Design of the glass system which allowed the Ti foil to be suspended 1-2mm above the bottom of the petri dish. (Bottom Image) The black part indicates the Co_3O_4 grown on the Ti foil after annealing it for 4 hours at 250°C	245
Figure E.2. Scanning electron images of cobalt oxide (Co_3O_4) nanowires grown on Ti foil.	246

ABSTRACT

Yadav, Gautam Ganapati. Ph.D., Purdue University, December 2013. Design and Assembly of Nanostructured Complex Metal Oxide Materials for the Construction of Batteries and Thermoelectric Devices. Major Professor: Yue Wu.

Thermoelectric devices and lithium-ion batteries are among the fastest growing energy technologies. Thermoelectric devices generate energy from waste heat, whereas lithium-ion batteries store energy for use in commercial applications. Two different topics are bound with a common thread in this thesis – nanotechnology! In fact, nanostructuring is a more preferred term for the approach I have taken herein. Another commonality between these two topics is the material system I have used to prove my hypotheses – complex metal oxides.

Complex metal oxides can be used for both energy generation and storage as they are stable at high temperatures, are benign and inexpensive, and are chemically stable. . Nevertheless, complex metal oxide-based materials have drawbacks when they are used in thermoelectric devices. Since they have high thermal conductivities and low power factors, they have lower thermoelectric figures of merit (ZT). This affects their performance as thermoelectric materials. Nanostructuring can solve this critical problem as thermal conductivity, electrical conductivity and Seebeck coefficient become quasi-independent of each other under these conditions. However, oxide-based materials have proven to be greatly recalcitrant to forming

nanostructures when traditional synthetic methods such as solid-state reactions have been employed. Solid-state reactions usually proceed at extremely high temperatures that are not particularly conducive to forming nanostructures. The first part of this thesis presents novel solution-based synthetic methods that were developed in order to produce novel nanostructured complex metal oxides. Typical structures include nanowires. The second part of this thesis extends this methodology to study the effect of nanostructuring on the thermal conductivity of strontium titanate (SrTiO_3), a promising high temperature thermoelectric material. Ultrathin nanowires of SrTiO_3 were synthesized using a novel hydrothermal reaction. These ultrathin nanowires were compressed into a ‘nanostructured’ bulk pellet through spark plasma sintering. The thermal conductivity measured on the nanostructured bulk pellet showed a drastic decrease compared to bulk SrTiO_3 . Through theoretical modeling it was realized that drastic decrease in thermal conductivity was due to scattering of phonons, which contribute to the lattice thermal conductivity, at the interface of the nanowires.

Another aspect of the thermoelectric research presented herein includes the development of a new phase of misfit layered oxide, calcium cobalt oxide ($\text{Ca}_9\text{Co}_{12}\text{O}_{28}$), for high temperature applications. This phase had hardly been researched in literature because of its high thermal conductivity, thus limiting its use in thermoelectric devices. Through a unique single source precursor-based technique, porous nanowire structures of $\text{Ca}_9\text{Co}_{12}\text{O}_{28}$ were prepared at much lower temperatures than conventional solid-state techniques. Significantly improved ZT were observed in our nanowire system up to 700K due to reduced thermal conductivity and enhanced Seebeck coefficient. The synthetic approach was also applied to prepare different nanostructures (porous nanowires and nanoparticles) of lithium cobalt oxide

(LiCoO₂) by tuning individual reaction parameters. The importance of reaction temperature and the role of nanostructures on the final electrochemical performance of LiCoO₂ was also deduced. Saliiently, the nanostructured electrodes so prepared can withstand high cycling rates and achieve capacities that are close to the theoretical capacity of LiCoO₂ at 0.1C.

CHAPTER 1. INTRODUCTION

The last twenty five years has seen a tremendous rise in the lifestyle of the general populous. This has been due to the parallel rapid development of technology and IT enabled services and e-governance. Energy availability, demand and supply have triggered vociferous debates and a general agreement is on use of non-fossil fuel based renewable sources for development economy. Fossil fuels have played a large role in this remarkable development. However, this development has come at a cost, where we are tackling issues like global warming, the natural flora and fauna being destroyed, and a realization that the fossil reserves may deplete in the near future. Figure 1.1, created by Lawrence Livermore National Laboratory, beautifully demonstrates the energy used only in the United States of America in the year 2012 (Various energy sources can be seen and its contribution to each sector).

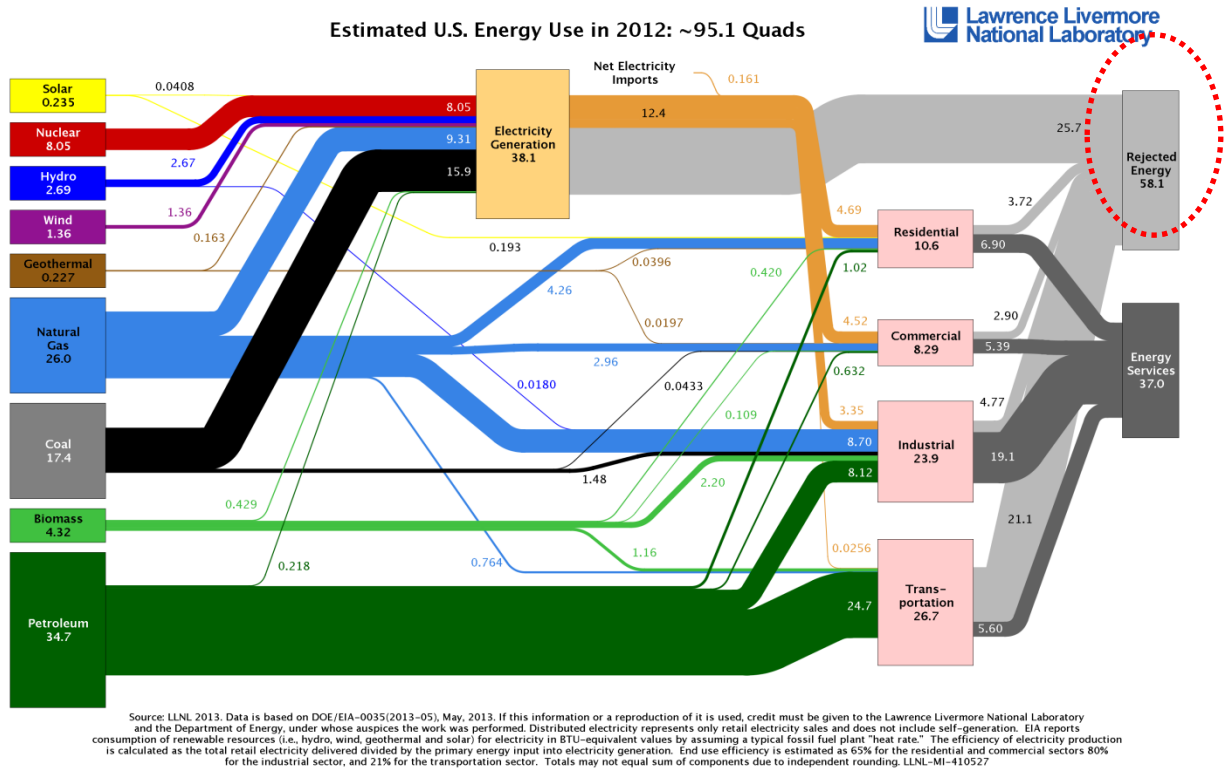


Figure 1.1. Energy flow chart in the United States for the year 2012. [Lawrence Livermore National Laboratory, 2012]

It clearly shows that around 82% of the energy used comes from fossil fuels. Electricity generated from fossil fuels is around 67%. The ramifications of using this large amount of fossil fuels are clearly faced by the environment and eventually by us. The carbon dioxide emissions that primarily come from these fossil fuel sources clearly affect the environment negatively. Figure 1.2 demonstrates the carbon emissions from the various sources as shown in Figure 1.1.

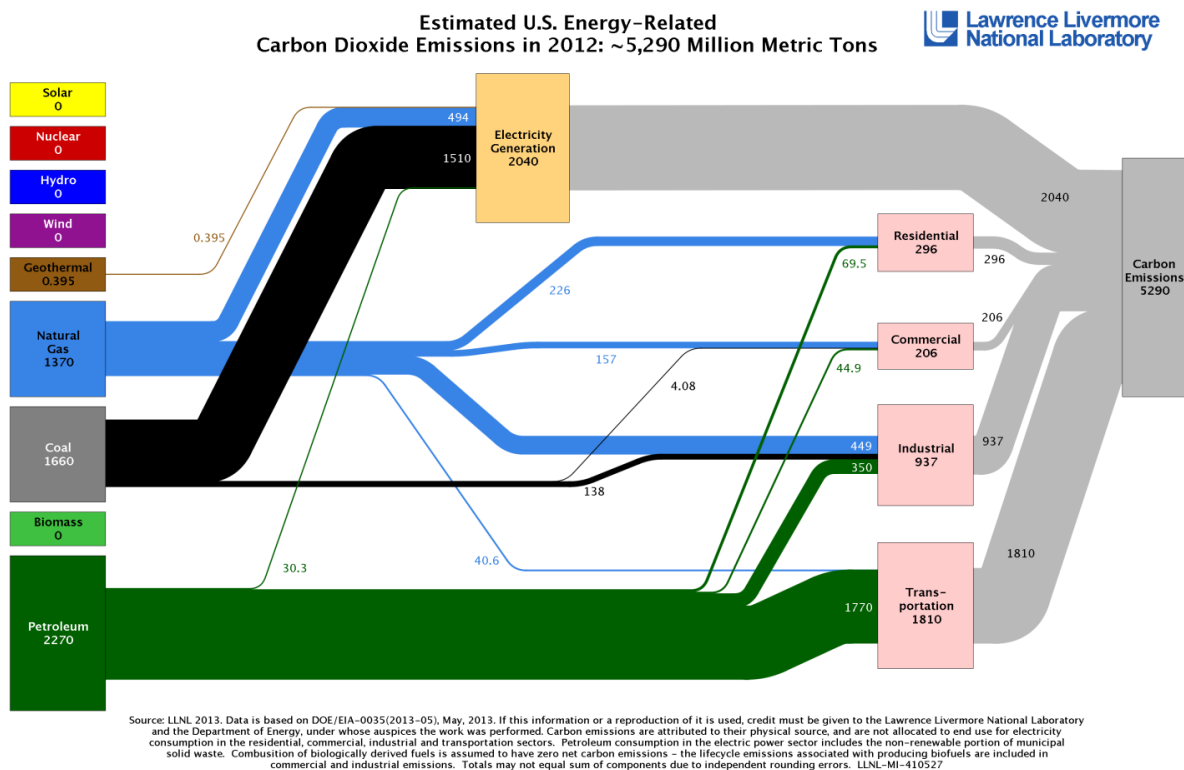


Figure 1.2. Carbon dioxide emission from the various sources shown in Figure 1.1. [Lawrence Livermore National Laboratory (Carbon Flow), 2012]

Around 67% of fossil fuels that contribute to electricity generation contribute almost 100% to carbon dioxide emissions in the environment. It becomes clear that our reliance on fossil fuel must end for the betterment of our future.

In Figure 1.1., the amount of rejected energy is more than 50%, as pointed by the red-dotted circle. This is a clear indication of bad energy management by users. If a small percentage of the wasted heat energy could be converted back to electricity this would have a really positive impact on our society and reduce our dependence on fossil fuels. The question that

comes to mind is there a technology that can convert waste heat to electricity? The answer is ‘thermoelectrics’. Thermoelectrics in the process of converting waste to electricity, which is a major theme of the current thesis. A brief introduction to this technology is given in Section 1.1., and the physics behind thermoelectrics is explained in Chapter 2.

Another vital part of the energy spectrum is storage. Much of the wasted energy shown in Figure 1.1., if stored properly, could potentially reduce the burden of electricity in the long run. Energy storage is also important in other technologies, for example - smart phones have become ubiquitous, electric cars are being introduced on the roads, and many other technologies that were once considered to be stuff of science fiction. Lithium-ion batteries are primarily to be credited for the rapid advancement of these technologies.

New low-carbon energy sources and energy conservation techniques need to be developed in order to improve the sustainability of our society and reverse the environmental impact of global climate change due to the combustion of fossil fuels.

In the next two sections are presented, a brief introduction of thermoelectrics and lithium-ion batteries, and the current trends that are being researched in the respective fields.

1.1 Thermoelectrics

Converting waste heat back to electricity with thermoelectric generators from various sources including residential heating, automotive exhaust, and industrial processes, seems to be particularly promising because thermoelectric generators are light-weight, silent, reliable, and scalable for power generation [Snyder, 2008]. The operating mechanism of a thermoelectric generator is based on the Seebeck effect. Briefly, when a thermoelectric material is bridged between a temperature gradient, charge carriers such as electrons and holes diffuse across the gradient and generate electricity (Figure 1.3). The performance of a thermoelectric device is evaluated by a metric known as the figure of merit, (ZT)

$$ZT = \frac{\sigma S^2 T}{\kappa} \dots\dots\dots(1.1)$$

Here σ is the electrical conductivity ($S.m^{-1}$), κ is the thermal conductivity ($W.m^{-1}.K^{-1}$), S is the Seebeck coefficient (conventionally in $\mu V.K^{-1}$), and T is the average temperature of two sides of the device *viz.* $\frac{(T_1+T_2)}{2}$. The quantity σS^2 is called the power factor. Greater values of ZT indicate greater thermodynamic efficiency, and values of at least 3-4 are considered to be essential for a thermoelectric device for it to be competitive with current mechanical generation and refrigeration methods.

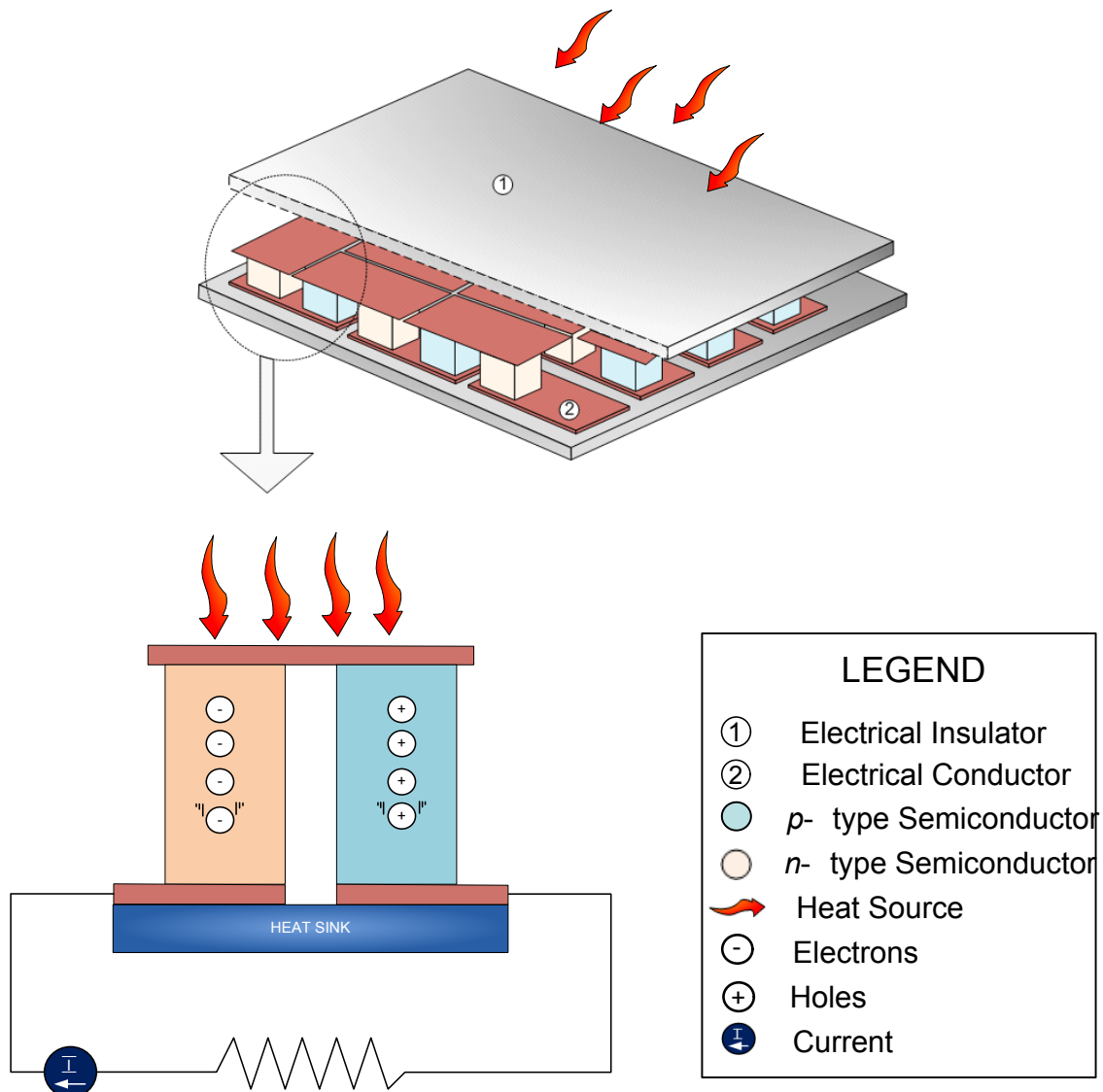


Figure 1.3. Schematic representation of a power generation thermoelectric device.

(Illustration by Gautam G. Yadav)

Interest in thermoelectric devices appears to have peaked in recent years, and considerable effort is now being directed to finding better thermoelectric materials, and synthesizing

materials with molecular characteristics that render themselves to higher ZT values is now a fervent research undertaking in materials science. One example of such research includes increasing the power factor and/or decreasing the thermal conductivity. The power factor of a material can be maximized by altering its molecular properties and architecture and include methods such as doping the material or synthesizing novel nanostructured materials. Conversely, thermal conductivity can be minimized through alloying, using materials with lower thermal conductivities, as well as nanostructuring [Sootsman, Chung & Kanatzidis, 2009].

Over the past three decades, much work has been directed at finding more efficient materials and trying to increase the ZT value, but until the last decade scientists were only able to demonstrate incremental gains in ZT values. However, in the last decade or so, sterling advances in materials science have greatly accelerated progress in this domain and the number of materials now being considered for thermoelectric applications has increased substantially. Two prominent examples include bulk thermoelectric materials doped with heavy ion species, and low-dimensional or nanomaterials. Doping bulk materials with heavy ion species causes the materials to exhibit large vibrational amplitudes when their structural sites are only partially filled, thereby providing effective phonon scattering. Nanomaterials, owing to their property of being able to introduce quantum confinement effects, makes good candidates for enhancing the power factor. Of these two classes of materials, nanomaterials have emerged as an early favorite, particularly since it is possible to conveniently vary S , σ and κ quasi-independently when the length scales are sufficiently small for quantum confinement to take place. The great difficulty in varying S , σ and κ

independently in bulk materials makes such materials slightly inferior alternatives. For example, as mentioned in Chapter 2, in bulk materials, an increase in S would result in a decrease in σ , and an increase in σ would increase the electronic and lattice contribution to κ [Dresselhaus, Chen, Tang, et al., 2007]. Amongst nanomaterials, use of one-dimensional nanowires as thermoelectric materials is gaining ground due to their unique properties that allow a ready increase in ZT . It is shown in Chapter 2 that the electronic density of states undergoes a dramatic change and becomes sharper near the band edge for a 1-D system, which results in a higher power factor for a given carrier concentration. Also, the lattice thermal conductivity is significantly reduced due to increased phonon scattering at the interfaces [Lin, Rabin & Dresselhaus, 2002]. Nanowires fabricated with materials such as $\text{Ca}_{0.18}\text{Ni}_{0.03}\text{Co}_2\text{Sb}_{14}$, $\text{Ba}_8\text{Ga}_{16}\text{Ge}_{30}$, and $\text{Yb}_{11}\text{MnSb}_{14}$ have been reported to yield high ZT values at various temperatures [Kuznetsov, Kuznetsova, Kaliazin & Rowe, 2003; Puyet, Dausher, Lenoir, et al., 2005; Akrap, Barisic, Forro, et al., 2007].

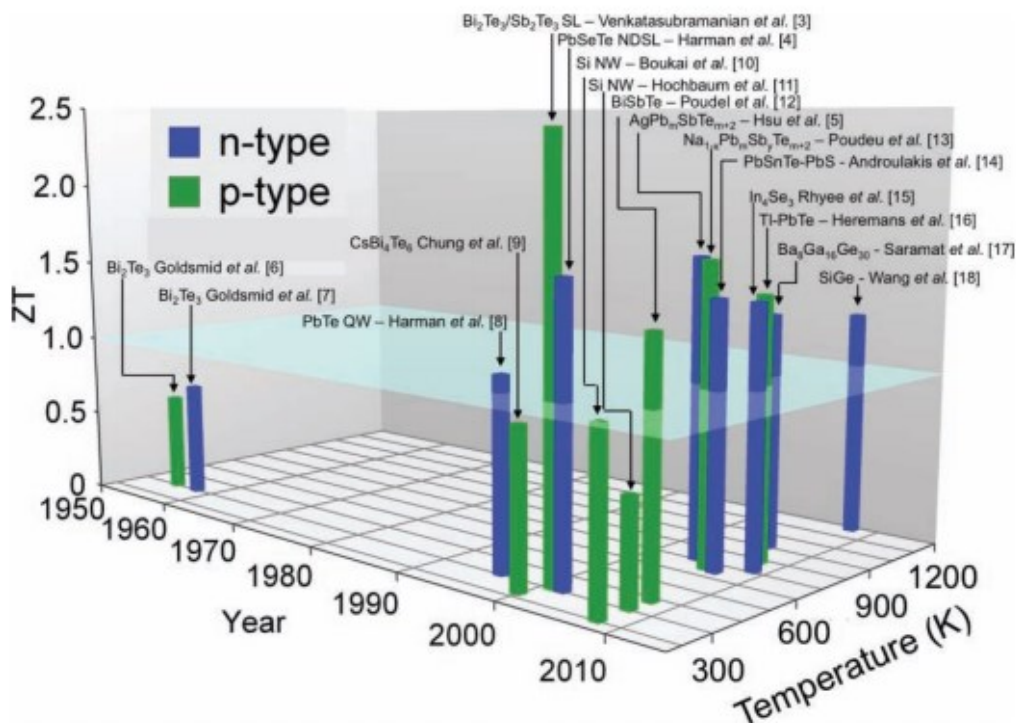


Figure 1.4. ZT improvement of various materials over the last 60 years. The improvements shown are all laboratory-based results and were some form of nanostructured-based materials. [Vineis, Shakouri, Majumdar & Kanatzidis, 2010]

Presently, commercially-available thermoelectric devices exhibit ZT values of 0.8 and operate at an efficiency of about 5-6% [Sootsman, Chung & Kanatzidis, 2007]. The device efficiency is directly related to the ZT value and could be increased to as high as 30% if the ZT value reaches 4. Incidentally, ZT values greater than 1 have been obtained in laboratory conditions at temperatures in excess of 600 K. For example, ZT values as high as 1.3 and 1.32 have been observed for $\text{Ba}_{0.30}\text{Ni}_{0.05}\text{Co}_{0.95}\text{Sb}_{12}$ and $\beta\text{-Zn}_4\text{Sb}_3$, respectively, at temperatures of 900K

and 670K, in that order [Tanga, Zhang, Chen, et al., 2005; Caillat, Fleurial & Borshchevsky, 1997]. Although these values are promising for practical applications, some of these materials are not quite suitable for high temperature operations above 1000 K due to melting, decomposition or vaporization [Ohta, Kim, Mune, et al., 2007].

1.2 Lithium-ion Batteries

Sony's introduction of lithium-ion batteries in the market in 1990's changed the world of batteries [Nazri & Pistoia, 2004]. Lithium-ion batteries now dominate the world of batteries. This is for a good reason – it provides the highest energy density compared to other battery systems in terms of weight and size (Figure 1.5). Lithium-ion batteries are now extensively used in many of our day-to-day activities like cell phones, laptop batteries, electric vehicles, etc. Compared to thermoelectrics, the term 'lithium-ion' has become ubiquitous. A thorough explanation behind the physics governing lithium-ion batteries is given in Chapter 3. However, a summary of its mechanism is still explained in the next paragraph to help the reader acquaint themselves with this technology.

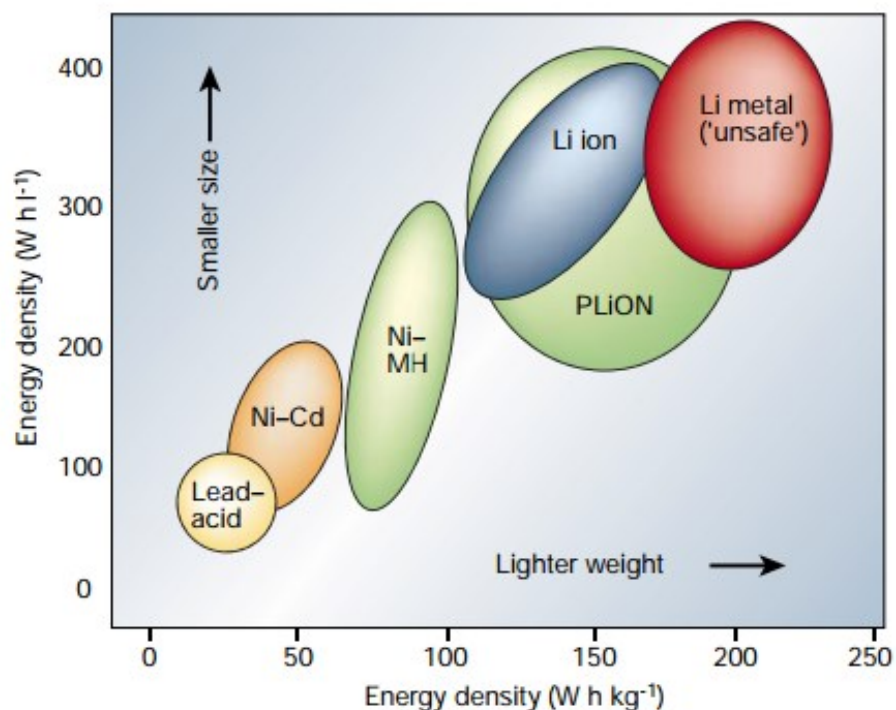


Figure 1.5. Energy density of various battery systems based on weight and size. [Tarascon & Armand, 2001]

Lithium-ion batteries consist of two electrodes - an anode and cathode. Either the anode or cathode, or both, contain lithium ions. The electrodes are separated by an electrolyte and separator. The lithium ions shuttle between the electrodes through the electrolyte solution, meanwhile at the same time, electrons are liberated that travel outside through the external circuit to perform work. This mechanism is explained in-detail in Chapter 3.

Performance of battery is judged by its capacity to store specific charge ($\text{Ah}^{-1}\text{kg}^{-1}$) and the electrical energy that is able to deliver as a function of voltage (V). Lithium-ion batteries

consist of material systems that are able to work at high potentials and store high amount of charge, hence making it the dominant battery system. The cathode material systems usually used are lithium transition metal oxide-based systems [Tarascon & Armand, 2001]. The cathode materials exhibit different crystal structure characteristics. Some are layered-based systems that are able to hold the lithium ions between layered sheets of transition metal oxides [Tarascon & Armand, 2001]. A few notable examples are lithium cobalt oxide (LiCoO_2), lithium nickel oxide (LiNiO_2), a unique phase of lithium manganese oxide and even combinations of the three transition metals like lithium cobalt nickel manganese oxide ($\text{LiCo}_{0.3}\text{Ni}_{0.3}\text{Mn}_{0.3}\text{O}_2$) [Tarascon & Armand, 2001]. LiCoO_2 was the first cathode material to be commercialized and it is still intensely researched today because of its very high capacity of 140mAh/g at 4.2V [Nazri & Pistoia, 2004]. Spinel-type structures are also used as cathode materials. The notable example is lithium manganese dioxide (LiMn_2O_4). Manganese comes before cobalt in the periodic table, so compounds containing manganese are able to store more specific charge compared to cobalt-based compounds. However, spinel-based compounds exhibit detrimental electrochemical characteristics due to crystal structure instability during cycling. The new cathode materials are olivine-based crystal structures like lithium iron phosphate (LiFePO_4). One important requirement of cathode materials is that they should operate at high potentials, as that is the important characteristic of lithium-ion batteries. The high potentials arise from bonding between the transition metal oxides with oxygen, the explanation for this concept, along with the materials crystal structures and electrochemical characteristics are discussed in Chapter 3.

Anode materials that are used in lithium-ion batteries also exhibit a wide range of crystal structures, and depending on the type of crystal structure, the reaction mechanisms are different. Lithium metal was the most commonly used anode in lithium-ion batteries as it provided the lowest potential and high capacity. However, due to the safety aspects of using lithium metal like dendrite growth, and its very reactive nature when exposed to air, researchers started looking to other materials [Nazri & Pistoia, 2004]. Graphite was the next material system to be handed down the torch. It also has a layered crystal structure that made it easy to be used as a counterpart to lithium cobalt oxide. It was also commercialized along with lithium cobalt oxide in the first commercial lithium-ion batteries. However, its capacity was quite low compared to that of lithium metal, and at high rates, lithium plated on the surface to grow dendrites that would penetrate the separator and short-circuit the battery. This results in explosion hazards and it became imperative to look at other materials as possible anodes in lithium-ion batteries. New anode materials like silicon are being researched as possible future anodes as well. Silicon has a very high capacity, around 4200mAh/g, and its potential range is close to that of lithium metal. Its reaction mechanism is based on alloying. However, it has a major disadvantage of very large volume expansion, more than 400%. The expansion and contraction of silicon during cycling makes it lose its electrical contact and, hence, exhibit a rapid drop in capacity within a few cycles. [McDowell, Lee, Wang & Cui, 2012] Researchers have found a way to mitigate this problem by coating a layer of silicon oxide over silica to negate the volume expansion [Wu, Chan, Choi, et al., 2012]. Another anode material that has been extensively researched is transition metal oxides like cobalt oxide (CoO , Co_3O_4), manganese oxide (Mn_2O_3), etc. These transition metal

oxides can operate at low potentials and deliver very high capacity. The reaction mechanism behind this system is based on displacement reaction [Obrovac, Dunlap, Sanderson & Dahn, 2001; Sharma, Shaju, Subba Rao & Chowdari, 2004]. The lithium ions get into the crystal structure of the transition metal oxides; however, it is not able to accommodate all of the lithium ions and it results in breakdown of the crystal structure into transition metal and lithium oxide (Li_2O) [Obrovac, Dunlap, Sanderson & Dahn, 2001; Sharma, Shaju, Subba Rao & Chowdari, 2004].

Lithium metal, graphite and transition metal oxides will be discussed in-detail in Chapter 3.

Figure 1.6 demonstrates the commonly used materials in lithium-ion batteries.

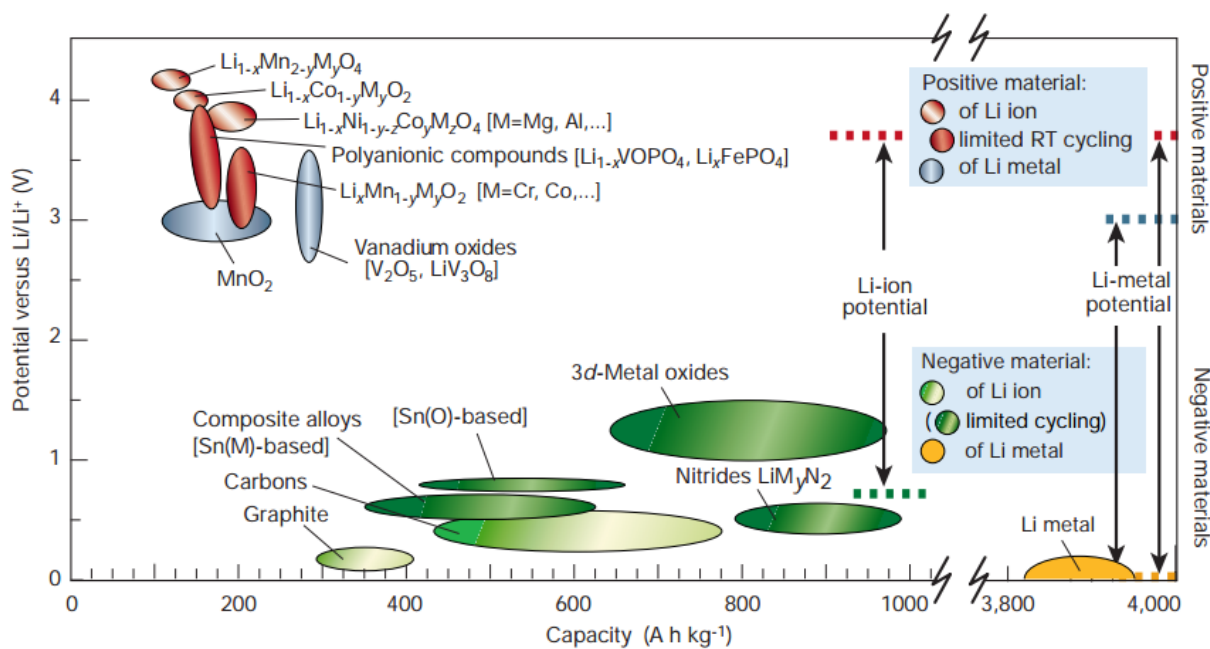


Figure 1.6. The potential ranges and the respective capacities of various cathode and anode materials used in lithium-ion batteries. [Tarascon & Armand, 2001]

The capacity of the materials described aforementioned fade over time and this fade is rapidly increased as the charging and discharging times are reduced. The batteries tested in research laboratories are charged and discharged for over 10 hours; however, for commercial purposes the batteries need to be charged within minutes and this brings about a failure in battery performance. This is crucial if electric vehicles need to be introduced in the market and more importantly, if they have to compete with the traditional fuel-based cars. Also, another requirement is that the batteries should last more than 2000 cycles to be deemed worthy to be used in electric vehicles. Also, it is generally considered that a battery has failed if it has lost more than 80% of its initial capacity. So, lithium-ion batteries are supposed to deliver high powered performance at rapid rates over 2000 cycles without losing a significant amount of its capacity. This is a remarkable challenge that is required for this battery system. The goals are not improbable; it can be achieved through astute means. New electrode architectures can be developed that allow for lithium ions to move freely and rapidly between the electrodes [Zhang, Yu & Braun, 2011]. The electrode materials need to be made conductive for rapid electron transfer. The electrodes need to come in contact with the electrolyte, so that all of the electrode material can deliver the needed performance. All of these requirements can be achieved through designing novel nanostructured electrodes. Nanostructures drastically reduce the diffusion time due to the reduced dimensions. The high surface areas of the electrodes allow the electrolyte to be in contact with all the nanomaterials and participate in the electrochemical processes.[Guo, Hu & Wan, 2008] Nanostructuring of the respective electrode materials can help in addressing some of the challenges facing this field.

1.3 Thesis Objective and Structure

Oxides are the primary materials that are used in lithium-ion batteries. They are chemically and physically stable, and it makes sense to use them as potential high temperature materials for high temperature thermoelectric materials as well. It must be apparent by now that transition metal oxides play a vital role in the energy story. It can be used to generate and store electricity. The two main characters – transition metal oxides and nanostructuring- if tailored properly, can play a major role in alleviating some of the challenges facing the respective fields.

This thesis is about designing of different nanostructures of transition metal oxides for thermoelectric and battery applications, especially nanowires. Designing and synthesizing nanostructures, let alone nanowires, is an arduous task. Solid state reactions are usually the method of choice to make complex oxide-based materials. However, solid-state reactions require long reaction times and very high temperatures to synthesize the right phase of the oxide material. These reaction conditions are not thermodynamically favorable to create nanostructures. These issues have been addressed and novel synthesis routes have been developed to create nanowires and nanostructures of perovskite – based materials like strontium titanate for thermoelectric applications and a new phase of layered-based structure, calcium cobalt oxide ($\text{Ca}_9\text{Co}_{12}\text{O}_{28}$) for thermoelectric and lithium-ion battery applications. The synthesis methods developed to create these materials were shown to be transferable to other systems like lead titanate, barium titanate and lithium cobalt oxide.

Different nanostructures of lithium cobalt oxide were synthesized and the relationship between the electrochemical properties and different nanostructures were studied as well.

The organization of this thesis is based on the idea of first, introducing the reader to various underlying physics behind the respective applications, and then studying the respective systems for the respective application. In Chapter 2, the efficiency of power-generation thermoelectric devices is derived and the origin of ZT is illustrated. The physical insight into each of the intrinsic material properties that affect ZT are discussed, with their relevant equations derived as well. Finally, the physical concepts behind nanostructuring are derived and discussed to give the reader a thorough understanding behind nanostructured thermoelectrics.

Chapter 3 explains the detailed mechanism behind lithium-ion batteries and the requirements of important components of the battery – cathode, anode and electrolyte. Also, the origin of voltage is explained and a general discussion of the crystal structure of the most common electrode materials is carried out.

Chapter 4 explains the thermoelectric properties of oxide-based systems. The relevant equations for Seebeck coefficient are derived and the electrical conduction mechanism is discussed.

Chapter 5 presents a detailed feasibility and sustainability analysis conducted on various material systems for different temperature thermoelectric applications. It lays the ground work for proving that oxides are indeed better for high temperature thermoelectric applications based on cost, abundance, toxicity and efficiency.

Chapter 6 describes the use of a novel synthesis method to produce ultrathin nanowires of perovskite-based systems like strontium titanate (SrTiO_3), barium titanate (BaTiO_3) and lead titanate (PbTiO_3). The thermal conductivity of the strontium titanate nanowires were compared to that of the bulk crystal and with the aid of theoretical work done by Dr. Bo Qiu, the results were analyzed.

Chapter 7 describes the development of a novel microemulsion method to synthesize porous nanowires of new phase layered-based compound, calcium cobalt oxide ($\text{Ca}_9\text{Co}_{12}\text{O}_{28}$). The results of the thermoelectric and electrochemical properties are presented and discussed.

Chapter 8 presents the study of the relationship of electrochemical properties and different nanostructures of lithium cobalt oxide (LiCoO_2). The different nanostructures of lithium cobalt oxide were synthesized through the microemulsion method described in Chapter 7. Interesting property relationships are seen and presented in the chapter.

Finally, Chapter 9 is the conclusion to the thesis including scope for future work.

1.4 Conclusion

In this chapter, a general introduction on the genesis of the current work is given including the structure of the thesis. The subsequent chapters will deal with the details of actual work.

1.5 References

Akrap, A.; Barišić, N.; Forro, L.; Mandrus, D.; Sales, B.C. High-Pressure resistivity and thermoelectric power in $\text{Yb}_{14}\text{MnSb}_{11}$. *Phys. Rev. B.* **2007**, *76* (8), 5203.

Caillat, T.; Fleurial, J.P.; Borshchevsky, A. Preparation and thermoelectric properties of semiconducting Zn_4Sb_3 . *J. Phys. Chem. Solids.* **1997**, *58* (7), 1119-1125.

Dresselhaus, M.S.; Chen, G.; Tang, M.Y.; Yang, R.G.; Lee, H.; Wang, D.Z.; Ren, Z.F.; Fleurial, J.P.; Gogna, P. New Directions for Low-Dimensional Thermoelectric Materials. *Adv. Mater.* **2007**, *19*, 1-12.

Guo, Y.-G.; Hu, J.-H.; Wan, L.-J. Nanostructured Materials for Electrochemical Energy Conversion and Storage Devices. *Adv. Mater.*, **2008**, *20*, 2878-2887.

Kuznetsov, V.L.; Kuznetsova, L.A.; Kaliazin, A.E.; Rowe, D.M. Effect of partial void filling on the transport properties of $\text{Nd}_x\text{Co}_4\text{Sb}_{12}$. *J. Phys.: Condens. Matter.* **2003**, *15* (29), 5035-5048.

Lawrence Livermore National Laboratory. Energy Flow: US Energy Flow 2012. https://flowcharts.llnl.gov/content/energy/energy_archive/energy_flow_2012/2012new2012newUSEnergy.png (accessed August 29, 2013)

Lawrence Livermore National Laboratory. Energy Flow: US Carbon Flow 2012. https://flowcharts.llnl.gov/content/carbon/carbon_emissions_2012/2012_US_Carbon.png (accessed August 29, 2013)

Lin, Y., Rabin.O, Dresselhaus, M.S. Segmented Nanowires: A theoretical study of thermoelectric properties. *Proc. 21st Int. Conf. Thermoelectrics*. **2002**, p.265.

McDowell, M.T.; Lee, S.W.; Wang, C.; Cui, Y. The Effect of Metallic Coatings and Crystallinity on The Volume Expansion of Silicon During Electrochemical Lithiation/Delithiation. *Nano Energy* **2012**, *1*, 401-410.

Nazri, G-A.; Pistoia, G. *Lithium Batteries: Science and Technology*; Kluwer Academic Publishers: Masschusetts, **2004**; pp 3-4.

Obrovac, M.N.; Dunlap, R.A.; Sanderson, R.J.; Dahn, J.R. The Electrochemical Displacement Reaction of Lithium with Metal Oxides. *J. Electrochem. Soc.* **2001**, *148*, A576-A588.

Ohta, H.; Kim, S.; Mune, Y. et al. . Giant thermoelectric Seebeck coefficient of a two-dimensional electron gas in SrTiO₃. *Nat. Mater.* **2007**, *6*, 129-134.

Puyet, M.; Dausher, A.; Lenoir, B.; Dehmas, M.; Steiwe, C.; Müller, E. Beneficial effect of Ni substitution on the thermoelectric properties in partially filled Ca_yCo_{4-x}Ni_xSb₁₂ skutterudites. *J. Appl. Phys.* **2005**, *97* (8), 083712.1-083712.4.

Sharma, N.; Shaju, K.M.; Subba Rao, G.V.; Chowdari, B.V.R. Mixed Oxides Ca₂Fe₂O₅ and Ca₂Co₂O₅ as Anode Materials for Li-Ion Batteries. *Electrochimica Acta* **2004**, *49*, 1035-1043.

Snyder, G.J. Small Thermoelectric Generators. *The Electrochemical Society Interface*.**2008**, 54-56.

Sootsman, J.R.; Chung, D.Y.; Kanatzidis, M.G. New and Old Concepts in Thermoelectric Materials. *Angew. Chem. Int. Ed.* **2009**, *48*, 8616-8639.

Sootsman, J.R.; Chung, D.Y.; Kanatzidis, M.G. Nanostructured Thermoelectric Materials and High-Efficiency Power-Generation Modules. *J. Electron. Mater.* **2007**, *36*, 704-710.

Tanga, X.; Zhang, Q.; Chen, L.; Goto, T.; Hirai, T. Synthesis and thermoelectric properties of p-type-and n-type filled skutterudite $R_yM_xCo_{4-x}Sb_{12}$. *J. Appl. Phys.* **2005**, *97* (9), 093712.1-093712.10.

Tarascon, J.M.; Armand, M. Issue and challenges facing rechargeable lithium batteries. *Nature*, **2001**, *414*, 359-367.

Wu, H.; Chan, G.; Choi, J.W.; Ryu, I.; Yao, Y.; McDowell, M.T.; Lee, S. W.; Jackson, A.; Yang, Y.; Hu, L.; Cui, Y. Stable cycling of double-walled silicon nanotube battery anodes through solid-electrolyte interphase control. *Nature Nanotechnology*, **2012**, *7*, 310-315.

Zhang, H.; Yu, X.; Braun, P.V. Three-dimension bicontinuous ultrafast-charge and – discharge bulk battery electrodes. *Nature Nanotechnology*, **2011**, *6*, 277-281.

CHAPTER 2. PHYSICAL PRINCIPLES BEHIND THERMOELECTRICS

As mentioned before, thermoelectrics is the science dealing with the conversion of heat into electricity. This chapter will delve deep into explaining the macroscopic derivations of the governing thermoelectric equations and principles. In addition to the macroscopic derivations, the concept of nanostructured thermoelectrics will be discussed as well. The derivations in this chapter are not unique; they have been taken from previous work.

2.1 Deriving the thermoelectric figure of merit (ZT), and efficiency of a device for power generation (η)

As mentioned before, the thermoelectric figure of merit (ZT) is dimensionless, and most importantly, it is used extensively as a metric in thermoelectric literature to give insight into the intrinsic properties of a material. ZT arises from deriving the efficiency or the coefficient of performance (related to refrigeration) of a thermoelectric device. In engineering, terms like efficiency or coefficient of performance are derived through utilizing first principle methods like shell balances. With this in mind, a detailed derivation for the respective terms is shown in the following paragraphs.

Consider a power generation device as shown in Figure 2.1.

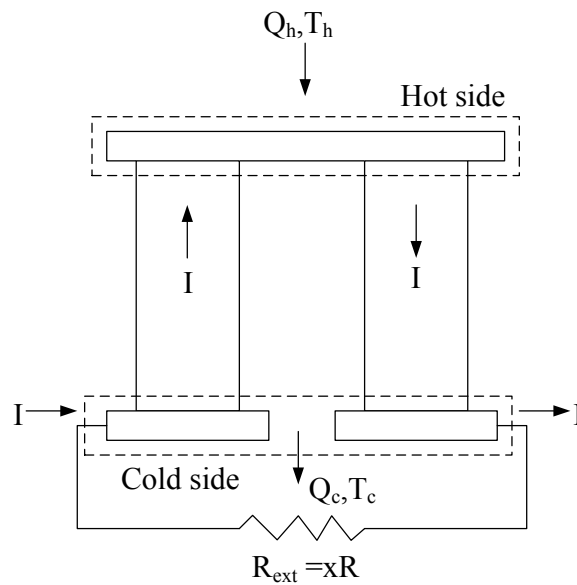


Figure 2.1. Thermoelectric power generation device. (Illustration by Gautam G. Yadav)

As explained previously, every material has a Seebeck coefficient (S) associated with it, so when a current passes through the material, a Seebeck effect is generated. Likewise, a thermal conductance (K) is also associated with any material experiencing heat flow through it. Another term that is of importance when current flows through a material is joule heating. Joule heating is the heat generated in a material due to current flow. These terms are vital when conducting shell balances. [Terasaki, 2010] Therefore, by applying a shell balance on the hot side of the power generation device, the following is obtained.

$$\text{Heat in} = \text{Heat out} \dots\dots\dots(2.1)$$

$$Q_h = S \cdot T_h \cdot I - \frac{1}{2} I^2 R + K \Delta T \dots\dots\dots(2.2)$$

Similarly for the cold side,

$$Q_c = S \cdot T_c \cdot I + \frac{1}{2} I^2 R + K \Delta T \dots\dots\dots(2.3)$$

The power generation is connected to an external load, R_{ext} , during device operation.

[Terasaki, 2010] Therefore, the power generated in the device is:

$$P = V \cdot I = I^2 \cdot R_{ext} \dots\dots\dots(2.4)$$

The current, I , is given by:

$$I = \frac{V}{R_T} \dots\dots\dots(2.5)$$

The total resistance, R_T , is comprised of the resistance of the material, R , and the external load resistance, R_{ext} . If we assume that the R_{ext} is proportional to R by a constant, x ($0 \leq x \leq 1$), then:

$$I = \frac{V}{R + R_{ext}} \dots\dots\dots(2.6)$$

$$I = \frac{V}{R + x \cdot R} \dots\dots\dots(2.7)$$

The voltage, V , is the Seebeck coefficient, S , times the temperature difference, ΔT .

$$I = \frac{S\Delta T}{(1+x)R} \dots\dots\dots(2.8)$$

Therefore, the complete expression for power generated in the device is [Terasaki, 2010]:

$$P = \frac{(S\Delta T)^2 x R}{(1+x)^2 R^2} = \frac{(S\Delta T)^2 x}{(1+x)^2 R} \dots\dots\dots(2.9)$$

If $x = 1$, then the maximum power, P_{max} , generated is [Terasaki, 2010]:

$$P_{max} = \frac{(S\Delta T)^2}{4R} = \frac{S^2 \Delta T^2}{4R} \dots\dots\dots(2.10)$$

The term $S^2 R^{-1}$ in the above equation represents the power factor, which is one of the most widely used terms in thermoelectric literature, and it directly influences the power delivered by the device.

The efficiency of the device is simply then the work performed by the device from the heat absorbed [Terasaki, 2010]:

$$\eta = \frac{W}{Q_h} \dots\dots\dots(2.11)$$

$$\eta = \frac{IV}{S.T_h.I - \frac{1}{2}I^2.R + K.\Delta T} \dots\dots\dots(2.12)$$

$$I = \frac{S\Delta T}{(1+x)R} \dots\dots\dots(2.13)$$

$$\eta = \frac{V}{S.T_h - \frac{1}{2}I.R + \frac{K.\Delta T}{I}} \dots\dots\dots(2.14)$$

$$\eta = \frac{V}{S.T_h - \frac{1}{2(1+x)}.R + \frac{K.\Delta T.R.(1+x)}{S.\Delta T}} \dots\dots\dots(2.15)$$

$$\eta = \frac{S.\Delta T}{S.T_h - \frac{1}{2(1+x)} + \frac{K.R.(1+x)}{S}} \dots\dots\dots(2.16)$$

$$\eta = \frac{S.\Delta T}{S.T_h - \frac{1}{2(1+x)} + \frac{K.R.S.(1+x)}{S^2}} \dots\dots\dots(2.17)$$

$$\eta = \frac{\Delta T}{T_h - \frac{1}{2(1+x)} + \frac{K.R.(1+x)}{S^2}} \dots\dots\dots(2.18)$$

From the above expression, the last term in the denominator comprises of the three intrinsic properties of a material that coin up to form the term – figure of merit, Z. Therefore,

$$Z = \frac{S^2}{K.R} \dots\dots\dots(2.19)$$

Hence,

$$\eta = \frac{\Delta T}{T_h - \frac{1}{2(1+x)} + \frac{(1+x)}{Z}} \dots\dots\dots(2.20)$$

$$\eta = \frac{(1+x).\Delta T}{(1+x).T_h - \frac{1}{2}\Delta T + \frac{(1+x)^2}{Z}} \dots\dots\dots(2.21)$$

Let $(1 + x) = a$

To get the maximum efficiency the derivative of efficiency with respect to ‘a’ should be zero, therefore:

$$\frac{d\eta}{da} = 0 = \frac{\Delta T}{aT_h - \frac{1}{2}\Delta T + \frac{a^2}{Z}} - \frac{a\Delta T}{\left(aT_h - \frac{1}{2}\Delta T + \frac{a^2}{Z}\right)^2} \left[T_h + \frac{2a}{Z}\right] \dots\dots\dots(2.22)$$

Solving the above equation for ‘a’:

$$a = \sqrt{\frac{Z(T_c - T_h)}{2}} \dots\dots\dots(2.23)$$

Therefore,

$$\eta_{max} = \frac{\sqrt{\frac{Z(T_c - T_h)}{2}} \cdot \Delta T}{\sqrt{\frac{Z(T_c - T_h)}{2}} \cdot T_h - \frac{1}{2}\Delta T + \frac{T_c - T_h}{2}} \dots\dots\dots(2.24)$$

After manipulating the above equation, we finally get the maximum efficiency of a thermoelectric device:

$$\eta_{max} = \frac{T_h - T_c}{T_h} \frac{\sqrt{ZT_{avg} + 1} - 1}{\sqrt{ZT_{avg} + 1} + \frac{T_c}{T_h}} \dots\dots\dots(2.25)$$

T_{avg} is the average temperature between the hot and cold ends of the thermoelectric device.

In the above equation, we finally see origin of the dimensionless thermoelectric figure of merit, ZT_{avg} . Before we delve into the thermoelectric figure of merit, it is of importance to

note that the thermoelectric device efficiency is dependent of the Carnot efficiency and it obeys the laws of thermodynamics.

$$\eta_{carnot} = \frac{T_h - T_c}{T_h} \dots \dots \dots (2.26)$$

$$\eta_{max} = \eta_{carnot} \cdot \frac{\sqrt{ZT_{avg}+1} - 1}{\sqrt{ZT_{avg}+1} + \frac{T_c}{T_h}} \dots \dots \dots (2.27)$$

From the above equation, a plot can be generated of efficiency versus temperature for various ZT values.

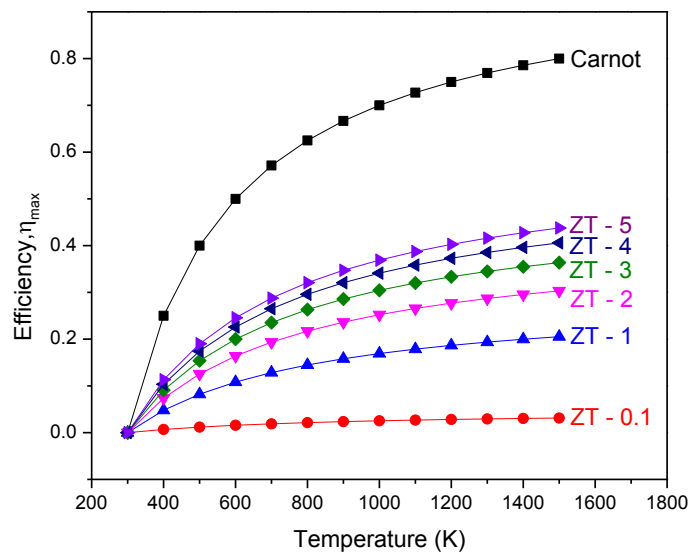


Figure 2.2. Plot of efficiency, η_{max} versus temperature. Temperature of the cold side was taken to be 300K.

From equation 2.27 and Figure 2.2, we can see that as ZT approaches infinity, the efficiency, η_{\max} , reaches the Carnot efficiency – this is also justified through generation of Joule heat accompanied by the irreversible process of charge transport that results in the conversion process in a thermoelectric device [Terasaki, 2010].

It is clear by now that ZT plays a vital role in determining the device efficiency. ZT was derived from equation 2.19, wherein T is factored into the equation to make it a dimensionless quantity.

$$ZT = \frac{S^2}{K.R} T \dots\dots\dots(2.28)$$

R , the resistance, and K , the thermal conductance, can be related to thermoelectric material geometric parameters – area, A , and length, l .

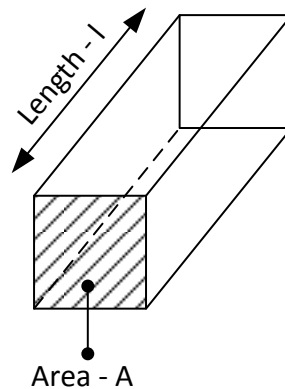


Figure 2.3. Geometric parameters of thermoelectric leg.(Illustration by Gautam G. Yadav)

$$K = \frac{k.A}{l} \dots\dots\dots(2.29)$$

$$R = \frac{\rho.l}{A} \dots\dots\dots(2.30)$$

k is the thermal conductivity of the thermoelectric material in equation 2.29, and ρ is the resistivity of the thermoelectric material in equation 2.30.

Inserting equations 2.29 and 2.30 into equation 2.28, we get

$$ZT = \frac{S^2.T}{k.\rho} \dots\dots\dots(2.31)$$

The resistivity, ρ , can be converted to electrical conductivity, σ , by simply taking the inverse, and this gives us the dimensionless figure of merit of a thermoelectric material, ZT .

$$ZT = \frac{\sigma.S^2.T}{k} \dots\dots\dots(2.32)$$

From the above equation, it is clear that the ZT of a thermoelectric material depends on three intrinsic material properties – electrical conductivity (σ), Seebeck coefficient (S), and thermal conductivity (k).

It is essential to understand the aforementioned intrinsic properties of a material and their relationship to ZT , hence each of the properties will be discussed in detail in the following paragraphs.

2.2 Electrical Conductivity

The theory of electronic structure of solids provides some insights into the conduction mechanism of electron in a periodic potential. The solutions of the equations in the theory are wavefunctions that are traveling waves, which explain the physical mechanism for conduction. [Kasap, Koughia, Ruda, et al., 2007] In an ideal crystal, the electrons would travel unimpeded, and thus provide the maximum conduction. However, imperfections do exist in crystals that lead to the scattering of electrons, and hence affect conduction [Kasap, Koughia, Ruda, et al., 2007]. To consider these scattering effects, concepts such as mean free time, τ , are incorporated wherein it represents the average time that an electron can travel between scattering events [Kasap, Koughia, Ruda, et al., 2007]. The distance that the electron travels in the mean free time τ is called the mean free path, l .

$$l = v_e \cdot \tau \dots \dots \dots (2.33)$$

The mean free path is simply the mean speed, v_e , times the mean free time, τ . The mean speed, v_e , is the average speed of the electrons. The average speed of the electrons is also referred to as the electron thermal velocity [Kasap, Koughia, Ruda, et al., 2007]. The speed or velocity of the electron can be found by solving an energy balance between the kinetic motions of the electrons with the mean thermal energy ($3k_B T/2$) in local equilibrium:

$$\frac{1}{2} m_e v_e^2 = \frac{3}{2} k_B T \dots \dots \dots (2.34)$$

$$v_e = \sqrt{\frac{3 \cdot k_B \cdot T}{m_e^*}} \dots \dots \dots (2.35)$$

The average electron velocity or speed is around 10^5 m/s for nondegenerate semiconductor.

The speeds of the electrons are random, but in the application of an electric field (E), acceleration, a , of the electrons is developed:

$$a = \frac{e.E}{m_e^*} \dots \dots \dots (2.36)$$

The velocity of the electron changes as a result of the electric field direction; and after taking into account collisions after an average time τ_{avg} , we get another important term called drift velocity, v_{drift} .

$$v_{drift} = a. \tau_{avg} = \frac{e.E.\tau_{avg}}{m_e^*} \dots \dots \dots (2.37)$$

The electronic mobility, μ , is depended on drift velocity.

$$\mu = \frac{v_{drift}}{E} = \frac{e.\tau_{avg}}{m_e^*} \dots \dots \dots (2.38)$$

The drift velocity also gives rise to the electric current. An electric current, I, passing through an area of a material gives the current density, J. If the density of the electrons or charge carrier concentration is n then J is given by:

$$J = e.n.v_{drift} = e.n.\mu.E \dots \dots \dots (2.39)$$

$$J = \sigma.E \dots \dots \dots (2.40)$$

$$\sigma = e.n.\mu \dots \dots \dots (2.41)$$

Equation 2.41 leads us to a very important relationship in thermoelectrics – the electrical conductivity, σ , dependence on the charge carrier concentration and mobility of the respective charge carriers. It is quite clear that mobility and carrier concentration need to be high to obtain high electrical conductivity.

The derivations shown till now have come from semi-classical theory of electron conduction. To understand the interaction of electrons with the crystal lattice of a material, and number of electrons that are actually involved in electron conduction, some of the important relationships derived from quantum mechanics will be discussed below.

In a crystal lattice of a material, there exist periodic potentials that interact with the electrons. This interaction leads to the formation of discrete energy bands, and the energy of the electrons lie in these discrete bands that are separated by energy gaps called band gaps. The probability that an electron state of energy, E , will be occupied in these bands is given by the Fermi-Dirac distribution function [Huang, 2012]

$$f_0 = \frac{1}{\left[e^{\left(\frac{E-E_F}{kT} \right)} + 1 \right]} \dots \dots \dots (2.42)$$

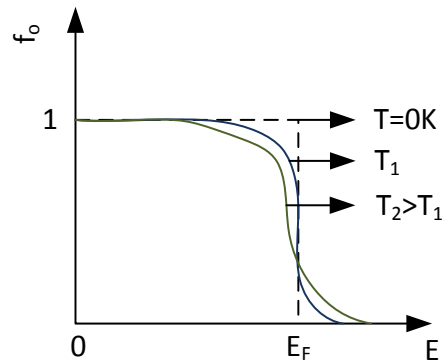


Figure 2.4. The Fermi-Dirac distribution function dependence on temperature. (Illustration by Gautam G. Yadav, Adapted from Huang, 2012)

Two electrons, one with spin up and another with spin down, can occupy a state. At temperature 0K, the energy is less than the Fermi energy, E_F , indicating that all the states are occupied ($f_0=1$) and the electrons are not available for conduction. As the temperature increases to T_1 and higher temperatures like T_2 , the energy becomes greater than the Fermi energy, E_F , and the curve shifts downwards indicating that there are states available for the electrons to occupy and take part in conduction.[Huang, 2012]

If there is an energy range between E and $E+dE$, represented by $g(E)dE$, with certain number of permitted electron states, then the total number of electrons is given by

$$n = \int_0^{\infty} f_0 g(E) dE \dots \dots \dots (2.43)$$

$g(E)$ is called the density of states, which describes the number of states per energy interval at each energy level that are available to be occupied by electrons [Goldsmid, 2010], as mentioned before. The number of electrons available for conduction depends on the Fermi-Dirac distribution function and the density of states. We have an understanding of the Fermi-Dirac distribution, but to really understand the availability of electrons in bulk material systems, we need to first derive and understand the density of states, $g(E)$, graphically.

In quantum mechanics, the energy and momentum of electrons are represented by wavevector, k . Therefore, we can picture an electron traveling in k -space. For bulk material systems, we will imagine a sphere in k -space with k as the radius; therefore the volume will be given by [Kuno, 2011]

$$V_k = \frac{4}{3}\pi k^3 \dots\dots\dots(2.44)$$

$$k^2 = k_x^2 + k_y^2 + k_z^2 \dots\dots\dots(2.45)$$

$$k_x = \frac{2\pi.n_x}{L_x} \dots\dots\dots(2.46)$$

$$k_y = \frac{2\pi.n_y}{L_y} \dots\dots\dots(2.47)$$

$$k_z = \frac{2\pi.n_z}{L_z} \dots\dots\dots(2.48)$$

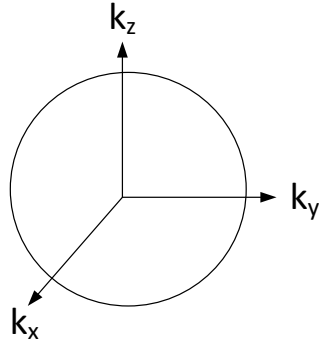


Figure 2.5. Density of states representation for three dimension sphere. (Illustration by Gautam G. Yadav)

If we consider the respective n values to be 1, then the volume of the overall state would be

$$V_{state} = k_x \cdot k_y \cdot k_z = \frac{8\pi^3}{L_x L_y L_z} \dots \dots \dots (2.49)$$

Therefore, within the spherical volume of k -space, the total number of states present, g_1 , is given by

$$g_1 = \frac{V_k}{V_{state}} = \frac{k^3 L_x L_y L_z}{6\pi^2} \dots \dots \dots (2.50)$$

However, as charge carriers – electrons and holes, have spin degeneracy, two carriers with opposite spin could occupy the same state. Therefore, the new total number of states for carriers accounting for spin, g_2 , is given by [Kuno, 2011]

$$g_2 = 2 \cdot g_1 = \frac{k^3 L_x L_y L_z}{3\pi^2} \dots \dots \dots (2.51)$$

The density of states is the total number states per unit volume, therefore we get

$$g = \frac{k^3}{3\pi^2} \dots \dots \dots (2.52)$$

It was mentioned earlier that the density of states as being the number of states per energy interval

$$g(E) = \frac{dg}{dE} \dots \dots \dots (2.53)$$

$$E = \frac{\hbar^2 k^2}{2m_e^*} \dots \dots \dots (2.54)$$

$$k = \left[\frac{2m_e^* E}{\hbar^2} \right]^{\frac{1}{2}} \dots \dots \dots (2.55)$$

$$g(E) = \frac{1}{3\pi^2} \frac{d \left(\frac{2m_e^* E}{\hbar^2} \right)^{\frac{3}{2}}}{dE} \dots \dots \dots (2.56)$$

After differentiating, we get

$$g(E) = \frac{1}{2\pi^2} \left(\frac{2m_e^*}{\hbar^2} \right)^{\frac{3}{2}} \sqrt{E} \dots \dots \dots (2.57)$$

We finally see that the density of states expression for a bulk three-dimensional solid has a characteristic square root energy dependency and a parabolic relation.

The concentration of electrons in a bulk semiconductor material can now be plotted graphically from equation 2.43.

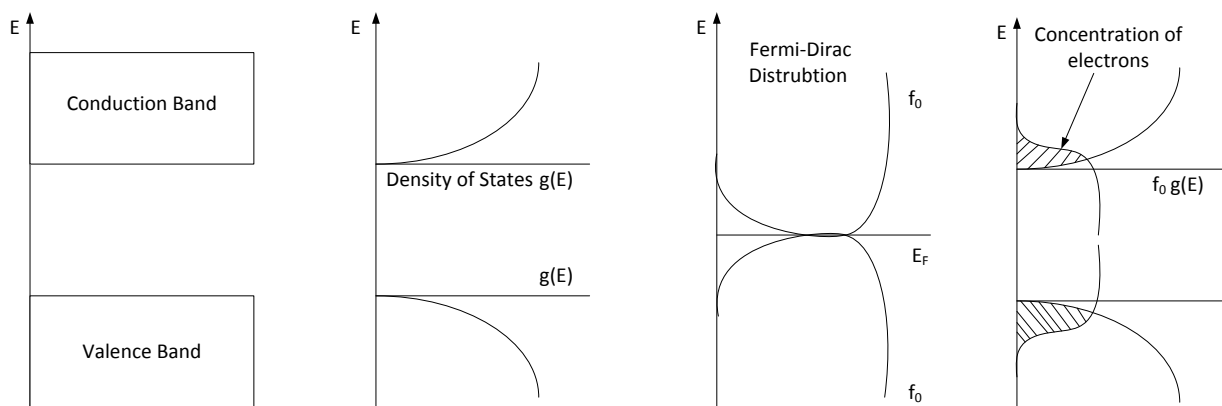


Figure 2.6. Illustration of concentration of charge carriers in bulk semiconductor through using density of states and Fermi-Dirac distribution. (Illustration by Gautam G. Yadav)

The density of states, $g(E)$, is small at the edge of the conduction band and it increases within the band like a parabolic curve. In metals, the Fermi level, E_F , lies within the conduction band with large number of electrons near the vacant states that make the metal very conductive. However, in semiconductors, the E_F lies either close to the conduction band for n-type semiconductors, or close to the valence band for p-type semiconductors, where only few electrons or holes participate in the conduction process. In the figure above, the carrier concentration for an intrinsic semiconductor is shown. An intrinsic semiconductor is not good as a thermoelectric material as both, electrons and holes, are

involved in the conduction process. The Seebeck coefficient is negative for electron conduction and positive for hole conduction. This opposing effect of the charge carriers reduces the overall Seebeck coefficient. The Seebeck coefficient for intrinsic semiconductors is given by the weighted average to the electrical conductivity of electrons and holes.[Tritt, 2002]

$$S = \frac{S_e\sigma_e + S_h\sigma_h}{\sigma_e + \sigma_h} \dots\dots\dots(2.58)$$

Therefore, it is necessary to either only have n-type or p-type semiconductors as a thermoelectric material to allow extrinsic conduction of only electrons or holes, respectively.

Continuing with electrical conduction, another important concept to note is that it only takes place when electrons in a band can move from one energy state to another. There are important implications by this statement – first, conduction will not take place if the bands are empty, and second, conduction will not take place even if the bands are full, as there are no empty states into which an electron can move. Therefore conduction only takes place when the electron states are partially filled.

In order to understand the transport phenomena the Boltzmann transport equation is used as a powerful tool which is used to analyze currents flowing in a system, thermal induced diffusion, transport coefficients and the relationships between them. This will help in further expanding our understanding of conductivity and other thermoelectric properties. The Boltzmann transport equation is given by [Pichanusakorn & Bandaru, 2010]

$$\left(\frac{df}{dt}\right)_{sc} = \frac{df}{dt} + \frac{dk}{dt} \nabla_k f + \frac{dr}{dt} \nabla_r f \dots\dots\dots(2.59)$$

In the equation 2.59, f is the non-equilibrium distribution function and k and r are the wave and position vectors of the electrons, respectively. ‘sc’ stands for scattering. The equation describes the evolution of electrons in the system under perturbations like an electric field, ϵ , or temperature gradient. [Pichanusakorn & Bandaru, 2010]

$$\frac{dk}{dt} = \frac{-e\epsilon}{\hbar} \dots\dots\dots(2.60)$$

$$\nabla_r = \frac{\partial f}{\partial T} \frac{dT}{dx} \dots\dots\dots(2.61)$$

To solve for ‘ f ’ in the Boltzmann transport equation the relaxation time, τ_r , is required, where the electrons equilibrate through random scattering. [Pichanusakorn & Bandaru, 2010]

$$\frac{df}{dt} = \frac{-(f-f_0)}{\tau_r} \dots\dots\dots(2.62)$$

f_0 is the Fermi-Dirac distribution as shown before. The relaxation time is determined by the type and magnitude of carrier scattering within the material, and we shall assume it to be of the form shown below [Lundstrom, 2010]

$$\tau_r = \tau_0 E^s \dots\dots\dots(2.63)$$

The ‘ s ’ in the above equation is called the scattering constant. The τ_0 is a constant that depends on material properties and scattering processes. Mobility-temperature measurements, variation of Seebeck coefficient with carrier concentration, and measurement

of the Nernst coefficient are often used to find the value of ‘s’. Some analytical methods also exist to find ‘s’, for example – for scattering by ionized impurities, s is equal to 3/2, while for neutral impurity scattering, s is equal to 0. For charge carriers scattered by acoustic phonons, s is equal to -1/2. Different scattering processes can cause ‘s’ to have different values, and if more than one scattering processes are dominant, the calculation of the relaxation time becomes complicated.[Lundstrom, 2010; Pichanusakorn & Bandaru, 2010]

Now that we have a firm understanding of the terms involved in the Boltzmann transport equation, we solve for the steady state solution as follows:

$$\frac{(f-f_o)}{\tau_r} = v_c \frac{df_o}{dE} \left[\pm e\epsilon - \left(\frac{E-E_F}{T} \right) \frac{dT}{dx} \right] \dots\dots\dots(2.64)$$

v_c in the above equation is the velocity of the carriers in the x direction and \pm takes into account hole or electron transport. The current density, J, can now be written as [Pichanusakorn & Bandaru, 2010]

$$J = \pm \int_0^\infty e v_c [f(E) - f_o(E)] g(E) dE \dots\dots\dots(2.65)$$

$$J = \pm \frac{2e}{3m_e^*} \int_0^\infty g(E) \tau_r E \frac{df_o}{dE} \left[\pm e\epsilon - \left(\frac{E-E_F}{T} \right) \frac{dT}{dx} \right] dE \dots\dots\dots(2.66)$$

Now that we have a more detailed expression for current density, we can finally find the electrical conductivity, which is given by the ratio of current density, J, to the electric field, ϵ , when the temperature gradient, dT/dx , is zero.[Pichanusakorn & Bandaru, 2010]

$$\sigma = \left[\frac{J}{\varepsilon} \right]_{\frac{dT}{dx}=0} \dots\dots\dots(2.67)$$

$$\sigma = \frac{-2e^2}{3m_e^*} \int_0^\infty g(E) \tau_r \frac{df_0}{dE} dE \dots\dots\dots(2.68)$$

The above expression represents the detailed expression derived for electrical conductivity, and thus gives some valuable insight into the dependence of conduction on certain important parameters that can help in designing the best thermoelectric material.

2.3 Thermal Conductivity

A thermoelectric device can only function in the presence of a temperature gradient, hence it is of utmost importance to minimize thermal conductivity to maintain operation of the device and obtain maximum efficiency and ZT . The thermal conductivity contributions to thermoelectric properties come from two parts – one, from the quantized vibrations of the lattice (κ_l) called phonons, and second, from the electronic contribution to the thermal conductivity (κ_e). [Tritt, 2002]

$$\kappa = \kappa_l + \kappa_e \dots\dots\dots(2.69)$$

The lattice part of the thermal conductivity, κ_l , is dependent on the lattice specific heat (C_l), the velocity of sound (v_s), and the phonon mean free path (l_{ph}). [Tritt, 2002]

$$\kappa_l = \frac{1}{3} C_l v_s l_{ph} \dots\dots\dots(2.70)$$

The electronic contribution to the thermal conductivity, κ_e , primarily comes from heat carried by the charge carriers during charge transport. A detailed expression for κ_e can be derived from the Boltzmann transport equation as well, but before we dive into deriving the expression, a simple relationship exists between the electronic contribution to the thermal conductivity and electrical conductivity through the Wiedemann-Franz law. [Tritt, 2002]

$$\kappa_e = L_o \sigma T \dots\dots\dots(2.71)$$

L_o is the Lorentz number and is given by

$$L_o = \frac{\pi^2}{3} \left(\frac{k_B}{e} \right)^2 = 2.45 \times 10^{-8} W \Omega K^{-2} \dots\dots\dots(2.72)$$

Now that we have seen that the electronic contribution to the thermal conductivity and electrical conductivity are tied to each other by the Lorentz number, we can continue on with the detailed derivation for the electronic contribution, κ_e . The heat flux density, Q , is depended on charge carriers that transport energy $(E-E_F)$ with a velocity, v_c . [Goldsmid, 2010]

$$Q = n(E - E_F)v_c = \int_0^\infty g(E)[f(E) - f_o(E)](E - E_F)v_c dE \dots\dots\dots(2.73)$$

We can see from the above equation that the heat flux density is dependent on the Fermi-Dirac distribution and the density of states. The complete expression is given below [Goldsmid, 2010]

$$Q = \pm \frac{E_F}{e} J + \frac{2}{3m_e^*} \int_0^\infty g(E)\tau_r E^2 \frac{df_o}{dE} \left[\pm e\mathcal{E} - \left(\frac{E-E_F}{T} \right) \frac{dT}{dx} \right] dE \dots\dots\dots(2.74)$$

The electronic contribution, κ_e , is the ratio of the heat flux density, Q , to the temperature gradient when the electric current density, J , is zero. [Goldsmid, 2010]

$$\kappa_e = \left[\frac{-Q}{dT/dx} \right]_{J=0} \dots\dots\dots(2.75)$$

$$\kappa_e = \frac{2}{3Tm_e^*} \left\{ \frac{[\int_0^\infty g(E)\tau_r E^2 \frac{df_0}{dE} dE]^2}{\int_0^\infty g(E)\tau_r \frac{df_0}{dE} dE} \right\} - \int_0^\infty g(E)\tau_r E^3 \frac{df_0}{dE} dE \dots\dots\dots(2.76)$$

The electronic contribution to the thermal conductivity, κ_e , also depends on the density of states and relaxation time. In a physical sense, the equation is stating that κ_e is sensitive to the hot carriers from the higher energy states as they carry more thermal energy.

2.4 Seebeck Coefficient

The Seebeck coefficient in the ZT equation is not as intuitive at first compared to the other properties - electrical conductivity and thermal conductivity. The Seebeck effect was discovered in 1821 by a German scientist, Thomas Johann Seebeck, when he made a circuit of two dissimilar metals, with junctions at different temperatures and found that it would deflect a compass magnet. He initially thought that this intriguing effect was due to the Earth's magnetic field; however, it was soon realized that a thermoelectric force due to the temperature gradient would induce an electric current that would deflect the compass magnet. [Rowe, 1995]

At first, it sounds strange that a temperature gradient induces a thermoelectric force, however this easily conceptualized by understanding the diagram shown below:

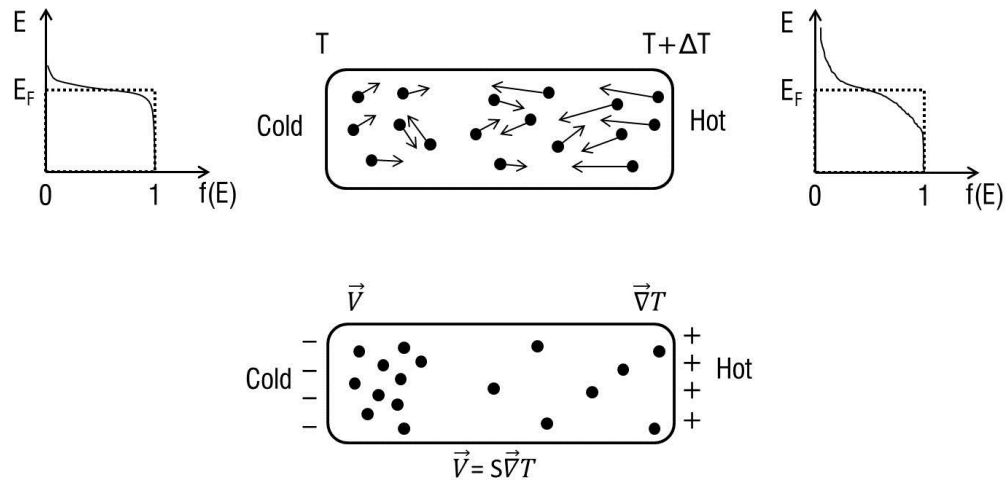


Figure 2.7. Explanation of Seebeck effect with the use of a conductor.(Illustration by Gautam G. Yadav, Adapted from Kasap, 1997)

Consider a box consisting of particles with a hot and cold end (Figure 2.7) that results in a temperature gradient. These particles can be electrons or holes. Consider the particles to be electrons for this explanation. The corresponding Fermi-Dirac distribution function for the electron energies at the respective ends is shown as well. The electrons at the hot end are high in energy and therefore diffuse to the cold side of the conductor. This diffusion of hot electrons to the cold side results in the build-up of electrons at the cold side, and the formation of positive metal ions at the hot end. This process continues until there is a build

of an electric field between the metal ions and the electrons that prevent the further diffusion of electrons at the cold end. This is essentially the electromotive force that is formed as a result of charge neutrality. Therefore, a voltage or a potential difference (ΔV) is developed between the hot and cold ends of the conductor. This effect, the potential difference generated by a temperature gradient, is called the Seebeck effect.[Kasap, 1997] The Seebeck coefficient, S , is used to measure the magnitude of this effect and is therefore defined by:

$$S = \frac{\Delta V}{\Delta T} \dots \dots \dots (2.77)$$

As the electrons diffuse from the hot side to the cold side, there is a build-up of negative electrons at the cold side which results in the cold side being negative with respect to the hot side. The Seebeck coefficient is measured as the potential of the cold side with respect to the hot side, and therefore is negative in the case of electrons and positive in the case of holes.[Kasap, 1997]

Now that a general concept of Seebeck effect is understood, a deeper physical insight can be obtained by doing a shell balance across a small portion of a conductor and applying expressions obtained by quantum mechanics.

$$-e\Delta V = E_{avg}(T + \Delta T) - E_{avg}(T) \dots \dots \dots (2.78)$$

Taking the limit of ΔT approaches 0, we get:

$$-e \frac{dV}{dT} = \frac{dE_{avg}}{dT} \dots \dots \dots (2.79)$$

In the left hand side of the equation, we get the Seebeck coefficient equation, and the average energy of metals is given by [Kasap, 1997]:

$$E_{avg} = \frac{3}{5} E_{FO} \left[1 + \frac{5\pi^2}{12} \left\{ \frac{kT}{E_{FO}} \right\}^2 \right] \dots\dots\dots(2.80)$$

By substituting the respective terms in the equation 2.79, we get:

$$S = \left(\frac{k}{e} \right) \frac{\pi^2 kT}{2E_{FO}} \dots\dots\dots(2.81)$$

$$\frac{k}{e} \sim 87 \frac{\mu V}{K} \dots\dots\dots(2.82)$$

The Fermi energies of metals are very high, therefore it is certain that the Seebeck coefficient for metals will be less than 87 $\mu V/K$ which is very low to be used in thermoelectric applications.

Equation 2.81 has a hidden relationship that gives a much deeper insight into the physical meaning of Seebeck effect.

The electronic specific heat, C_{el} , is given by

$$C_{el} = \frac{\pi^2 k_B^2 T n}{2E_F} \dots\dots\dots(2.83)$$

Rearranging equation 2.81 and comparing with equation 2.83, we see that

$$S = \frac{C_{el}}{n.e} \dots\dots\dots(2.84)$$

Manipulating the above equation,

$$S = \frac{C_{el} \cdot T}{n \cdot e \cdot T} \dots \dots \dots (2.85)$$

The specific heat, C, is given by

$$C = \frac{C_{el}}{n} \dots \dots \dots (2.86)$$

Therefore, we get

$$S = \frac{C \cdot T}{e \cdot T} \dots \dots \dots (2.87)$$

Before we proceed on further with our understanding of Seebeck effect, we have to understand another thermoelectric phenomenon which has an important relationship with Seebeck coefficient. This thermoelectric phenomenon deals with the flow of electric current through a material, for example a metal, with no temperature difference which leads to heat generation or loss. This is known as the peltier effect, named after Peltier who discovered this effect 12 years after Seebeck discovered the Seebeck effect. This is better understood when charge carriers or electrons are considered as gaseous particles that expand during current flow and contract when there is no flow. This leads to temperature differences, and this effect has found applications in solid-state refrigeration. Similarly to the Seebeck coefficient, there is a Peltier coefficient that relates to the Peltier effect. Again if we consider a box with particles, and for simplicity, consider these particles to be electrons, then as current flows through the box, the electrons flow in the opposite direction. However, the

electrons carry heat as well; hence there are two types of current – electrical (\vec{j}) and heat (\vec{h}).[Chaikin, 1990]

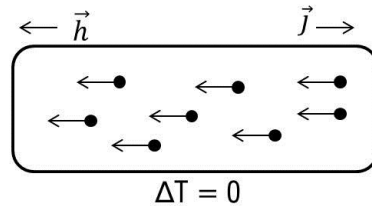


Figure 2.8. Explanation of Peltier effect with the use of a conductor.(Illustration by Gautam G. Yadav, Adapted from Chaikin, 1990)

However, the electrons carry heat as well; hence there are two types of current – electrical (\vec{j}) and heat (\vec{h}). The ratio of heat to electric current is the Peltier coefficient (Π).

$$\vec{j} = n \cdot e \cdot \vec{v} \dots\dots\dots(2.88)$$

$$\vec{h} = C_{el} \cdot \vec{v} \dots\dots\dots(2.89)$$

$$\Pi = \frac{\text{heat current}}{\text{electric current}} = \frac{\vec{h}}{\vec{j}} = \frac{C_{el} \cdot T}{n \cdot e} = \frac{C \cdot T}{e} \dots\dots\dots(2.90)$$

Comparing equations 2.87 and 2.90, we get

$$S = \frac{\Pi}{T} \dots\dots\dots(2.91)$$

From equation 2.91, the connection between the Seebeck and Peltier effect is finally seen.

This is also called the Thomson relation.[Chaikin, 1990]

Taking a closer look at equation 2.84, it is seen that the Seebeck coefficient is the ratio of electronic specific heat and charge of the carrier.[Chaikin, 1990; Kasap, 1997; Tritt, 2002]

$$S = \frac{C_{el}}{n.e} = \frac{C_{el}}{q} = \frac{\text{Electronic Specific Heat}}{\text{Charge of the carrier}} = \frac{\text{Heat or Entropy carried by the carrier}}{\text{Charge of the carrier}} \dots\dots\dots(2.92)$$

The above equation reveals an important point, i.e. that high Seebeck coefficients are achieved with carriers of high energy.

Now that the reason behind the bad thermoelectric properties of metals is explained, and firm understanding behind the physical meaning of the Seebeck effect is developed, we can proceed to understand the reason to pursue semiconductors as ideal thermoelectric materials.

In semiconductors, the heat of the carrier is the distance between the Fermi energy (E_f) and the conduction and valence band edges, i.e. the band gap (E_g). Since the Fermi energy (E_f) is located approximately half-way between the band gap (E_g), the heat of the carrier can be approximated to half of the band gap (E_g).[Chaikin, 1990]

$$\text{Heat of the carrier} = E_g - E_f \sim E_g - \frac{E_g}{2} \sim \frac{E_g}{2} \dots\dots\dots(2.93)$$

Substituting the equation 2.93 in equation 2.92, we get

$$S = \frac{\text{Heat of the carrier}}{\text{Charge of the carrier}} = \frac{E_g}{2.e.T} = \frac{k_B.E_g}{2.e.T.k_B} = \left(\frac{k_B}{e}\right) \frac{E_g}{2.T.k_B} \dots\dots\dots(2.94)$$

From equation 2.94, it is clear that in the case of semiconductors, energy has to be imparted to cross the band gap (E_g), hence the Seebeck coefficient will always be greater than $\frac{k_B}{e}$ or 87 $\mu\text{V}/\text{K}$.

To understand the dependence of the Seebeck coefficient on the density of states, we derive an expression very similar to the equations derived for electrical conductivity and the electronic contribution to the thermal conductivity. The Seebeck coefficient is equal to the ratio of electric field to the temperature gradient when the electric current is zero. [Pichanusakorn & Bandaru, 2010]

$$S = \left(\frac{\epsilon}{\frac{dT}{dx}}\right)_{J=0} \dots\dots\dots(2.95)$$

$$S = \pm \frac{1}{eT} \left[\frac{\int_0^\infty g(E)\tau_r E^2 \frac{df_0(E)}{dE} dE}{\int_0^\infty g(E)\tau_r E \frac{df_0(E)}{dE} dE} - E_F \right] \dots\dots\dots(2.96)$$

In the equation 2.96, the first term goes to zero as $T \rightarrow 0$. However, the second term can be written in terms of entropy, s , and carrier concentration, n . [Terasaki, 2010]

$$-\frac{E_F}{T} = \left(\frac{\partial s}{\partial n}\right)_{E,V} \dots\dots\dots(2.97)$$

From statistical thermodynamics, the entropy has a dependence on the total number of configurations, g . [Terasaki, 2010]

$$s = k_B \log(g) \dots \dots \dots (2.98)$$

Substituting the equation 2.98 into equation 2.97 and finally into equation 2.96, it is again seen that the Seebeck effect is associated with the entropy per carrier.

$$S = -\frac{k_B}{e} \frac{\partial \log(g)}{\partial n} \dots \dots \dots (2.99)$$

The Seebeck coefficient's dependence on the electrical conductivity can also be derived by equating the two equations (2.68 and 2.96) derived earlier:

$$\sigma = \frac{-2e^2}{3m_e^*} \int_0^\infty g(E) \tau_r \frac{df_0}{dE} dE \dots \dots \dots (2.68)$$

$$S = \pm \frac{1}{eT} \left[\frac{\int_0^\infty g(E) \tau_r E^2 \frac{df_0(E)}{dE} dE}{\int_0^\infty g(E) \tau_r E \frac{df_0(E)}{dE} dE} - E_F \right] \dots \dots \dots (2.96)$$

The above two equations can be associated when E_F is much higher than the thermal energy $k_B T$, and by expanding the Fermi-Dirac distribution in series of $k_B T/E_F$; therefore, we get [Terasaki, 2010]

$$S = \frac{\pi^2}{3} \frac{k_B^2 T}{e} \left[\frac{\partial \log \sigma(E)}{\partial E} \right]_{E_F} \dots \dots \dots (2.100)$$

$$S = \frac{\pi^2}{3} \frac{k_B^2 T}{e} \left[\frac{1}{n} \frac{\partial n(E)}{\partial E} + \frac{1}{\mu} \frac{\partial \mu(E)}{\partial E} \right]_{E_F} \dots \dots \dots (2.101)$$

Equation 2.101 is known as the Mott equation, which is one of the most important equations in thermoelectrics, as it illustrates the inverse dependence of the Seebeck coefficient with carrier concentration, n , and mobility, μ .

Now that we have a basic understanding of the respective intrinsic material properties involved in ZT , we can now get to the root of the problem when dealing with thermoelectric materials.

2.5 The Challenge in Thermoelectrics

To understand the challenge that researchers face when dealing with thermoelectric materials, it would be beneficial to state equations 2.41, 2.69, 2.101 again.

$$\sigma = e \cdot n \cdot \mu \dots \dots \dots (2.41)$$

$$\kappa = \kappa_l + \kappa_e \dots \dots \dots (2.69)$$

$$S = \frac{\pi^2 k_B^2 T}{3 e} \left[\frac{1}{n} \frac{\partial n(E)}{\partial E} + \frac{1}{\mu} \frac{\partial \mu(E)}{\partial E} \right]_{E_F} \dots \dots \dots (2.101)$$

Some of the problems become quite obvious when one compares the above three equations.

The plot below illustrates the problem of increasing ZT for a bulk thermoelectric system.

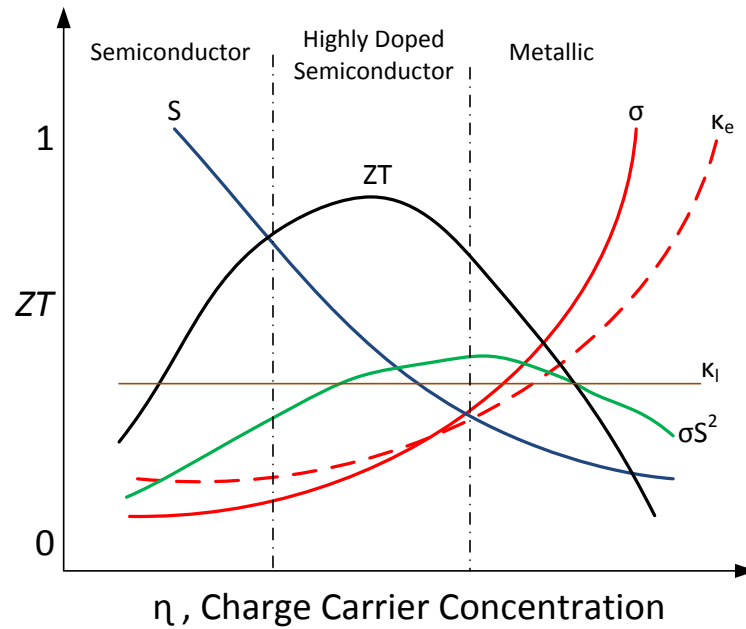


Figure 2.9. The inter relationships of various parameters and their ultimate effect on ZT .
(Illustration by Gautam G. Yadav)

From the Figure 2.9 and equations (2.41, 2.69 and 2.101), we can clearly see the three intrinsic properties have opposing trends that limit the value of ZT for a thermoelectric material. When a lightly-doped or non-degenerate semiconductor is used as a thermoelectric material, the Seebeck coefficient is high, while the electrical conductivity is low and phonons are the dominant carriers of heat. In a heavily-doped or degenerate semiconductor, the Seebeck coefficient decreases as the electrical conductivity increases, and both, the charge carriers and phonons, contribute to the heat. In a metal, as previously explained, the Seebeck coefficient decreases to a very low value, while the electrical conductivity is high as expected,

and as a result of high electrical conductivity, the electronic contribution is the highest to the thermal conductivity.

It becomes clear that there is no win-win situation when dealing with increasing the efficiency of thermoelectric materials. The solution to this challenge in thermoelectrics is optimizing each of the parameters through controlled methods, for example like doping. However, with the advent of nanotechnology, new solutions like nanostructuring of thermoelectric materials have been proposed to tackle this problem. The current trends in thermoelectric literature use nanostructuring as one of the ways to increase efficiency, these trends will be discussed in the next section.

2.6 Advent of Nanotechnology: Nanostructuring of Thermoelectric Materials

Nanotechnology has made improvements to many fields, and thermoelectrics is another addition. As shown in Figure 1.4 of Chapter 1, nanostructuring has had an immense impact on the field of thermoelectrics. Two aspects of nanostructuring will be discussed – first, fundamentally understanding the impact of reducing dimension, from 3D bulk systems to 1D nanowire or 0D quantum dots, on the individual properties involved in the ZT equation, and second, combining the nanostructured materials to form a nanostructured bulk pellet and again understanding its effect on certain properties involved in the ZT equation.

2.6.1 Nanostructuring and its impact on intrinsic properties

The density of states, $g(E)$, as seen in the previous equations, play an important role in altering the individual properties. The density of states, $g(E)$, for a bulk system was derived before:

$$g(E) = \frac{1}{2\pi^2} \left(\frac{2m_e^*}{\hbar^2} \right)^{\frac{3}{2}} \sqrt{E} \dots\dots\dots(2.57)$$

The density of states depends on dimensionality, as the dimensions are reduced from bulk (3D) to quantum wells (2D), nanowire (1D), and quantum dots (0D). To differentiate the respective density of states, the dimensionality will be mentioned in the annotation; for example, the bulk density of states is renamed as

$$g(E) = g_{3D}(E) = \frac{1}{2\pi^2} \left(\frac{2m_e^*}{\hbar^2} \right)^{\frac{3}{2}} \sqrt{E} \dots\dots\dots(2.102)$$

The derivation for the other respective density of states is similar to that of the bulk, which was derived in the earlier section. The difference arises from the reduction in the dimension. For the 2D density of states, instead of a sphere, we deal with a circle. Physically this means that the carrier momentum is discretized in the quantum confined direction, for example in our case we will consider the z-direction.[Kuno, 2011]

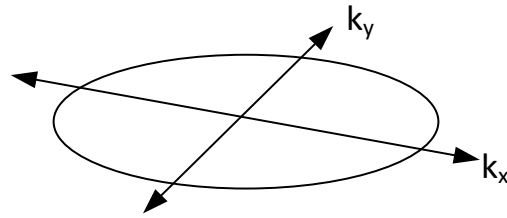


Figure 2.10. Density of States in Two Dimensions.(Illustration by Gautam G. Yadav)

For a sphere, we dealt with volume, but for a 2D circle, we deal with area, which is given by

$$A_k = \pi k^2 \dots\dots\dots(2.103)$$

The state within the circle occupies an area given by

$$A_{state} = k_x k_y \dots\dots\dots(2.104)$$

$$k_x = \frac{2\pi}{L_x} \dots\dots\dots(2.105)$$

$$k_y = \frac{2\pi}{L_y} \dots\dots\dots(2.106)$$

Therefore, within the circular area of k-space, the total number of states present, g_1 , is given by [Kuno, 2011]

$$g_1 = \frac{A_k}{A_{state}} = \frac{k^2 L_x L_y}{4\pi} \dots\dots\dots(2.107)$$

Spin degeneracy has to be accounted, therefore

$$g_2 = 2 \cdot g_1 = \frac{k^2 L_x L_y}{2\pi} \dots \dots \dots (2.108)$$

For a 2D system, the density of states is the total number states per unit area, therefore we get

$$g_{2D} = \frac{k^2}{2\pi} \dots \dots \dots (2.109)$$

It was mentioned earlier that the density of states as being the number of states per energy interval

$$g(E) = \frac{dg}{dE} \dots \dots \dots (2.110)$$

$$E = \frac{\hbar^2 k^2}{2m_e^*} \dots \dots \dots (2.111)$$

$$k = \left[\frac{2m_e^* E}{\hbar^2} \right]^{\frac{1}{2}} \dots \dots \dots (2.112)$$

$$g_{2D}(E) = \frac{m_e^*}{\pi \hbar^2} \dots \dots \dots (2.113)$$

Now, in 2D systems, it was mentioned before that the confinement is in z-direction, therefore the electron dispersion function for the ‘sub-band’ of each k_z is given by
 [[Pichanusakorn & Bandaru, 2010]

$$E_{2D}(k) = \frac{\hbar^2}{2} \left(\frac{k_x^2}{m_x} + \frac{k_y^2}{m_y} \right) + E_{nz} \dots \dots \dots (2.114)$$

$$E_{nz} = \frac{\hbar^2 \pi^2 n z^2}{2a^2 m_z}, n z = 1, 2, 3, \dots, \dots \dots \dots (2.115)$$

'a' is defined as the quantum well thickness, and E_{nz} is defined as the confinement energy in the z-direction. Therefore, the density of states for 2D system becomes [Kuno, 2011]

$$g_{2D}(E) = \frac{m_e^*}{\pi a \hbar^2} \sum_{nz} \Theta(E - E_{nz}) \dots \dots \dots (2.116)$$

$$\Theta(E - E_{nz}) = 1 \text{ if } E > E_{nz} \dots \dots \dots (2.117)$$

$\Theta(E - E_{nz})$ is the Heaviside unit step function. Therefore, the final expression that we get is

$$g_{2D}(E) = \frac{m_e^*}{\pi a \hbar^2} \dots \dots \dots (2.118)$$

A similar method can be approached for deriving the density of states for a nanowire (1D) and quantum dot (0D). For 1D systems, we deal with lengths, and the carrier confinement takes place in two directions, for our case we can consider x and y- directions. Therefore, the following equations develop, which are very similar to the ones that we derived for 3D and 2D systems.

$$L_k = 2k \dots \dots \dots (2.119)$$

The length in k-space is given by the above equation. Therefore, the width occupied by a given state is given by [Kuno, 2011]

$$L_{state} = \frac{2\pi}{k} \dots \dots \dots (2.120)$$

$$k_z = \frac{2\pi}{L_z} \dots \dots \dots (2.121)$$

Therefore, within the length of k-space, the total number of states present, g_1 , is given by

$$g_1 = \frac{L_k}{L_{state}} = \frac{kL_z}{\pi} \dots \dots \dots (2.122)$$

Spin degeneracy has to be accounted, therefore

$$g_2 = 2 \cdot g_1 = \frac{2kL_z}{\pi} \dots \dots \dots (2.123)$$

For a 1D system, the density of states is the total number states per unit length, therefore we get

$$g_{1D} = \frac{2}{\pi} \sqrt{\frac{2m_e^* E}{\hbar^2}} \dots \dots \dots (2.124)$$

As mentioned earlier, the density of states is the number of states per energy interval, therefore

$$g(E) = \frac{dg}{dE} \dots \dots \dots (2.125)$$

$$g_{1D}(E) = \frac{2}{\pi} \sqrt{\frac{2m_e^*}{\hbar^2}} \frac{1}{\sqrt{E}} \dots \dots \dots (2.126)$$

Similar to the explanation for 2D systems, in 1D system the confinement takes place in two directions, x and y-direction, therefore the electron dispersion function for the ‘sub-band’ of each k_x and k_y is given by [Pichanusakorn & Bandaru, 2010]

$$E_{1D}(k) = \frac{\hbar^2}{2} \left(\frac{k_x^2}{m_x} \right) + E_{nx,ny} \dots \dots \dots (2.127)$$

$$E_{nx,ny} = \frac{\hbar^2 \pi^2}{2a^2} \left(\frac{nx^2}{m_x} + \frac{ny^2}{m_y} \right), nx \text{ and } ny = 1, 2, 3, \dots, \dots \dots (2.128)$$

‘a’ is defined to be the width of the wire. , and $E_{nx,ny}$ is defined as the confinement energy in the x and y-directions. Therefore, the density of states for 1D system becomes [Kuno, 2011]

$$g_{1D}(E) = \frac{2}{a^2 \pi} \sqrt{\frac{2m_e^*}{\hbar^2}} \frac{1}{\sqrt{E - E_{nx,ny}}} \dots \dots \dots (2.129)$$

The density of states for quantum dots, $g_{0D}(E)$, is a series of delta functions due to the carrier confinement taking place in all three directions. Therefore, we can simply write it as [Kuno, 2011]

$$g_{0D}(E) = 2 \sum_{nx,ny,nz} \delta(E - E_{nx,ny,nz}) \dots \dots \dots (2.130)$$

Now that we have the density of state equations derived for the respective dimensions, we can plot them and talk about some of the physical meanings behind the equations.

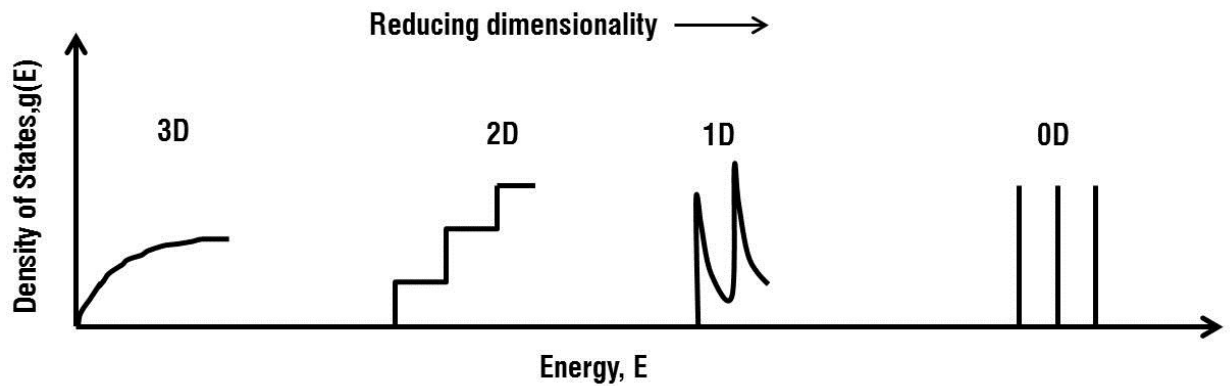


Figure 2.11. Density of States versus Energy for different dimensions.(Illustration by Gautam G. Yadav)

The proportional dependence of carrier concentration, electrical conductivity and Seebeck coefficient on density of states has been showed earlier. As the dimensions are reduced, the dimensionality factor ‘a’ comes into play in the density of states, and its presence in the denominator has a profound effect on the properties. The Mott relation, as shown in equation 2.101, shows that the enhancement of the energy-dependence of the conductivity will enhance the Seebeck coefficient. Enhancing the energy-dependence of the conductivity ($\frac{\partial \log \sigma(E)}{\partial E}$) translates to enhancing the energy-dependence of the charge carrier concentration ($\frac{\partial n(E)}{\partial E}$) or mobility ($\frac{\partial \mu(E)}{\partial E}$). [Heremans, 2005]

The enhancement of the energy-dependence on the charge carrier concentration ($\frac{\partial n(E)}{\partial E}$) can be achieved by enhancing the dependence of the density of states, $g(E)$, on energy. In the case of nanowires, the density of states is inversely proportional to the square of the wire thickness (a^2) which increases its energy dependence, and thus, enhance the $\frac{\partial n(E)}{\partial E}$ factor.

[Heremans, 2005]

Similarly, from equation 2.101, the mobility depends on the scattering or relaxation time; therefore, the enhancement of the energy-dependence on the mobility ($\frac{\partial \mu(E)}{\partial E}$) depends on the enhancement of the scattering or relaxation time's dependence on energy. This can be achieved by preferentially scattering electrons depending on their energy. This concept is called energy filtering. In 2D systems, potential barriers are used to create mini-bands in the energy band structure that filter electrons. In a physical sense, the concept of energy filtering tells us that high energy charge carriers carry more heat that would enhance the Seebeck coefficient compared to low energy carriers, which would in fact have a negative effect.

[Heremans, 2005]

The concepts that we have talked about in the aforementioned paragraphs would work great if we were testing properties on single nanowire systems, and would be ideal for very niche applications; however, the testing of thermoelectric properties have to take place on a bulk scale to be viable for commercial technology.

2.6.2 Nanostructured Bulk Thermoelectrics

Bulk materials do not give the best thermoelectric properties as explained in the previous sections. However, they do turn out to be the simplest way to measure properties and the ideal type suited for commercial applications. Nanostructured bulk thermoelectrics are essentially taking nanostructured forms of materials and combining them to make bulk systems by using pressure-sintering based techniques like hot-press or spark plasma sintering (Process explained in Appendix A) and yet maintain its 'nano' characteristics. There are various concepts behind nanostructured bulk thermoelectrics that have inspired this line of thinking. One of them lies behind reducing the grain size of the materials to reduce thermal conductivity. The intention of reducing the grain size is to affect the lattice part of the thermal conductivity. Equation 2.70 showed that lattice thermal conductivity depended on the mean free path of the phonons. Reducing the grain size affects the mean free path of the phonons, as smaller grain sizes scatter the large mean free path phonons.[Bux, Fleurial & Kaner, 2010] In theory the electrical conductivity should remain unaffected due to its shorter mean free paths; however, in practical situations, scattering of charge carriers can also happen that affect electrical conductivity. Nanostructuring is a game of compromise. This concept was tested on silicon through theoretical modeling, where a large portion (around 90%) of the thermal conductivity is attributed to phonons that have a mean free path greater than 20 nm. The modeling showed that a reducing of grain size less than 20 nm resulted in the lattice thermal conductivity reduction of around 90%. [Henry & Chen, 2008]

Phonons have different wavelengths, each with varying magnitude that affect the lattice thermal conductivity. Grain size reduction affects only a certain portion of phonons. A way to scatter different wavelength of phonons is through incorporating varying particle sizes of a different phase along with grain size reduction. This technique is termed as 'nanoinclusions'. In nanoinclusions, a nanostructured bulk material is embedded with various nano precipitations of different materials, which are formed by a solid state partitioning on cooling due to process of formation and deformation of a metastable phase, or a process of fast condensation into a material combined with heat treatment, or by crossing into the mixed phase behavior. The size confinement of the nanoinclusion or dispersed phase filters out the large wavelength phonons. [Liu, Ren & Chen, 2013] This has proven to be extremely effective as one of the highest ZT s was achieved recently in literature. [Biswas, He, Blum, et al., 2012]

Another line of thinking is through achieving voids or 'nano' holes in the material system. Voids can affect the lattice thermal conductivity, and it was shown for a silicon film that ordered nano holes reduced the lattice thermal conductivity drastically without affecting the electrical conductivity. [Tang, Wang, Lee, et al., 2010] However, achieving these kinds of designs in a commercial thermoelectric device seems to require a technological leap. [Liu, Ren & Chen, 2013]

Doping is another method of in the domain of nanostructured bulk thermoelectrics. It was shown earlier that electrical conductivity and Seebeck coefficient depend on charge carrier concentration, where it could heavily influence the respective properties in contrasting ways.

Coupled with the methods described above, a dopant can be added to the material system to alter the carrier concentration of the material system where the electrical conductivity and Seebeck coefficient could be optimized. Traditionally dopants occupy empty lattice sites in structures like skutterudites or other special lattice sites that help in the electrical conduction. However, in some cases it can act as an ionized impurity dopant that can have a negative impact on carrier mobility. To avoid this negative effect on carrier mobility, modulation doping can be performed to minimize the impurity-electron scattering. In modulation doping, the dopants are doped into only one phase of a two-phase composite. This allows for the charge carriers to be separated from their parent grains and move into undoped grains that enhance the carrier mobility, and thus conduction. [Liu, Ren & Chen, 2013]

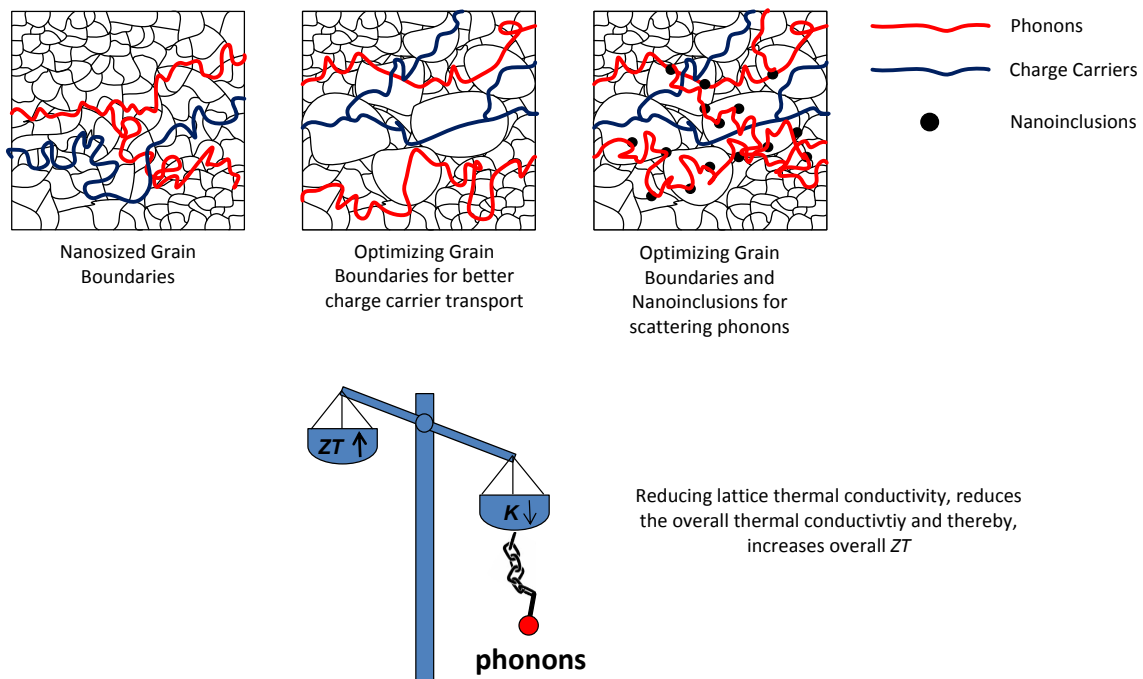


Figure 2.12. Illustration of nanostructuring methods to reduce the lattice thermal conductivity. (Illustration by Gautam G. Yadav)

2.7 Conclusions

It is clear that nanostructuring can play a vital role in improving the properties of a thermoelectric material. In Section 2.6.2, it was mentioned that nanostructured materials are sintered and pressed to form nanostructured bulk pellets. There are two ways of obtaining nanostructured materials – through either physical means or chemical reactions. The physical methods usually involve processes like ball-milling that pulverize bulk materials between ceramic or stainless steel balls into nanosized materials. This process can usually last for days

and there is little control over the size range of the material. Additionally, unnecessary dopants can be introduced into the final mixture that could have a detrimental effect on the thermoelectric properties. The other way is through chemical means where by using innovative chemical precursors the material size and morphology can be tweaked and controlled to achieve the desired properties. Chapter 6 and 7 describe novel methods to drastically affect the thermal conductivity of oxide-based systems for high temperature thermoelectrics using the methods described in Section 2.6.2.

2.8 References

Biswas, K.; He, J.; Blum, I.D.; Wu, C.-I.; Hogan, T.P.; Seidman, D.N.; Dravid, V.P.; Kanatzidis, M.G. High-performance bulk thermoelectrics with all-scale hierarchical architectures. *Nature*, **2012**, 489,414-418.

Bux, S.K.; Fleurial, J.-P.; Kaner, R.B. Nanostructured materials for thermoelectric applications. *Chem. Commun.*, **2010**, 46, 8311-8324.

Chaikin, P. M. An Introduction to Thermopower for those who might want to use it to study Organic Conductors and Superconductors. *ORGANIC SUPERCONDUCTIVITY* ed, Kresin V.Z.; Little, W.A. Plenum Press, New York, **1990**, 101.

Goldsmid, H.J. *Introduction to Thermoelectricity*; Springer Series in Materials Science 121. Springer-Verlag Berlin Heidelberg, **2010**.

Henry, A.; Chen, G. Spectral Phonon Transport Properties of Silicon Based on Molecular Dynamics Simulations and Lattice Dynamics. *J.Comput. Theor. Nanosci.*, **2008**, 5, 141.

Heremans, J.P. Low Dimensional Thermoelectricity. *Acta Physica Polonica A*, **2005**, 108,609-634.

Huang, Y.M. Solid State Physics. **2012**. <http://www.lcst.cn.org/Solid%20State%20Physics/Ch63.html> (accessed August 28, 2013)

Kasap, S. *Thermoelectric Effects in Metals*. 1997, pg 2.

<http://www.kasap.usask.ca/samples/Thermoelectric-Seebeck.pdf> (accessed August 29, 2013)

Kasap, S.; Koughia, C.; Ruda, H.; Johanson, R. *Electrical Conduction in Metals and Semiconductors*; in Springer Handbook of Electronic and Photonic Materials. Springer-Verlag Berlin Heidelberg, 2007, 19-45.

Kuno, M. *Introductory Nanoscience, 1st ed*; Garland Science: USA, 2011.

Liu, W.; Ren, Z.; Chen, G. *Nanostructured Thermoelectric Materials*; in Thermoelectric Nanomaterials. Koumoto, K.; Mori, T. Springer Series in Materials Science 182; Springer-Verlag Berlin Heidelberg, 2013. Chapter 11, 255-285.

Pichanusakorn, P.; Bandaru, P. Nanostructured thermoelectrics. *Materials Science and Engineering R*, 2010, 67, 19-63.

Rowe, D.M. *CRC Handbook of Thermoelectrics: Introduction*; CRC Press: USA, 1995.

Tang, J.Y.; Wang, H.T.; Lee D.H.; Fardy, M.; Huo, Z.; Russell, T.P.; Yang, P. Holey silicon as an efficient thermoelectric material. *Nano Lett.*, 2010, 4279-4283.

Terasaki, I. Introduction to Thermoelectricity. 2010. <http://vlab-nu.jp/assets/files/pdf/thermoelectricity.pdf> (accessed August 27, 2013)

Tritt, T.M. Thermoelectric Materials: Principles, Structure, Properties, and Applications. *Encyclopedia of Materials: Science and Technology*, 2002, 1-11.

CHAPTER 3. LITHIUM-ION BATTERIES: AN OVERVIEW

The components in lithium-ion batteries are the same as other battery systems – cathode, anode, separator and electrolyte. Each component plays a vital role in determining the characteristic nature of battery performance. This chapter will explain first, the mechanism behind lithium-ion batteries; second, an overview of the common crystal structures and requirements of the respective electrode materials, i.e. cathode and anode; third, explain the origin of characteristic high voltage present in lithium-ion batteries; and finally, some discussion on the requirement of the electrolytes to deliver the high performance of lithium-ion batteries. This chapter is more about the characteristics that make lithium-ion batteries an interesting topic to study and the dominant form of energy storage of all the other technologies. For review of material systems and their performances, there are many excellent reviews that the reader is suggested to have a read.

3.1 Mechanism of Lithium-ion Batteries

Figure 3.1 illustrates the mechanism behind lithium-ion batteries. The cathode materials operate at high potentials (greater than 3.7V) and the anode materials operate at low potentials (generally till 0.01V). The cathode and anode electrode materials are usually coated on aluminum and copper foil, respectively. Aluminum is electrochemically unstable at high potentials; however, its stability is due to a passivation layer of aluminum fluoride formed on its surface due to the degradation of electrolyte, lithium hexafluorophosphate (LiPF_6) [van Schalkwijk & Scrosati, 2002]. Copper is electrochemically stable at low potentials [van Schalkwijk & Scrosati, 2002]. Two of the most common materials used in commercial batteries are lithium cobalt oxide (LiCoO_2) as cathode and mesocarbon microbeads (MCMB) graphite as an anode [Park, 2012; Yuan, Liu & Zhang, 2012], and they are used as examples in Figure 3.1 to explain the working mechanism. Most of the electrode materials used in lithium-ion batteries exhibit layered characteristics; however, this is not a strict rule. The electrolyte used most commonly is lithium hexafluorophosphate (LiPF_6) with ethylene carbonate (EC) and dimethyl carbonate (DMC) as additives [Goodenough & Kim, 2010]. A separator exists to separate the respective electrodes to prevent short-circuiting the battery. The battery performs work during the discharge process.

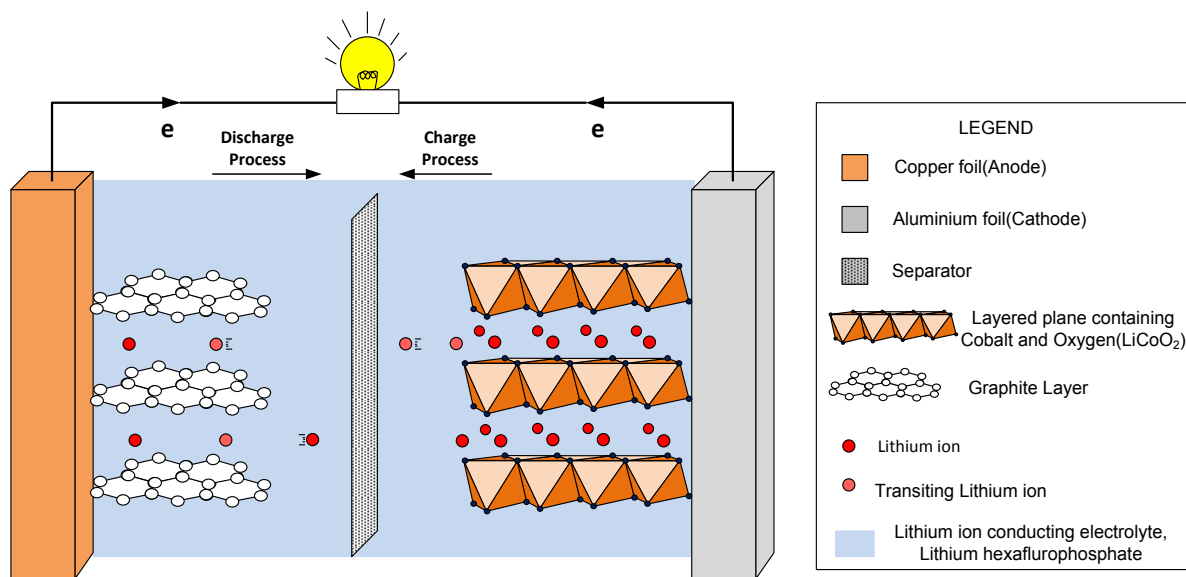
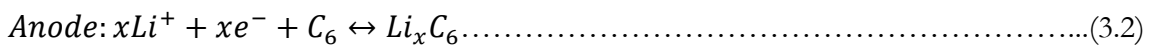
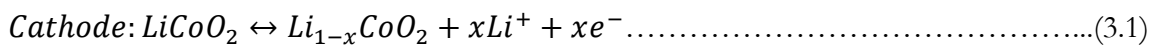


Figure 3.1. Mechanism of lithium-ion batteries. (Illustration by Gautam G. Yadav)

LiCoO_2 and MCMC graphite are layered materials. In the charging process, the lithium ions exit the layered structure of LiCoO_2 and move through the electrolyte and separator to enter the layered MCMC graphite anode. At the cathode, an oxidation reaction takes place, while at the anode a reduction reaction takes place.



In the above reactions, we see that not all the lithium (Li^+) ions are removed from the LiCoO_2 crystal structure. Only 'x' amount of lithium ions are removed till the (1-x) in

LiCoO_2 reaches a value that indicates stability in the crystal structure. Complete removal of lithium ions from LiCoO_2 would result in crystal structure breakdown, and thus, degradation in battery performance. For LiCoO_2 , 'x' corresponds to 0.5 lithium ions, at which the charging process is stopped, and this corresponds to the cathode phase of $\text{Li}_{0.5}\text{CoO}_2$. Further removal of lithium ions ($x > 0.5$) destabilizes the structure causing rapid capacity fade in later cycles. As the potential increases on the cathode side till it reaches a voltage of 4.2V for a stable cathode structure, the potential of the MCMB graphite decreases till it reaches its lowest potential (0.05V) that corresponds to the cathode's 4.2V. The maximum theoretical specific capacity obtained at 4.2V for LiCoO_2 is 140mAh/g [Nazri & Pistoia, 2004].

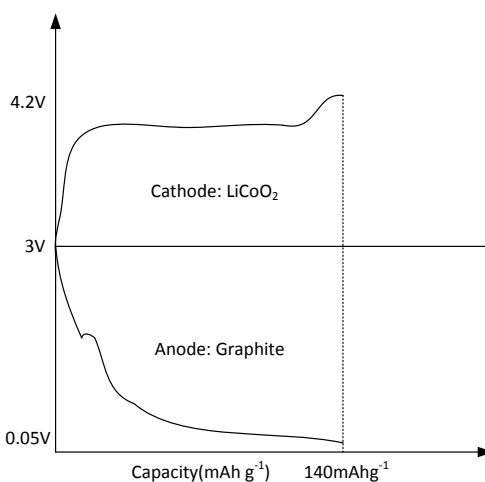
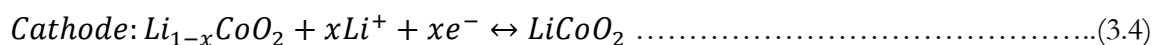
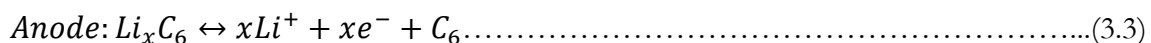


Figure 3.2. The change in potential in the cathode and anode associated with the charging step.

In the discharging process, the reverse process occurs, where lithium ions exit the layered MCMB graphite and enter the layered cathode. Therefore, the main reactions taking place are oxidation at the anode and reduction at the cathode. When oxidation is taking place at the anode, the electrons travel through the outside circuit to perform work and then reduce the lithium ions at the cathode as shown in Figure 3.1.



The process described above is called intercalation. Intercalation is the process of lithium ions entering or exiting a layered structure. This is the mechanism by which most of the layered cathodes and anodes used in lithium-ion batteries work. However, other mechanisms do exist as well like displacement reactions, which will be discussed more in detail in another chapter.

Cathode and anode materials play a vital role in determining the capacity or energy density of a lithium-ion battery. These electrode materials have the added burden of promising some of the high expectations of a lithium-ion battery. Therefore, in the next few sections, some of the requirements are discussed that are needed of electrode materials in terms of elements, crystal structure, etc., to optimize performance.

3.2 Overview of requirements and crystal structure of cathode electrodes

For a cathode material to be successfully used in a rechargeable lithium-ion cell, some of the requirements are as follows [Nazri & Pistoia, 2004; Whittingham, 2004]:

- a] One of the components of the material be comprised of an easily reducible or oxidizable ion.
- b] React reversibly with the lithium ions, so that there is no considerable change in the crystal structure as lithium is added or removed; this is essentially an intercalation mechanism.
- c] Deliver high capacity (at least one lithium per transition metal), and also work at high voltages, preferably around or more than 4V. The combinations of high capacity and high voltage would give high energy density.
- d] Rapidly react with lithium on insertion and removal as this would lead to high power density. This is an essential requirement for hybrid electric vehicles (HEV).
- e] Exhibit good electronic properties as this would ease the electron addition and extraction process, and also allow all of the material to participate in the electrochemical reaction when in contact with the electrolyte. This would also eliminate the need to add extra conductive agents like carbon black (CB) and inactive binder like polyvinylidene difluoride (PVDF) that reduce the overall energy density.

f] Electrochemically and thermally stable to prevent side reactions taking place with the electrolyte.

f] Be inexpensive.

g] Contain elements that are environmentally friendly.

Based on the above requirement, a glance at the periodic table will reveal the best elements that could be beneficial when used as cathode material.

1 H 1.0079																	2 He 4.0026	
3 Li 6.941	4 Be 9.0122											5 B 10.811	6 C 12.011	7 N 14.007	8 O 15.999	9 F 18.998	10 Ne 20.180	
11 Na 22.990	12 Mg 24.305	TRANSITION METALS										13 Al 26.982	14 Si 28.086	15 P 30.974	16 S 32.065	17 Cl 35.453	18 Ar 39.948	
19 K 39.098	20 Ca 40.078	21 Sc 44.956	22 Ti 47.867	23 V 50.942	24 Cr 51.996	25 Mn 54.938	26 Fe 55.845	27 Co 58.933	28 Ni 58.693	29 Cu 63.546	30 Zn 65.39	31 Ga 69.723	32 Ge 72.61	33 As 74.922	34 Se 78.96	35 Br 79.904	36 Kr 83.80	
37 Rb 85.468	38 Sr 87.62	39 Y 88.906	40 Zr 91.224	41 Nb 92.906	42 Mo 95.94	43 Tc [98]	44 Ru 101.07	45 Rh 102.91	46 Pd 106.42	47 Ag 107.87	48 Cd 112.41	49 In 114.82	50 Sn 118.71	51 Sb 121.76	52 Te 127.60	53 I 126.90	54 Xe 131.29	
55 Cs 132.91	56 Ba 137.33	57-70 * Lanthanide series	71 Lu 174.97	72 Hf 178.49	73 Ta 180.95	74 W 183.84	75 Re 186.21	76 Os 190.23	77 Ir 192.22	78 Pt 195.08	79 Au 196.97	80 Hg 200.59	81 Tl 204.38	82 Pb 207.2	83 Bi 208.98	84 Po [209]	85 At [210]	86 Rn [222]
87 Fr [223]	88 Ra [226]	89-102 ** Actinide series	103 Lr [262]	104 Rf [261]	105 Db [262]	106 Sg [263]	107 Bh [264]	108 Hs [265]	109 Mt [268]	110 Uun [271]	111 Uuu [272]	112 Uub [277]						

* Lanthanide series	57 La 138.91	58 Ce 140.12	59 Pr 140.91	60 Nd 144.24	61 Pm [145]	62 Sm 150.36	63 Eu 151.96	64 Gd 157.25	65 Tb 158.93	66 Dy 162.50	67 Ho 164.93	68 Er 167.26	69 Tm 168.93	70 Yb 173.04
** Actinide series	89 Ac [227]	90 Th 232.04	91 Pa 231.04	92 U 238.03	93 Np [237]	94 Pu [244]	95 Am [243]	96 Cm [247]	97 Bk [247]	98 Cf [251]	99 Es [252]	100 Fm [257]	101 Md [258]	102 No [259]

Figure 3.3. Periodic table with a red box highlighting the elements that could be useful in lithium-ion batteries. [Adapted from UC DAVIS, 2010]

The red box in Figure 3.3 highlights the elements that would be useful in satisfying the aforementioned requirements. The first series of 3d transition metals has been particularly pointed out as it plays a vital role in lithium-ion chemistry and delivering high capacity and voltage. 3d transition metals are also easily oxidizable and reducible. The origin of high voltage in 3d transition metals will be explained later in section 3.4; however, the high capacity that is obtained is due to its light weight and small size. The 3d transition metals form weak bonds with low-charge lithium that help in minimizing changes in the crystal structure during the charging and discharging cycles.

As mentioned in section, layered-based compounds are the most common types of materials used in lithium-ion batteries. There are lithium transition metal (M) oxides, LiMO_2 , that form layered structures with strong ionic character and a densely packed crystal structure [Park, 2012]. The ionic radii and co-ordination number of the different elements play a role in determining the packing density. Oxygen forms a dense packed layer as it has the largest ionic radii among the elements. The lithium and transition metal ions fill the spaces (tetrahedral and octahedral sites) between the oxygen ions to increase the density of the material system. From crystallography, it is known that a crystal structure exhibiting hexagonal close packed (HCP) arrangement satisfies the layering requirements. Some of the most common cathode materials used LiCoO_2 and lithium nickel oxide (LiNiO_2) exhibit HCP arrangements. These HCP arrangements lead to two-dimensional corner sharing between the oxygen ions, which result in the creation of slabs of transition metal-oxygen (MO_2) layers with strong ionic bonds, and lithium ions occupying sites in between the slabs. This results in a transition metal (M) – transition metal (M) mutual interaction that increases

electrical conductivity and curtails volume change during the charge and discharge steps. The MO_2 layers are separated by a coulombic repulsion that allow the lithium ions to intercalate and deintercalate during the discharging and charging steps, respectively. The two-dimensional plane allows for ions to diffuse easily and conduct rapidly. [Park, 2012]

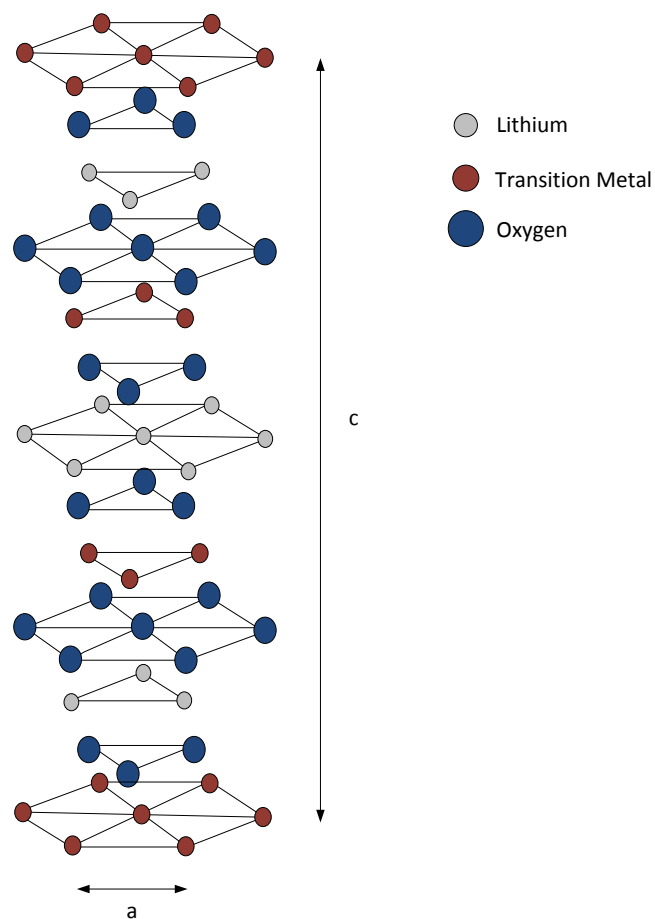


Figure 3.4. Crystal structure of layered lithium transition metal(M) oxides, LiMO_2 . (Illustration by Gautam G. Yadav, Adapted from Park, 2012)

Spinel-type transition metal oxides (LiM_2O_4 , $\text{M}=\text{Ti}, \text{V}, \text{Mn}$) are also used as cathode materials. Cubic close packed (CCP) arrangements lead to spinel-type phases. A common characteristic of spinel-type phases is their varying oxidation states [Park, 2012]. The most common spinel phase material used in lithium-ion batteries is lithium manganese oxide (LiMn_2O_4). It is widely researched as Mn is inexpensive, widely available, and environmentally benign; and it can deliver high capacity due to its low weight. However, manganese oxide [$(\text{MnO}_2)_x$] is a known polymorph, with Mn oxidation number varying from 2+ to 4+. For LiMn_2O_4 , Mn has oxidation states of 3+ and 4+. As will be shown later, oxidation number of a transition metal plays a vital role in determining the voltage of the material. Very similar to layered-based structures, the transition metals and lithium ions occupy the empty sites between oxygen in spinel-type phases. Their arrangement is determined by ionic radius and electrostatic attraction and repulsion. The radii of the different oxidation states of the transition metal determine their octahedral site location. Also, as a result of their different oxidation state, there is difference in charge distribution and the transition metal-oxygen bond length (M-O), which ultimately results in the transition metal-oxygen (MO_6) octahedrons being arranged three-dimensionally for greater uniformity in spinel-type phases compared to the two-dimensional layered phases. The three-dimensional connection of the face-sharing octahedra of the MO_6 octahedron allow vacant pathway for lithium migration during charging and discharging. [Park, 2012]

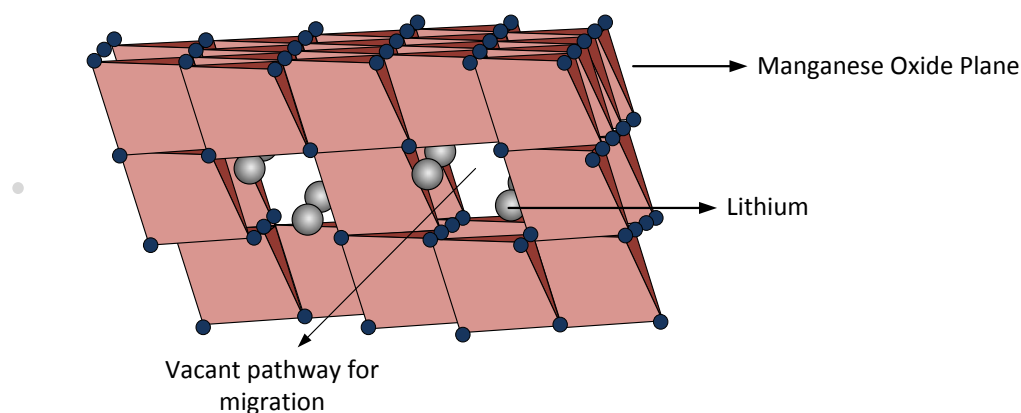


Figure 3.5. Spinel phase of LiMn_2O_4 (Illustration by Gautam G. Yadav, Adapted from Gateshki, 2006)

The new generations of cathode materials being studied are olivine-type structures. Lithium iron phosphate (LiFePO_4) is the most researched olivine-based material system as iron is cheap and abundant. More importantly it is much safer than cobalt in terms of toxicity. However, it operates at a lower voltage compared to LiCoO_2 . [Park, 2012] In the crystal structure of LiFePO_4 , Fe occupies 50% of the octahedral sites and P occupies 1/8 of the tetrahedral sites. The arrangement is very similar to that of spinel-type phase, but it is the presence of small ionic radius of phosphate ions (P^{5+}) that imparts the olivine characteristic instead of the spinel. The interesting electrochemical characteristics of LiFePO_4 are due to the presence of PO_4^{2-} in the crystal structure. The covalent bond between P-O reduces the Fe-O bond length in F-O-P, thereby preventing the oxidation of Fe in LiFePO_4 , and thus allowing it to obtain a stable voltage. A phase of lithium iron oxide (LiFeO_2) also exists

which exhibits poor electrochemical characteristics due to the absence of phosphate ions. Olivine-based compounds are also hexagonal close packed structures. In these structures, the oxygen is distorted due to the electrostatic repulsion between cations that cut across shared edges. In LiFePO_4 , the lithium ions are arranged in a linear chain of the edge-shared FeO_6 octahedron, which are arranged as zigzag rows. Therefore, each lithium ion has an edge shared with two Fe ions and two PO_4 tetrahedra. This results in formation of a uniform structure which allows lithium ions to diffuse in a one-dimensional path. The disadvantage of using PO_4^{2-} is that it reduces the electrical conductivity, thus making LiFePO_4 a poor electrical conductor and hampering its performance. [Park, 2012]

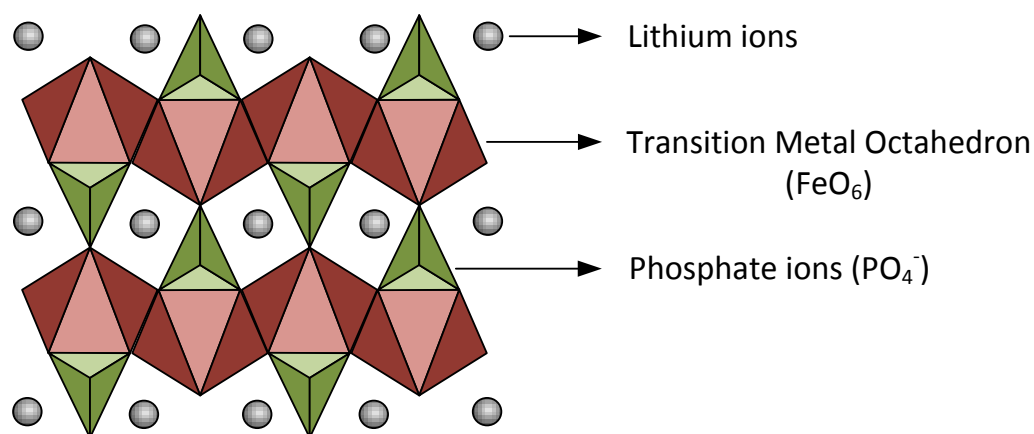


Figure 3.6. Olivine structure of Lithium Iron Phosphate (LiFePO_4). (Illustration by Gautam G. Yadav, Adapted from Park, 2012)

The three crystal structures given in Figures 3.4, 3.5 and 3.6 are the most researched in literature for cathode materials in lithium-ion batteries. It is interesting to note the role of crystal structure in performance of materials.

3.3 Overview of requirements and crystal structure of anode electrodes

Anode materials are very important and influence the performance of lithium-ion batteries. Similar to the outline of the section 3.2., the requirements of an anode material to be successfully used in rechargeable lithium-ion batteries are as follows [Nazri & Pistoia, 2004]:

- a] They should have low potentials corresponding to a standard electrode.
- b] They should combine with the cathode to provide an overall high cell voltage. The potentials of the electrochemical reactions must be a close approximation of the electrochemical potential of lithium metal.
- c] They should undergo reactions with lithium ions that do not cause significant changes in the crystal structure. Any significant changes in crystal structure can drastically affect the battery performance.
- d] They should undergo complete reversible reactions with lithium ions. This would entail that the ideal reaction would have a ratio of discharge capacity to charge capacity to be 1.

e] They should possess crystal structures that allow for fast diffusion of lithium ions to maximize cell performance.

f] They should have good electronic properties like high electrical conductivity to facilitate movement of electrons during the charge and discharge steps.

g] They should be sufficiently dense to obtain high electrode density, which relates to enhancing energy density of the battery.

h] They should possess high capacity, preferably close to lithium metal (3800mAh/g), to maximize performance.

There are many interesting anode material systems that are researched for use in lithium-ion batteries; however, only the most common and pertinent crystal structures studied in this thesis are discussed in the following paragraphs. The reader is encouraged to read some of the references to gain some insight into other anode based systems.

Lithium metal is commonly used as the anode in research laboratories. Its application in commercial devices has faced considerable barriers due to the safety issues that are related to it. Lithium has a body-centered cubic crystal structure with a small atomic weight and low density [Park, 2012]. It is the most electropositive metal with a very low standard electrode potential of -3.04V versus standard hydrogen electrode (SHE). These characteristics impart lithium with a very high capacity of 3860 mAh/g. It is the ideal anode; however, it has the capacity to grow dendrites (outward protrusions of lithium) in high rate batteries or long cycle life batteries. These dendrites can damage the separator to create a short-circuit in the

battery and in turn cause an explosion. Therefore, other materials have been researched to find a replacement for lithium metal. [Park, 2012]

Various carbonaceous materials are used as anodes in lithium-ion batteries. The most commonly used in commercial batteries are graphite, as mentioned section 3.1. Graphite consists of conductive graphene layers with sp^2 hybridized carbon atoms arranged in layers along a hexagonal plane. Each carbon atom covalently bonds to three other carbon atoms in a plane; however, it uses only 3 of its 4 outer energy level electrons. [Park, 2012] Therefore, an electron is contributed by each carbon atom to a delocalized system of π electrons. These π electrons are bonded between graphene layers by van der Waals forces. Graphite's good electronic conductivity arises from the π electrons freedom to move between graphene layers. During the charging and discharging steps, the lithium ions intercalate and deintercalate between these layers. However, the crystal structure of graphite is highly anisotropic due to perpendicular basal plane and parallel edge plane which affect the electrochemical reactions. For electrochemical reactions, the edge plane is the active plane, while the basal plane is inactive. Therefore, to increase the amount of edge planes compared to basal plane, artificial graphite is synthesized by heating pitch coke to temperatures above 2500°C . [Park, 2012]

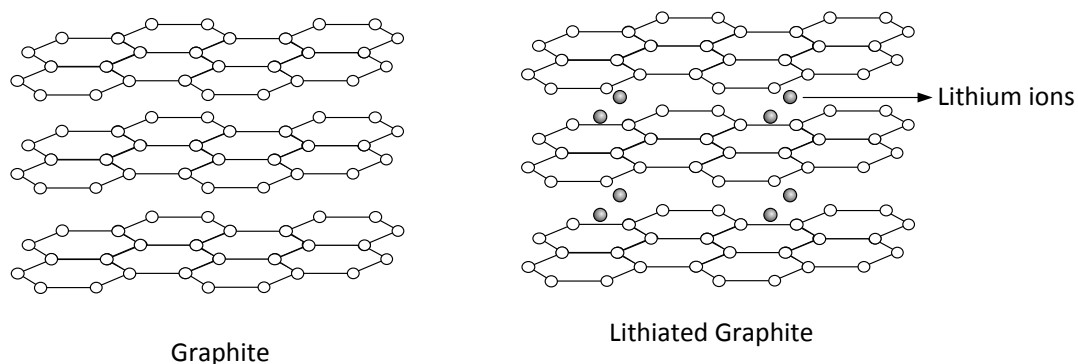
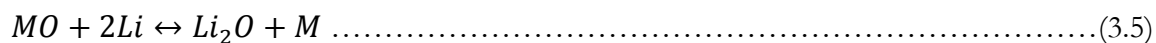


Figure 3.7. Structure of Graphite in its delithiated and lithiated phase.(Illustration by Gautam G. Yadav, Adapted from Park, 2012)

Another type of anode structure which has been increasingly been researched in literature is the transition metal oxide structure. Common examples are cobalt oxide (CoO , Co_3O_4), titanium oxide (TiO_2), nickel oxide (NiO), iron oxide (FeO , Fe_3O_4) and manganese oxide (MnO_2 , Mn_3O_4). [Park, 2012] Most of these types of transition metal oxides have a cubic rock-salt type structure, while materials like titanium oxide and manganese oxide exhibit polymorphism. The electrochemical characteristics of the rock-salt type materials exhibit two phase reactions. During the initial discharge step, lithium intercalates into the crystal structure; however, the lithium intercalation exceeds the crystal structure's capacity and breaks down into forming lithium oxide and transition metal. [Obrovac, Dunlap, Sanderson & Dahn, 2001; Sharma, Shaju, Subba Rao & Chowdari, 2004; Park, 2012]



The capacity that is derived in subsequent cycles is from the oxidation and reduction of the transition metal and the formation and decomposition of lithium oxide. These are termed as ‘displacement reactions’, as the lithium displaces the transition metal oxide crystal structure. In terms of performance, the crystal structure breakdown hinders the battery performance and a dramatic loss in capacity is observed initially. The crystal structure breakdown also results in a loss of electrical conductivity which hinders the anode’s performance at high charge and discharge rates. [Obrovac, Dunlap, Sanderson & Dahn, 2001; Sharma, Shaju, Subba Rao & Chowdari, 2004; Park, 2012]

3.4 Origin of voltage in transition metal oxides

Voltage for an electrochemical reaction can be theoretically determined from the standard potentials that are available for different materials. The standard potential of a cell is simply the addition of the anode’s oxidation potential and cathode’s reduction potential. For this section, all the discussions will be made with using standard examples of lithium metal as the anode and lithium cobalt oxide ($LiCoO_2$) as the cathode. In the case of Li_xCoO_2 as the cathode and lithium metal as the anode, lithium metal is the most electropositive element having a standard potential of -3.04V versus standard hydrogen electrode and Li_xCoO_2 has a standard potential of 1.25V [Linden & Reddy, 2010], thereby giving an overall theoretical cell

potential of 4.29V. In practical cells the voltage used is 4.2V for reasons explained previously.

Another way of understanding voltage is through its dependence on crystal structure and electronic properties of the material system [Johannes, 2010]. In sections 3.2. and 3.3., the role of crystal structure and phase change determining the voltage range of a battery was delineated. Thermodynamically the electrochemical cell potential depends on the concentration of lithium ions at the anode and cathode. More specifically the difference in chemical potentials at the anode and cathode determine the open circuit voltage of the cell (V_{OC}) [Nazri & Pistoia, 2004].

$$V_{OC} = \frac{\mu_{Li(c)} - \mu_{Li(a)}}{e} \dots\dots\dots(3.6)$$

$\mu_{Li(c)}$ and $\mu_{Li(a)}$ are the electrochemical potentials at the cathode and anode, respectively. For lithium metal, the chemical potential is constant. The electrical energy obtained by discharging the cathode, $LiCoO_2$, between $Li_{x_1}CoO_2$ and $Li_{x_2}CoO_2$ is the integral of the voltage times the discharge charge (q). However, q is simply the electron charge (e) times the difference in lithium concentration (x_2-x_1) [Aydinol, Kohan, Ceder, et al., 1997].

$$E = \int_{x_1}^{x_2} - \frac{\mu_{Li,cathode(x)} - \mu_{Li,anode}}{e} dx \dots\dots\dots(3.7)$$

The above equation is simply the Gibb's free energy (ΔG) equation. Therefore, the electrical energy is equal to ΔG . Therefore, the voltage is given by

$$V = -\frac{\Delta G}{(x_2-x_1)F} = \frac{\Delta E}{(x_2-x_1)F} \dots\dots\dots(3.8)$$

F is the Faraday's constant and n is the number of moles involved in the reaction. In terms of understanding this concept from a band diagram perspective, the voltage is the difference between the highest occupied electronic levels in the anode and the lowest unoccupied electronic levels in the cathode. In transition metal oxide cathodes and lithium metal anode/reference electrode, the voltage will be the difference in energy between the lithium metal and the d-states of the transition metal.

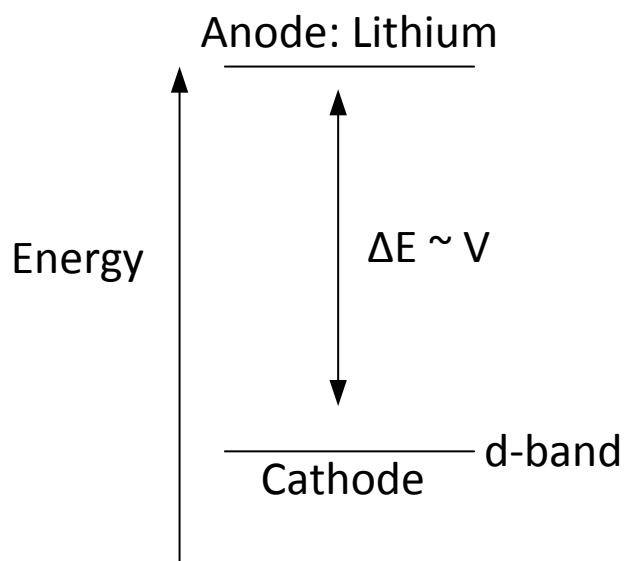


Figure 3.8. Anode and Cathode band levels in terms of an energy diagram.

From the figure above, it becomes clear that the location of the d-states level is important in increasing the voltage range. There are a few factors that determine the level of d-states—first, the oxidation state of the transition metal ion; second, the atomic weight of the transition metal ion; third, the bonding between the transition metal ion and oxygen; and fourth, the crystal structure bonding.[Aydinol, Kohan, Ceder, et al., 1997; Johannes, 2010]

Before the concept of oxidation state is explained, it is most important to point out that the ten d-states of transition metal split into five bands with two electrons of opposite spin occupying each band. The valence electrons for the different transition metals occupy these bands. Figure 3.9 illustrates the ground state configuration for some of the common transition elements used in lithium-ion batteries.

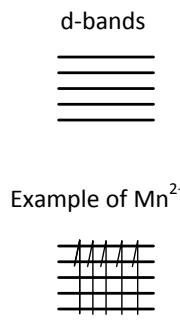
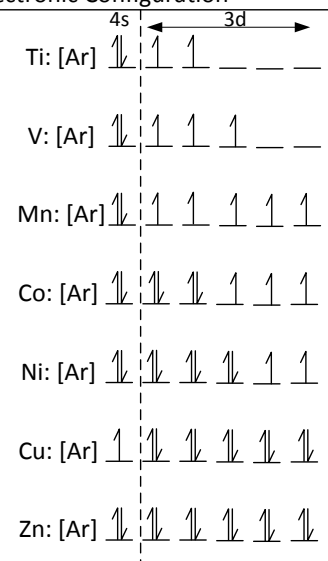
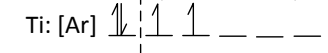
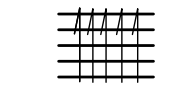
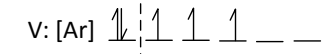
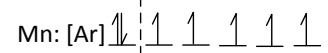
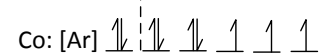
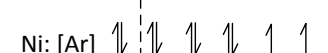
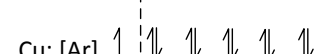
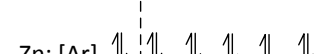
Element	Oxidation States	Electronic Configuration		d-bands 
			$4s$ ← $3d$ → 	
Titanium (Ti)	+4	Ti: [Ar]4s ² 3d ²	Ti: [Ar] 	Example of Mn ²⁺ 
Vanadium (V)	+2,+3,+4,+5	V: [Ar]4s ² 3d ³	V: [Ar] 	
Manganese (Mn)	+2,+3,+4,+6,+7	Mn: [Ar]4s ² 3d ⁵	Mn: [Ar] 	
Cobalt (Co)	+2,+3,+4	Co: [Ar]4s ² 3d ⁶	Co: [Ar] 	
Nickel (Ni)	+2	Ni: [Ar]4s ² 3d ⁷	Ni: [Ar] 	
Copper (Cu)	+2	Cu: [Ar]4s ¹ 3d ¹⁰	Cu: [Ar] 	
Zinc (Zn)	+2	Zn: [Ar]4s ² 3d ¹⁰	Zn: [Ar] 	

Figure 3.9. Electronic configurations of different transition elements. (Illustration by Gautam G. Yadav, Adapted from Wood & Chu, 2010)

Different oxidation states have different valence electrons. The elements with lower oxidation states tend to have higher energy, this energy decreases with increase in oxidation number. The diagram below illustrates an example of manganese (Mn) with different oxidation states compared to lithium. The d-states of Mn²⁺ are close to lithium, thus reducing its voltage range.

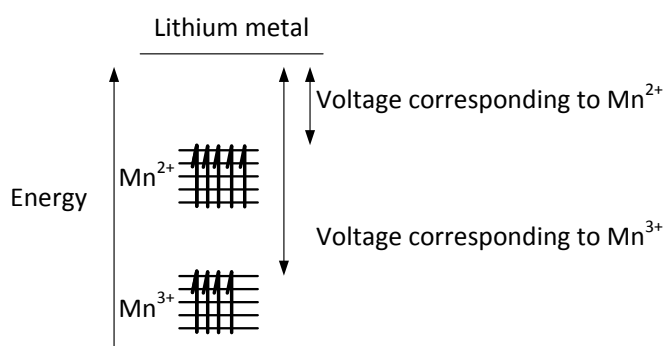


Figure 3.10. Voltage dependence on oxidation state.(Illustration by Gautam G. Yadav, Adapted from Johannes, 2010)

The d-state levels are also affected by the bonding between the transition metal and oxygen. When the transition metal ion and the oxygen come in close contact with each other, bonding and anti-bonding orbitals are formed. The bonding characteristics determine the splitting range between the bonding and anti-bonding orbitals. Strong bonds create a large split, while weak bonds create small splits. The d-orbitals of the transition metal ion have different ways of bonding with the oxygen orbitals. Some bonding types form strong anti-bonding, while some form weak anti-bonding. This results in the splitting of the five bands of d-states of transition metal into two e_g bands due to strong anti-bonding and three t_{2g} bands due to weak anti-bonding. Electrons first occupy the t_{2g} bands, and if extra electrons are present, they jump to the e_g bands. This entire mechanism is illustrated in the figure below. It is also important to note that as the bands split, the voltage is now measured as the

distance between the lithium metal and where the electrons are present. The physics behind the bonding types are important to understand the effect of other factors on voltage.

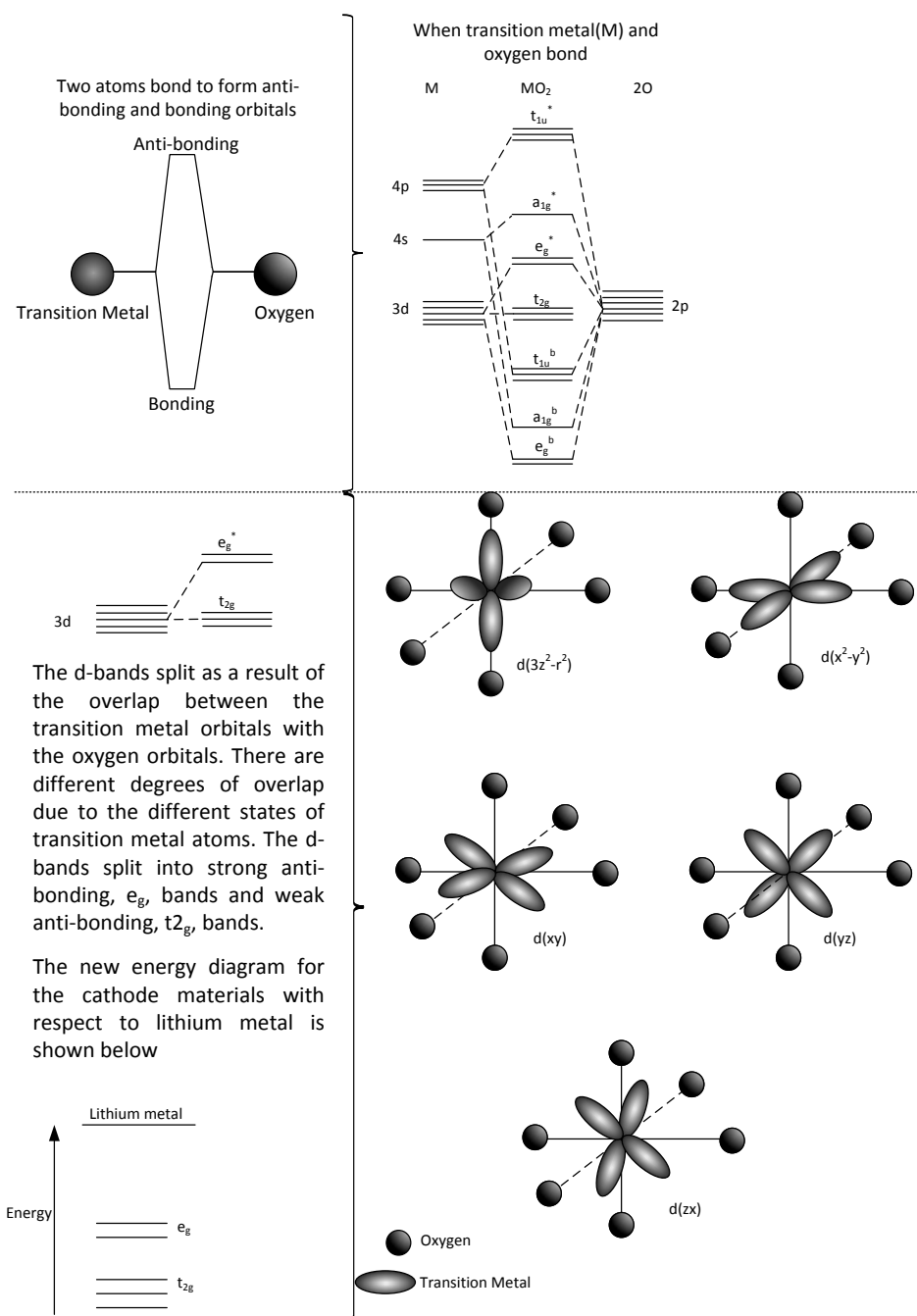


Figure 3.11. Graphical illustration of bonding between transition metal and oxygen. (Illustration by Gautam G. Yadav, Adapted from Aydinol, Kohan, Ceder, et al., 1997; Johannes, 2010)

Another factor in determining voltage is the atomic weight. In Figure 3.12, it is seen that the atomic weights of 3d transition elements increase from left to right till cobalt, but it dips at nickel. To understand this trend, it is necessary to look at the electronic configurations of cobalt and nickel, and identify the number of electrons that sit in the bands. We now know that the d-bands of transition metals split, and electrons first fill the lower t_{2g} bands and then fill the upper e_g bands. The voltage is now measured as the distance between the lithium metal and where the first electron is located. In the case of nickel, six electrons fill the lower t_{2g} bands first and the extra electron moves up to the e_g bands. The voltage for nickel is measured from the e_g bands to the lithium metal, and as this distance is small compared to that of cobalt and lithium, the voltage dips at nickel instead of following the trend.

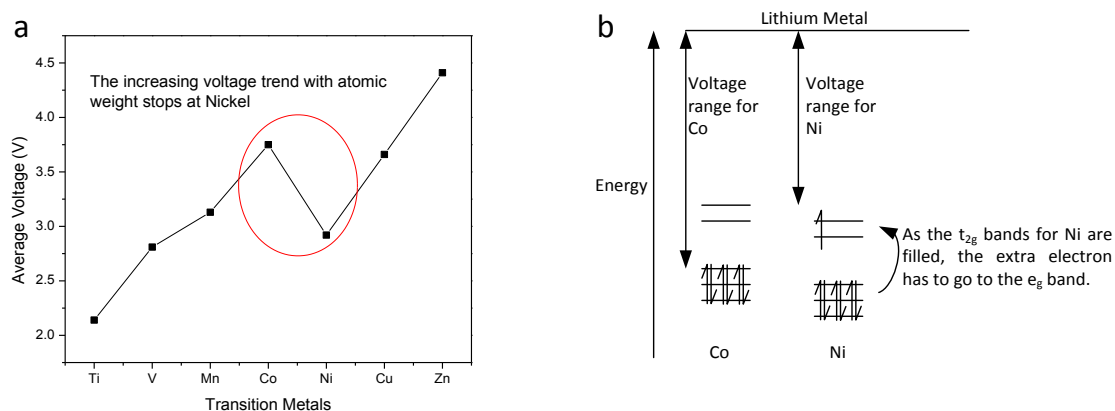
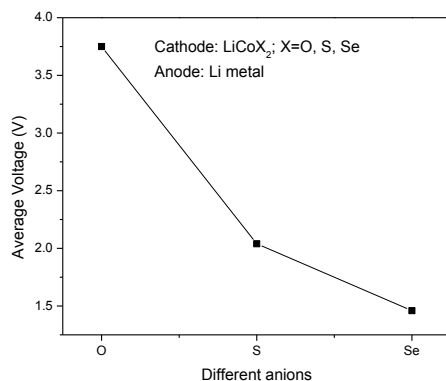


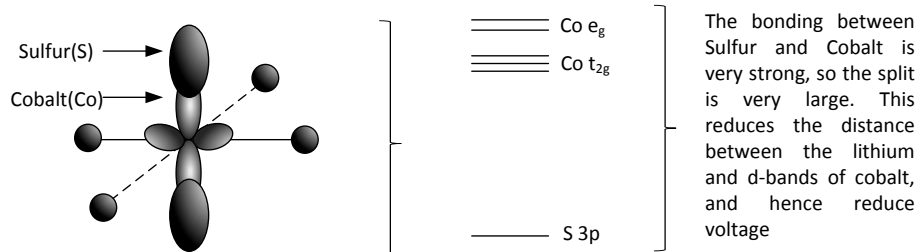
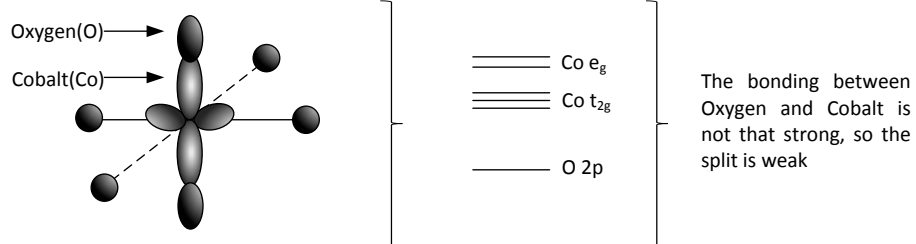
Figure 3.12. (a) Trend of voltage with increasing atomic weight of transition metals. [Adapted from Aydinol, Kohan, Ceder, Cho & Joannopoulos, 1997] (b) Explanation for the drop in voltage at Nickel. (Illustration by Gautam G. Yadav, Adapted from Aydinol, Kohan, Ceder, et al., 1997; Johannes, 2010)

The above mentioned bonding theory can also be used to explain the use of oxides in lithium-ion batteries. Theoretical work was done to find out if oxygen could be replaced by elements like sulfur and selenium. Figure 3.13a illustrates the drop in potential as oxygen is replaced by sulfur or selenium. It becomes clear from the plot that oxygen is an important anion that contributes to the high potentials of transition metal oxides. The drop in potential for sulfur and selenium are due to the strong overlap between their orbitals with the transition metal ion. The strong overlap creates a strong bonding that enlarges the split between the d-states of the transition metal ion and the p-orbitals of sulfur or selenium. As a result of this large split, the d-states of the transition metal ion are pushed closer to the potential of the lithium metal that reduces the voltage.[Aydinol, Kohan, Ceder, et al., 1997; Johannes, 2010]

a



b



c

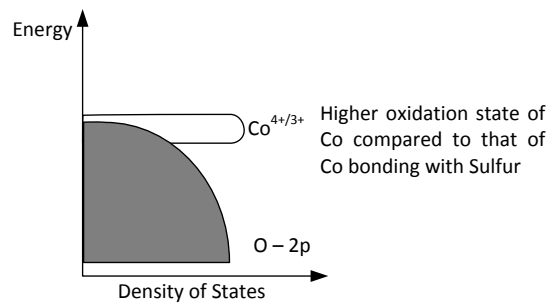
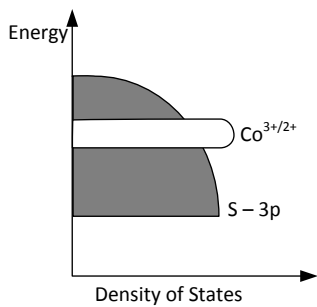


Figure 3.13. (a) Voltage trend with respect to anion in LiCoX_2 . (Adapted from Aydinol, Kohan, Ceder, Cho & Joannopoulos, 1997) (b) Explanation for drop in voltage for sulfur. (Adapted from Johannes, 2010) (c) Density of States explanation for drop in voltage for sulfur. (Adapted from Nazri & Pistoia, 2004) (a,b & c illustrations are done by Gautam G. Yadav)

The last factor that affects the voltage is the crystal structure bonding (Figure 3.13.). In sections 3.2. and 3.3., crystal structures of different materials and their relationship to the electrochemical properties were discussed. The cathodes with the good electrochemical properties are rhombohedral with hexagonal closed packed structures. The materials with rocksalt type structures do not have good electrochemical characteristics. The reason for these different electrochemical characteristics with different crystal structures can again be explained through bonding. In rocksalt type structures, the atoms are arranged in cubic form. This arrangement leads to 180° bonding with strong overlap between the oxygen and transition metal ion. This ultimately leads to large splitting between the p-states of oxygen and the d-states of transition metal ion. Therefore, as explained earlier, the d-states get pushed more towards the lithium potential, and hence the reduction in voltage. While, for the rhombohedral-type structure, not all orbitals of the transition metal ion and oxygen overlap with each other, and this leads to weak splitting between the p-orbitals of oxygen and the d-states of transition metal ion. [Johannes, 2010] As a result of this, the voltage range is large for cathodes with rhombohedral-type structures. A notable example is LiCoO_2 .

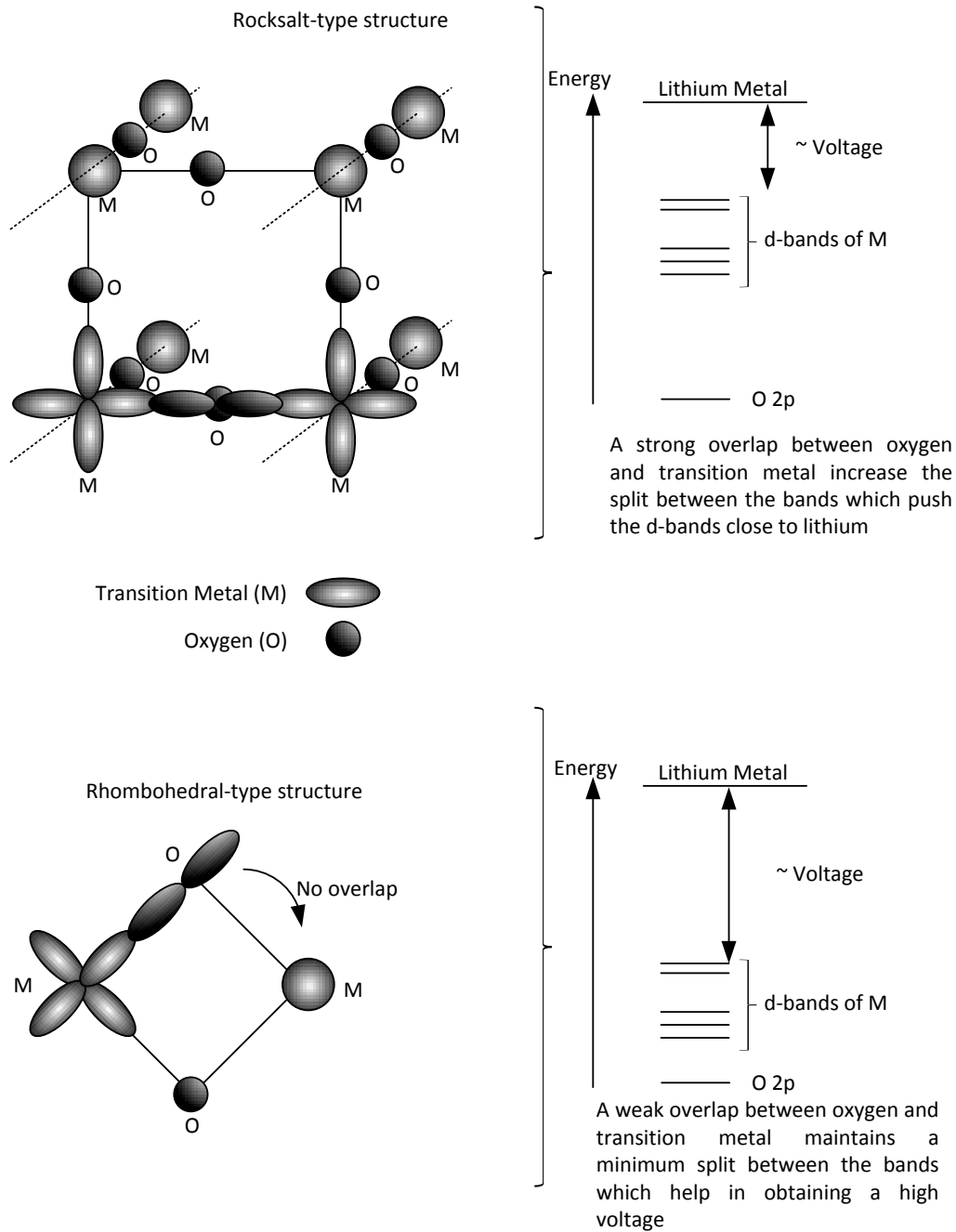


Figure 3.14. Illustration of crystal structure bonding influence on voltage. (Illustration by Gautam G. Yadav, Adapted from Johannes, 2010)

3.5 Brief overview of requirements of electrolyte

Electrolyte is another important component of a lithium-ion battery. Lithium-ion batteries operate at high potentials; therefore it is a must that the electrolytes are stable in the range that the batteries are operated. Some of the requirements of an electrolyte for lithium-ion batteries are as follows [Nazri & Pistoia, 2004; Goodenough & Kim, 2010]:

a] Low electronic conductivity to prevent electrons from interacting with the electrolyte and cause side reactions.

b] High ionic conductivity to allow fast movement of lithium ions to between electrodes. This minimizes cell resistance. An electrolyte with a transference number of 1 is ideal.

c] High chemical stability, so that electrolyte does not decompose on the surface of reducing anode materials like lithium metal or graphite, and oxidize on delithiated cathode electrodes like LiCoO_2 .

d] Electrochemical stability to handle the high voltage difference between anode and cathode.

e] Low melting point to prevent solidification, phase separation, and provide sufficient ionic conductivity at low temperatures.

f] High boiling points to prevent exothermic side-reactions that lead to explosions.

g] Non-toxic, so that it is environmentally friendly, easy to handle and safe for commercial applications.

h] Low cost to be commercially competitive to other batteries using aqueous electrolytes; for example, potassium hydroxide (KOH) used in alkaline batteries.

To expand more on point (d), the band gap ($E_{g,electrolyte}$) of the electrolyte must be higher than the open circuit voltage between the anode and the cathode.[Nazri & Pistoia, 2004]

$$V_{OC} = \frac{\mu_{Li(c)} - \mu_{Li(a)}}{e} \dots \dots \dots (3.9)$$

$$eV_{OC} = \mu_{Li(c)} - \mu_{Li(a)} < E_{g,electrolyte} \dots \dots \dots (3.10)$$

The above equation states that the chemical potentials of the anode and cathode must lie between the band gap of the electrolyte. This is an important point and it is visually illustrated in the figure below. If the chemical potential of the cathode lies below the highest occupied molecular orbital (HOMO) of the electrolyte, then electrons can fall from the HOMO band to cathode band, thereby causing oxidation of the electrolyte. Likewise, if the chemical potential of the anode lies above the lowest unoccupied molecular orbital (LUMO) band of the electrolyte, then it is easier for electrons to fall to the LUMO band to reduce the electrolyte. The oxidation or reduction of the electrolyte causes electrolyte to degrade and form a solid electrolyte interface (SEI). The SEI's cause interference for the lithium ions to shuttle back and forth between the anode and cathode, thereby increasing resistance and ultimately resulting to a loss in capacity.

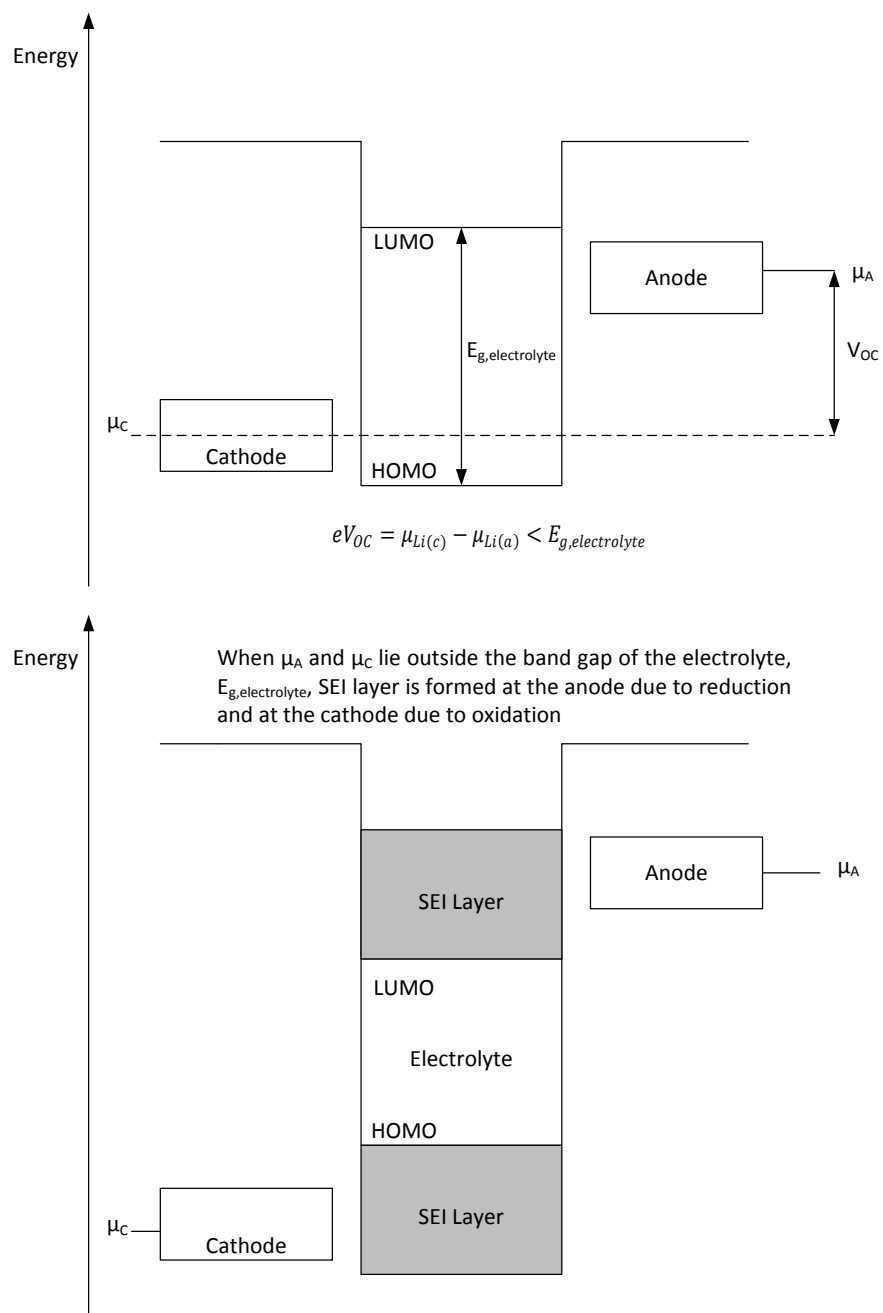


Figure 3.15. Illustration of the ideal scenario for an electrolyte (top diagram); and SEI layer formation (bottom diagram). (Illustration by Gautam G. Yadav, Adapted from Goodenough & Kim, 2010)

Electrolytes containing lithium salt like lithium perchlorate (LiClO_4), lithium hexafluorophosphate (LiPF_6), etc., are used in lithium-ion batteries. The organic electrolyte, LiPF_6 , is the most commonly used electrolyte. LiPF_6 is usually blended with ethylene carbonate (EC) and dimethyl carbonate (DMC) to reduce the viscosity and increase the HOMO to 4.7V and reduce the LUMO to near 1.0V versus lithium metal. The low viscosity helps in lowering the activation energy for lithium ion diffusion. Graphite, the most commonly used anode material, however, has a chemical potential which lies outside of the LUMO range of the electrolyte. In this case, it becomes paramount to EC as an additive because EC provides a passivating SEI layer on the surface of the graphite that protects the electrolyte from further degradation after SEI formation. Also, as lithium conducts easily in carbonates, it is better to have a SEI layer comprising of carbonates to allow lithium ion diffusion. LiPF_6 is flammable, and it is also sensitive to any presence of moisture. LiPF_6 has the tendency to undergo autocatalytic decomposition to form lithium fluoride (LiF) and phosphorus pentafluoride (PF_5). PF_5 reacts with the moisture to form hydrogen fluoride (HF), which is not only detrimental to the cell performance, but also extremely dangerous. LiF is also a poor ionic conductor and increases the impedance of the electrode/electrolyte interface.

3.6 References

Aydinol, M.K.; Kohan, A.F.; Ceder, G.; Cho, K.; Joannopoulos, J. Ab initio study of lithium intercalation in metal oxides and metal dichalcogenides. *Phys. Rev. B*, **1997**, 56(3), 1354-1365.

Gateshki, M. Structure of nanocrystals by the Atomic Pair Distribution Function Technique: A case study of K-Li-Mn-O-I. 2006. <http://people.cst.cmich.edu/petko1vg/nano.html> (accessed August 27, 2013)

Goodenough, J.B.; Kim, Y. Challenges for Rechargeable Batteries. *Chem. Mater.*, **2010**, 22, 587-603.

Johannes, M. The Physics of Li ion Battery Materials, The University of Tennessee. 2010. <http://160.36.161.128/UTK/Viewer/?peid=1e13ddc7cd164a45ad0f3e2b3195719e> (accessed on August 26, 2013)

Linden, D.; Reddy, T.B. Linden's Handbook of Batteries, 4th Edition. McGraw-Hill Professional, 2010, pg 9-12.

Nazri, G-A.; Pistoia, G. *Lithium Batteries: Science and Technology*; Kluwer Academic Publishers: Massachusetts, 2004; pp 3-4.

Obrovac, M.N.; Dunlap, R.A.; Sanderson, R.J.; Dahn, J.R. The Electrochemical Displacement Reaction of Lithium with Metal Oxides. *J. Electrochem. Soc.* **2001**, 148, A576-A588.

Park, J.-K. *Principles and Applications of Lithium Secondary Batteries*. Wiley-VCH Verlag GmbH & Co. KGaA, 2012.

Sharma, N.; Shaju, K.M.; Subba Rao, G.V.; Chowdari, B.V.R. Mixed Oxides $\text{Ca}_2\text{Fe}_2\text{O}_5$ and $\text{Ca}_2\text{Co}_2\text{O}_5$ as Anode Materials for Li-Ion Batteries. *Electrochimica Acta* **2004**, *49*, 1035-1043.

UC Davis. Periodic Table. 2010. http://lsc.ucdavis.edu/~ahart/Alicia118A/periodic_table.jpg
(accessed on August 27, 2013)

van Schalkwijk, W.; Scrosati, B. *Advances in Lithium-Ion Batteries*. Springer: US, 2002, pg 30.

Whittingham, M.S. Lithium Batteries and Cathode Materials. *Chem. Rev.*, **2004**, *104*, 4271-4301.

Wood, J.; Chu, L. Oxidation States of Transition Metals. UC Davis Chem Wiki.
http://chemwiki.ucdavis.edu/Inorganic_Chemistry/Descriptive_Chemistry/Chem_2C_Transition_Metals_and_Coordination_Complexes/Oxidation_States_of_Transition_Metals (accessed August 27, 2013)

Yuan, X.; Liu, H.; Zhang, J. *Lithium-Ion Batteries: Advanced Materials and Technologies*; CRC Press: Florida, 2012.

CHAPTER 4. OXIDE THERMOELECTRICS

This chapter will give a general introduction to oxide thermoelectric materials. However, for more information on the oxide thermoelectric materials, the reader is referred to certain excellent review papers [He, Liu & Funahashi, 2011; Ohtaki, 2010]. The main content of this chapter will be the derivation of the Seebeck coefficient for the high temperature limit. Also, some insight into the electrical conductivity mechanism will be discussed. These derivations are inspired from the original sources. The application of these derived equations is shown as an example for a new phase of calcium cobalt oxide ($\text{Ca}_9\text{Co}_{12}\text{O}_{28}$) in Chapter 7.

4.1 General introduction

The oxide materials used in thermoelectrics consist of transition metals. They are essentially ionic compounds joined together by coulombic forces. The transition metal and oxygen bonds are polarized which tend to localize the electrons around the lattice inducing lattice distortion. These localized electrons are called polarons. Polarons are essentially the charge carriers in oxide-based systems. Polarons will be talked more in-detail in Section 4.3. Chapter 3 explained the weak bonding characteristics of transition metals and oxygen. This had

positive effects for lithium-ion batteries; however, the weak overlapping leads to carrier mobility's that are two to three orders of magnitude lower to other compounds like silicon. Thus, the electrical conductivity is drastically affected. Also, the small atomic mass of oxygen and the nature of ionic bonding make the atoms vibrate intensely and release high velocity elastic waves, or essentially phonons, to travel through the oxide lattice, thus, contributing to the lattice part of the thermal conductivity (κ_l), and ultimately leading to the overall increase in thermal conductivity [Ohtaki, 2010]. As a result of this, oxides were never considered to be good thermoelectric materials. However, it was the discovery an oxide material with a unique structure that changed this negative notion.

In 1997, Terasaki discovered that sodium cobalt oxide (Na_xCoO_2 or NaCo_2O_4) exhibited large a Seebeck coefficient value of $100\mu\text{V}/\text{K}$ at 300K [Terasaki, Sasago & Uchinokura, 1997]. Sodium cobalt oxide has a layered structure, very similar to lithium cobalt oxide. Sodium (Na) and cobalt oxide (CoO_2) layers are alternately stacked along the c-axis to give the structure its layered characteristic [Koumoto, Terasaki & Funahashi, 2006]. The sodium layer is highly disordered due to its random distribution that creates randomly distributed vacant sites. The large Seebeck coefficient in these structures was an open question and it was initially hypothesized to be attributed to the spin fluctuations [Terasaki, Sasago & Uchinokura, 1997]. However, it was Koshibae's detailed analysis that took into account the different oxidation states of cobalt and the ratio of the degeneracies of the spins of the different cobalt ions that explained the high Seebeck coefficient in these layered-based systems [Koshibae, Tsutsui & Maekawa, 2000].

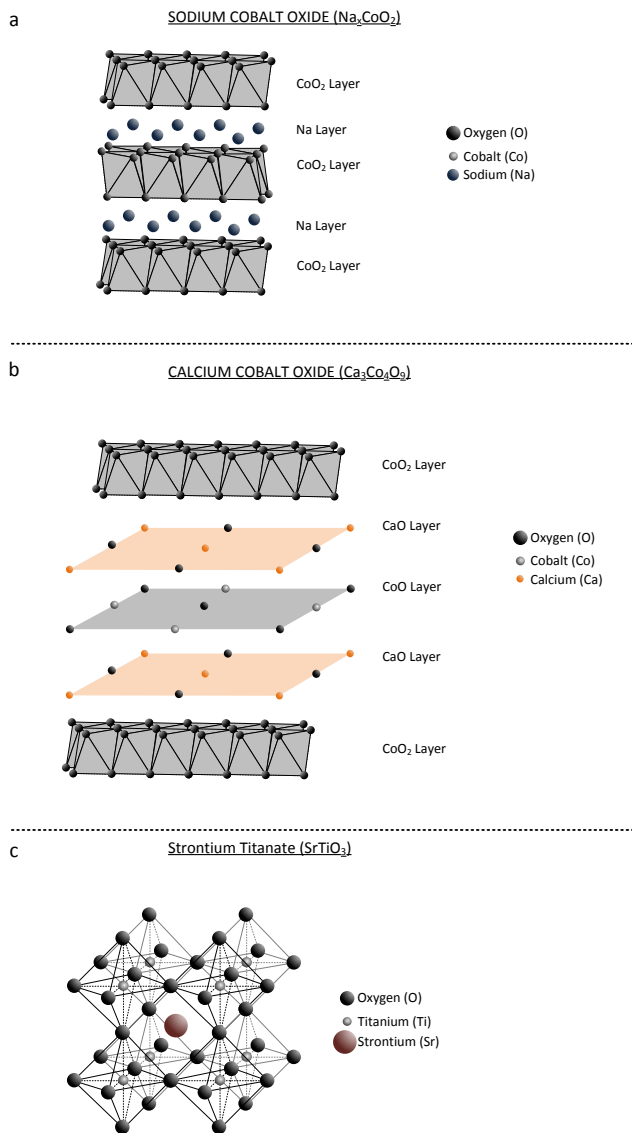


Figure 4.1. (a) Illustration of Sodium Cobalt Oxide (Na_xCoO_2). (b) Illustration of Calcium Cobalt Oxide ($\text{Ca}_3\text{Co}_2\text{O}_9$). (c) Illustration of Strontium Titanate (SrTiO_3). (Illustrations by Gautam G. Yadav)

The equation for the Seebeck coefficient of layered oxide-based materials for a high-temperature approximation will be derived in Section 4.2. Moreover, the randomly

distributed vacant sites act as strong phonon scattering sites that help in reducing the lattice part of the thermal conductivity [Koumoto, Terasaki & Funahashi, 2006]. These advantageous thermoelectric properties changed the field of high temperature thermoelectrics and ushered in new research on layered-based compounds.

Calcium cobalt oxide ($\text{Ca}_3\text{Co}_4\text{O}_9$) is another layered-based compound that was found to be a good thermoelectric material. Similar to sodium cobalt oxide, it has cobalt oxide (CoO_2) sheets; however, in between the sheets there is a rock-salt type structure of Ca_2CoO_3 [Koumoto, Terasaki & Funahashi, 2006]. This type of structure creates a distorted interface and lattice misfit. It is known in literature by its more popular name – misfit layered oxide [Koumoto, Terasaki & Funahashi, 2006]. Due to its complicated structure, it is expected to scatter more phonons and thus, decrease the lattice thermal conductivity [Koumoto, Terasaki & Funahashi, 2006]. However, in bulk crystals this is not often seen. Calcium cobalt oxide can exist in many phases and it is imperative to get the right phase of calcium cobalt oxide exhibiting layered characteristics. In Chapter 7, a new phase of calcium cobalt oxide ($\text{Ca}_9\text{Co}_{12}\text{O}_{28}$) was studied for its thermoelectric properties through using methods like nanostructuring.

In layered structures, the phonons are scattered through defects or complicated structures present between sheets, while it has been shown the electric current can flow through the cobalt oxide sheets through a certain direction in space, thus not affecting the electrical conductivity [Koumoto, Terasaki & Funahashi, 2006]. This concept of separating the paths for different currents through layering blocks is called nanoblock integration. This term is

used quite a lot in literature to describe the advantageous characteristics of layered-based compounds. However, it should be noted that the layered-based structures are anisotropic, so electrical conductivity values will differ depending on the direction of the measurement [Ohtaki, 2010].

Another material that has helped oxide claim a stake over high temperature thermoelectric applications is strontium titanate (SrTiO_3). Strontium titanate has a perovskite-type crystal structure. It also has a transition metal present in its crystal structure – titanium (Ti). It has a large bandgap of around 3.2eV, and the d-nature of the bands imparts the carrier electrons to have high effective mass (m_e^*) [Koumoto, Terasaki & Funahashi, 2006]. From Chapter 2, we know that this characteristic should help the material system to have low mobility, and thus have high Seebeck coefficient. However, the high effective mass does impact electrical conductivity as well. This can be bettered through doping with lanthanum (La) or niobium (Nb). As a result of this, really high power factors (σS^2) were obtained for doped- SrTiO_3 [Koumoto, Terasaki & Funahashi, 2006]. However, the ZT's obtained were quite low due to the really high thermal conductivity in this system. As the crystal structure is not complex compared to the layered-cobaltates, scattering phonons through crystal structure alone becomes improbable. Therefore, a novel synthesis method was developed to create ultrathin nanowires of SrTiO_3 and pressed into nanostructure bulk pellet to reduce the overall thermal conductivity by utilizing the scattering effects of nanosized grain boundaries, as outlined in Chapter 2. The results and experimental details are in Chapter 6.

Oxide-based compounds have unique structures that offer their own intriguing physics. Over the next few sections, the high Seebeck coefficient of the layered-cobalt based compounds and their electrical conductivity mechanism will be explained.

4.2 Seebeck coefficient in oxides

The Seebeck coefficient values obtained in layered oxides are related to their crystal structures and the interesting transition metal and oxygen interactions. As explained in Chapter 3, the interactions between the transition metal ions and oxygen anions split the five d-states of the 3d transition metals into two upper e_g bands and three lower t_{2g} bands. However, it is important to note that this only happens in a crystal field of an octahedron. If it happened in a tetrahedral field then the orderings of the band would be different. Hence, it is important to note the bonding orbitals and the field in which the bondings take place. The theory that is commonly used to refer to the band split is called crystal-field splitting. The energy between the last band of e_g and top-most band of t_{2g} is $10Dq$. [Maekawa, Tohyama, Barnes, et al., 2004]

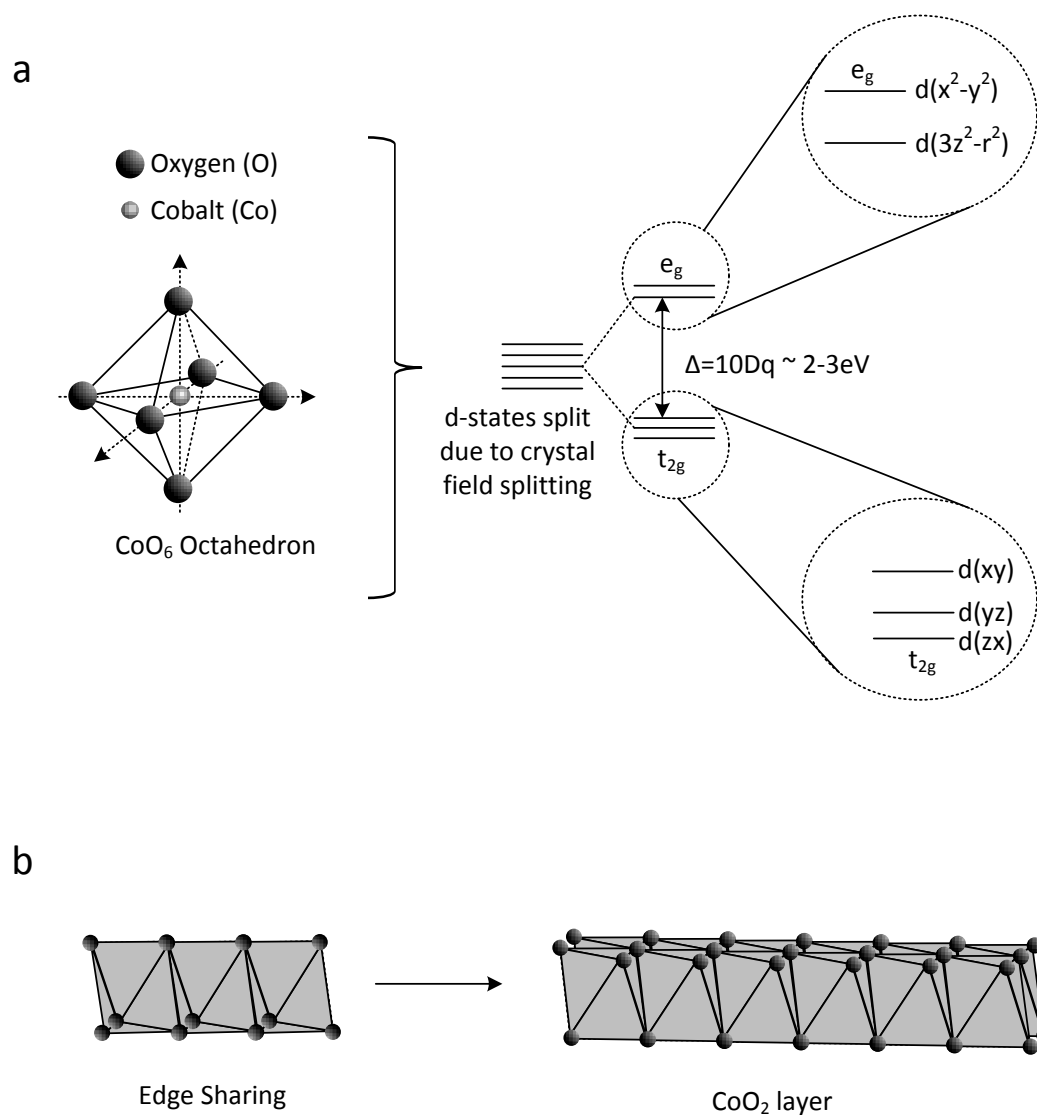


Figure 4.2. (a) Illustration of CoO₆ octahedron and the splitting of its band due to crystal field splitting.(b) Illustration of edge sharing in CoO₂ layer. (Illustrations by Gautam G. Yadav)

The cobalt oxide (CoO_2) sheets in the layered cobaltates are edge shared, which help in creating a π bond between the cobalt-oxygen-cobalt [Koumoto, Terasaki & Funahashi, 2006]. This helps the electrons to hop between the neighboring sites for conduction. The edge sharing in the cobalt oxide layer also results in the cobalt ions having mixed oxidation states. The occupation of the electrons in the different oxidation sites and the spins associated with the electrons need to be determined as a result of mixed oxidation states.

The oxidation states of cobalt in the layered structure are usually Co^{3+} and Co^{4+} . As shown in Chapter 3, there are six and five electrons in the 3d shell of Co^{3+} and Co^{4+} , respectively. The strong crystal field splitting cause all the electrons to go to the t_{2g} bands of Co^{3+} and Co^{4+} , respectively. If two electrons are allowed to jump into the e_g band, then they need an overall energy of $20Dq$ is required that makes the system unstable. However, the spin degree of freedom also contributes to the stability of the system. Hund's rule of coupling prefers four electrons in the t_{2g} bands and 2 electrons in the e_g bands for Co^{3+} , thereby giving it an electronic configuration of $t_{2g}^4 e_g^2$, and similarly for Co^{4+} , an electronic configuration of $t_{2g}^3 e_g^2$. The condition where the crystal field splitting dominates is called the low spin state of the respective oxidation states, while the high spin states occur when the Hund's rule of coupling dominates. When neither coupling dominates, the state is called the intermediate spin state with electronic configuration of $t_{2g}^5 e_g^1$ and $t_{2g}^4 e_g^1$ for Co^{3+} and Co^{4+} , respectively. [Maekawa, Tohyama, Barnes, et al., 2004] The different spin states are schematically illustrated in Figure 4.3. The competition between the low spin, intermediate spin, and high spin states lead to some of the interesting thermoelectric properties of layered cobaltates.

In Chapter 2, the Seebeck coefficient was derived in terms of entropy, s , and the number of particles in the system, N for the high temperature limit.

$$S = -\frac{1}{e} \left(\frac{\partial s}{\partial N} \right)_{E,V} \dots\dots\dots(4.1)$$

where E is the internal energy and V is the volume of the electron system. The above equation simply states that the Seebeck coefficient is the entropy per carrier. For the high temperature limit, the entropy is given by

$$s = k_B \ln(g) \dots\dots\dots(4.2)$$

' g ' in the above equation denotes the degeneracy.

Therefore, the Seebeck coefficient can be written as

$$S = -\frac{k_B}{e} \frac{\partial \ln g}{\partial N} \dots\dots\dots(4.3)$$

In the high temperature limit, the kinetic energy and inter-site coulombic interaction can be neglected and the entropy can be obtained by considering all the possible states, g , between Co^{3+} and Co^{4+} . The number of configurations of degeneracies of Co^{3+} and Co^{4+} ions are labeled as g_3 and g_4 , respectively. ' g_3 ' and ' g_4 ' values are determined by crystal field splitting, Hund's rule coupling and temperature. [Koshibae, Tsutsui & Maekawa, 2000; Maekawa, Tohyama, Barnes, et al., 2004] The total number of ways of arranging Co^{3+} and Co^{4+} sites, g_3 and g_4 in a total number of possible states, g , is given by

$$g = g_3^{N_A - M} g_4^M \frac{N_A!}{M!(N_A - M)!} \dots \dots \dots (4.4)$$

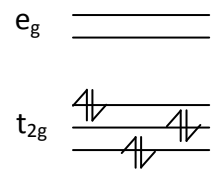
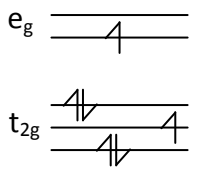
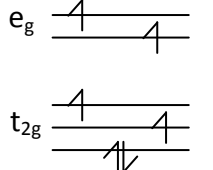
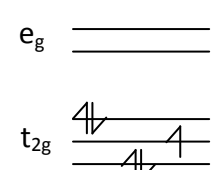
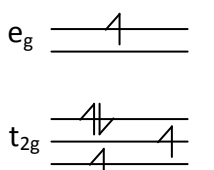
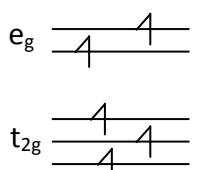
Where $\frac{N_A!}{M!(N_A - M)!}$ is the number of ways of arranging Co³⁺ and Co⁴⁺ sites.[Koshibae, Tsutsui & Maekawa, 2000]

N_A is the system size and M is the number of Co⁴⁺ sites. Plugging equation 4.4 into equation 4.3 and using Stirling's approximation, we get

$$S = -\frac{k_B}{e} \ln \left(\frac{g_3}{g_4} \frac{x}{1-x} \right) \dots \dots \dots (4.5)$$

'x' is the ratio of M to N_A , which is the concentration of Co⁴⁺ ions. Equation 4.5 states that a large value of Seebeck coefficient can be expected for an unbalance of spin and orbital degrees of freedom between Co³⁺ and Co⁴⁺ sites.[Koshibae, Tsutsui & Maekawa, 2000]

The trick is in figuring out the values of g_3 and g_4 , and as stated before that the parameters used are Hund's coupling (Hc), the crystal field splitting (Δ), and temperature (T). The different electronic configurations for Co³⁺ and Co⁴⁺ ions obtained at low spin, intermediate spin and high spin states were also explained earlier.

	Low Spin	Intermediate Spin	High Spin
Co^{3+}	$g_3=1, S=0$ 	$g_3=18, S=1$ 	$g_3=15, S=2$ 
Co^{4+}	 $g_4=6, S=1/2$	 $g_4=24, S=3/2$	 $g_4=6, S=5/2$

g is the degeneracy of the respective oxidation state
 S is the spin number; For \uparrow S is $\frac{1}{2}$ and for \downarrow S is $-\frac{1}{2}$

Figure 4.3. Illustration of the electronic configurations of cobalt ions, Co^{3+} and Co^{4+} .

(Illustration by Gautam G. Yadav)

Consider a system having low spin states of Co^{3+} and Co^{4+} ions, this corresponds to electronic configuration of t_{2g}^6 and t_{2g}^5 , respectively. This configuration can be understood as removing an electron from t_{2g}^6 to obtain t_{2g}^5 . There are six ways to remove an electron to obtain the t_{2g}^5 state, hence t_{2g}^5 has a sixfold degeneracy ($g_4 = 6$). t_{2g}^6 has no degeneracy, hence g_3 equals 1. The low spin states of Co^{3+} and Co^{4+} are stable when crystal field dominates (Δ) over Hund's coupling (H_c) and temperature (T). This condition can be

summarized as $\Delta \gg k_B T, H_c$. Similarly other conditions can be derived, and they are summarized in the table below.

Table 4.1. Various Conditions for the ratio of degeneracies, g_3 and g_4 . [Koshibae, Tsutsui & Maekawa, 2000]

Number	Co ³⁺ state (g_3)	Co ⁴⁺ state (g_4)	g_3/g_4	Condition
1.	Low Spin (1)	Low Spin (6)	1/6	$\Delta \gg k_B T, H_c$
2.	High Spin (15)	High Spin (6)	15/6	$H_c \gg k_B T, \Delta$
3.	High Spin + Low Spin (16)	High Spin (6)	16/6	$H_c, \Delta \gg k_B T,$
4.	Low Spin (1)	High Spin + Low Spin (12)	1/12	$H_c, \Delta \gg k_B T,$
5.	High Spin + Low Spin + Intermediate Spin (34)	High Spin + Low Spin + Intermediate Spin (36)	34/36	All conditions are close to each other

In Table 4.1., whenever the respective ions had a combination of states, for example in Condition 3, it simply meant that high spin and low spin states of Co³⁺ are close in energy and the high spin state of Co⁴⁺ is stable. Using the conditions stated in Table 4.1, the Seebeck coefficient for various layered cobaltates can be calculated. For example, in sodium cobalt oxides (Na_xCoO₂) there are mixed oxidation states of cobalt – Co³⁺ and Co⁴⁺. The

average valence of a cobalt ion is 3.5, therefore the concentration of Co^{4+} ions (x) is 0.5. Using equation 4.5 and considering the conditions stated in Table 4.1, condition 1 comes closest to matching the experimental Seebeck coefficient value of $154\mu\text{V}/\text{K}$. The stability of the low spin states of Co^{3+} and Co^{4+} ions are critical for obtaining the high Seebeck coefficient value in Na_xCoO_2 . In terms of a physical sense, it can be understood as the d^6 and d^5 states of Co^{3+} and Co^{4+} are close to each other, and the charge carrier moves between these two states. As the charge carrier moves, the states change from $d^6(\text{Co}^{3+})$ - $d^5(\text{Co}^{4+})$ into $d^5(\text{Co}^{4+})$ - $d^6(\text{Co}^{3+})$. This also corresponds to a change in degeneracy from g_3 - g_4 to g_4 - g_3 . The motion of degeneracy corresponds to the motion of entropy per carrier, and hence this relates to a high Seebeck coefficient value. [Koshibae, Tsutsui & Maekawa, 2000]

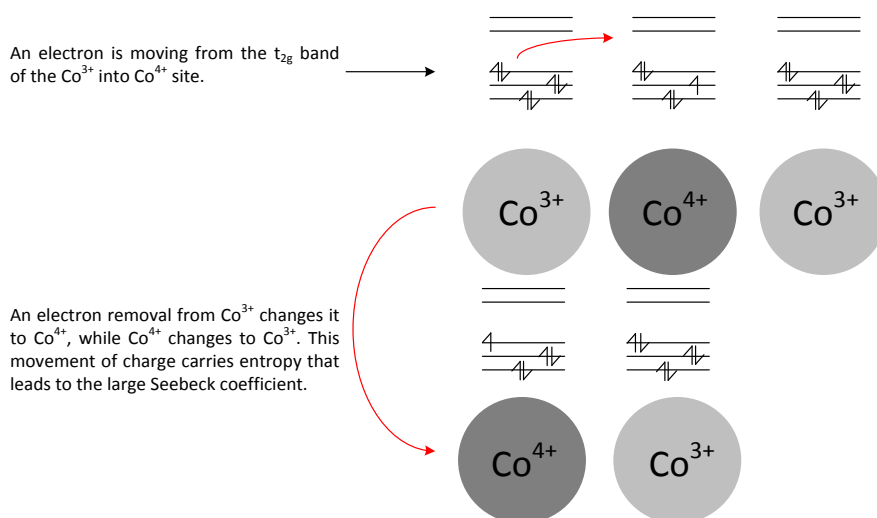


Figure 4.4. Illustration of charge conduction in layered cobaltates. (Illustration by Gautam G. Yadav)

4.3 Electrical conductivity in oxides

The charge carriers in oxide materials were briefly introduced in Section 4.1. In ionic compounds like oxides, the charge carriers that are free or bound to their centers induce polarization in the crystal to form a quasiparticle called polaron [Bosman & van Daal, 1970]. Polarons are characterized by their binding energy, effective mass, and the distortion created in the ionic lattice by the charge carriers [Bosman & van Daal, 1970; Devreese, 1996]. As the slow conduction charge carrier moves through the lattice, it polarizes and thereby distorts the ionic lattice. The moving charge carrier carries along the distortion of the lattice. If the distortion in the lattice extends over distances larger than the lattice constant then the polarons are called large. Similarly if the distortion is over distances smaller than the lattice constant then the polarons are called small. [Bosman & van Daal, 1970] For small polarons, the kinetic energy of the charge carrier in a rigid lattice is considered to arise from the intersite transfer. The lattice distortion can be described by the energy of the ionic displacement field. The interaction of the lattice vibrations and the localized charge carrier causes the charge carrier to jump from an ion to ion or atom to atom. This type of conduction is called the hopping mechanism.

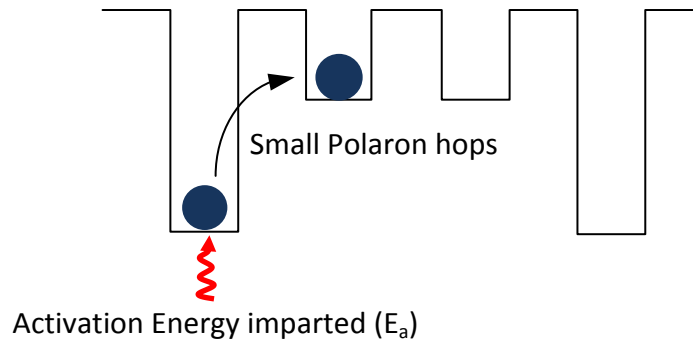


Figure 4.5. Illustration of small polaron hopping mechanism. (Illustration by Gautam G. Yadav)

A small polaron migrates through hopping of a charge carrier and polarized atomic configuration from one site to the adjacent one. The mobility for this hopping is given by [Tuller & Nowick, 1977]

$$\mu = \frac{(1-c)ea^2\varphi}{k_B T} \dots\dots\dots(4.6)$$

$$c = \frac{n}{N} \dots\dots\dots(4.7)$$

$$\varphi = P v_o \exp\left(\frac{-E_a}{k_B T}\right) \dots\dots\dots(4.8)$$

Where e is the electronic charge and a is the hopping distance. ‘ c ’ is the fraction of sites which contain an electron; therefore, n is the number of electrons and N the number of available sites per unit volume. φ is the jump rate of a polaron from one site to the

neighboring one. ν_o is the optical mode phonon frequency, P is the probability that the charge carrier will transfer the polarized configuration to the neighboring site. P is usually 1 [Tuller & Nowick, 1977]. E_a is the activation energy for hopping. Some of the terms can be lumped up into one variable that depend on the scattering mechanism. This variable will be called the pre-exponential term describing the scattering mechanism.

$$A = \frac{Nc(1-c)e^2\nu_o}{k_B} \dots\dots\dots(4.9)$$

Therefore, the new mobility equation is given by

$$\mu = \frac{Aa^2 \exp\left(\frac{-E_a}{k_B T}\right)}{T} \dots\dots\dots(4.10)$$

Substituting the above equation into the electrical conductivity equation derived in Chapter 2, we get the small polaron hopping conduction equation, which is given by

$$\sigma = ne\mu = \frac{nea^2A}{T} \exp\left(-\frac{E_a}{k_B T}\right) = \frac{C}{T} \exp\left(-\frac{E_a}{k_B T}\right) \dots\dots\dots(4.11)$$

Where n is the charge carrier concentration, and C is the combination of the other terms.

Equation 4.11 states that a strong charge carrier-lattice interaction exists due to a large effective mass and this causes the charge carrier moves slowly. The charge carrier imagines itself to be trapped in its own polarization field, and thus become localized. The only way to make it move is through imparting some activation energy that makes it hop from site and site, and thus conduct through the material. [Bosman & van Daal, 1970]

4.4 Summary

Layered oxides present some intriguing thermoelectric properties due to its crystal structure. The necessary physics relating to the Seebeck coefficient and electrical conducting mechanism have been presented. These equations and concepts will be applied in Chapter 7 to understand the interesting properties of the new layered phase of calcium cobalt oxide ($\text{Ca}_9\text{Co}_{12}\text{O}_{28}$).

4.5 References

Bosman, A.J.; van Daal, H.J. Small-polaron versus band conduction in some transition-metal oxides, *Advances in Physics*, **1970**, 19(77), 1-117.

Devreese, J.T. Polarons. *Encyclopedia of Applied Physics*, **1996**, 14, 383.

He, J.; Liu, Y.; Funahashi, R. Oxide thermoelectrics: The challenges, progress, and outlook. *J. Mater. Res.*, **2011**, 26(15), 1762-1772.

Koumoto, K.; Terasaki, I.; Funahashi, R. Complex Oxide Materials for Potential Thermoelectric Applications. *MRS Bulletin*, **2006**, 31, 206-210.

Koshibae, W.; Tsutsui, K.; Maekawa, S. Thermopower in cobalt oxides. *Phy. Rev. B*, **2000**, 62(11), 6869-6872.

Physics of Transition Metal Oxides; Maekawa, S.; Tohyama, T.; Barnes, S.E.; Ishihara, S.; Koshibae, W.; Khaliullin, G.; Springer Series in Solid State Sciences 144; Springer: Germany, Heidelberg, 2004.

Ohtaki, M. Oxide Thermoelectric Materials for Heat-to-Electricity Direct Energy Conversion. *Kyushu University Global COE Program Novel Carbon Resources Sciences Newsletter Vol. 3(Special Issue)*, **2010**, 1-6.

Terasaki, I.; Sasago, Y.; Uchinokura, K. Large thermoelectric power in NaCo₂O₄ single crystals. *Phys. Rev. B*, **1997**, 56(20), 685-687.

Tuller, H.L.; Nowick, A.S. Small Polaron Electron Transport in Reduced CeO₂ Single Crystals. *J. Phys. Chem. Solids*, **1977**, 38, 859-867.

CHAPTER 5. FEASIBILITY AND SUSTAINABILITY OF OXIDES FOR THERMOELECTRICS

This chapter deals with the systematic assessment of the deployability of thermoelectric materials for large-scale power generation. Herein, a framework is laid out for evaluating thermoelectric materials for near-term, large-scale power generation that is based on factors such as the ZT value of the material, its cost, abundance, and toxicity. These diverse characteristics are amalgamated into a metric we term the ‘efficiency ratio’ that selectively weighs each of the aforementioned parameters to suit the technological needs of power generation. The need for studying oxide-based thermoelectric materials is concluded based on the aforementioned parameters. The results of this assessment have been published in *Nanoscale*, [Yadav et al., 2011].

5.1 Introduction

The last 30 years has witnessed considerable research directed at finding more efficient materials and trying to increase their ZT values. A number of materials such as $\text{Ca}_{0.18}\text{Ni}_{0.03}\text{Co}_2\text{Sb}_{14}$, $\text{Ba}_8\text{Ga}_{16}\text{Ge}_{30}$, and $\text{Yb}_{11}\text{MnSb}_{14}$ have been reported to yield high ZT values at several temperatures [Kuznetsov et al., 2003; Puyet et al., 2005; Akrap et al., 2007]. However, the best commercial thermoelectric devices report ZT values and an operating efficiency of only 0.8 and around 5-6% respectively [Sootsman et al., 2007]. The device efficiency is directly related to the ZT value and could be increased to 30% if the ZT value can reach to 4. In fact, maximum ZT values greater than 1 have been obtained in laboratory conditions at temperatures in excess of 600K. For example, maximum ZT values as high as 1.3 for $\text{Ba}_{0.30}\text{Ni}_{0.05}\text{Co}_{0.95}\text{Sb}_{12}$ and 1.32 for $\beta\text{-Zn}_4\text{Sb}_3$ have been reached at temperatures of 900K and 670K respectively [Tanga et al., 2005; Caillat et al., 1997]. Although these values are promising for practical applications, some of these materials are not quite suitable for high temperature operations above 1000K due to adverse effects such as melting, decomposition, or vaporization [Ohta et al., 2007]. In addition, quantifying material costs and considering abundance presents a critical metric for helping to determine the most appropriate thermoelectric material.

In a competitive industry, the net price of materials combines marketing and extraction costs. At any given time, the price of a material is dependent on a number of factors such as production rate, the customer's willingness to pay, the grade of the ore, and material prices

have previously been modeled using linear and polynomial functions [Slade, 1982]. For example, aluminum (Al) has seen a decrease in price from \$1.50/pound to around \$0.25/pound over the past 100 years and has become relatively stable while lead (Pb) has seen very little variation in price [9]. Silver (Ag) dropped in price for a period of 40 years and following the 1950's has been steadily increasing [Slade, 1982]. Moreover, the development of cheap plastics and ceramics over the years has resulted in a substitution of some of these materials [Maltusians and Tierney, 1990].

Entrepreneurship, continuing technological improvements, and recycling seem to cushion the effects of higher demand and lower availability [Maltusians and Tierney, 1990]. However, despite overall decreases in the prices of most minerals [Kula, 1982; Napier-Munn and Wills, 2006], the price of minerals still depends heavily on their availability. There are twelve elements that comprise 99% of the earth's crust. These elements include oxygen (O), silicon (Si), aluminum (Al), iron (Fe), calcium (Ca), magnesium (Mg), sodium (Na), potassium (K), titanium (Ti), hydrogen (H), manganese (Mn), and phosphorous (P) [Taylor, 1964]. A good majority of these elements are locked up in oxides of some sort and occur naturally in granite and basalt. Reserves of germanium (Ge) hold around 450,000 kg while the price of germanium is close to \$900/kilogram [USGS, 2010]. Aluminum reserves hold close to 79 billion kilogram and the price is around \$1.8/kilogram [USGS, 2010]. In the next few sections, we look at the current ZT values as well as current availability and prices as a guide for choosing the best thermoelectric materials.

5.2 Methods

The materials chosen for this analysis are taken from M. G. Kanatzidis' recent review paper [Kanatzidis, 2009] and are listed in **Table 5.1**. All the materials are allocated a reference number for convenient labeling in the ensuing figures and are arranged by their operational temperature where the maximum ZT values are obtained experimentally. The maximum ZT values are chosen as it provides a clear understanding of the feasibility of these materials and the limitation that these materials face after certain temperature ranges. It should be noted that many research activities are still under progress to find ways to increase the ZT values of a material at different temperature or wider temperature range.

Table 5.1. Materials allocated with a reference number for convenient representation in ensuing figures. The materials have been arranged from low to high temperature. Please note that these ZT values are approximate values obtained experimentally. [Yadav et al., 2011]

MATERIAL NUMBER	THERMOELECTRIC MATERIALS	ZT	References
1.	FeSb ₂	0.005	[Kanatzidis et al.,2009; Bientien et al., 2007]
2.	BiSb	0.62	[Kanatzidis et al.,2009]

3.	CsBi_4Te_6	0.84	[Kanatzidis et al.,2009]
4.	$\beta\text{-K}_2\text{Bi}_8\text{Se}_{13}$	0.23	[Kanatzidis et al.,2009; Chung et al., 1997]
5.	Bi_2Te_3	0.9	[Kanatzidis et al.,2009]
6.	PbTe	0.81	[Kanatzidis et al.,2009]
7.	$(\text{AgSbTe}_2)(\text{GeTe})$	1.2	[Kanatzidis et al.,2009; Plachkova,1984]
8.	Tl_9BiTe_6	1.2	[Kanatzidis et al.,2009; Wölfing et al., 2001]
9.	Tl_2SnTe_5	1	[Kanatzidis et al.,2009; Sharp, 1999]
10.	$\text{Yb}_{0.19}\text{Co}_4\text{Sb}_{12}$	1	[Bentien et al., 2007; Nolas et al., 2000]
11.	Sb doped TiNiSn	0.45	[Bentien et al., 2007; Bhattacharya, 2000]
12.	Polycrystalline $\text{Ag}_{0.8}\text{Pb}_{22}\text{SbTe}_{20}$	1.5	[Kanatzidis et al.,2009; Zhou et al., 2008]
13.	$\beta\text{-Zn}_4\text{Sb}_3$	1.32	[Kanatzidis et al.,2009; Caillat et al., 1997]
14.	$(\text{Zr}_{0.5}\text{Hf}_{0.5})_{0.5}\text{Ti}_{0.5}\text{NiSn}_{0.998}\text{S}$ $\text{b}_{0.002}$	1.4	[Kanatzidis et al.,2009; Sakurada and Shutoh, 2005]
15.	Ag_9TiTe_5	1.23	[Kanatzidis et al.,2009; Kurosaki et al., 2005]

16.	$\text{TlIn}_{0.94}\text{Yb}_{0.06}\text{Te}_2$	1.8	[Kanatzidis et al.,2009; Godzhaev and Kerimova, 2004]
17.	$\text{AgPb}_{18}\text{SbTe}_{20}$	1.7	[Kanatzidis et al.,2009; Hsu et al., 2004]
18.	AgSbTe_2	1.3	[Kanatzidis et al.,2009; Wood, 1988]
19.	$\text{Ce}_{0.9}\text{Fe}_3\text{CoSb}_{12}$	1.1	[Kanatzidis et al.,2009; Sales et al., 1996; Tang et al., 2001]
20.	$(\text{AgSbTe}_2)_{0.2}(\text{GeTe})_{0.8}$	1.4	[Kanatzidis et al.,2009; Yang et al., 2008]
21.	$(\text{AgSbTe}_2)_{.15}(\text{GeTe})_{.85}$	1.5	[Kanatzidis et al.,2009; Yang et al., 2008]
22.	$\text{NaCoO}_2(\text{crystal})$	1	[Kanatzidis et al.,2009; Terasaki, 2005]
23.	PbTe with Tl	1.5	[Kanatzidis et al.,2009; Heremans et al., 2008]
24.	$\text{Ca}_{0.18}\text{Ni}_{0.03}\text{Co}_{3.97}\text{Sb}_{12.4}$	1	[Kanatzidis et al.,2009; Puyet et al., 2005]
25.	$\text{Ba}_{0.3}\text{Co}_4\text{Sb}_{12}$	0.8	[Kanatzidis et al.,2009; Dyck, 2002]
26.	$\text{Ca}_{0.08}\text{Co}_4\text{Sb}_{12.45}$	0.45	[Kanatzidis et al.,2009; Puyet et al., 2004]
27.	$\text{Zr}_{0.5}\text{Hf}_{0.5}\text{Ni}_{0.8}\text{Pd}_{0.2}\text{Sn}_{0.99}\text{Sb}$ 0.01	0.7	[Kanatzidis et al.,2009; Shen et al., 2001]
28.	$\text{NaCo}_2\text{O}_4(\text{single crystal})$	1	[Kanatzidis et al.,2009; Terasaki, 2005]

	sample)		
29.	$\text{Ba}_{0.30}\text{Ni}_{0.05}\text{Co}_{3.95}\text{Sb}_{12}$	1.3	[Tang et al., 2005; Kanatzidis et al.,2009]
30.	$\text{Ba}_8\text{Ga}_{16}\text{Ge}_{30}$	1.35	[Kanatzidis et al.,2009; Saramat et al., 2006]
31.	$\text{Ca}_3\text{Co}_4\text{O}_9$ (crystal)	0.9	[Kanatzidis et al.,2009; Terasaki, 2005]
32.	NaCo_2O_4 (polycrystalline sample)	0.8	[Bentien et al., 2007; Koumoto et al., 2006]
33.	$\text{Bi}_2\text{Sr}_2\text{Co}_2\text{O}_y$ (crystal)	1.14	[Kanatzidis et al.,2009; Terasaki, 2005]
34.	Nb doped SrTiO_3	0.37	[Kanatzidis et al.,2009; Koumoto et al., 2006]
35.	La doped SrTiO_3	0.26	[Kanatzidis et al.,2009; Koumoto et al., 2006]
36.	$\text{Al}_{0.02}\text{Zn}_{0.98}\text{O}$	0.3	[Kanatzidis et al.,2009; Ohtaki et al., 1996; Tsubota, 1997]
37.	$\text{Hf}_{0.75}\text{Zr}_{0.25}\text{NiSn}_{0.975}\text{Sb}_{0.025}$	0.8	[Kanatzidis et al.,2009]
38.	$\text{Si}_{0.8}\text{Ge}_{0.2}$	0.6	[Kanatzidis et al.,2009; Fleurial, 1993]
39.	NaCoO_2 (ceramic)	0.78	[Kanatzidis et al.,2009; Terasaki, 2005]

40.	Ca doped $(\text{ZnO})_3(\text{In}_2\text{O}_3)$	0.31	[Kanatzidis et al.,2009; Kaga and Tani, 2004]
41	$\text{Yb}_{11}\text{MnSb}_{14}$	1	[Kanatzidis et al.,2009]

5.3 Results & discussion

To better understand the thermoelectric materials and their applications at different temperature ranges, we divide the 41 materials listed in Table 5.1. into three categories shown in Figure 5.1. Categories are demarcated from each other using red lines. Materials are classified under low temperature applications if their maximum ZT values fall below 200K, under moderate temperatures application if their ZT values fall in between 200K and 1000K, and any material having maximum ZT at temperatures above 1000K is grouped under the high temperature application group. Such a classification scheme allows easy comparisons between material cost (price), material abundance (sustainability), material feasibility (efficiency ratio), and materials safety (toxicity) for the three working temperature ranges respectively.

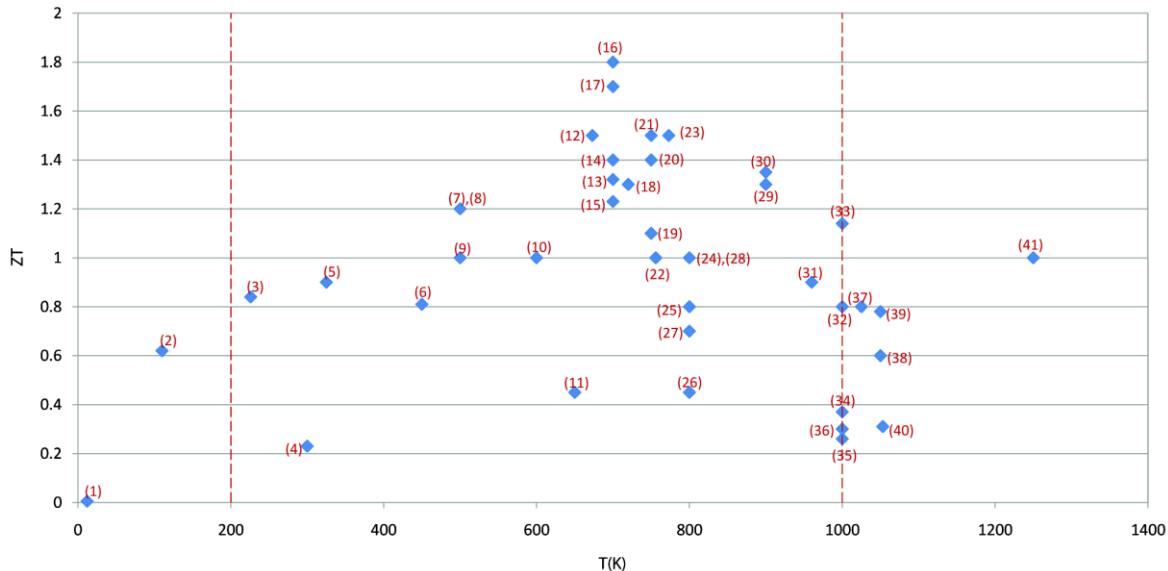


Figure 5.1. A plot of maximum ZT value of different materials versus temperature (K) labeled by the corresponding material numbers. [Yadav et al., 2011]

5.3.1 Price

The cost of various thermoelectric materials is shown in Figure 5.2. The price calculations are performed on an elemental basis as most thermoelectric bulk materials are produced by mixing the elements together followed by a high temperature growth process. The costs of the elements are taken from Sigma Aldrich handbook [Sigma-Aldrich, 2009-2010]. Notably, only the cheapest and 99% or more purity elements are chosen for the analysis here because the ZT values of these materials strongly depend on the purity of the element. Oxygen has been excluded from this exercise. In addition, for some doped materials in Table 5.1., the percentage is assumed to be 5% if the doping level was not clearly indicated. The decision to

use the vendor price was based on the assumption that mining and extraction costs are already factored in when the prices are quoted. Although there are a few formulas for cost estimation existing in several previous reports [Solow, 1974; Wadia, 2009], we decide against using them so as to remove any grey areas in our price calculation as there are some parameters in these formulae that are too cumbersome to acquire or are just unavailable. We do acknowledge that even the cheapest vendor price may vary from the industrial-scale bulk order price; however, the vendor price is used here as an index to simply reflect a consistent baseline for the materials cost estimation.

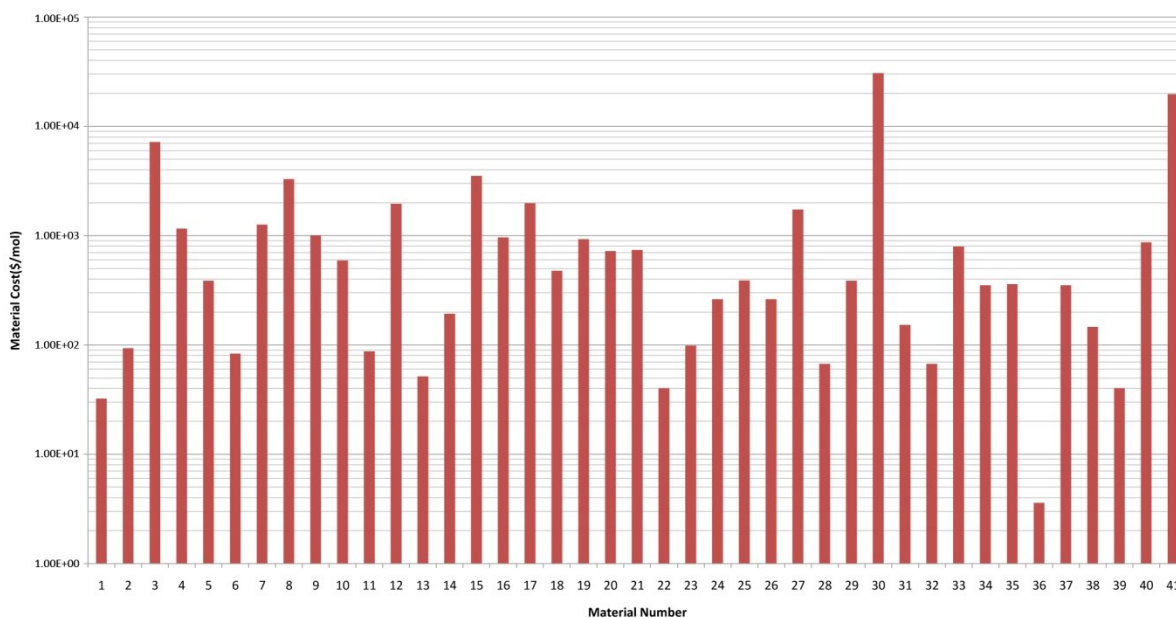


Figure 5.2. A logarithmic-scale plot of price in dollars per mole for different materials. The material numbers correspond to the respective thermoelectric materials mentioned in Table 5.1. [Yadav et al., 2011]

5.3.2 Sustainability

Sustainability is another important parameter for determining the usability of a material. For a material to be considered usable in a product, a producer must be able to produce it for a long period of time without worrying about material shortage or shelf life. There are several ways to look at sustainability, of which reserve availability and resource availability are the most intuitive. Resource availability of an element is defined as its availability in the earth's crust. Reserve availability is defined as the amount of the element that is currently available for extraction. For the purposes of this paper we focus on reserve availability because it takes into consideration the ease of extraction. Sustainability analysis here is built on two assumptions: (1) once the material is incorporated into the product there will relatively be little or no degradation of the material over time (i.e. it will not lose its effectiveness), and (2) the reserve availability serves as a good indicator of the availability for future use based on resource availability and ease of recovery. Figure 5.3. lays out the reserve availability of most of the elements (28 out of totally 33 elements) existing in the thermoelectric materials listed in Table 5.1. Conclusive data are not available for the reserve availability of cerium. For oxygen, sodium, calcium, and silicon, their reserve availabilities are nearly inexhaustable.

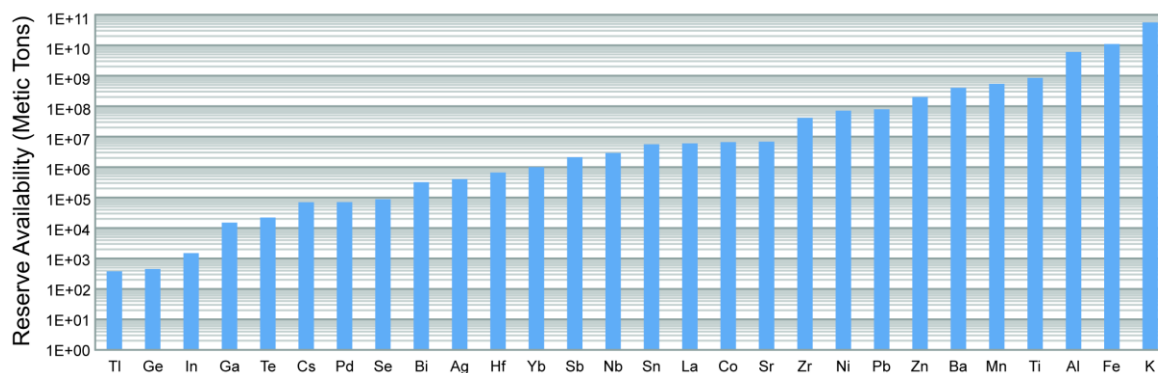


Figure 5.3. A logarithmic-scale plot of the abundance of different elements existing in various thermoelectric materials. [Yadav et al., 2011]

From the analysis of reserve availability in Figure 5.3., Fe, Ca, Si, Na, and K appear to constitute a substantial part of the earth's crust, while Si, Al, Fe, and Mg present the top 4 oxides in terms of wt % in the earth' crust.¹⁴ SiO₂ comprises 60% by weight of igneous rocks [Taylor, 1964]. The reserve availability of Fe is approximately 11 billion tons [USGS, 2010]. This is a crude estimate because most of the iron is locked in the soil and it not readily available for extraction. Elements such as Bi or Ag have a reserve availability of approximately 500,000 metric tons [USGS, 2010]. Some of the least produced elements are the rare earth elements. Mining of rare earth elements such as those in the lanthanide and actinide series covers a small percentage of the mining industry due to the scarcity of these elements. For this reason, any compounds that contain these elements could suffer from price fluctuations, and most compounds are limited by the availability of these less available elements. As cofactors in determining the most viable material, mining difficulties, toxicity,

and recyclability should be also included in this discussion. However, for the ease of simplicity, they will only be briefly mentioned in the following paragraphs. In addition, by considering the reserve availability of the element in terms of tonne mole and the mole fraction of each element in the thermoelectric compounds in our calculations, we can clearly identify the limiting elements for the large-scale production of each thermoelectric materials, which have been summarized in Table 5.2., and Te, Sb, and Ge seem to be the most frequent limitations in the relative availability of the materials.

Table 5.2. Table of limiting elements for various thermoelectric materials by calculating the mole fraction/unit of different elements in the materials and the reserve availability. [Yadav et al., 2011]

MATERIAL NUMBER	THERMOELECTRIC MATERIALS	Limiting Element
1.	FeSb_2	Sb
2.	BiSb	Bi
3.	CsBi_4Te_6	Se
4.	$\beta\text{-K}_2\text{Bi}_8\text{Se}_{13}$	Bi
5.	Bi_2Te_3	Te
6.	PbTe	Te

7.	$(\text{AgSbTe}_2)(\text{GeTe})$	Ge
8.	Tl_9BiTe_6	Te
9.	Tl_2SnTe_5	Tl
10.	$\text{Yb}_{0.19}\text{Co}_4\text{Sb}_{12}$	Sb
11.	Sb doped TiNiSn	Ni
12.	Polycrystalline $\text{Ag}_{0.8}\text{Pb}_{22}\text{SbTe}_{20}$	Te
13.	$\beta\text{-Zn}_4\text{Sb}_3$	Sb
14.	$(\text{Zr}_{0.5}\text{Hf}_{0.5})_{0.5}\text{Ti}_{0.5}\text{NiSn}_{0.998}\text{Sb}_{0.002}$	Hf
15.	Ag_9TiTe_5	Te
16.	$\text{TlIn}_{0.94}\text{Yb}_{0.06}\text{Te}_2$	In
17.	$\text{AgPb}_{18}\text{SbTe}_{20}$	Te
18.	AgSbTe_2	Te
19.	$\text{Ce}_{0.9}\text{Fe}_3\text{CoSb}_{12}$	Ce
20.	$(\text{AgSbTe}_2)_{0.2}(\text{GeTe})_{0.8}$	Ge
21.	$(\text{AgSbTe}_2)_{.15}(\text{GeTe})_{.85}$	Ge
22.	$\text{NaCoO}_2(\text{crystal})$	Co

23.	PbTe with Tl	Tl
24.	$\text{Ca}_{0.18}\text{Ni}_{0.05}\text{Co}_{3.97}\text{Sb}_{12.4}$	Sb
25.	$\text{Ba}_{0.3}\text{Co}_4\text{Sb}_{12}$	Sb
26.	$\text{Ca}_{0.08}\text{Co}_4\text{Sb}_{12.45}$	Co
27.	$\text{Zr}_{0.5}\text{Hf}_{0.5}\text{Ni}_{0.8}\text{Pd}_{0.2}\text{Sn}_{0.99}\text{Sb}_{0.01}$	Pd
28.	NaCo_2O_4 (single crystal sample)	Co
29.	$\text{Ba}_{0.30}\text{Ni}_{0.05}\text{Co}_{3.95}\text{Sb}_{12}$	Sb
30.	$\text{Ba}_8\text{Ga}_{16}\text{Ge}_{30}$	Ga
31.	$\text{Ca}_3\text{Co}_4\text{O}_9$ (crystal)	Co
32.	NaCo_2O_4 (polycrystalline sample)	Co
33.	$\text{Bi}_2\text{Sr}_2\text{Co}_2\text{O}_y$ (crystal)	Bi
34.	Nb doped SrTiO_3	Ti
35.	La doped SrTiO_3	Ti
36.	$\text{Al}_{0.02}\text{Zn}_{0.98}\text{O}$	Al
37.	$\text{Hf}_{0.75}\text{Zr}_{0.25}\text{NiSn}_{0.975}\text{Sb}_{0.025}$	Sb
38.	$\text{Si}_{0.8}\text{Ge}_{0.2}$	Ge

39.	NaCoO ₂ (ceramic)	Co
40.	Ca doped (ZnO) ₃ (In ₂ O ₃)	In
41	Yb ₁₁ MnSb ₁₄	Yb

5.3.3 Efficiency ratio

A new term called ‘efficiency ratio’ has been calculated and depicted in Figure 5.4. for all the thermoelectric materials in Table 5.1. as a method to estimate which thermoelectric material would provide the most feasibility for scaling up. Obviously, a high ratio would be beneficial as the ZT value would be high and the cost of the material would be low. The materials containing rare earth elements have dwarfed ratios owing to their higher costs of such elements. An overall view of Fig. 4 indicates Al_{0.02}Zn_{0.98}O (#36) as the most feasible material for high temperature application. For low temperature applications, BiSb (#2) stands out because of its low price. β -Zn₄Sb₃ (#13) is the best material for moderate temperature applications because of the combination of its maximum ZT value and low price.

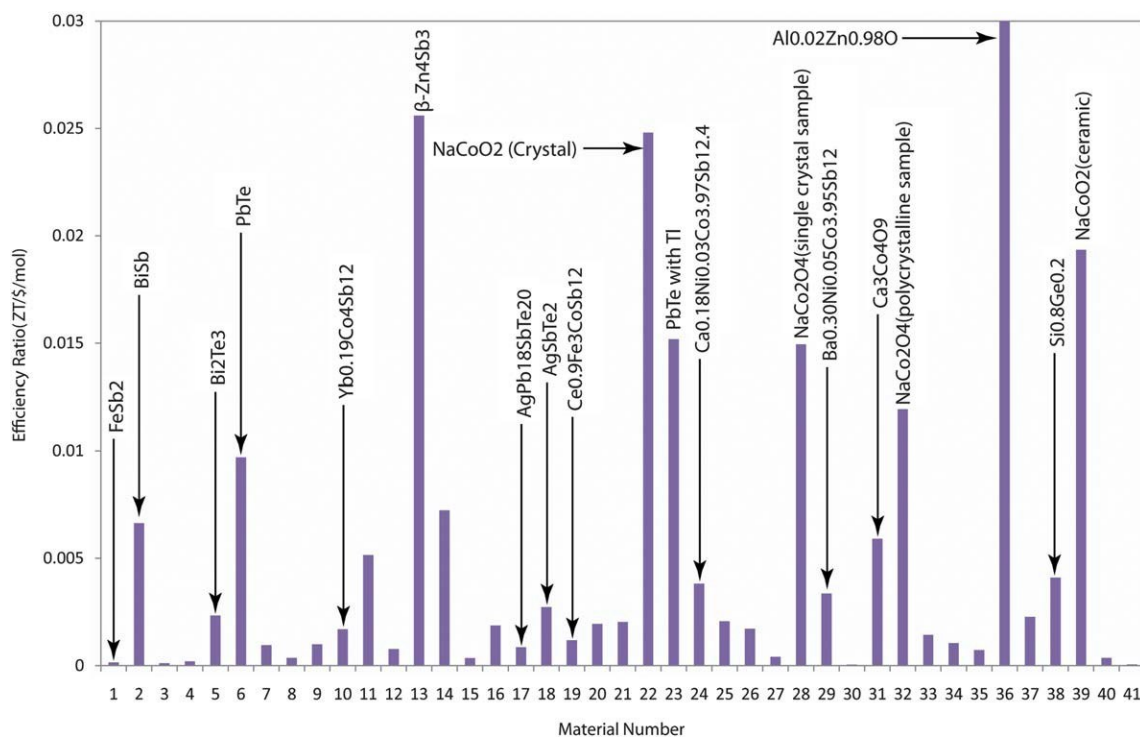


Figure 5.4. A plot of efficiency ratio for various materials. Material numbers correspond to the respective thermoelectric materials as mentioned in Table 5.1. [Yadav et al., 2011]

5.3.4 Toxicity

Ideally, toxicity should be factored in the analysis to help us better estimate and understand the recycling cost of thermoelectric materials mentioned in Table 5.1. Moreover, toxicity and after-use life are important aspects of life cycle assessments. However, toxicity cannot be easily quantified to conduct a better analysis and can be easily considered to be prejudicial. There are several values used to quantify the toxicity of a material or element, which include TLV (Threshold Limiting Value) and LD50 (Lethal Dosage). Threshold limiting value (TLV)

is defined as the amount of substance (amount of dust in per volume of air) that a person can be exposed for certain duration during their working lifetime without experiencing any adverse effects to their health, which will play an important role in determining the manufacturing costs (personal protection, cleaning the manufacturing area, waste disposal, etc) [International Union of Pure and Applied Chemistry, 2010]. LD50 is defined as the dose of a substance to kill 50% of a population, which will affect the cost of material packaging and recycling to minimize the environmental residual [U.S. Environmental Protection Agency, 2010]. Tellurium, thallium, cobalt, which comprise a large number of the thermoelectric materials listed in Table 1, are considered to be highly toxic metals, which have LD50 values of 83, 41.3, and 6.171mg/kg along with TLV values of 0.1, 0.1, and 0.01 mg/m³, respectively [ACIAALLOYS, 2000a, 200b; ESPIMETALS, 2006]. Germanium and antimony are also used in a number of materials however they are not nearly as toxic as Te, Tl, and Co, but materials with a high concentration of these elements should be avoided [ESPIMETALS, 2004, 2007]. Thermoelectric materials containing tellurium and thallium should particularly be avoided for high temperature applications because of the materials tend to decompose and release harmful vapor to the environment.

5.4 Conclusions

Thermoelectrics is a vast and yet unexplored research field. Considerable research is being undertaken to understand this field thoroughly. We decide to broach this field from a different perspective and try to understand it better by providing a feasibility and

sustainability analysis. Based on our analysis, the most expensive materials are the ones that contain some form of rare earth elements. Some of these materials with rare earth elements have high ZT values, but it does not necessarily mean they are feasible to be used in large-scale applications. In low temperature applications, FeSb_2 is the cheapest material as iron is fairly abundant in the earth's crust. Particularly, it represents the only inorganic material capable of operation at cryogenic temperature around 10 K that would enable solid state cooling for high performance IR imaging systems. On the other hand, BiSb has the highest efficiency ratio because its ZT value is two orders higher than FeSb_2 . BiSb might present a problem in the future in terms of price fluctuations and due to the low reserve availability of Bi and Sb because the availability of Bi is nearly ten times less than the availability of Sb. For the moderate temperature applications, a number of thermoelectric materials look to be feasible, but $\beta\text{-Zn}_4\text{Sb}_3$ is the best as it has both a high ZT value and a low material cost. Several chalcogenides materials including PbTe and Bi_2Te_3 are beneficial to be used in moderate temperature applications as well, however, they exhibit a few obvious drawbacks, among which material instability (oxidation or decomposition), environmental concern of toxicity, and high recycling cost are a few. Compared to chalcogenides, oxides are more stable in oxidative atmospheres, especially at high temperature. However, ZT values of oxides are too low for most practical applications due to the much larger thermal conductivity, although they can possess similar electrical conductivity and Seebeck coefficient as those of the chalcogenides. By converting the bulk materials of these oxides into nanostructures, the thermal conductivity could be significantly reduced and a significant improvement in ZT will be expected. Among the oxide-based thermoelectric materials,

$\text{Al}_{0.02}\text{Zn}_{0.98}\text{O}$ appears to be the most feasible since its highest efficiency ratio, although a significant concern of the material stability/compatibility with water vapor at high temperature should be noted. Besides $\text{Al}_{0.02}\text{Zn}_{0.98}\text{O}$, several cobalt oxide-based materials, such as NaCoO_2 (#39), NaCo_2O_4 (#32), and $\text{Ca}_3\text{Co}_4\text{O}_9$ (#31) are also potentially good candidates for high temperature applications because of their relatively high efficiency ratio. Strontium titanate (SrTiO_3 , #34 and #35) should also be considered for large-scale applications if a new type of dopant other than La^{3+} and Nb^{5+} could be developed to lower the material cost. SrTiO_3 has a few advantages: (1) the melting point of SrTiO_3 is 2060°C , making it applicable at extremely high temperature; (2) all the elements of SrTiO_3 are naturally abundant and non-toxic; (3) the electrical conductivity of SrTiO_3 can be easily tuned by substitutional doping [Sigma-Aldrich, 2008]. Currently, research on the thermoelectric properties of these complex oxides (especially their nanostructures) is still fairly inchoate, however they represent an efficient way for the power generation from high grade thermal sources such as the exhaust from turbine engines.

5.5 References

Akrap, A.; Barisic, N.; Forro, L.; Mandrus, D.; Sales, B.C. High-Pressure resistivity and thermoelectric power in $\text{Yb}_{14}\text{MnSb}_{11}$. *Phys. Rev. B.*, **2007**, 76 (8), 5203.

Bentien, A.; Johnsen, S.; Madsen, G.K.H.; Iversen, B.B.; Steglich, F. Colossal seebeck coefficient in strongly correlated semiconductor FeSb_2 . *EPL*, **2007**, 80(1), 17008.1-17008.5.

Bhattacharya, S. Effect of Sb doping on the thermoelectric properties of Ti-based half-Heusler compounds $\text{TiNiSn}_{1-x}\text{Sb}_x$. *Appl. Phys. Lett.*, **2000**, 77(16), 2476.1-2476.3.

Caillat, T.; Fleurial, J.P.; Borschevesky, A. Preparation and thermoelectric properties of semiconducting Zn_4Sb_3 . *J. Phys. Chem. Solids.*, **1997**, 58(7), 1119-1125.

Chung, D.Y.; Choi, K.S.; Iordanidis, L.; Schindler, J.L.; Brazis, P.W.; Kannewurf, C.R.; Chen, B., Hu, S.; Uher, C.; Kanatzidis, M.G. High thermopower and low thermal conductivity in semiconducting ternary K-Bi-Se compounds: synthesis and properties of $\beta\text{-K}_2\text{Bi}_8\text{Se}_{13}$ and $\text{K}_{2.5}\text{Bi}_{8.5}$ and the Sb analogies. *Chem. Mater.*, **1997**, 9(12), 3060-3071.

Dyck, J.S. Thermoelectric properties of the n-type filled skutterudite $\text{Ba}_{0.3}\text{Co}_4\text{Sb}_{12}$ doped with Ni. *J. Appl. Phys.*, **2002**, 91(6), 3698-3706.

Fleurial, J.P. Short Course on Thermoelectrics. The International Thermoelectric Society, Japan. **1993**, 1-27.

Godzhaev, E.M.; Kerimova, R.A. Thermoelectric Properties of $\text{TlIn}_{1-x}\text{Yb}_x\text{Te}_2$ ($0.01 \leq x \leq 0.09$) Crystals. *Inorg. Mater.*, **2004**, 40(11), 1153-1155.

Heremans, J.P.; Jovovic, V.; Toberer, E.S.; Saramat, A.; Kurosaki, K.; Charoenphakdee, A.; Yamanaka, S.; Snyder, G.J. Enhancement of thermoelectric efficiency in PbTe by distortion of the electronic density of states. *Science.*, **2008**, 321 (5888), 554-557.

Hsu, K.F.; Loo, S.; Chen, W.; Dyck, J.S.; Uher, C.; Hogan, T., Polychroniadis, E.K., Kanatzidis, M.G. Cubic $\text{AgPb}_m\text{SbTe}_{2+m}$: Bulk Thermoelectric Materials with High Figure of Merit. *Science.*, **2004**, 303(5659), 818-821.

Kaga, H.; Tani, T. Thermoelectric Properties of Highly Textured Ca-Doped $(\text{ZnO})_m\text{In}_2\text{O}_3$ Ceramics. *Jpn. J. Appl. Phys.*, **2004**, 43(1), 7133-7136.

Sootsman, J.S.; Chung, D.Y.; Kanatzidis, M.G. New and old concepts in thermoelectric materials. *Angew. Chem. Int. Ed.*, **2009**, 48, 8616-8639.

Koumoto, K.; Terasaki, I.; Funahashi, R. Complex oxide materials for potential thermoelectric applications. *Mater. Res. Soc. Bull.*, **2006**, 31(3), 206-210.

Kula, E. Economics of Natural Resources and the Environment, 1st ed. Chapman & Hall, London. **1992**.

Kurosaki, K.; Kosuga, S.; Muta, H.; Uno, M.; Yamanaka, S. A high-performance thermoelectric bulk material with extremely low thermal conductivity. *Appl. Phys. Lett.*, **2005**, 87(6), 06919.1-06919.3.

Kuznetsov, V.L.; Kuznetsova, L.A.; Kaliazin, A.E.; Rowe, D.M. Effect of partial void filling on the transport properties of $\text{Nd}_x\text{Co}_4\text{Sb}_{12}$. *J.Phys. Condense. Matter.*, **2003**, 15(29), 5035-5048.

Nolas, G.S.; Kaeser, M.; Littleton, R.T.; Tritt, T.M. High figure of merit in partially filled ytterbium skutterudite materials, *Appl. Phys. Lett.*, **2000**, 77(12), 1855.1-1855.3.

Ohta, H.; Kim, S.; Mune, Y., et al. Giant thermoelectric seebeck coefficient of a two dimensional electron gas in SrTiO_3 . *Nature Materials*, **2000**, 9, 129-134.

Ohtaki, M.;Tsubota, T.; Eguchi, K.; Arai, H.. High-temperature thermoelectric properties of $(\text{Zn}_{1-x}\text{Al}_x)\text{O}$. *J. Appl. Phys.*, **1996**, 79(3), 1816.1-1816.3.

Plachkova, S.K. Thermoelectric figure of merit of the system $(\text{GeTe})_{1-x}(\text{AgSbTe}_2)_x$. *Phys. Status. Solid. A.*, **1984**, 83(1), 349-356.

Puyet, M.;Lenoir, B.; Dauscher, A.; Dehmas, M.; Stiewe, C.; Müller, E. High temperature transport properties of partially filled $\text{Ca}_x\text{Co}_4\text{Sb}_{12}$ skutterudites. *J. Appl. Phys.*, **2004**, 95(9), 4852.1-4852.4.

Puyet, M.; Dauscher, A.; Lenoir, B.; Dehmas, M.; Stiewe, C.; Müller, E.; Hejtmanek, J. Beneficial effect of Ni substitution on the thermoelectric properties in partially filled $\text{Ca}_y\text{Co}_{4-x}\text{Ni}_x\text{Sb}_{12}$ skutterudites. *J. Appl. Phys.*, **2005**, 97(8), 083712.1-083712.4.

Sakurada, S.; Shutoh, N. Effect of Ti substitution on the thermoelectric properties of $(\text{Zr,Hf})\text{NiSn}$ half-Heusler compounds. *Appl. Phys. Lett.*, **2005**, 86(8), 082105.1-082105.3.

Sales, B.C.; Mandrus, D.; Williams, R.K. Filled Skutterudite Antimonides: A new class of thermoelectric materials. *Science.*, **1996**, 272(5266), 1325-1328.

Saramat, A.; Svensson, G.; Palmqvist, A.E.C.; Stiewe, C.; Müller, E.; Platzek, D.; Williams, S.G.K.; Rowe, D.M.; Bryan, J.D.; Stucky, G.D. Large thermoelectric figure of merit at high temperature in Czochralski-grown clathrate $\text{Ba}_8\text{Ga}_{16}\text{Ge}_{30}$. *J. Appl. Phys.*, **2006**, 99(2), 023708.1-023708.5.

Sharp, J.W.; Sales, B.C.; Mandrus, D.G.; Chakoumakos, B.C. Thermoelectric properties of Tl_2SnTe_5 and Tl_2GeTe_5 . *Appl. Phys. Lett.*, **1999**, 74(25), 3794-3796.

Shen, Q.; Chen, L.; Goto, T.; Hirai, T.; Yang, J.; Meisner, G.P.; Uher, C. Effects of partial substitution of Ni by Pd on the thermoelectric properties of ZrNiSn- based half-Heusler compounds. *Appl. Phys. Lett.*, **2001**, 79(25), 4165.1-4165.3.

Sigma-Aldrich, 2009-2010. Handbook of Fine Chemicals. Sigma-Aldrich, United States.

Slade, M.E. Trends in natural-resource commodity prices- An analysis of the time domain. *J. Environ. Econ. Manage.*, **1982**, 9(2), 122-137.

Snyder, G.J.; Toberer, E.S. Complex thermoelectric materials. *Nature Mater.*, **2008**, 105-114.

Solow, R.M. Economics of resources or resources of economics. *Am. Econ. Rev.*, **1974**, 64(2), 1-14.

Sootsman, J.R.; Chung, D.Y.; Kanatzidis, M.G. Nanostructured thermoelectric materials and high efficiency power-generation modules. *J. Electron. Mater.*, **2007**, 36, 704-710.

Tang, X. Effects of Ce filling fraction and Fe content thermoelectric properties of Co-rich $Ce_yFe_xCo_{4-x}Sb_{12}$. *J. Mater. Res.*, **2001**, 16(3), 837-843.

Tang, X.; Zhang, Q.; Chen, L.; Takashi, G.; Toshio, H., et al. Synthesis and thermoelectric properties of p-type and n-type filled skutterdite $R_yM_xCo_{4-x}Sb_{12}$. *J. Appl. Phys.*, **2005**, 97(9), 093712.1-093712.10.

Taylor, S.R. Abundance of chemical elements in the continent. *Gechim. Cosmochim. Acta.*, **1964**, 28, 1273-1285.

Terasaki, I. Physics of the thermoelectric oxide $NaCo_2O_4$: a guide to new thermoelectric oxides. Proc. 21st Int. Conf. Thermoelectrics. **2002**, 185.

Terasaki, I. Thermoelectric materials in layered transition-metal oxides. *Mater. Integr.*, **2005**, 18 (9), 7-11.

Tierney, J., Maltusians, C., 1990. Betting On the Planet. The New York Times, New York.

Tsubota, T. Thermoelectric properties of Al-doped ZnO as a promising oxide material for high temperature thermoelectric conversion. *J. Mater. Chem.*, **1997**, 7(1), 85-90.

Wadia, C. Materials availability expands the opportunity for large-scale photovoltaic's deployment. *Environ. Sci. Technol.*, **2009**, 43(6), 2072-2077.

Wills, B.A., Napier-Munn, T.J. Wills' Mineral Processing Technology: An Introduction to the Practical Aspects of Ore Treatment and Mineral Recovery, 7th ed. Elsevier. 2006

Wölfing, B.; Kloc, C.; Teubner, J.; Bucher, E. High Performance Thermoelectric Tl_9BiTe_6 with an extremely low thermal conductivity. *Phys. Rev. Lett.*, **2001**, 86(19), 4350-4353.

Wood, C. Materials for thermoelectric energy conversion. *Rep. Prog. Phys.*, **1988**, 51, 459-539.

Yadav, G.G.; Susoreny, J.A.; Zhang, G.; Yang, H.; Wu, Y. Nanostructure-based thermoelectric conversion: An insight into the feasibility and sustainability for large-scale deployment. *Nanoscale*, **2011**, 3, 3555-3562.

Yang, S.H.; Zhu, T.J.; Sun, T.; He, J.; Zhang, S.N.; Zhao, X.B. Nanostructures in high-performance $(GeTe)_x(AgSbTe_2)_{100-x}$ thermoelectric materials. *Nanotechnology*, **2008**, 19(24), 245707.1-245707.5.

Zhou, M.; Li, J.F.; Kita, T. Nanostructured $AgPb_mSbTe_{m+2}$ system bulk materials with enhanced thermoelectric performance. *J. Am. Chem. Soc.*, **2008**, 30(13), 4527-4532.

5.6 Web references

Antimony; MSDS CAS No. 7440-36-0[Online]; ESPI Metals: Ashland, OR, Dec. 3, 2004. <http://www.espimetals.com/msds's /antimony.htm> (accessed June 14, 2010)

Cobalt; MSDS CAS No. 7440-48-4[Online]; Fischer Scientific: Fairlawn, NJ, Aug. 2, 2000. <http://www.acialloys.com/msds/co.html> (accessed May 16, 2010).

Germanium; MSDS CAS No. 7440-56-4[Online]; ESPI Metals: Ashland, OR, June, 2007.
<http://www.espimetals.com/msds's/germanium.htm> (accessed May 16, 2010).

International Union of Pure and Applied Chemistry. The Gold Book: Compendium of Chemical Terminology. <http://www.iupac.org/goldbook/TT06915.pdf> (accessed June 14, 2010).

Strontium Titanate; Product No. 517011[Online]; SIGMA-ALDRICH: Saint Louis, MO, Apr. 7, 2008.
http://simaldrich.com/catalog/ProductDetail.do?lang=en&N4=517011|ALDRICH&N5=SEARCH_CONCAT_PNO|BRAND_KEY&f=SPEC (accessed May 10, 2010).

Tellurium; MSDS CAS No. 13494-80-09 [Online]; Acros Organics: Fairlawn, NJ, Aug. 2, 2000. <http://www.acialloys.com/msds/te.html> (accessed May 16, 2010).

Thallium; MSDS CAS No. 7440-28-0[Online]; ESPI Metals: Ashland, OR, May, 2006.
<http://www.espimetals.com/msds's/thallium.htm> (accessed May 16, 2010).

U.S. Environmental Protection Agency. Lethal Dosage (LD50) Values. <http://www.epa.gov/oecaagct/ag101/pestlethal.html> (accessed June 14, 2010).

USGS, Mineral Commodity Summaries, (2010).
<http://minerals.usgs.gov/minerals/pub/msc/2010/mcs2010.pdf>

CHAPTER 6. ULTRATHIN NANOWIRES OF STRONTIUM TITANATE

Chapter 5 concluded with some important points – oxide-based thermoelectrics have the capacity to achieve high efficiencies; and strontium titanate (SrTiO_3) is one of promising oxide-based thermoelectrics that could deliver the promise of high efficiency for low cost. However, the large thermal conductivity of bulk SrTiO_3 has set a barrier for the improvement of thermoelectric figure of merit and its applications in high temperature thermoelectric energy harvesting and solid-state cooling.

In this chapter, a novel self-templated synthesis method is presented to grow ultrathin strontium titanate nanowires with an average diameter of 6nm in large quantity. Spark plasma sintering is used to create nanostructured bulk pellets of strontium titanate. Thermal conductivity measurements are presented and it is shown, that through nanostructuring, a drastic reduction in thermal conductivity is possible by scattering phonons. A theoretical analysis of the thermal conductivity reduction in the nanostructured bulk pellet sample is also presented to get a better idea behind the thermal transport process in the ultrathin nanowires. The generality of the novel self-templated synthesis method is also presented by demonstrating the growth of lead titanate (PbTiO_3) and barium titanate (BaTiO_3) ultrathin nanowires.

6.1 Motivation and need

Strontium titanate has an unusually high power factor of $20\mu\text{W cm}^{-1} \text{K}^{-2}$. Yet, its thermal conductivity is only $10 \text{ W m}^{-1} \text{K}^{-1}$, resulting in a ZT value of only 0.26 at 1000 K. The low thermal conductivity is a major barrier in achieving a high ZT value. From the analysis presented in Chapter 5, it can be shown that by adapting the favorable chemical and structural properties of complex metal oxides into controllable nanowire structures having finite diameters, their thermal conductivities can be significantly reduced due to phonon scattering at the nanowire-surface interface. This approach provides a promising approach to improve the ZT values above the state of the art. At the same time, a rational yet scalable synthetic approach has to be developed in order for these materials to have a real technological impact.

Our interest in SrTiO_3 is motivated by its high power factor, high temperature stability and the fact that it is composed of non-toxic and abundant elements. Previous studies on SrTiO_3 by other groups either involved the synthesis, oxidation or decomposition of a highly flammable, bimetallic alkoxide precursor of strontium titanium isopropoxide [Urban et al., 2002] or high-temperature ($>800^\circ\text{C}$) solid-state reactions between strontium oxalate and TiO_2 [Banerjee et al., 2003], yet neither have yielded uniform nanowires in large quantities with diameters below 10 nm or narrow size distributions.

In this study, we demonstrate the synthesis of ultrathin SrTiO_3 nanowires with an average diameter of 6 nm through a novel ‘self-template’ approach and show that the thermal

conductivity of the bulk pellet fabricated by compressing the SrTiO₃ nanowire powder using spark plasma sintering (SPS) can indeed be reduced by 64% at 1000 K.

6.2 Synthesis method

The titanates are synthesized by a hydrothermal reaction (**Figure 6.1**). The synthesis is a two-step reaction, the first of which involves production of potassium titanate nanowires, followed by addition of a metal precursor that leads to formation of the respective titanates. Also, the reactions are carried out in the presence of a solution containing varying concentrations of potassium hydroxide.

6.2.1 Formation of potassium titanate nanowires

0.08 g of commercially available titanium oxide (TiO₂) nanoparticles (radius < 25 nm) are added to a glass vial containing 6.8 g of potassium hydroxide (KOH) dissolved in 12 mL of de-ionized (DI) water. The mixture is then thoroughly mixed and later poured into a Teflon liner. The Teflon liner is placed inside an autoclave and heated at 200°C and atmospheric pressure for 3 days. This results in the transformation of all the particles into nanowires. After the reaction has ended, the autoclave is allowed to cool down to room temperature and the contents from the Teflon lined cylinder are transferred to a plastic tube, where they are thoroughly washed with DI water to remove any unreacted potassium hydroxide that may be present.

6.2.2 Preparation of strontium precursor

0.16 g of strontium nitrate is mixed with a solution of 0.7 g of KOH dissolved in 10 mL of DI water in a glass vial. The mixture is thoroughly mixed until the strontium nitrate has been well dispersed in the solution. This mixture is then added to the washed potassium titanate nanowires and mixed thoroughly before addition to a Teflon liner. The cylinder is then placed in an autoclave and heated at 200°C for one day.

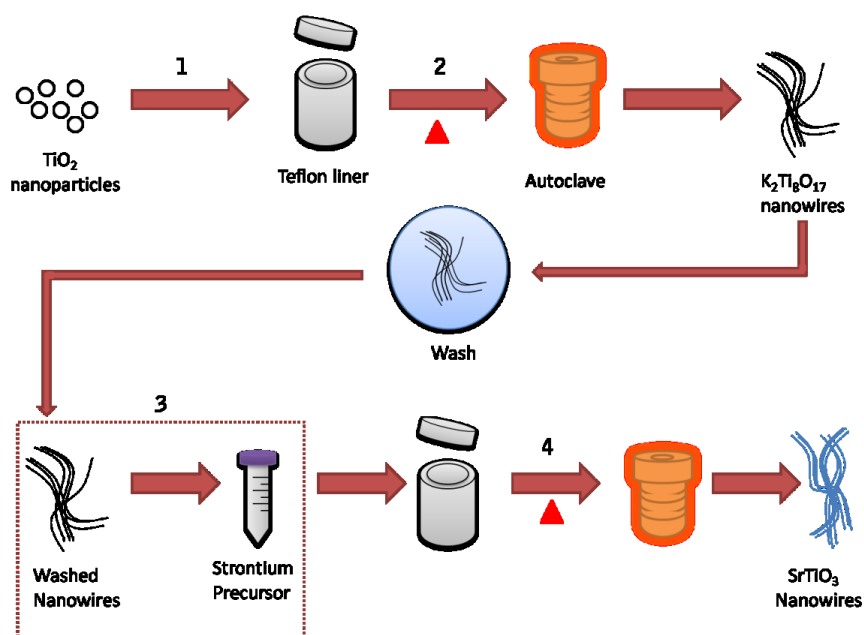


Figure 6.1. General synthesis method for SrTiO₃ nanowires. (Illustration by Gautam G. Yadav)

6.3 Results

The overall yield of SrTiO₃ nanowires has been estimated to be 60% by weight of the starting precursors. Conversion to SrTiO₃ and the phase purity of the product samples were analyzed using X-ray diffraction (XRD). The analysis revealed that the intermediate is indeed potassium titanate (K₂Ti₈O₁₇), while the final product is a pure phase of strontium titanate (SrTiO₃). The XRD results (**Figure 6.2a.**) indicate that in the first step, TiO₂ nanoparticles react with KOH to form K₂Ti₈O₁₇ nanowires, and, cation exchange occurs in the final step of the process to form SrTiO₃. Transmission electron microscope (TEM) analysis (**Figure 6.2b,c,d.**) confirmed the formation of the nanowires with a very narrow diameter distribution. The average diameter for K₂Ti₈O₁₇ is measured to be 6.79 ± 1.18 nm. On the other hand, the average diameter for the SrTiO₃ nanowires is 5.8 ± 0.89 nm. Moreover, the TEM images reveal that the nanowires tend to bundle together due to the lack of organic capping ligands while surprisingly maintaining as a stable suspension in water without overgrowth even after a four day process. This is mainly due to the colloidal behavior associated with their finite diameters. High-resolution TEM (HRTEM) analysis suggests that both K₂Ti₈O₁₇ and SrTiO₃ are single crystals and the lattice fringes have been identified as $(\bar{3}11)$ and (110), respectively.

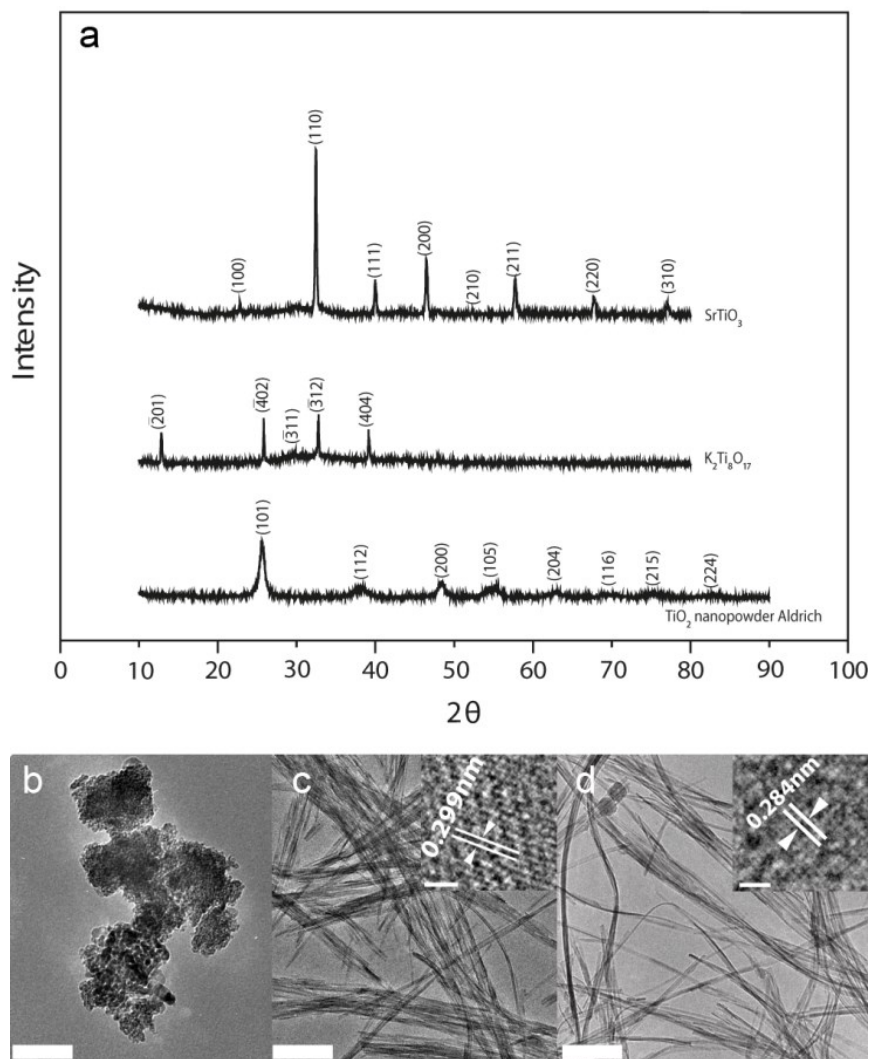


Figure 6.2. (a) XRD patterns of SrTiO₃, K₂Ti₈O₁₇ and TiO₂ nanopowder Aldrich, respectively. (b) TEM image of TiO₂ nanopowder Aldrich (scale bar, 50nm). (c) TEM image of K₂Ti₈O₁₇ nanowires (scale bar, 100 nm), inset at the top corner is a HRTEM image of a K₂Ti₈O₁₇ (scale bar, 2nm). (d) TEM image of SrTiO₃ nanowires (scale bar, 100nm), inset at the top corner is a HRTEM image of SrTiO₃ nanowire (scale bar, 2 nm). [Yadav et al., 2011]

6.4 Thermal conductivity: measurement

The uniform SrTiO₃ nanowires with diameters less than 10 nm could significantly increase the scattering of phonons at the nanowire-surface interface, thus reducing thermal conductivity. In order to measure the thermal conductivity of the ultrathin SrTiO₃ nanowires, we fabricated bulk pellets of SrTiO₃ nanowires with 1 in. diameter and 0.1 in. thickness by performing SPS on the dried nanowire powders. The large DC current (15 kA) and high pressure (50 MPa) have helped to obtain a relative density of 54.4% within 10 minutes of sintering at 800 K. Thermal diffusivity measurements performed on these pellet samples show that the thermal conductivity rises from its value at room temperature to 1.95 W m⁻¹ K⁻¹ at 1000 K.

6.4.1 Analyzing the thermal conductivity

In order to understand the reduction in the thermal conductivity in these ultrathin nanowires and the dependence of this quantity on temperature, an effective porous medium approximation together with empirical fitting was applied. The prepared sample has a relatively low electronic carrier concentration. As a result, its electronic contribution to the thermal conductivity can be neglected, implying that the thermal conductivity is solely contributed by phonons. In bulk SrTiO₃ crystals, phonon transport is dominated by phonon-phonon scattering. However, in the SPS processed sample, the SrTiO₃ nanowires are randomly oriented and interconnected. As a consequence, phonons are mainly transported along 1D nanowires and across nanowire-nanowire contacts. Therefore, intrinsic

phonon-phonon scattering is no longer important while phonon scattering at nanowire surfaces and contacts becomes essential. The value of interfacial thermal resistance is typically in the order of 10^{-9} to 10^{-7} $\text{m}^2 \text{K W}^{-1}$ [Huxtable et al., 2003; Lyeo & Cahill, 2006; Grundum, Cahill & Averback, 2005]. The average length of the SrTiO_3 nanowires is around 100 nm, and if the thermal conductivity of an individual SrTiO_3 nanowire is assumed to be $2 \text{ W m}^{-1} \text{K}^{-1}$, the corresponding nanowire axial thermal resistance is about 10^9 to 10^{10} K W^{-1} . It is apparent that the contact thermal resistance is generally lower than that of nanowire axial resistance and is not important when arranged in series. Therefore, the thermal resistance of nanowire contacts can be neglected.

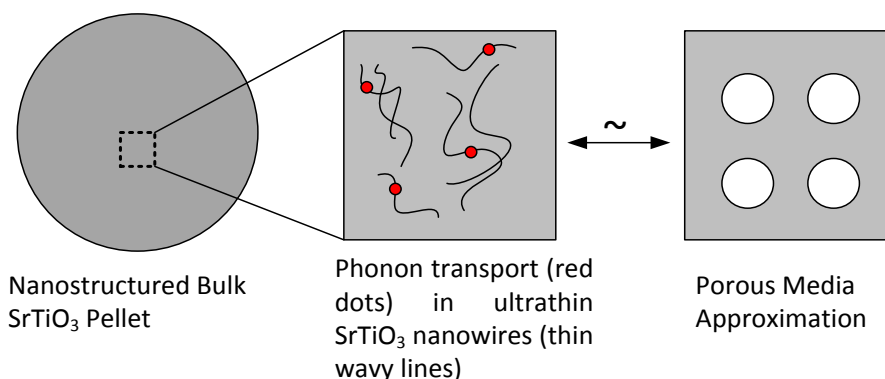


Figure 6.3. Illustration showing the phonon transport in the SrTiO_3 nanostructured bulk pellet and its approximation as a continuous porous medium. (Illustration by Gautam G. Yadav)

Following these simplifications, nanowire composite can be viewed as a continuous porous medium (Figure 6.3.), where the ‘solids’ are the interconnected SrTiO₃ nanowires and the ‘pores’ are the gaps between them. The thermal conductivity of air is very low, so a relationship between the effective thermal conductivity of the nanoporous medium and that of the unperturbed continuous medium can be obtained as [Bauer, 1993]:

$$k_{\text{eff}}/k_o = (1-P)^{1/e} \dots\dots\dots(6.1)$$

where k_{eff} is the effective thermal conductivity of the nanocomposite and k_o is the average thermal conductivity of an individual nanowire. $\left(P \left\{ \frac{\rho - \rho_{\text{eff}}}{\rho} \right\}\right)$ is the porosity and it is equal to 0.46 in this case. It is obtained by dividing the differences in the bulk and sample densities with the bulk density. ρ , the bulk density of SrTiO₃, is 5.13 g cm⁻³ while the density of the sample, ρ_{eff} is 2.787 g cm⁻³. The parameter e is the shape factor of the pores and is taken to be 2/3 to account for the fully random shapes of the air gaps. Therefore, a simple relationship between k_{eff} and k_o can be established as:

$$k_{\text{eff}} = 0.543k_o \dots\dots\dots(6.2)$$

The measured thermal conductivity can only be interpreted if we take into account an empirical model which underlies the temperature dependency of the thermal conductivity [Liang & Li, 2006; Qiu, Sun & Ruan, 2011]:

$$\frac{k_o(T)}{c_o(T)} = \frac{k_b(T)}{c_b(T)} p \exp\left(-\alpha \frac{l_b(T)}{D}\right) \left(-\frac{\beta}{\left[\frac{D}{L}-1\right]}\right)^{3/2} \dots\dots\dots(6.3)$$

Where c is the specific heat, p is the specularly parameter ranging from 0 to 1, $l_b = \frac{l_r T_r}{T}$ is the temperature dependent mean free path, D is the nanowire diameter and is 6 nm, L is the critical size at which almost all atoms are localized at the nanowire surface and is equal to = 1.1 nm, and a , a geometrical factor, is 0.5. β is related to the melting entropy and is kept as an adjustable parameter since no experimental data is available. The subscripts o , b and r indicate nanowire, bulk and reference, respectively. For the analysis, the bulk specific heat data had to be extrapolated [de Ligny & Richet, 1996]. The bulk mean free path, l_r , at a T_r of 300 K is estimated to be 18 nm by comparing it to the corresponding value for Bi_2Te_3 since simple calculation from the kinetic theory is found to severely underestimate the effective mean free path [Jeong, Datta & Lundstrom, 2011]. The values for the specularly parameter, p , and β that best fits the thermal conductivity data for SrTiO_3 nanowires were 1 and 1.2, respectively.

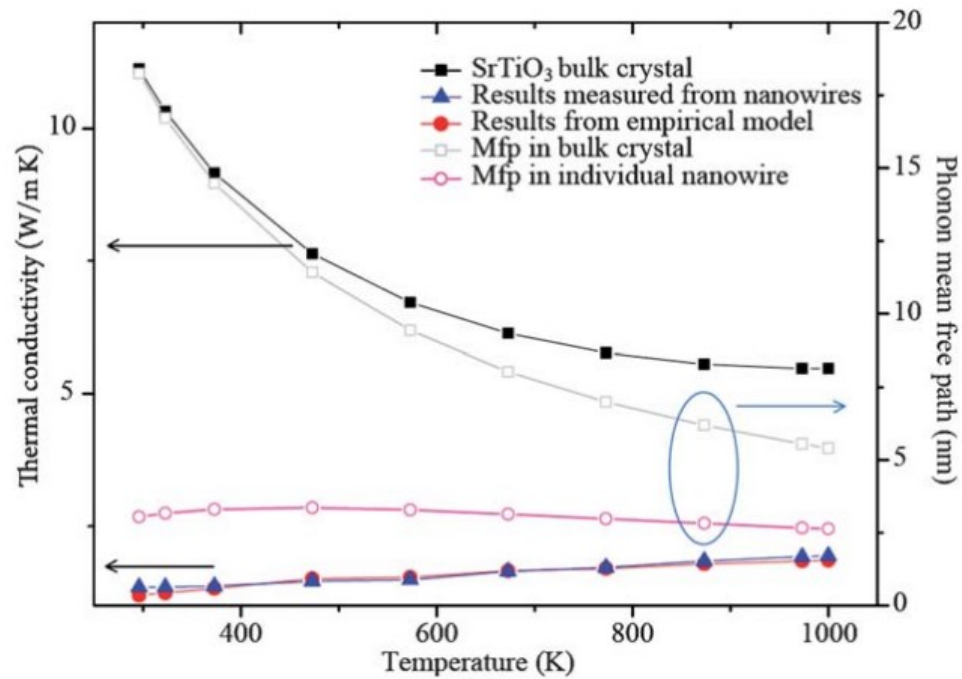


Figure 6.4. Comparison of thermal conductivity plot between bulk crystal data, empirical model and experimental measurements of SrTiO₃ nanowires. Also presented are the effective phonon mean free paths in bulk crystal and SrTiO₃ individual nanowires. [Yadav et al. 2011]

Excellent agreement is observed between experimental and model-predicted results (**Figure 6.4**). The slight underestimation in the modeled thermal conductivity at higher temperatures is likely due to the alleviation of defects and better thermal contacts among nanowires at high temperatures, which might lead to an apparent increase in the mean free path, which, in turn, might lead to higher thermal conductivities. It can also be seen that the phonon mean free paths in individual nanowires (hollow pink circles) are found to be only weakly

dependent on temperature with values much less than those in the bulk phase (hollow grey squares). The aforementioned observation indicates that strong phonon scattering at nanowire surfaces dominates over the Umklapp scattering due to the wires' very small diameters and that this greatly limits the effective mean free path.

Also, the temperature insensitive nature of such scattering leads to weak temperature dependence of the mean free paths in SrTiO₃ nanowires. Therefore, the trend that thermal conductivity slowly increases with temperature can be attributed to the weak temperature dependence in mean free path, and the increase in the measure specific heat with temperature due to the relatively high Debye temperature of SrTiO₃ (513K) [Ahrens et al., 2007]. From the analysis, it can be summarized that the boundary scattering contributes to about 45% (at 1000 K) to 85% (at 300 K) reduction in thermal conductivity, while the porosity contributes to an additional 45% percent reduction. The former mechanism will not affect electrical conductivity much since electrons have much shorter intrinsic mean free paths, indicating a potential for significant *ZT* enhancement.

6.5 Generality of the synthesis method

The self-templated synthesis approach can also be used to grow other perovskite nanowires (**Figure 6.5.**) such as barium titanate (BaTiO₃) and lead titanate (PbTiO₃) by replacing strontium nitrate Sr(NO₃)₂ with 0.131 g barium nitrate, Ba(NO₃)₂, and 0.166 g lead nitrate, Pb(NO₃)₂. Nanowires with diameters of 8.15 ± 1.35 nm and 9.49 ± 1.48 nm were achieved for BaTiO₃ and PbTiO₃, respectively. The generality of this synthetic approach could enable

us to further explore the thermoelectric properties of the complicated layered perovskite nanowires by mixing various cation precursors.

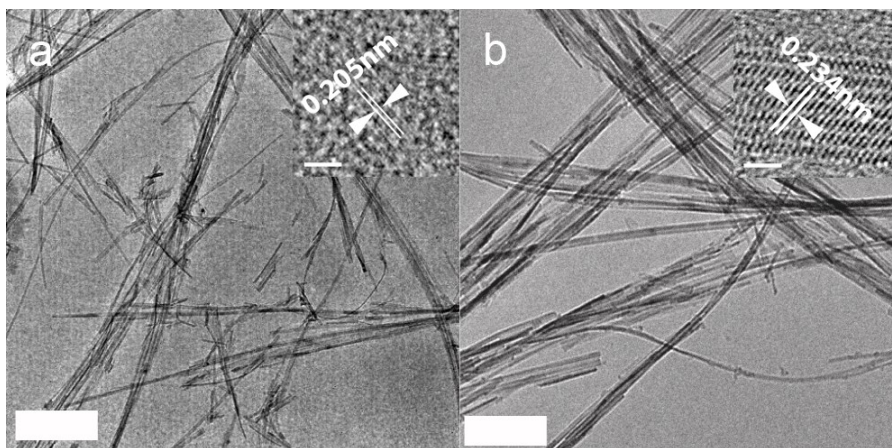


Figure 6.5. (a) TEM image of BaTiO₃ nanowires (scale bar, 0.2 μ m), inset at the top corner is the HRTEM image of BaTiO₃ nanowire (scale bar, 5nm). (b) TEM image of PbTiO₃ nanowires (scale bar, 100nm), inset at the top corner is the HRTEM image of PbTiO₃ nanowire (scale bar, 2nm). [Yadav et al., 2011]

6.6 Conclusions

Results suggest that the novel preparation method outlined earlier can successfully synthesize nanowires with desirable dimensions. Furthermore, this methodology can be extended to the synthesis of other titanate systems as well. The small diameter marks an encouraging step towards the aim of achieving a high ZT because small diameters result in

phonon scattering and assist in good electron transport, which, in turn, helps in reducing the thermal conductivity as shown in the case of SrTiO_3 . This opens up the possibility to improve the thermoelectric performance of these non-toxic and abundant metal oxide based materials as alternatives for skutterudites and Si/Ge for high temperature energy harvesting and solid-state cooling.

6.7 References

Ahrens, M.; Merkle, R.; Maier, J.; Rahmati, B. Effective masses of electrons in n-type SrTiO₃ determined from low-temperature specific heat capacities. *Phys. B*, **2007**, 393, 239.

Banerjee, S.; Mao, Y.; Wong, S.S. Large-Scale Synthesis of Single-Crystalline Perovskite Nanostructures. *J. Am. Chem. Soc.*, 2003, 125(51), 15718-15719.

Bauer, T.H. A general analytical approach toward the thermal conductivity of porous media. *Int. J. Heat Mass Transfer*, 1993, 36, 4181.

de Ligny, D.; Richet, P. High-temperature heat capacity and thermal expansion of SrTiO₃ and SrZrO₃ perovskites. *Phys. Rev. B*, **1996**, 53, 3013.

Grundum, B.C.; Cahill, D.G.; Averback, R.S. Thermal conductance of metal-metal interfaces. *Phys. Rev. B*, 2005, 72, 245426.

Huxtable, S.T.; Cahill, D.G.; Shenogin, S.; Xue, L.; Ozisik, R.; Barone, P.; Usrey, M.; Strano, M.S.; Siddons, G.; Shim, M.; Keblinski, P. Interfacial heat flow in carbon nanotube suspensions. *Nat. Mater.*, 2003, 2, 731.

Jeong, C.; Datta, S.; Lundstrom, M. Full dispersion versus Debye model evaluation of lattice thermal conductivity with a Landauer approach. *J. Appl. Phys.*, **2011**, 109, 073718.

Liang, L.H.; Li, B. Size-dependent thermal conductivity of nanoscale semiconducting systems. *Phys. Rev. B:Condens. Matter Mater. Phys.*, 2006, 73, 153303.

Lyeo, H.; Cahill, D.G. Thermal conductance of interfaces between highly dissimilar materials. *Phys. Rev. B*, 2006, 73, 144301.

Qiu, B.; Sun, L.; Ruan, X. Lattice thermal conductivity reduction in Bi_2Te_3 quantum wires with smooth and rough surfaces: A molecular dynamics study. *Phys. Rev. B: Condens. Matter Mater. Phys.*, **2011**, 83, 035312.

Urban, J.J.; Yun, W.S.; Gu, Q.; Park, H. Synthesis of Single-Crystalline Perovskite Nanorods Composed of Barium Titanate and Strontium Titanate. *J. Am. Chem. Soc.*, 2002, 124(7), 1186-1187.

Yadav, G.G.; Zhang, G.; Qiu, B.; Susoreny, J.A.; Ruan, X.; Wu, Y. Self-templated synthesis and thermal conductivity investigation for ultrathin perovskite oxide nanowires. *Nanoscale*, **2011**, 3, 4078-4081.

CHAPTER 7. POROUS NANOWIRES OF NEW PHASE OF CALCIUM COBALT OXIDE FOR THERMOELECTRIC AND LITHIUM-ION BATTERY APPLICATIONS

There is a tremendous requirement of different material systems for high temperature thermoelectric and energy storage applications in view of their immense potential in energy industry. A substantial body of current research in thermoelectrics is heavily concentrated on improving efficiency of traditionally-best materials like lead telluride (PbTe) and bismuth telluride (Bi_2Te_3) which are not stable at high temperatures. Chapter 6 was also about a study on the nanostructuring of a known promising oxide thermoelectric material, strontium titanate. A similar trend is observed in lithium-ion battery research where much of the research is involved in improving and finding new cathode materials, while anode materials have received scarce attention. A unique phase of calcium cobalt oxide, $\text{Ca}_9\text{Co}_{12}\text{O}_{28}$, has been investigated as a potential p-type thermoelectric and anode material. For the first time, synthesis of one dimensional nanowires of $\text{Ca}_9\text{Co}_{12}\text{O}_{28}$ through a novel single source precursor based technique is reported. Improved thermoelectric properties were observed, where the thermal conductivity was 1.06 W/mK and Seebeck coefficient was 213.3 $\mu\text{V}/\text{K}$ at 700K, which are the lowest and highest values, respectively vis-à-vis those reported in literature. Also, electrochemical characteristics of $\text{Ca}_9\text{Co}_{12}\text{O}_{28}$ nanowires with lithium metal were evaluated and found to exhibit unique behavior. A first cycle discharge capacity of

around 540mAh/g was observed at 100(0.1C)mA/g cycling, followed by rapid fade during the initial cycles, but in subsequent cycles exhibited excellent rate capability and increasing discharge capacity. Through a unique single source precursor based technique, porous nanowire structures of $\text{Ca}_9\text{Co}_{12}\text{O}_{28}$ are synthesized much lower temperature than conventional solid state techniques. The work is novel and will stimulate further activities in this area. The results of this work have been published in Journal of Materials Chemistry, 2013. [Yadav et al., 2013]

7.1 Introduction

A unique of phase of calcium cobalt oxide ($\text{Ca}_9\text{Co}_{12}\text{O}_{28}$), which is a layered oxide, is researched and presented in this chapter. This phase has hardly been researched in literature because of its high thermal conductivity, thus limiting its use in thermoelectric devices. [Li et al., 1999] There have been other phases of calcium cobalt oxide that have been studied in literature, although these phases have faced similar problems. [Ohta, Sugiura & Koumoto, 2008; Masuda et al., 2003; Tang et al., 2010; Yin et al., 2010]

$\text{Ca}_3\text{Co}_4\text{O}_9$ has been the most common phase that has been studied in literature.[Ohta, Sugiura & Koumoto, 2008; Masuda et al., 2003; Tang et al., 2010; Yin et al., 2010] The most common methods of synthesizing this phase have been solid state reactions and sol-gel method. [Tang et al., 2010; Yin et al., 2010; Hao, Zhao & Hu, 2009] Both of these methods require long reaction times and are highly energy intensive. The electrical conductivity has

been quite high for these bulk samples, but its ZT has greatly been affected by the high thermal conductivity. Nanostructuring of oxide materials into one dimensional structure like nanowires of these materials has been a challenge as well. An artificial process like electrospinning has been used to make nanofibers of $\text{Ca}_3\text{Co}_4\text{O}_9$, where the thermal conductivity was brought down from approximately 1.8W/mK at around 350 K to approximately 1.25 W/mK at around 800 K . [Yin et al., 2010] No solution based technique exists to make nanowires of any phase of calcium cobalt oxide.

There is only one paper experimenting $\text{Ca}_9\text{Co}_{12}\text{O}_{28}$ as a potential thermoelectric material. [Li et al., 1999] A bulk pellet of $\text{Ca}_9\text{Co}_{12}\text{O}_{28}$ was prepared through a solid state reaction route. The Seebeck coefficient, electrical conductivity and thermal conductivity values were $118\mu\text{V/K}$, 8340 S/m and 1.73 W/mK at 700°C , respectively. The thermal conductivity is quite high and the Seebeck coefficient is low, which affects the ZT . A potentially good thermoelectric material is affected by the negative effects of a bulk structured material, but through nanostructuring this negative effect can be mitigated.

As mentioned in Chapter 3, another application of these layered oxides is in the field of energy storage, especially lithium-ion batteries. A major challenge in secondary lithium ion batteries is the limited availability of anode materials which are safe and stable at the operating voltage limits. Primarily, graphite is used as the most common anode in secondary batteries, but current research has also focused on lithium titanate and silicon as possible replacements for graphite due to its poor cycle life and safety issues caused by the solid electrolyte interface. [Mosa et al., 2012; Shen et al., 2012; Armand & Tarascon, 2008;

Whittingham, 2008; McDowell et al., 2012; Marom et al., 2011; Yang, Feng & Mullen, 2011] But the former mentioned materials have their disadvantages- mainly, limited capacity for lithium titanate and considerably volume expansion upon lithium insertion in silicon [Kasavajjula, Wang & Appleby, 2012]. Hence, it is important to research in other possible anode materials and $\text{Ca}_9\text{Co}_{12}\text{O}_{28}$ is looked at as a possible option.

A few phases of calcium cobalt oxide have been studied as possible anode materials- namely, $\text{Ca}_3\text{Co}_4\text{O}_9$ and $\text{Ca}_2\text{Co}_2\text{O}_5$. [Kim et al., 2007; Sharma et al., 2004] $\text{Ca}_3\text{Co}_4\text{O}_9$ and $\text{Ca}_2\text{Co}_2\text{O}_5$ have a theoretical capacity of 643.3 mAh/g and 578 mAh/g, respectively; but the experimental values obtained for the first discharge cycles were around 1230 mAh/g and 809 mAh/g, respectively. The first discharge cycle current densities were 246 mA/g and 10 mA/g, respectively, for $\text{Ca}_3\text{Co}_4\text{O}_9$ and $\text{Ca}_2\text{Co}_2\text{O}_5$. However, over subsequent cycles, the fade observed was rapid till it reached stability. Also, recently Mei et al. published a paper on the electrochemical performance of $\text{Ca}_9\text{Co}_{12}\text{O}_{28}$. [Mei et al., 2012] They obtained a first cycle discharge capacity of 816mAh/g at a current density of 200mA/g. But the behavior of their $\text{Ca}_9\text{Co}_{12}\text{O}_{28}$ was not characteristic of a calcium cobalt oxide phase as shown for $\text{Ca}_3\text{Co}_4\text{O}_9$ and $\text{Ca}_2\text{Co}_2\text{O}_5$. Mei et al. obtained a first cycle charge capacity higher than discharge capacity, while the other two phases of calcium cobalt oxide had a first cycle charge capacity much lesser than the first cycle discharge capacity. Irrespective of the phase of calcium cobalt oxide, the first discharge reaction for the complex metal oxide phase leads to an irreversible destruction of the crystal structure with formation of metal nanoparticles. [Kim et al., 2007; Sharma et al., 2004] These metal nanoparticles get converted to their oxides in subsequent

cycles. Porous nanowires of any phase of calcium cobalt oxide have not been tested for batteries before and neither their electrochemical performance.

Through a unique single source precursor based technique, for the first time porous nanowire structures of $\text{Ca}_9\text{Co}_{12}\text{O}_{28}$ have been synthesized at temperatures much lower than conventional solid state techniques. The thermoelectric properties – thermal conductivity and Seebeck coefficient, were measured till 700K and, respectively, are the lowest and highest reported in literature. The electrochemical properties of $\text{Ca}_9\text{Co}_{12}\text{O}_{28}$ nanowires follow the characteristic behavior as shown for other phases of calcium cobalt oxide. Its first discharge capacity is also higher than the theoretical followed by a rapid loss in the initial few cycles. However, in subsequent cycles the discharge capacity increases.

7.2 Synthesis of porous nanowires

The $\text{Ca}_9\text{Co}_{12}\text{O}_{28}$ nanowires were prepared through a microemulsion synthesis route (Figure 7.1a). Cobalt nitrate hexahydrate, oxalic acid and 1-pentanol were purchased from Sigma-Aldrich. Calcium nitrate tetrahydrate was purchased from Mallinckrodt, cyclohexane from EMD Millipore and cetyltrimethyl ammonium bromide from J.T. Baker, USA. Calcium nitrate tetrahydrate ($\text{Ca}(\text{NO}_3)_2 \cdot 4\text{H}_2\text{O}$) and cobalt nitrate hexahydrate ($\text{Co}(\text{NO}_3)_2 \cdot 6\text{H}_2\text{O}$) were used as precursors. In a standard microemulsion synthesis, the first step involved the creation of an emulsion with solvents, cyclohexane and 1-pentanol. Cetyltrimethylammoniumbromide(CTAB) was used as the cationic surfactant. 0.1 mol of

CTAB was mixed vigorously with 1.4 L cyclohexane and 60 mL 1-pentanol for 1 h. Next, 0.024 mol of oxalic acid in 40mL of deionized(DI) water was added to the stirring solution and mixed for 2 hours. In the final step, 5.32mmol of $\text{Ca}(\text{NO}_3)_2 \cdot 4\text{H}_2\text{O}$ and 3.4 mmol of $\text{Co}(\text{NO}_3)_2 \cdot 6\text{H}_2\text{O}$ in 80mL of DI water, respectively were added and stirred till the solution color changed from pink to a homogenous whitish color. After the reaction was over, the solution was centrifuged and a precipitate was obtained and dried at 80 °C. The dried precipitate was pink in color and this precipitate was heated in an open tube furnace at 650 °C. The tube furnace heating rate was ramped up from room temperature to 650 °C at 9.7 °C/min and it was maintained at 650 °C for 1.5 h. The tube furnace was cooled down to room temperature naturally. The obtained products are black in color and washed with DI water three times and once with ethanol, in that order.

7.3 Material characterization techniques

The final product was then analyzed by X-ray diffraction(XRD) on a Bruker D8 Focus X-ray diffractometer with Cu K(alpha) source, a scanning electron microscope(Hitachi S-4800 Field Emission Microscope) and transmission electron microscope(Titan 80-300 kV Environmental Electron Microscope).Thermogravimetric analysis, Fourier-transform infrared spectroscopy(Thermo-Nicolet Nexus FT-IR) and energy dispersive X-ray spectroscopy(JEOL JSM-840 Scanning Electron Microscope) was performed on the pink precipitate.

7.4 Results

The XRD pattern of the CTAB, precipitate and $\text{Ca}_9\text{Co}_{12}\text{O}_{28}$ nanowires is shown in Figure 7.1b. CTAB peaks are not visible in the final $\text{Ca}_9\text{Co}_{12}\text{O}_{28}$ spectrum. It is unlikely to exist after the annealing step at 650°C . The precipitate XRD spectrum has peaks indexed to both, calcium oxalate and cobalt oxalate, with the green colored peaks indicating cobalt oxalate. The precipitates are nanowires too, as shown in Figure 7.3. However, from the XRD spectrum it is difficult to detect any presence of CTAB in the precipitate. The $\text{Ca}_9\text{Co}_{12}\text{O}_{28}$ phase crystallizes in the orthorhombic system and the major peaks can all be indexed to the JCPDS card no.21-0139. The peaks can also be indexed on the basis of $\text{Ca}_2\text{Co}_2\text{O}_5$ structure indicating pure $\text{Ca}_9\text{Co}_{12}\text{O}_{28}$ being synthesized. [Li et al., 1999] It is reported that $\text{Ca}_9\text{Co}_{12}\text{O}_{28}$ can be considered as having the same structure as $\text{Ca}_2\text{Co}_2\text{O}_5$, but with having 25% vacant Ca sites, thus can also be written as $\text{Ca}_{1.5}\text{Co}_2\text{O}_{4.67}$. [Li et al., 1999]

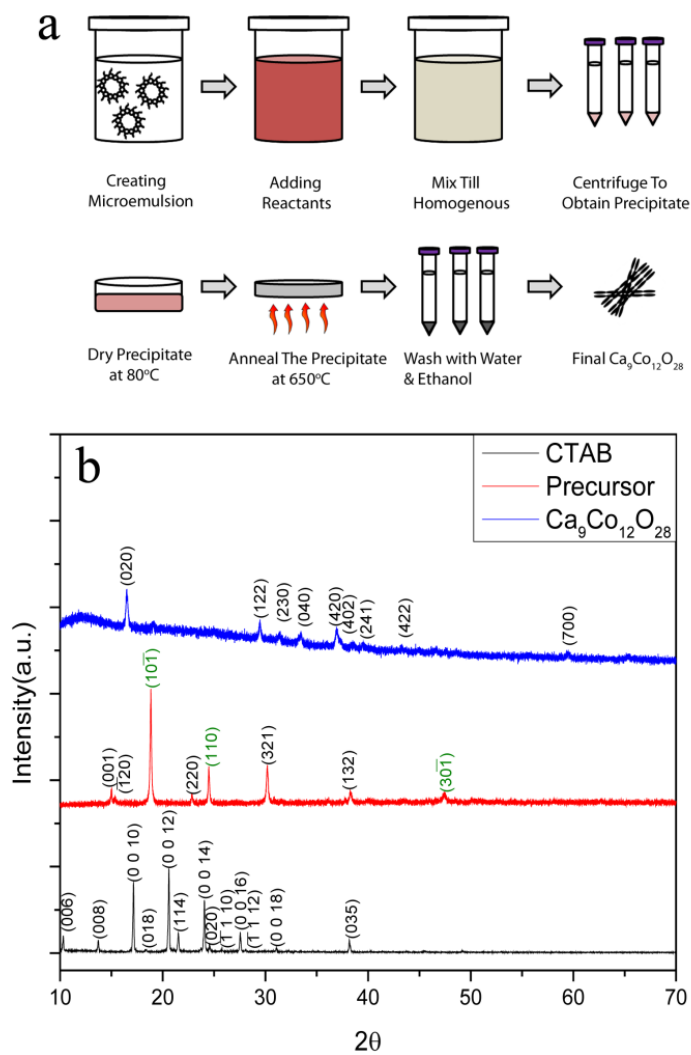


Figure 7.1. (a) Schematic representation of the microemulsion synthesis of porous $\text{Ca}_9\text{Co}_{12}\text{O}_{28}$ nanowires. (b) XRD pattern of the precipitate and final $\text{Ca}_9\text{Co}_{12}\text{O}_{28}$ nanowires. [Yadav et al., 2013]

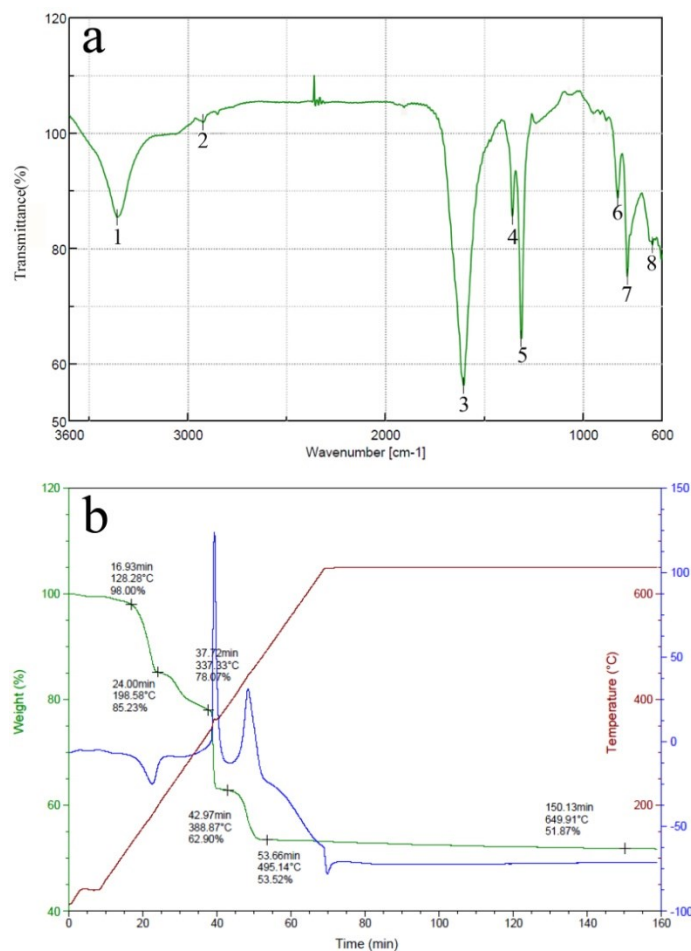


Figure 7.2. (a) FTIR spectrum of the precipitate precursor. (b) TGA analysis on the precipitate precursor. (The blue line corresponds to the heat generated (exothermic) or heat imparted (endothermic) in the annealing process; the red line corresponds to the temperature ramp rate in the annealing process; the green line corresponds to the weight loss in the annealing process) [Yadav et al., 2013]

The FTIR spectrum is shown in Figure 7.2a. It was used to further understand the precipitate composition and identify the surface functional groups of the precipitate nanowires. The broad band at 3357.46 cm^{-1} (1) can be ascribed to water of hydration. This could possibly mean that the precipitate formed is a hydrate of calcium and cobalt oxalate. The weak band at 2923 cm^{-1} (2) is assigned to vibrational C-H mode which indicates the presence of residual amount of CTAB that acts as a surfactant to direct the formation of the precipitate nanowires. The bands at 1606.41 , 1359.57 and 1315.21 cm^{-1} (3,4,and 5) can be ascribed to the C-O mode. This indicates the bridging of oxalate with all four oxygen atoms coordinated with the metal atoms. The presence of 827.31 cm^{-1} (6) indicates O-C-O band and the remaining bands between 600 and 800 cm^{-1} (7, and 8) can be attributed to Ca-O and Co-O.

TGA was also performed to investigate the thermal behavior of the precursor in air and the parameters of the experimental run like ramp speed were set exactly as to mimic the actual reaction process. From Figure 2(b), it can be observed that a constant mass is lost (around 47%) during the ramp from room temperature to around $490\text{ }^{\circ}\text{C}$. The loss in mass is caused due to a series of endothermic and exothermic reactions occurring till 490°C . The loss in mass occurring until about 200°C could correspond to the evaporation of water from the precursor and result in the formation of an anhydrous calcium and cobalt oxalate precursor. From 200 to 490°C , two exothermic curves can be observed. This suggests that carbon dioxide might be released and the precursor may be converted to calcium cobalt oxide. There is a minor material loss of less than 2% from 490°C to 650°C . This occurs in a time frame of around 2 hours. The endothermic curve corresponding to the 2% material loss

might be an indicator of the final phase change to $\text{Ca}_9\text{Co}_{12}\text{O}_{28}$. The isothermal annealing step for 90 minutes in the final annealing process is important so that there is enough time for the endothermic reaction to occur and complete the final phase change to $\text{Ca}_9\text{Co}_{12}\text{O}_{28}$.

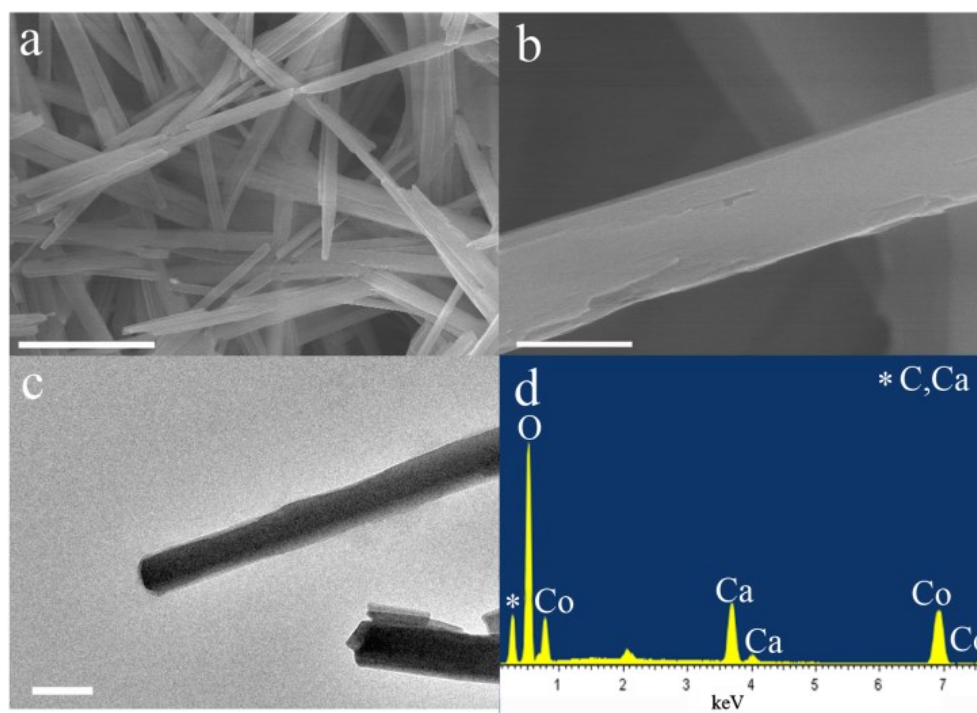


Figure 7.3. (a) SEM overview of the precipitate nanowires (scale bar is $5\mu\text{m}$). (b) SEM of individual precipitate nanowire (scale bar is 500nm). (c) TEM image of precipitate nanowires (scale bar is $0.2\mu\text{m}$). (d) EDX of the precipitate nanowires (unidentified peak is from the chamber). [Yadav et al., 2013]

The scanning electron microscope (SEM) and the transmission electron microscope (TEM) images of the precipitate nanowires are shown in Figure 7.3a-c. The precipitate is also

nanowire-shaped and has a diameter of around 350 nm to 500nm. Its length is on the order of tens of micrometers. Energy dispersive X-ray spectroscopy (EDX) was used to identify the elements present in the precursor and the atomic percentage of each element. EDX was performed on a glass coated with the precipitate. From Figure 7.3d., it can be clearly seen that calcium, cobalt and oxygen, along with carbon, are present in nanowire precipitate. The approximate ratio of cobalt and calcium is 2.2 to 1 in the precipitate. This ratio is slightly higher compared to the final ratio of cobalt to calcium in the final product, $\text{Ca}_9\text{Co}_{12}\text{O}_{28}$. The final endothermic reaction shown in the thermogravimetric analysis (Figure 7.2b) could possibly be compensating this slightly higher ratio to create the final pure phase of $\text{Ca}_9\text{Co}_{12}\text{O}_{28}$. The approximate atomic percentage of oxygen in the sample was 62. The amount of oxygen could be overestimated because of the presence of water of hydration in the sample, oxalate presence and possibly due to detection from the glass substrate. The presence of carbon again indicates that the precipitate could possibly be a mixture of calcium and cobalt oxalate. This overestimated percentage of oxygen is compensated through the loss of water of hydration and carbon dioxide during the annealing procedure as shown in Figure 7.2b. This finally leads to formation of a pure phase of $\text{Ca}_9\text{Co}_{12}\text{O}_{28}$. CTAB plays a vital role in guiding the growth of the nanowires in the reaction. The oxalate group in the precipitate has a negative surface charge and as CTAB is a cationic surfactant, it limits the growth of the calcium and cobalt oxalate nanowire precipitate in other directions. [Ganguly, Ganguly & Vaidya, 2010]

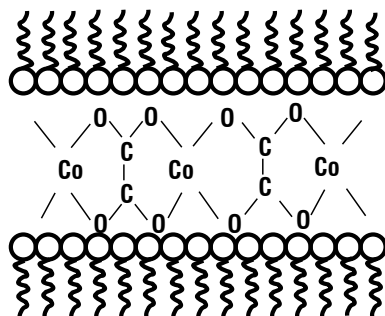


Figure 7.4. Illustration of the role of CTAB in the precipitate nanowire formation.

(Illustration by Gautam G. Yadav)

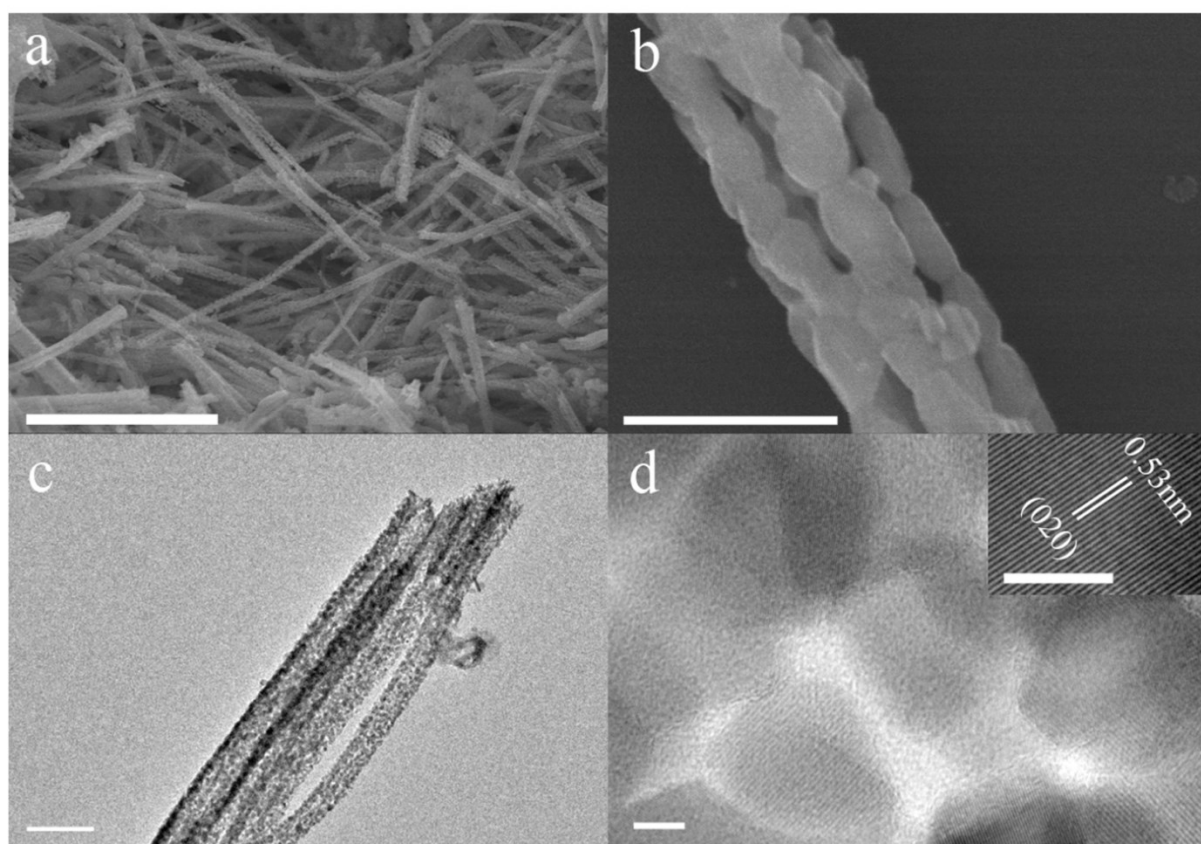


Figure 7.5. (a) SEM overview of the $\text{Ca}_9\text{Co}_{12}\text{O}_{28}$ nanowires (scale bar is $5\mu\text{m}$). (b) SEM of individual $\text{Ca}_9\text{Co}_{12}\text{O}_{28}$ nanowire (scale bar is 300nm). (c) TEM image of $\text{Ca}_9\text{Co}_{12}\text{O}_{28}$

nanowires (scale bar is 0.5 μ m). (d) TEM image of the individual particles making the $\text{Ca}_9\text{Co}_{12}\text{O}_{28}$ nanowire (scale bar is 5nm), inset showing the high resolution TEM image of $\text{Ca}_9\text{Co}_{12}\text{O}_{28}$ (scale bar is 5nm) [Yadav et al., 2013]

In Figure 7.5a., the SEM image of the $\text{Ca}_9\text{Co}_{12}\text{O}_{28}$ nanowires shows large bundles of nanowires being formed. A closer inspection of these nanowires indicates that particles are joined together to give the porous shape of the nanowire. The calcium cobalt oxalate nanowire precursor disintegrates giving the final porous nanowire shape of the $\text{Ca}_9\text{Co}_{12}\text{O}_{28}$ nanowire during the annealing process. The size of the nanowire diameter is around 260 nm. These porous nanowires could play a vital role in the scattering of phonons at their interface which might bring down the thermal conductivity. In Figure 7.5d., the TEM and HRTEM images of the $\text{Ca}_9\text{Co}_{12}\text{O}_{28}$ nanowire and the individual particles that make up the nanowire can be seen. The nanoparticles are around 18nm in size. The lattice fringes in the HRTEM image has been identified to (020) of the $\text{Ca}_9\text{Co}_{12}\text{O}_{28}$ phase.

7.5 Spark plasma sintering & thermoelectric property measurements

The $\text{Ca}_9\text{Co}_{12}\text{O}_{28}$ nanowire powders were consolidated by using spark plasma sintering (SPS). The powder was placed in a graphite die and initially pressed to 2000 pounds at room temperature. The graphite die was then placed in the SPS under nitrogen atmosphere and sintered at 750 $^{\circ}\text{C}$ with a temperature ramp of 30 $^{\circ}\text{C}$ per min, and a constant force of 25kN

during the sintering. The sintering process was kept constant for 10 min under a high DC current. The pressure was released after the sintering process and the sample was cooled to room temperature. The obtained pellet had an average diameter of 1 inch and average thickness of 0.057 inches. The surface of the pellet was polished to remove the graphite.

The Seebeck coefficient(MMR System Technology Inc.) was measured under vacuum by placing the sample between a heater and a heat sink. The voltage difference was tested between the hot and cold side with a maximum fluctuation of ± 0.2 K. The electrical resistivity was measured on a home built system. The thermal conductivity was calculated from the product of thermal diffusivity, specific heat, and density. The thermal diffusivity was measured by laser flash method on a home built system. The specific heat was measured on a Perkin-Elmer Model DSC-4 Differential Scanning Calorimeter. The density was calculated from the sample's geometry and mass.

7.6 Discussion of thermoelectric properties

Spark plasma sintering (SPS) was performed on the $\text{Ca}_9\text{Co}_{12}\text{O}_{28}$ nanowire powders to make a pellet for the measurement of its thermoelectric properties. A relative density of around 81% was achieved through SPS which is quite high compared to conventional methods of sintering like hot press. Its thermoelectric properties were measured from room temperature to 700K. Although $\text{Ca}_9\text{Co}_{12}\text{O}_{28}$ would be more suitable for higher temperature applications due to instrumental limitations we were able to perform the measurements only till 700K.

In Figure 7.6a., the overall thermal conductivity with the respective phonon and electronic contributions of the SPS nanowires are shown. Compared to the reference paper, we can clearly see the drastic drop in thermal conductivity of the nanostructured $\text{Ca}_9\text{Co}_{12}\text{O}_{28}$ pellet. There is a very slight variation in the measured temperature range. The slight increase at the end is due to the increase in specific heat of the sample. The phonon and electronic contributions were calculated through the Weidemann-Franz law, where the Lorentz number used was $2.44 \times 10^{-8} \text{W}\Omega\text{K}^{-2}$. There is hardly any electronic contribution to the overall thermal conductivity. Phonon transport is the major contributor to the thermal conductivity. However, the phonon transport is impeded due to possible scattering of the phonons at the interface of the porous nanowires. The drastic drop in the thermal conductivity compared to the reference could be due to creation of many grain boundaries at the interface of the porous nanowires during the SPS process. This is the lowest thermal conductivity value to be reported in literature for $\text{Ca}_9\text{Co}_{12}\text{O}_{28}$ phase.

The electrical conductivity, shown in Figure 7.6b., is not as high compared to the conventionally prepared solid state reaction route reported by Li, et al. [Li et al., 1999] It is almost 9 times lower which greatly affects the power factor as shown in Figure 7.6c. The grain boundaries that play a vital role in decreasing thermal conductivity drastically, could possibly be affecting electrical conductivity negatively by scattering charge carriers as well. As described in Chapter 4, generally in oxide based compounds the transport mechanism is dominated by polarons. Polarons are essentially charge carriers that bring about a distortion in the lattice. If the distance of the distortion in the lattice is larger or smaller than the lattice constant then we classify the polarons as large or small, respectively. In material systems with

large effective mass and strong carrier-lattice interactions, the small polaron hopping conduction theory applies. [Bosman & van Daal, 1970] Based on the theory, the electrical conductivity can be written as [Bosman & van Daal, 1970]:

$$\sigma = n \cdot e \cdot \mu = \frac{ne a^2 A}{T} \exp\left(-\frac{E_a}{k_B T}\right) = \frac{C}{T} \exp\left(-\frac{E_a}{k_B T}\right) \dots \dots \dots (7.1)$$

$$\ln(\sigma T) = \ln(C) - \frac{E_a}{k_B T} \dots \dots \dots (7.2)$$

Where n , μ , a , A and E_a are the charge carrier concentration, the charge mobility, the hopping distance, the pre-exponential term related to scattering mechanism and the activation energy, respectively. As can be seen from Figure 7.6c, we obtain a good linear fit which strongly suggests that the small polaron hopping conduction theory is obeyed in the $\text{Ca}_9\text{Co}_{12}\text{O}_{28}$ system. The activation energy is calculated to be 0.076eV. This is high compared to the other calcium cobalt oxide systems [Liu et al., 2008; Lan et al., 2010] and hence, may point out to the low electrical conductivity values obtained in this system. Nevertheless, we see an increasing trend in electrical conductivity with rising temperature and this probably points out to carriers being imparted with thermal energy at the higher temperature ranges. Oxide based compounds are highly anisotropic [Ohtaki, 2011] and this could be another reason for the poor electrical conductivity values obtained in polycrystalline $\text{Ca}_9\text{Co}_{12}\text{O}_{28}$. To enhance the electrical conductivity in $\text{Ca}_9\text{Co}_{12}\text{O}_{28}$, the difficult task of grain alignment in the most conducting direction during the SPS process could be conducted or it could be doped with elements like bismuth (Bi), sodium (Na) and other elements to decrease the effective

mass and the activation energy. [Tang et al., 2010; Yin et al., 2010; Liu et al., 2008; Lan et al., 2010]

The Seebeck coefficient data is shown in Figure 7.6d. The Seebeck coefficient is positive indicating a p-type thermoelectric material. To explain the high Seebeck coefficient and its increasing trend with rise in temperature, we use Heike's formula generalized for the high temperature limit as shown in Chapter 4 [Koshibae, Tsutsui & Maekawa, 2000]:

$$S = -\frac{k_B}{e} \ln \left[\left(\frac{g_3}{g_4} \right) \left(\frac{x}{1-x} \right) \right] \dots \dots \dots (7.3)$$

Where k_B , e and x are the Boltzmann constant, the charge of an electron and the concentration of Co^{4+} ions, respectively. In the formula above, g is given by the total number of configurations of charge and the degeneracy of spin, so g_3 and g_4 represent the total number of configurations of Co^{3+} and Co^{4+} , respectively. [Koshibae, Tsutsui & Maekawa, 2000] From the generalized Heike's formula, it is clear that large Seebeck coefficient is dependent on large degeneracies and ratio of the degeneracies at the Co^{3+} and Co^{4+} sites. For the concentration of Co^{4+} ions in $\text{Ca}_9\text{Co}_{12}\text{O}_{28}$, we assume that it is similar to that of $\text{Ca}_3\text{Co}_4\text{O}_9$. [Lan et al., 2010; Wakisaka, Hirata & Mizokawa, 2008] X-ray and ultraviolet photoemission studies were done on $\text{Ca}_3\text{Co}_4\text{O}_9$ and the charge ordering of Co^{3+} to Co^{4+} ions was found to be 2:1. [Wakisaka, Hirata & Mizokawa, 2008] This would suggest that the concentration of Co^{4+} ions, x , is 1/3. From Koshibae *et al.*, analyses, large Seebeck coefficient values in cobaltates are obtained when the ratio of $g_3:g_4$ is 1:6 and 1:12. When $g_3:g_4$ is 1:6, the low spin states of Co^{3+} and Co^{4+} are stable; which on inserting into the

equation gives a S of $214\mu\text{V}/\text{K}$, which is close to our experimental value. When $g_3:g_4$ is 1:12, the low spin states of Co^{3+} are stable and the low and high spin states of Co^{4+} are close in energy- and this gives a S of $274\mu\text{V}/\text{K}$. This initial analysis would indicate that in the $\text{Ca}_9\text{Co}_{12}\text{O}_{28}$ system, the stable low spin states of Co^{3+} and Co^{4+} contribute to the large Seebeck coefficient. However, the generalized Heike's formula is for the high temperature limit, and our measurements go only till 700K, which suggests that the latter case could be contributing to the large Seebeck coefficient and in turn predicting a value of $274\mu\text{V}/\text{K}$ at high temperatures.

The figure of merit, ZT , of $\text{Ca}_9\text{Co}_{12}\text{O}_{28}$ is shown in Figure 7.6f. The average calculated ZT at 700K is 0.026. Although the ZT is low, it is still the highest for the $\text{Ca}_9\text{Co}_{12}\text{O}_{28}$ phase and the temperature range reported. The ZT was severely affected due to the low electrical conductivity.

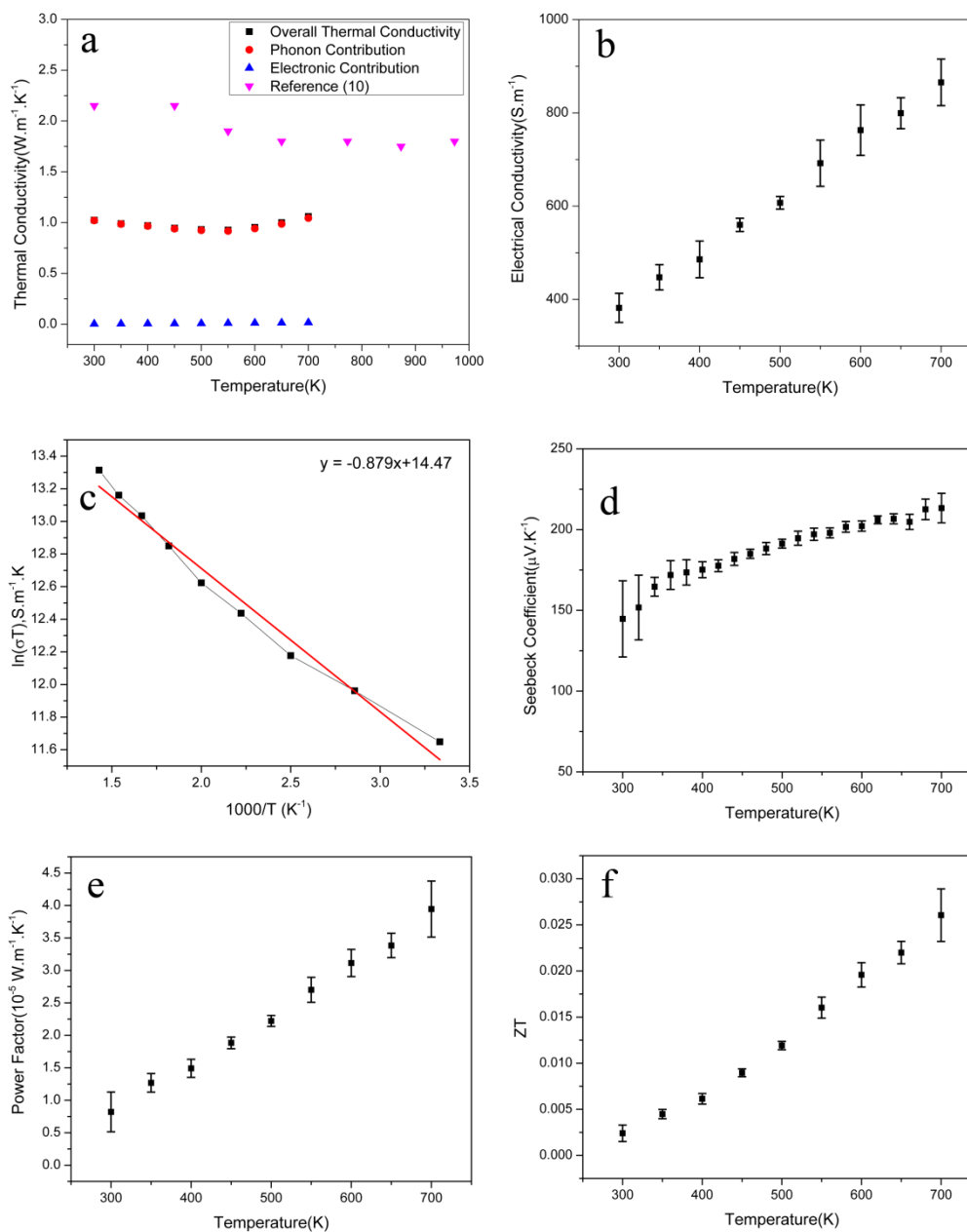


Figure 7.6. (a) Thermal conductivity of the SPS $\text{Ca}_9\text{Co}_{12}\text{O}_{28}$ nanowires and the respective phonon and electrical contributions. (b) Electrical conductivity of the SPS $\text{Ca}_9\text{Co}_{12}\text{O}_{28}$ nanowires. (c) Plot of $\ln(\sigma T)$ versus $1000/T$ with linear fit and respective equation shown. (d) Seebeck coefficient of the SPS $\text{Ca}_9\text{Co}_{12}\text{O}_{28}$ nanowires. (e) Power Factor of the SPS

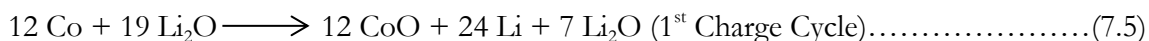
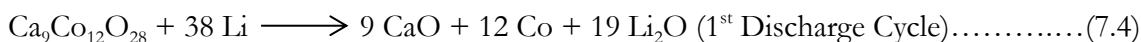
$\text{Ca}_9\text{Co}_{12}\text{O}_{28}$ nanowires. (f) Figure of Merit, ZT, of the SPS $\text{Ca}_9\text{Co}_{12}\text{O}_{28}$ nanowires. [Yadav et al., 2013]

7.7 Electrode fabrication procedure

The electrochemical evaluation was performed by firstly mixing $\text{Ca}_9\text{Co}_{12}\text{O}_{28}$ nanowires with Super C65 carbon black (TIMCAL Graphite and Carbon) and Kynar HSV 900 PVDF (Arkema Inc.) in a mass ratio of 80:20:20. The powders were initially ground using mortar and pestle. The ground powders were then mixed with N-methyl-2-pyrrolidone (Sigma-Aldrich) and vortexed and sonicated alternatively. The slurry was coated on copper foil with a wet thickness of $200\mu\text{m}$. The electrode sheet was dried in vacuum overnight at 100°C . Cells with 12mm diameter were cut and dried in vacuum for 4h at 100°C . Coin cells (2032) were then assembled in an argon filled glove box. The half cells consisted of lithium metal as the anode, Celgard 2325 as the separator, and 1M LiPF_6 in a mixed solvent of ethylene carbonate, dimethyl carbonate and diethyl carbonate(1:1:1 volume ratio). The cells were galvanostatically cycled between 2.5 and 0.01V by using a BST8-MA analyzer (MTI Corporation).

7.8 Electrochemical evaluation

In Figure 7.7a, the characteristic first charge-discharge curve of $\text{Ca}_9\text{Co}_{12}\text{O}_{28}$ nanowires is shown for a charge current density of 100 mA/g(0.1C) and follows quite similarly to the characteristic behavior of other phases like $\text{Ca}_3\text{Co}_4\text{O}_9$ and $\text{Ca}_2\text{Co}_2\text{O}_5$. [Kim et al., 2007; Sharma et al., 2004] There are three regions of interest in the first discharge cycle curve. The voltage drops quickly to around 1.09V and is quite stable till it drops to region (2) when the discharge capacity is around 125mAh/g. In region (2), the discharge capacity is quite stable till around 325mAh/g and at that point, the curve slowly steepens till it reaches its final capacity of around 541mAh/g. It is established that for transition metal oxides their reversible capacity is contributed from reversible oxidation of metal and Li_2O formation and decomposition. [Sharma et al., 2004; Obrovac et al., 2001] Therefore, for the first discharge-charge cycle of $\text{Ca}_9\text{Co}_{12}\text{O}_{28}/\text{Li}$, the following reaction takes place:



From the first charge and discharge cycle, the theoretical capacity of $\text{Ca}_9\text{Co}_{12}\text{O}_{28}$ can be calculated out to be 328.5(24 Li per formula unit) and 520mAh/g (38 Li per formula unit), respectively. However, the observed charge and discharge capacity from Figure 6 (a) are 279.3 (20.4 Li per formula unit) and 541mAh/g (39.5 Li per formula unit), respectively, at 100mA/g. The recyclability of Li is reduced during the first charge probably due to the formation of polymeric gel type surface film over the metal nanoparticles [Kim et al., 2007;

Sharma et al., 2004] and break down of the crystal structure. Thus, the three regions of interest in the first discharge curve could probably shed light over the subsequent electrochemical performance of the cell – where in region (1) there might a small amount of insertion of Li ions inside $\text{Ca}_9\text{Co}_{12}\text{O}_{28}$, then in region (2) the subsequent destruction of the structure must be taking place to form CaO , Co and Li_2O , and finally in region (3), the formation of the polymeric gel over the metal nanoparticles hinders the recyclability of Li ions. Based on this, it can be concluded that $\text{Ca}_9\text{Co}_{12}\text{O}_{28}$ does not follow an intercalation mechanism, but infact a displacement mechanism. As shown in figure 7.7a. and the blue curve in figure 7.7b., the discharge fade is quite apparent till the 10th cycle, after which, the fade stabilizes and in later cycles, the discharge capacity keeps on increasing till the 90th cycle, after which it is stabilized completely. This could possibly be due to the time that it takes to completely destroy the crystal structure, after which, there are three completely separate entities present – CaO , Co and Li_2O . The 10th, 20th, 30th, 50th and 190th cycle discharge capacities are 178.1, 154.9, 162.1, 195.2, and 255.9 mAh/g, respectively. The good recyclability could be due to the good electrical conductivity between the interconnecting nanoparticles that form the nanowires.

The electrochemical performance of the $\text{Ca}_9\text{Co}_{12}\text{O}_{28}$ nanowires were also tested at higher current densities. As shown by red curve in Figure 7.7b., the half cell was cycled at 1000mAh/g(1C) after 5 cycles of cycling at 100mA/g. Initially, the fade is quite quick, but after 50 cycles, the capacity retention becomes excellent and even increases till 500 cycles. Moreover, similar behavior can be observed in Figure 7.7d. In Figure 7.7d., the charge rates increased periodically every 3 cycles, except for the first 5 cycles, where the cell was cycled

at 0.1C to allow formation of the polymeric gel. A constant discharge rate of 0.1C was kept for the whole study to test the retention capacity of the battery. The end discharge capacity of 0.1, 1, 2, 3, 4 and 0.1C current rates were 241, 115, 72, 55, 46, and 208mAh/g, respectively. The retention was excellent as it barely decreased and maintained a very high coulombic efficiency. Interestingly, the discharge capacity at the last rate of 0.1C, fades slowly in the next few cycles to a value similar to the one obtained in Figure 7.7a., and then it becomes stable and starts to increase in subsequent cycles. This is very much similar to the trends as shown in Figure 7.7a and 7.7b. for long term cycling at 0.1 and 1C, respectively. It could be that the complete destruction of the crystal structure and the complete formation of the polymeric gel film may not have finished due to the change in charge rates in short number of cycles and hence, the slight drop at the start of the last change in charge rate of 0.1C.

The coulombic efficiencies of cycling the half-cells at 100(0.1C) and 1000(1C) mA/g are shown in Figure 7.7c. The trends for both the half-cells are very similar, showing a coulombic efficiency of more than 99% in subsequent cycles. For the half-cell cycled at 0.1C, the spikes in coulombic efficiency at random intervals is due to power fluctuations faced during the study. The initial coulombic efficiency of around 52% is well understood due to the aforementioned analyses of the first discharge curve.

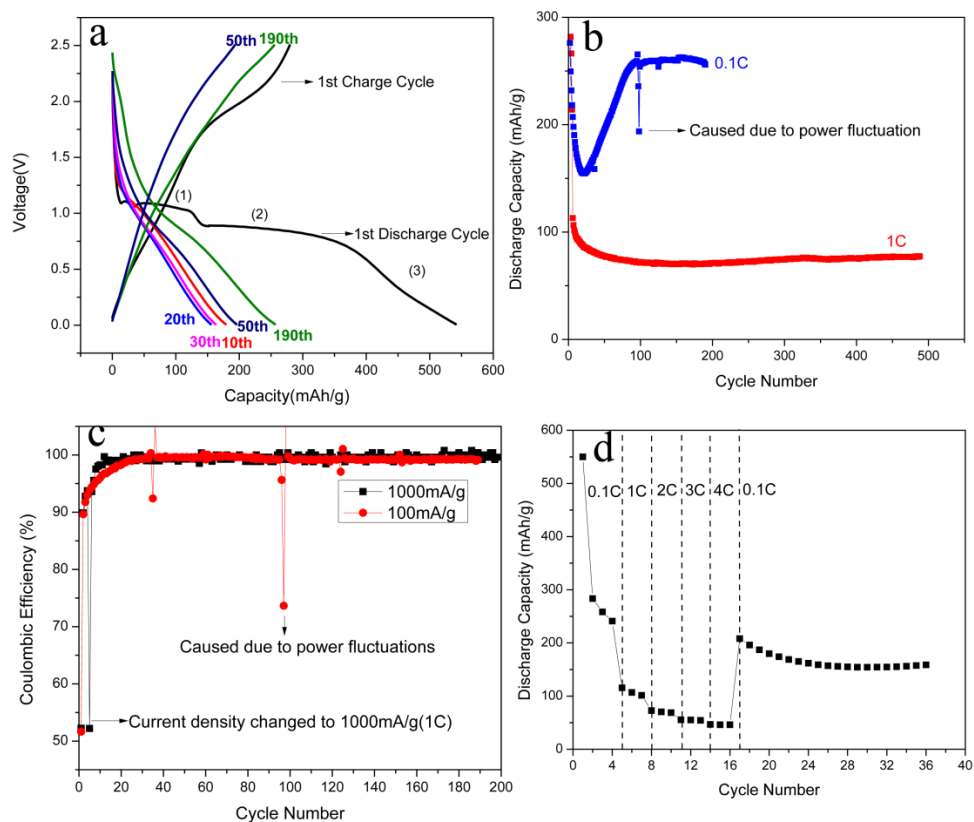


Figure 7.7. (a) Charging-discharging curves of $\text{Ca}_9\text{Co}_{12}\text{O}_{28}/\text{Li}$ half-cell cycled at 100 mA/g (0.1C). (b) Discharge capacity of $\text{Ca}_9\text{Co}_{12}\text{O}_{28}/\text{Li}$ half-cell cycled at 100 (0.1C) and 1000 (1C) mA/g. (c) Coulombic efficiency of $\text{Ca}_9\text{Co}_{12}\text{O}_{28}/\text{Li}$ half-cell cycled at 100 (0.1C) and 1000 (1C) mA/g. (d) Retention of discharge capacity of $\text{Ca}_9\text{Co}_{12}\text{O}_{28}/\text{Li}$ half-cell at different charge rates. [Yadav et al., 2013]

The porous nanowires, in theory, should result in good rate capability. Unfortunately due to a displacement reaction mechanism the porous nanowires break down into different

particles consisting of electrochemical active phases and inactive phases like CaO. As the porous nanowires have high surface area as well, there are high chances of side reactions taking place, and thus, accelerating the rate of solid electrolyte interface(SEI) growth or the polymeric film forming on the surface of the active material as mentioned previously. This triggers a rapid capacity fade initially, however, in latter cycles, the capacity is very stable although quite low as shown in Fig. 6b. $\text{Ca}_9\text{Co}_{12}\text{O}_{28}$ compared to Co_3O_4 , does not perform well in terms of maintaining a stable capacity fade in the initial cycles. [Wu et al., 2010] However, some of Co_3O_4 good electrochemical properties have resulted from combining it with other good electrical conductors like graphene [Wu et al., 2010]. When electrochemical properties of only Co_3O_4 nanoparticles were tested, dramatic capacity fade at 50mA/g was observed – a decrease from around 1000mAh/g at 1st cycle to around 200mAh/g at the 30th cycle. [Wu et al., 2010]The $\text{Ca}_9\text{Co}_{12}\text{O}_{28}$ material performs poorly compared to graphite, which is a traditional anode material used in lithium ion batteries. Although the initial capacity(541 mAh/g) is high for the layered $\text{Ca}_9\text{Co}_{12}\text{O}_{28}$ material compared to graphite(372 mAh/g) [Zhang, 2011], the dramatic capacity fade degrades its performance, thus leading to a much lower capacity compared to graphite in later cycles. However, the problem of dramatic capacity fade was also observed in silicon, where its high capacity(4200mAh/g) [Zhang, 2011] was lost in later cycles due to large volume expansion(approximately 400%) [Jung, Choi & Han, 2012], and thus ultimately leading to destruction in the crystal structure. Some have solved the volume expansion problem by curtailing the growth through coating of the silicon with an oxide based layer like silicon oxide [Wu et al., 2012]. Similar methods

need to be developed for the layered transition metal oxide anodes to maintain its high initial capacity.

7.9 Conclusions

For the first time porous nanowires of a unique phase of calcium cobalt oxide, $\text{Ca}_9\text{Co}_{12}\text{O}_{28}$, has been achieved through solution based synthesis. SPS was used to consolidate a nanostructured bulk pellet of $\text{Ca}_9\text{Co}_{12}\text{O}_{28}$ and its thermoelectric properties were measured. A record low thermal conductivity of 1.06 W/mK has been measured at 700K for any calcium cobalt oxide phase which could be due to the phonon scattering happening at the interfaces of the porous network of nanowires. Although a record high Seebeck coefficient has also been measured, its final ZT has been affected due to the low electrical conductivity compared to its bulk counterpart. It could be that the charge carriers get scattered, but greater insight was obtained by using the theory of small polaron hopping. The huge anisotropy attributed with oxides coupled with the large effective mass and activation energy are the main reasons for the poor electrical conductivity. For further enhancement of electrical conductivity, doping with elements like Bi and Na have been suggested to decrease activation energy and effective mass and thus increase mobility. The large Seebeck coefficient was explained with the generalized Heike's model and Koshibae *et al.*, theory. [Koshibae, Tsutsui & Maekawa, 2000] Nonetheless, the ZT is the highest at 700 K and it is another promising thermoelectric material that needs to be researched even further for high temperature applications.

Electrochemical characteristics of half-cells of $\text{Ca}_9\text{Co}_{12}\text{O}_{28}$ were evaluated at different current densities or rates. At 100(0.1C) mA/g, a first cycle discharge capacity of around 540mAh/g can be observed. In the first discharge cycle three unique regions are observed which are indicative of the subsequent cycling performance. A breakdown of the crystal structure happens which creates a rapid discharge fade in the initial cycling. However, in subsequent cycles, this fade stabilizes and starts increasing exhibiting excellent rate cyclability. A test of different charge current densities indicated good rate performance and the ability to handle high current stresses. Coulombic efficiencies in subsequent cycles were more than 99%.

Overall investigation into the thermoelectric and battery properties of $\text{Ca}_9\text{Co}_{12}\text{O}_{28}$ has shown that it is definitely a promising material for both applications requiring further research to increase its performance.

7.10 References

Armand, M.; Tarascon, J.M. Building Better Batteries. *Nature* **2008**, *451*, 652-657.

Bosman, A.J.; van Daal, H.J. Small-Polaron Versus Band Conduction in Some Transition-Metal Oxides. *Adv. Phys.* **1970**, *19*, 1-117.

Ganguli, A.K.; Ganguly, A.; Vaidya, S. Microemulsion-Based Synthesis of Nanocrystalline Materials. *Chem. Soc. Rev.* **2010**, *39*, 474-485.

Hao, H.; Zhao, L.; Hu, X. Microstructure and Thermoelectric Properties of Bi- and Cu-Substituted $\text{Ca}_3\text{Co}_4\text{O}_9$ Oxides. *J. Mater. Sci. Technol.* **2009**, *25*, 105-108.

Jung, S. C.; Choi, J. W.; Han, Y-K. Anisotropic Volume Expansion of Crystalline Silicon during Electrochemical Lithium Insertion: An Atomic Level Rationale. *Nano Lett.*, **2012**, *12*(10), 5342.

Kasavajjula, U.; Wang, C.; Appleby, A.J. Nano- and Bulk-Silicon-Based Insertion Anodes for Lithium-Ion Secondary Cells. *J. Power Sources* **2012**, *163*, 1003-1039.

Kim, D-W.; Ko, Y-D.; Park, J-G.; Kim, B-K. Formation of Lithium-Driven Active/Inactive Nanocomposite Electrodes Based on $\text{Ca}_3\text{Co}_4\text{O}_9$ Nanoplates. *Angew. Chem. Int. Ed.* **2007**, *46*, 6654-6657.

Koshibae, W.; Tsutsui, K.; Maekawa, S. Thermopower in Cobalt Oxides. *Phys. Rev. B* **2000**, *62*, 6869-6872.

Lan, J.; Lin, Y-H.; Li, G-J.; Xu, S.; Liu, Y.; Nan, C-W.; Zhao, S-J. High-Temperature Electrical Transport Behaviors of The Layered $\text{Ca}_2\text{Co}_2\text{O}_5$ -Based Ceramics. *App. Phys. Lett.* **2010**, *96*, 192104-3.

Li, S.; Funahashi, R.; Matsubara, I.; Ueno, K.; Yamada, H. High Temperature Thermoelectric Properties of Oxide $\text{Ca}_9\text{Co}_{12}\text{O}_{28}$. *J.Mater. Chem.* **1999**, *9*, 1659-1660.

Liu, P.S.; Chen, G.; Pei, J.; Cui, Y.; Lu, D.Q.; Zhou, N.; Xian, H.Z. Preparation and Characterization of The New Oxides $\text{Ca}_{2-x}\text{Na}_x\text{Co}_2\text{O}_5$. *Physica B* **2008**, *403*, 1808-1812.

Marom, R.; Amalraj, S.F.; Leifer, N.; Jacob, D.; Aurbach, D. A Review of Advanced and Practical Lithium Battery Materials. *J. Mater. Chem.* **2011**, *21*, 9938-9954.

Masuda, Y.; Nagahama, D.; Itahara H.; Tani, T.; Seo, W.S.; Koumoto, K. Thermoelectric Performance of Bi- and Na-Substituted $\text{Ca}_3\text{Co}_4\text{O}_9$ improved through ceramic texturing. *J. Mater. Chem.* **2003**, *13*, 1094-1099

McDowell, M.T.; Lee, S.W.; Wang, C.; Cui, Y. The Effect of Metallic Coatings and Crystallinity on The Volume Expansion of Silicon During Electrochemical Lithiation/Delithiation. *Nano Energy* **2012**, *1*, 401-410.

Mei, T.; Zhang, J.; Wang, L.; Xing, Z.; Zhu, Y.; Qian, Y. Preparation of Mixed Oxides $\text{Ca}_9\text{Co}_{12}\text{O}_{28}$ and Their Electrochemical Properties. *Materials Letters* **2012**, *82*, 1-3.

Mosa, J.; Velez, J.F.; Lorite, I.; Arconada, N.; Aparicio, M. Film-Shaped Sol-Gel $\text{Li}_4\text{Ti}_5\text{O}_{12}$ electrode for Lithium-Ion Microbatteries. *J. Power Sources* **2012**, *205*, 491-494.

Obrovac, M.N.; Dunlap, R.A.; Sanderson, R.J.; Dahn, J.R. The Electrochemical Displacement Reaction of Lithium with Metal Oxides. *J. Electrochem. Soc.* **2001**, *148*, A576-A588.

Ohta, H.; Sugiura, K.; Koumoto, K. Recent Progress in Oxide Thermoelectric Materials: p-Type $\text{Ca}_3\text{Co}_4\text{O}_9$ and n-Type SrTiO_3 . *Inorg. Chem.* **2008**, *47*, 8429-8436.

Ohtaki, M. Recent Aspects of Oxide Thermoelectric Materials for Power Generation from Mid-to-High Temperature Heat Source. *Journal of the Ceramic Society of Japan* **2011**, *11*, 770-775.

Sharma, N.; Shaju, K.M.; Subba Rao, G.V.; Chowdari, B.V.R. Mixed Oxides $\text{Ca}_2\text{Fe}_2\text{O}_5$ and $\text{Ca}_2\text{Co}_2\text{O}_5$ as Anode Materials for Li-Ion Batteries. *Electrochimica Acta* **2004**, *49*, 1035-1043.

Shen, L.; Uchaker, E.; Zhang, X.; Cao, G. Hydrogenated $\text{Li}_4\text{Ti}_5\text{O}_{12}$ Nanowire Arrays for High Rate Lithium Ion Batteries. *Adv. Mater.* **2012**, *24*, 6502-6506.

Tang, G.D.; Wang, Z.H.; Xu, X.N.; Qiu, L.; Xing, L.; Du, Y.W. Thermoelectric Properties of $\text{Ca}_3\text{Co}_4\text{O}_{9+\delta}$ with Lu Substitution. *J. Mater. Sci.* **2010**, *45*, 3969-3973.

Wakisaka, Y.; Hirata, S.; Mizokawa, T. Electronic Structure of $\text{Ca}_3\text{Co}_4\text{O}_9$ Studied by Photoemission Spectroscopy: Phase Separation and Charge Localization. *Phys. Rev. B* **2008**, *78*, 235107-5.

Whittingham, M.S. Materials Challenges Facing Electrical Energy Storage. *MRS Bull.* **2008**, *33*, 411-419.

Wu, H.; Chan, G.; Choi, J.W.; Ryu, I.; Yao, Y.; McDowell, M.T.; Lee, S. W.; Jackson, A.; Yang, Y.; Hu, L.; Cui, Y. Stable cycling of double-walled silicon nanotube battery anodes through solid-electrolyte interphase control. *Nature Nanotechnology*, **2012**, 7, 310-315.

Wu, Z. S.; Ren, W.; Wen, L.; Gao, L.; Zhao, J.; Chen, Z.; Zhou, G.; Li, F.; Cheng, H. M. Graphene Anchored with Co_3O_4 Nanoparticles as Anode of Lithium Ion Batteries with Enhanced Reversible Capacity and Cyclic Performance. *ACS Nano.*, **2010**,4, 3187-3194.

Yang, S.B.; Feng, X.L.; Mullen, K. Sandwich-Like, Graphene-Based Titania Nanosheets with High Surface Area for Fast Lithium Storage. *Adv. Mater.* **2011**, 23, 3575.

Yin, T.; Liu, D.; Ou, Y.; Ma, F.; Xie, S.; Li, J-F.; Li, J. Nanocrystalline Thermoelectric $\text{Ca}_3\text{Co}_4\text{O}_9$ Ceramics by Sol-Gel Based Electrospinning and Spark Plasma Sintering. *J. Phys. Chem. C.* **2010**, 114, 10061-10065.

Zhang, W.J.J. A review of the electrochemical performance of alloy anodes for lithium-ion batteries. *J. Power Sources.*, **2011**, 196(1), 13-12

Yadav, G. G.; David, A.; Favaloro, T.; Yang, H. ; Shakouri, A.; Caruthers, J.; Wu, Y. Synthesis and investigation of thermoelectric and electrochemical properties of porous $\text{Ca}_9\text{Co}_{12}\text{O}_{28}$ nanowires. *J. Mater. Chem. A*, **2013**, 1, 11901-11908.

CHAPTER 8. LITHIUM COBALT OXIDE: A STUDY OF DIFFERENT NANOSTRUCTURE'S RELATIONSHIP TO ELECTROCHEMICAL PROPERTIES

The microemulsion method developed in Chapter 7 is used to synthesize different nanostructure of the traditional cathode material, lithium cobalt oxide (LiCoO_2). Through varying the annealing temperature and time, porous nanowires and nanoparticles of LiCoO_2 are obtained. The electrochemical performances of these different nanostructures obtained at the respective annealing conditions are evaluated. It is shown that nanoparticles formed at annealing condition of 700°C , 1.5 hours performs the best, delivering an initial capacity of around 135mAh/g and exhibiting a capacity of retention of around 93% by 100 cycles at 0.1C. Comparisons are made with the microemulsion synthesized LiCoO_2 material obtained at different annealing conditions with those in literature.

8.1 Introduction

Lithium ion batteries, primarily lithium cobalt oxide (LiCoO_2), have been a major area of interest due to its large gravimetric and volumetric energy densities compared to other batteries which makes them a great candidate for electric vehicles and portable

electronics.[Nazri & Pistoia, 2004] LiCoO_2 is one of the most extensively studied cathode materials, and it is used in cell phones and many small scale technological applications since its introduction in the market by Sony in 1990's.[Nazri & Pistoia, 2004] One of the requirements of batteries is to have a long cycle life without any degradation in performance. Nanostructured electrodes in lithium-ion batteries drastically reduce the diffusion time for lithium ions, achieving higher capacities and longer cycle times.[Nazri & Pistoia, 2004; Yuan, Liu & Zhang, 2012; Mosa et al., 2012; Sekizawa et al., 2011; Wu et al., 2012] However, the oxide-based materials that constitute the cathodes in lithium-ion batteries have proven to be greatly recalcitrant to forming nanostructures. The solid-state reactions that are typically employed to produce oxide-based materials, like LiCoO_2 , in their desired phases are long and proceed at extremely high temperatures that are not particularly conducive to forming nanostructures.[Lundblad & Bergman, 1997; Berbenni et al., 2005; Yilmaz et al., 2012]

Alternatives such as hydrothermal reactions fare better and achieve the desired architectures at considerably lower temperatures.[Dong et al., 2011; Jo et al., 2009] However, the use of high annealing temperatures eventually destabilizes the nanostructures, greatly diminishing the utility of the methodology.[Jiao, Shaju & Bruce, 2005] More recent techniques such as the templating methodology suffer from the converse problem, often producing the preferred nanostructural morphology of an undesired phase of the material.[Jiao, Shaju & Bruce, 2005] This combination of characteristics also negatively impacts battery performance. Moreover, neither of these alternatives is scalable to the industrial scale.

Microemulsion-based techniques, in contrast, are scalable, proceed at conditions that favor the formation of desired phases and architectures, and are generalizable to a variety of materials – for example calcium cobalt oxide, as shown in Chapter 7.[Ganguli, Ganguly & Vaidya, 2010] Herein, we elaborate a microemulsion-based nanostructuring approach that we developed to synthesize LiCoO_2 . Commercial batteries that incorporate LiCoO_2 cathodes often deliver about 140mAh/g. Although this power capacity is fairly close to the theoretical limit achievable by the material, it fades quite rapidly at higher cycle rates.[Zhao et al., 2008;Jung et al., 2010] Emulsion-based methods using kerosene as the oil phase have been previously implemented to synthesize nanoparticles of LiCoO_2 . [Myung et al., 2000; Lu & Yeh, 2001] However, this method exhibits poor control over the morphology of the nanostructures that are formed. The microemulsion-based technique used in Chapter 7 exhibits much better control over morphology. In brief, we used cetyltrimethylammonium bromide (CTAB), a surfactant, to direct the formation of nanowire templates comprising of lithium and cobalt oxalate. We then annealed the templates under controlled conditions to finally produce nanostructured LiCoO_2 . We also observed that the morphology of the nanostructures was dependent on the annealing temperature and time. The electrochemical characteristics of the LiCoO_2 nanowires thus synthesized were also favorable when compared to similar morphology in literature. In summary, not only are the templating and annealing conditions much gentler, but altering the surfactant, solvents, and surfactant-to-water ratio also influences the nanoarchitecture of the material, imbuing the methodology with an additional parameter for process control.

8.2 Experimental

8.2.1 Microemulsion-based synthesis procedure

Cobalt nitrate hexahydrate, oxalic acid and 1-pentanol were purchased from Sigma-Aldrich. Lithium nitrate was purchased from Alfa Aesar, cyclohexane from EMD Millipore and cetyltrimethyl ammonium bromide from J.T. Baker. Lithium nitrate (LiNO_3) and cobalt nitrate hexahydrate [$\text{Co}(\text{NO}_3)_2 \cdot 6\text{H}_2\text{O}$] were used as precursors. In a standard microemulsion synthesis (Figure 1a), an emulsion was produced by vigorously mixing 0.1 mole of cetyl trimethylammonium bromide (CTAB), a cationic surfactant, with 1.4 L cyclohexane and 60 mL 1-pentanol for 1 hour. Next, 0.024 moles of oxalic acid in 40 mL of DI water was added to the stirring solution and mixed for 3 hour. In the final step, 0.02 moles of LiNO_3 and 0.0034 moles of $\text{Co}(\text{NO}_3)_2 \cdot 6\text{H}_2\text{O}$ in 80 mL of DI water were added and stirred until the color of the solution changed from pink to white. Following completion of the reaction, the solution was centrifuged and a precipitate was obtained and dried at 80°C . The dried pink precipitate is the precursor as shown in Figure 8.1a.

8.2.2 Post-Annealing Procedure

The precursor was annealed in an open tube furnace at different temperatures and times in a 2-factor, 2-level study. The annealing temperatures chosen were 600°C and 700°C , and the annealing times used were 1.5 and 3 hours. The tube furnace heating rate was ramped up from room temperature to 600°C and 700°C at $9.7^\circ\text{C}/\text{min}$ and $11.4^\circ\text{C}/\text{min}$, respectively; and

the temperatures were maintained for the annealing times used in the experiment. The tube furnace was then allowed to cool down to room temperature. The products were then washed with DI water three times and then once more with ethanol. Nanowires were obtained for the annealing condition of 600°C for 1.5 hours. A mixture of nanowires and nanoparticles was obtained for the other annealing conditions. The products were also analyzed by X-ray diffraction (XRD) on a Bruker D8 Focus X-ray diffractometer with Cu K(alpha) source, a scanning electron microscope (Hitachi S-4800 Field Emission Microscope), an electron dispersive X-ray analysis system (Oxford INCA 250 X-MAX silicon drift with 80mm collection window on a Phillips CM-100 Transmission Electron Microscope) and transmission electron microscope (Titan 80-300 kV Environmental Electron Microscope).

8.2.3 Electrochemical Characterization

The electrochemical characteristics of the products were tested by fabricating coin cells. LiCoO₂ was mixed with Super C65 carbon black (TIMCAL Graphite and Carbon) and Kynar HSV 900 PVDF (Arkema Inc.) in a mass ratio of 80:10:10. Samples containing mixtures of nanowires and nanoparticles were ground using a mortar and pestle, mixed with N-methyl-2-pyrrolidone (Sigma-Aldrich) and later vortexed and sonicated. Samples consisting only of LiCoO₂ nanowires were not sonicated. The processed mixtures were coated with aluminium foil with a wet thickness of 145 µm. The electrode sheet was dried in vacuum at 120°C for 1.5 hours. Coin cells with 12 mm diameter were cut and dried in

vacuum for 2 hours at 120°C and later assembled in an argon-filled glove box. The half cells consisted of lithium metal as the reference electrode, Celgard 2325 as the separator, and 1M LiPF₆ in a mixed solvent of ethylene carbonate, dimethyl carbonate and diethyl carbonate (1:1:1 volume ratio). The cells were galvanostatically cycled between 3.0 and 4.2V by using a BST8-MA analyzer (MTI Corporation).

8.3 Results

The XRD patterns for the different annealing conditions are shown in Figure 1b. LiCoO₂ prepared at annealing conditions of 600°C contained some impurities of cobalt oxide (Co₃O₄). Pure LiCoO₂ was achieved for the 700°C annealing conditions. LiCoO₂ is known to crystallize in two phases – layered α -NaFeO₂ and spinel-type structure.[Gummow et al., 1992; Okubo et al., 2007] Moreover, it is difficult to distinguish between the two phases as the XRD patterns are similar. However, it has been reported that a weak (003) is indicative of a spinel structure as it represents the stacking of CoO₂ layers.[Myung et al., 2000; Okubo et al., 2007] In Figure 8.1b. none of XRD patterns indicate weak (003) peak, and in conjunction with peaks representing (101) and (104) planes, it seems that LiCoO₂ crystallizes in the layered rhombohedral α -NaFeO₂ crystal structure.

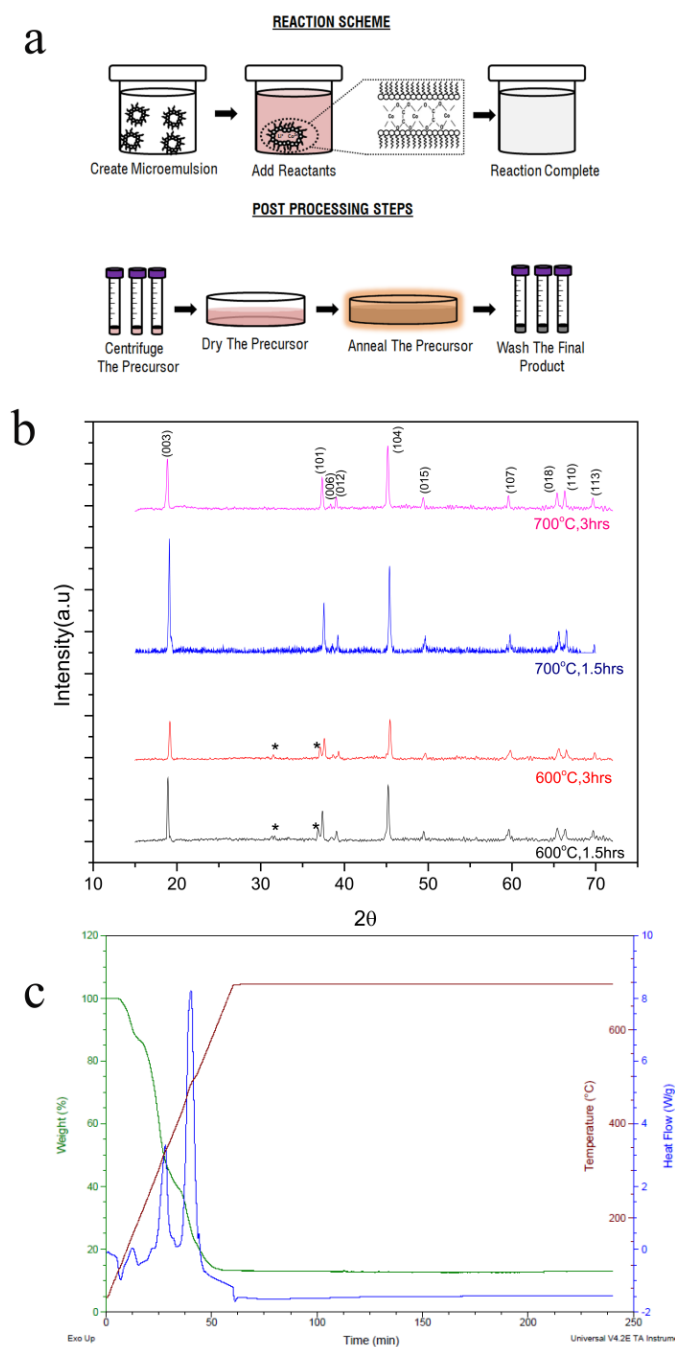


Figure 8.1. (a) Schematic representation of the LiCoO_2 synthesis method.(b) XRD spectrum for the different annealing conditions used to synthesize LiCoO_2 (* indicates Cobalt Oxide impurity).(c) TGA curve of the precursor mimicking the 700°C , 3hour annealing run.

A Raman analysis (Figure 8.2.) was also done on the four different annealing conditions. Two characteristic peaks for the layered LiCoO_2 can be identified around $486\text{-}487\text{cm}^{-1}$ and 596cm^{-1} for all the annealing conditions. They correspond to the oxygen vibrations involving Co-O stretching (A_{1g}) at around 596cm^{-1} , and O-Co-O bending (E_g) at around $486\text{-}487\text{cm}^{-1}$. For the 600°C annealing conditions, two more peaks can be identified around 451cm^{-1} and 608cm^{-1} . They are characteristic peaks of low temperature phase of LiCoO_2 that have residual impurities of cobalt oxide. This explains the cobalt oxide impurity peaks seen in the XRD spectrum for the 600°C annealing conditions.

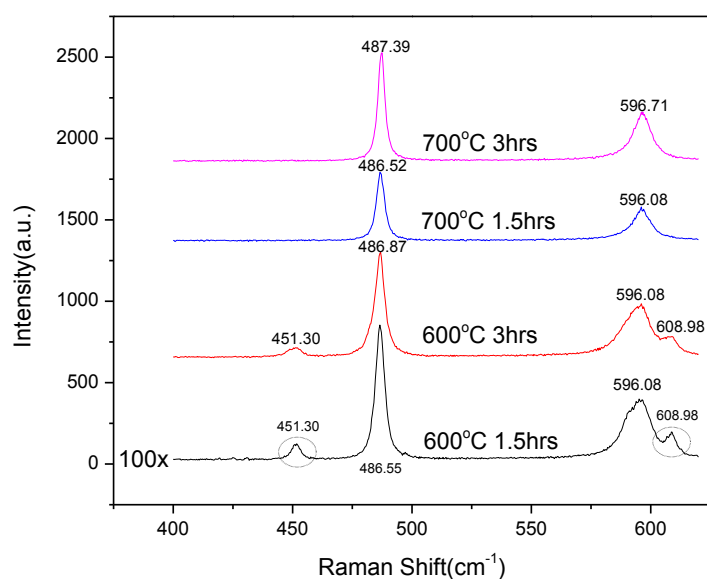


Figure 8.2. Raman shift of all the different annealing conditions of LiCoO_2 . The Raman shift for the 600°C 1.5 hour sample was done at 100x magnification.

The precursor that was obtained in the post-processing step (Figure 8.1a) was a mixture of lithium and cobalt oxalate salt. Thermogravimetric analyses (TGA) mimicking the annealing step for a 700°C, 3hour procedure (where the temperature was increased from room temperature to 700°C in 1 hour and then held constant for 3 hours) exhibited a sharp drop in weight as the temperature was increased. An endothermic curve was observed around 100°C which indicates that water may have escaped from the precursor. Two exothermic curves were observed at around 350°C and 480°C. This result indicates that carbon dioxide was generated during the annealing step, as shown in Chapter 7 as well. Weight loss was no longer observed after 660°C and a final endothermic curve at that temperature indicates the final phase formation of layered pure LiCoO_2 . The precursor was a hydrate salt of lithium and cobalt oxalate, where water of hydration and probably carbon dioxide, which could be generated from the decomposition of the oxalate group, leave during the annealing step, as indicated by the TGA. At 600°C weight loss is still occurring and the final endothermic curve is observed much later at around 660°C – which would explain the impurities observed in the XRD spectrum for the 600°C annealing conditions.

The SEM images of the precursor and LiCoO_2 for the respective annealing conditions are shown in Figure 8.3. The precursors are nanowire shaped (Figure 8.3a and b) which act as templates to form the LiCoO_2 nanowires for the 600°C, 1.5 hours annealing condition. The average diameter for the precursor nanowires is around 350nm. The effect of the different annealing conditions can be seen in Figures 8.3c-f. Porous nanowires of LiCoO_2 are formed

for the 600°C, 1.5 hours annealing condition. These nanowires, when looked at closely, are networks of particles attached together. The porosity observed in these nanowires would ideally be beneficial because the electrolyte can come into contact with more of the active material area. However, negative effects are observed during cycling as will be shown later. Less porous nanowires were observed as annealing temperature and time increased. The remaining annealing conditions exhibited more of nanoparticles with varying sizes. A HRTEM image of LiCoO_2 for the 700°C, 1.5 hours annealing condition is shown in the inset of Figure 8.3e. A lattice fringe spacing of 0.202 nm is observed which corresponds to the (104) plane. Energy Dispersive Spectroscopy (EDX) was performed on the nanoparticles obtained in the 700°C, 1.5 hours annealing condition. In Figure 8.3g the cobalt and oxygen peaks can be clearly seen and the ratio obtained between cobalt to oxygen is approximately 1:2 which is exactly the ratio in LiCoO_2 . Lithium cannot be detected under an EDX because of its low atomic number.

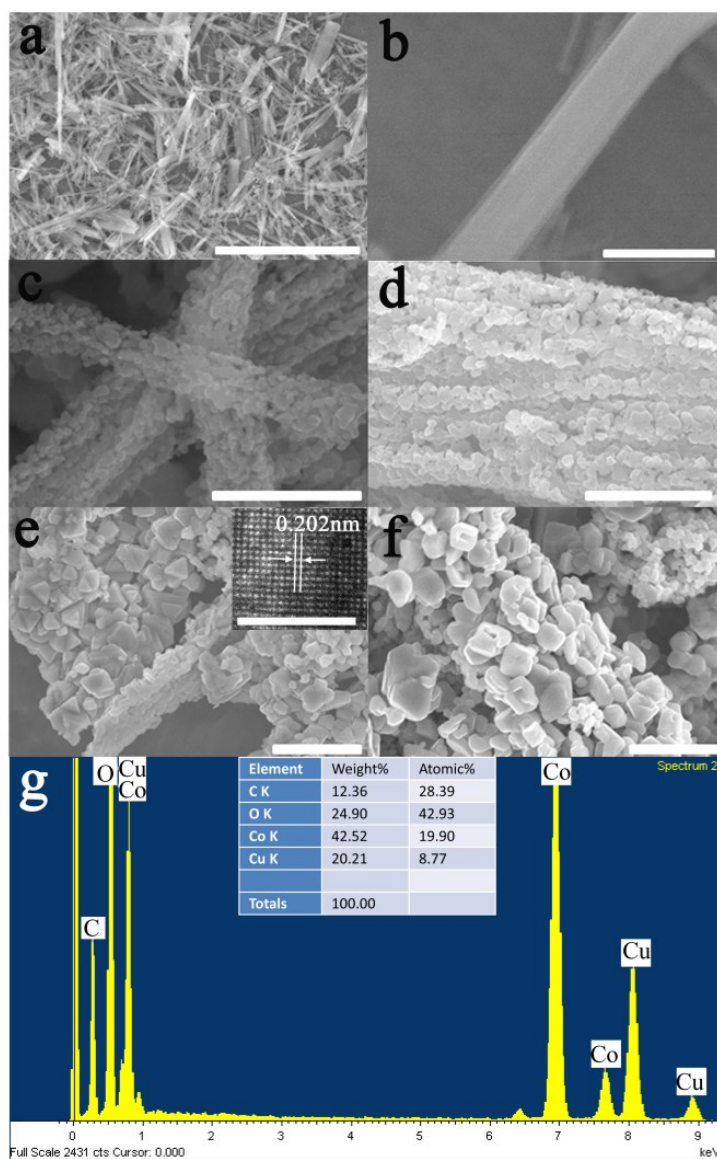


Figure 8.3. (a) Overview SEM image of the precursor (scale bar 20 μ m). (b) Magnified SEM image of a single nanowire precursor (scale bar 500nm). (c) SEM image of LiCoO₂ nanowires synthesized at 600°C for 1.5h (scale bar 500nm). (d) SEM image of LiCoO₂ nanoparticles synthesized at 600°C for 3h (scale bar 3 μ m). (e) SEM image of LiCoO₂ nanoparticles synthesized at 700°C for 1.5h (scale bar 5 μ m), inset showing HRTEM image of LiCoO₂

nanoparticle (scale bar 2nm). (f) SEM image of LiCoO_2 nanoparticles synthesized at 700°C for 3h (scale bar $5\mu\text{m}$). (g) EDX spectrum of LiCoO_2 synthesized at 700°C for 1.5h.

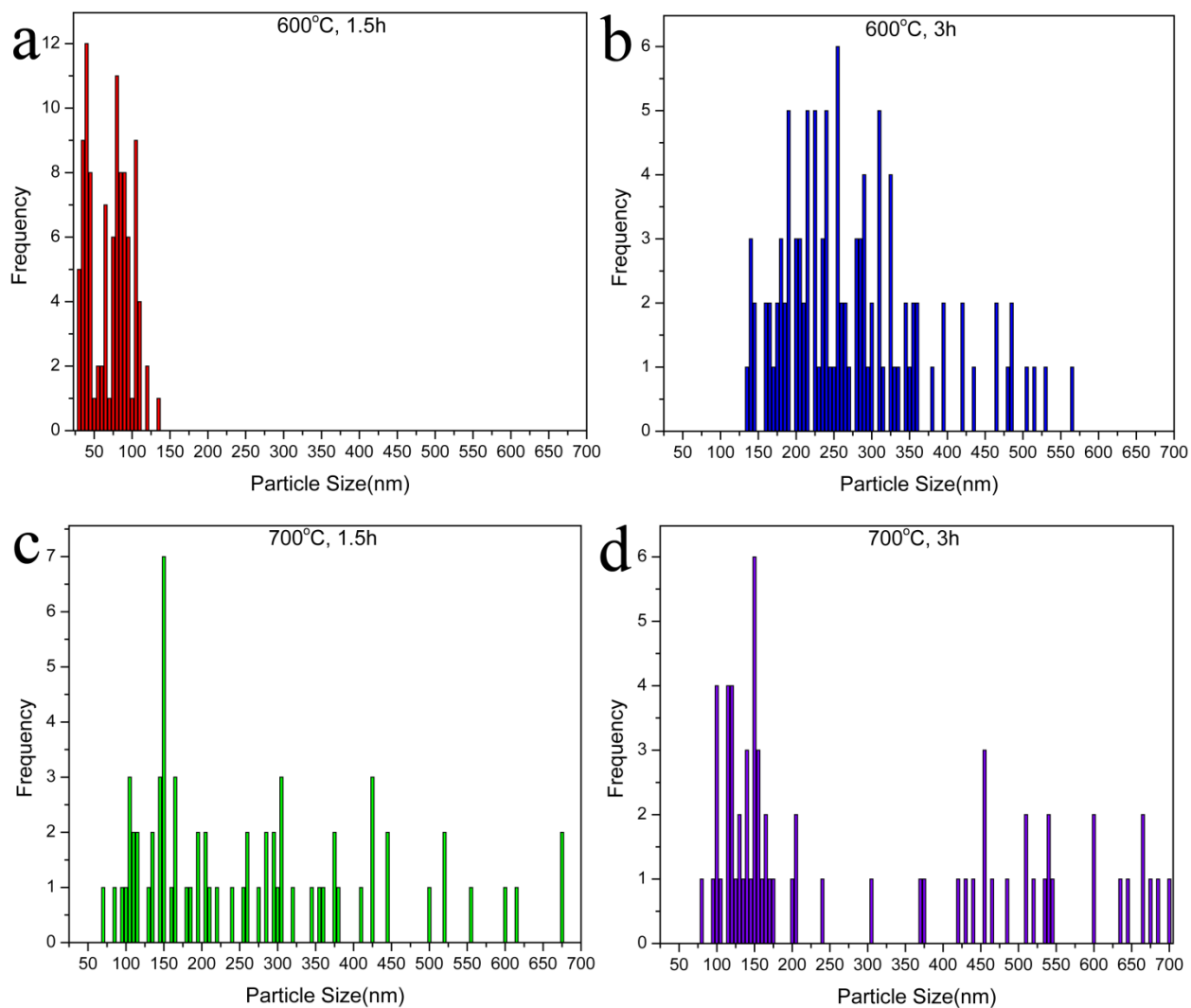


Figure 8.4. (a) Size analysis chart for 600°C, 1.5 hours annealing condition. (b) Size analysis chart for 600°C, 3 hours annealing condition. (c) Size analysis chart for 700°C, 1.5 hours annealing condition. (d) Size analysis chart for 700°C, 3 hours annealing condition.

In Figure 8.4. size analyses of LiCoO_2 at different annealing conditions is shown. The nanowires from the 600°C , 1.5 hours annealing condition had particles with narrow size distribution. The particle size can be controlled relatively well for the nanowire LiCoO_2 . For the remaining annealing conditions a very wide distribution is seen. Controlling the size of the LiCoO_2 particles becomes difficult as annealing temperature and time are increased. For the 700°C , 3 hours there are some particles that reach the micron sized range, but most of them are in the nanometer range as shown in Figure 8.4d.

To explain the electrochemical tests in a clear and concise manner, the annealing conditions will be renamed for the remainder of this chapter as follows: 600°C 1.5 hours - Sample 1; 600°C 3 hours – Sample 2; 700°C 1.5 hours – Sample 3; 700°C 3 hours – Sample 4.

8.4 Electrochemical tests

Figure 8.5. is a compilation of electrochemical analyses performed on LiCoO_2 synthesized through different annealing conditions at 0.1C. In Figure 8.5a the discharge capacities of LiCoO_2 coin cells is shown and it is clear that the Sample 3 coin cell performed the best, while the coin cell with nanowires obtained at Sample 1 annealing condition performed the worst. The first cycle capacity for the Sample 3 coin cell is around 135mAh/g, which is close to the theoretical capacity of LiCoO_2 , 140mAh/g. This is in stark contrast to the first cycle capacity of the nanowire LiCoO_2 which is around 80mAh/g.

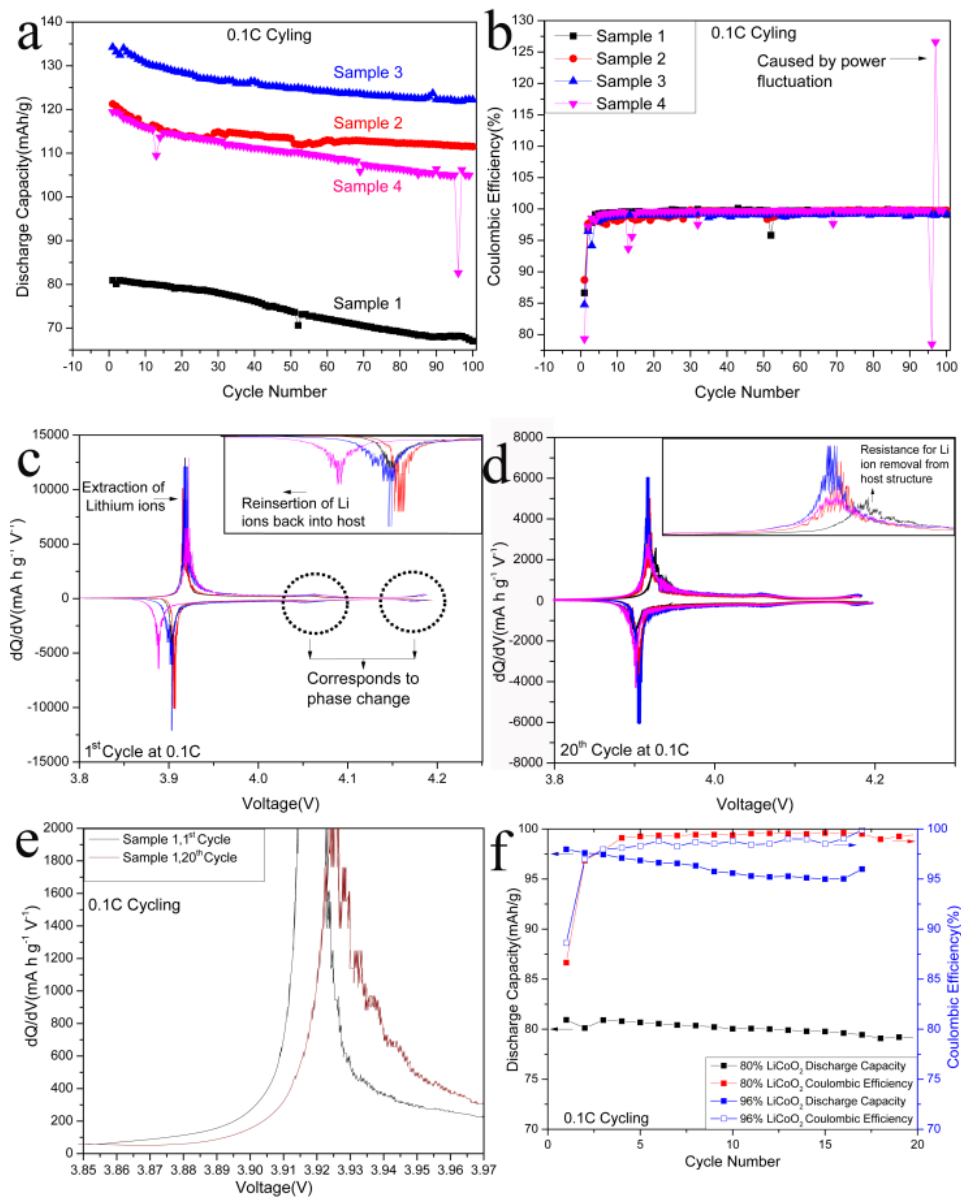


Figure 8.5. (a) Discharge fade plot of the LiCoO₂ coin cells at 0.1C. (b) Coulombic efficiency plot of the LiCoO₂ coin cells at 0.1C. (c) Differential capacity plot of the LiCoO₂ coin cells for the first cycle at 0.1C, inset is a magnification of the discharge sequence [the colors represent the same conditions as shown in (a) and (b)]. (d) Differential capacity plot

of the LiCoO_2 coin cells for the twentieth cycle at 0.1C, inset is a magnification of the charge sequence [the colors represent the same conditions as shown in (a) and (b)]. (e) Differential capacity plot of the nanowire (Sample 1) LiCoO_2 coin cell showing the shift in voltage from first to twentieth cycle at 0.1C. (f) Discharge fade plot of the nanowire (Sample 1) LiCoO_2 coin cells at 0.1C showing the comparison between 80 and 96 weight % LiCoO_2 .

The first cycle capacity for the Sample 2 and Sample 4 coin cells are very similar, around 120mAh/g. The Sample 4 coin cell does not follow the trend of achieving higher capacity as annealing temperature and time are increased. To get a better understanding of this peculiarity, differential capacity curves were created from the voltage versus capacity curves.

The differential capacity curves for the first cycle of the different coin cells are shown in Figure 8.5c. During the charging sequence a peak is observed around 3.92V for Sample 4 and around 3.918V for the other samples. The peaks are attributed to the extraction of lithium ions from the hexagonal phase of LiCoO_2 . [Inaba et al., 1997] The shift detected for Sample 4 could be due to a possible resistance building up on the surface of the particles. The two small bumps near 4.06V and 4.18V indicate the occurrence of a phase transformation. Lithium ions are extracted around 4.06V from the monoclinic phase, and around 4.18V from the second hexagonal phase. [Song et al., 2009; Kosova & Devyatkina, 2010] During the discharging sequence, the position of the peak for Sample 4 is shifted at higher voltage (due to the opposite direction) compared to the other coin cells (Figure 4c

and inset). This could probably indicate that resistance is higher for the lithium ions to get back into the host structure, hence affecting its final discharge capacity.

To understand the capacity in later cycles, the differential capacity was shown for the twentieth cycle as well (Figure 4d). In the charging sequence the peaks for the Sample 2 and Sample 4 are slightly shifted to a higher voltage (around 3.918V) compared to Sample 3 (around 3.916V), however, the Sample 1 coin cell (nanowire) has the largest shift (around 3.926V). This could possibly mean that lithium ions face more resistance to deintercalate from the host, nanowire LiCoO_2 , compared to the other coin cells, where nanoparticles of LiCoO_2 are used. To see the shift, the differential capacity curves for the charging sequence of the first and twentieth cycle of the nanowires are shown in Figure 8.5e. The shift to high voltage is clear for the nanowire LiCoO_2 . The highly porous nature of the nanowires could be the reason for the increase in resistance which ultimately leads to the rapid capacity fade in later cycles. The pores of the nanowires may be getting filled with conductive carbon and PVDF binder which could lead to increase in side reactions due to the interaction with electrolyte, and ultimately the creation of additional secondary electrolyte interface (SEI), and thus increase resistance for extraction of lithium ions. To test the effect of amount conductive carbon and PVDF binder on the capacity of the nanowire LiCoO_2 , a coin cell was created with the cathode containing 96 weight % nanowire LiCoO_2 with 2 weight % carbon black and PVDF, each. The performance of the 96 weight % nanowire LiCoO_2 compared to the 80 weight % is shown in Figure 8.5f. An increase in capacity of approximately 18% is observed for the first cycle, while there is not much difference in the capacity fade behavior. The capacity of the nanowire LiCoO_2 is still much lower compared

to the Sample 3 annealing condition. This difference could be due to the nanowire LiCoO_2 displaying low temperature electrochemical characteristics where it is not a stable layered structure and disordering exists between lithium and cobalt ions.[Myung et al., 2000] This disordering could lead to additional degradation of the capacity.

In terms of best electrochemical performance at 0.1C it is very clear that Sample 4 is the best. As shown in Figure 8.5b, the coulombic efficiencies are near 99% for the coin cells except for Sample 1 and Sample 4 coin cells at certain cycle numbers. The low first cycle coulombic efficiency exhibited by Sample 4 coin cell is explained by the differential capacity plot. A large spike is observed in the coulombic efficiency for Sample 4 at around cycle number 95. This was due to a power fluctuation in the laboratory. None of the coin cells had reached 80% of its initial capacity after 100 cycles. The Sample 2 and Sample 3 coin cells, had only reached approximately 93% of its initial capacity and it seemed that it would not reach 80% anytime soon. However, the nanowire LiCoO_2 and the Sample 4 coin cells, would reach 80% of its initial capacity very soon.

Comparing material performance with those reported in literature is hard due to varying factors (battery construction, electrode composition, cell potentials used for testing, etc.) used in electrochemical evaluation. Nonetheless some distinction is made to get an idea of the material performance, and comparison is done only with similar parameters that were used in evaluating our LiCoO_2 material. In an emulsion-based method with kerosene as the oil phase[Myung et al., 2000], LiCoO_2 was obtained at 600°C annealed for 24h. The cell performance was tested between 3.4 and 4.3V at the slowest rate of 0.1mA/cm². The initial

discharge capacity was around 115mAh/g, and by the 20th cycle 70% of its initial capacity had been reached. In terms of capacity retention, all of our coin cells perform better, and in terms of delivering the initial discharge capacity except for the Sample 1 coin cell. In a hydrothermal method¹⁰, LiCoO₂ nanoparticles were obtained initially at 200°C and then further annealed at 700°C for 5h. The cell performance was tested between 3 and 4.5V at the slowest rate of 0.1C. At 4.2V the first cycle charge capacity extracted from the voltage versus capacity curve was around 150mAh/g, which when multiplied by the coulombic efficiency of 86% gives a first cycle discharge capacity of around 129mAh/g. Our 700°C, 1.5h coin cell delivers a slightly higher first cycle discharge capacity (around 135mAh/g), but the 700°C, 3h slightly lags behind. Nanowires of LiCoO₂ were synthesized through a templating procedure where sequence of calcination steps (maximum temperature of 500°C and time of 3h) and etching with HF were used.[Jiao, Shaju & Bruce, 2005] The cell performance was tested between 3.0 and 4.2V at the slowest rate of 30mA/g. The initial discharge capacity of the nanowires was around 78mAh/g, and around 52% of the initial discharge capacity was reached by the 50th cycle. Our Sample 1 battery delivers a slightly higher first cycle discharge capacity of around 80mAh/g, and manages to retain around 83% of its initial discharge capacity.

Figure 8.6. is a compilation of the high rate studies evaluated on the coin cells. In all the high rate tests Sample 3 performed the best. For the 1C rate test, shown in Figure 8.6a, the initial capacity was around 120mAh/g for the Sample 3 coin cell. While the initial 1C rate capacities for the Sample 2 and Sample 4 were almost similar, the Sample 1 coin cell performed the worst, delivering a capacity of around 78mAh/g. The fade is drastic for all the

coin cells in the 1C rate test and all of them reach 80% of their initial capacity in less than 100 cycles. The corresponding coulombic efficiencies are shown in Figure 8.6b. All the coin cells have their coulombic efficiencies around 99% except for the Sample 2 coin cell where the efficiency is around 97% between cycle numbers 40 to 60.

For the 5C rate study, shown in Figure 8.6c, the Sample 3 coin cell performed the best again. The initial capacity was around 110mAh/g which is quite good at high rates. The nanowire LiCoO_2 performed the worst again delivering a very low capacity, while that of Sample 2 and Sample 4 coin cells delivered capacities less than 100mAh/g. All the coin cells reached 80% of their initial capacity before 100 cycles. The corresponding coulombic efficiencies are shown in Figure 8.6d. The efficiencies are around 99% for all the coin cells.

Appropriate comparisons are hard to find for high rate tests. In the hydrothermal method paper [Jo et al., 2009], mentioned previously, the initial capacity (annealed at 700°C for 5h) obtained for 1C was 155mAh/g at 4.5V. Since coulombic efficiency's and voltage versus capacity curves are not given for 1C rate, the capacity for 1C at 4.2V could not be calculated for comparison. In another paper [Zhao et al., 2008], high-rate mesoporous LiCoO_2 spherical particles were created using carbon nanotubes and a microemulsion-based route. The cell performance was evaluated between 2.75 and 4.2V at rates of 1C and 5C. The initial discharge capacity's at 1C and 5C were around 90 and 80mAh/g. At 5C after 50 cycles, the capacity retention was around 67%. Comparing these results to our best coin cell, Sample 3, it does not fare well. Our best coin cell delivers a capacity of around 120mAh/g at 1C and

around 110mAh/g at 5C. At 5C, our best coin cell has capacity retention of around 80% until 80 cycles.

Rate studies were conducted on the coin cells and the results are shown in Figure 8.6e. The rate test procedure was followed as shown in literature.[Zheng et al., 2010] The charge rate was kept constant at 0.1C, while the discharge rate was changed every 3 cycles to the respective rates as shown in Figure 8.6e. The coin cells delivering capacity was tested at high rates. From the results, it is seen that all the coin cells exhibit modest capacity fade until 2C rate, after which the fade is drastic at higher rates, especially for the coin cell containing nanowire LiCoO₂. After subjugating the coin cells at high discharge rates, the discharge rate was changed back to 0.1C, and it is seen that all the coin cells regain their initial capacities. The corresponding coulombic efficiencies are shown in Figure 8.6f, and all the batteries exhibit efficiencies near 99%.

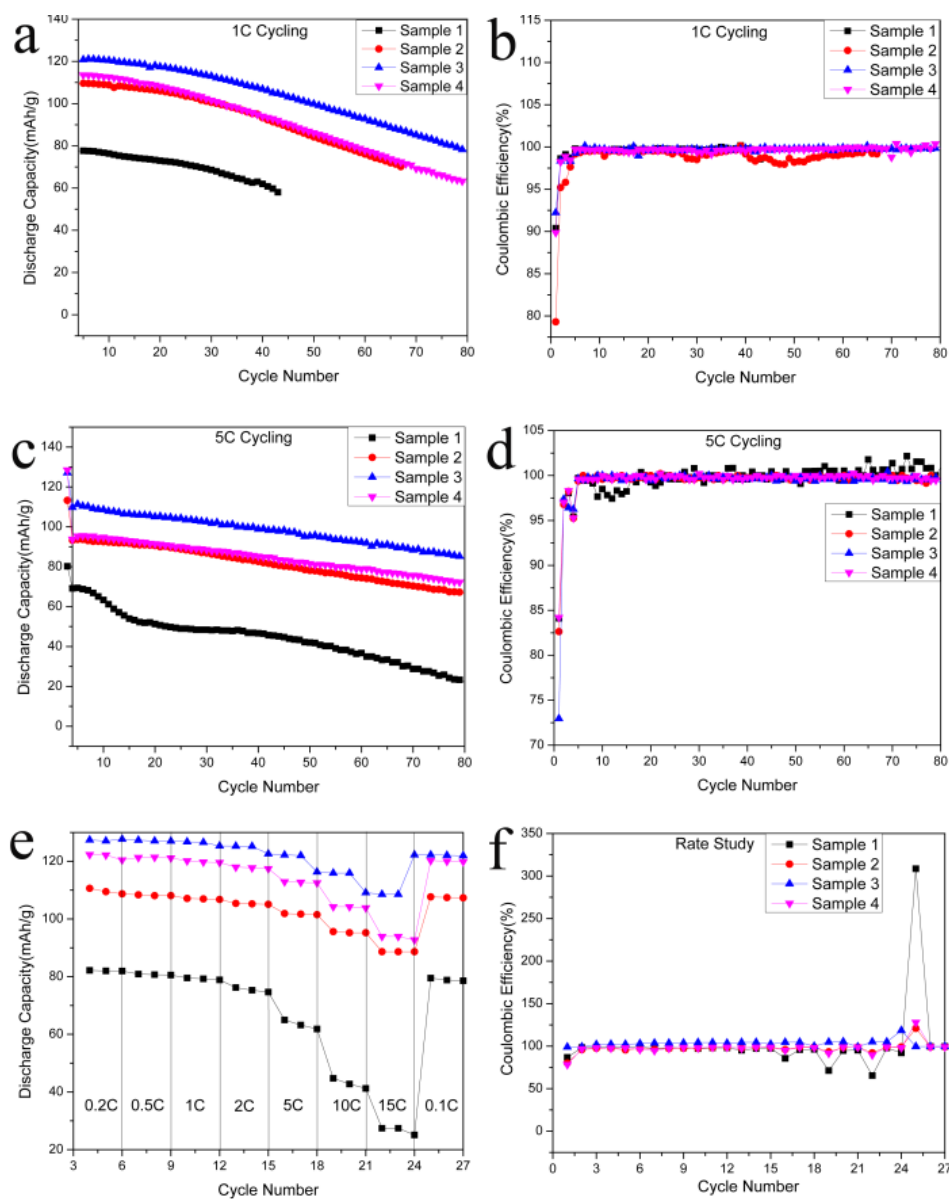


Figure 8.6. (a) Discharge fade plot of the LiCoO₂ batteries at 1C. (b) Coulombic efficiency plot of the LiCoO₂ batteries at 1C. (c) Discharge fade plot of the LiCoO₂ batteries at 5C. (d) Coulombic efficiency plot of the LiCoO₂ batteries at 5C. (e) Different rate tests conducted on the LiCoO₂ batteries. (f) Coulombic efficiency plot of the different rate tests conducted on the LiCoO₂ batteries.

8.5 Conclusion

A microemulsion method is demonstrated to synthesize nanowire templates of lithium and cobalt oxalate salt which forms LiCoO_2 of various nanostructure formations when subjected to different annealing conditions. Electrochemical tests were carried out on nanowires and nanoparticles of LiCoO_2 synthesized through varying the annealing conditions. The best performance obtained was from the Sample 3 annealing condition, delivering the highest capacity, around 135mAh/g, of all the coin cells at 0.1C, and also for the high rate tests. Nanowires of LiCoO_2 performed very poorly compared to the rest of the batteries due to probable blocking of the pores with carbon black and PVDF binder and possibly exhibiting electrochemical characteristics of low temperature LiCoO_2 . When compared to relevant results found in literature, our LiCoO_2 material performed very well at the respective conditions. To improve the stability of our best LiCoO_2 it could be coated with a thin layer of Al_2O_3 . It has been proven that a thin layer of Al_2O_3 can drastically affect performance. [Scott et al., 2011] In the rate test study the reversible nature of the coin cells were seen where it could revert back to its initial capacity after being subjugated to high rate currents.

8.6 References

Berbenni, V.; Milanese, C.; Bruni, G.; Merini, A. Solid state synthesis of stoichiometric LiCoO_2 from mechanically activated $\text{Co-Li}_2\text{CO}_3$ mixtures. *Materials Chemistry and Physics*, **2005**, 100, 251-256.

Dong, Q.; Kumada, N.; Yonesaki, Y.; Takei, T.; Kinomura, N. Synthesis of LiCoO_2 via a facile hydrothermal-assisted route. *Journal of the Ceramic Society of Japan*, **2011**, 119, 538-540.

Dong, Q.; Kumada, N.; Yonesaki, Y.; Takei, T.; Kinomura, N. Synthesis of LiCoO_2 via a facile hydrothermal-assisted route. *Journal of the Ceramic Society of Japan*, **2011**, 119, 538-540.

Ganguli, A. K.; Ganguly, A.; Vaidya, S. Microemulsion-based synthesis of nanocrystalline materials. *Chem. Soc. Rev.*, **2010**, 39, 474-485.

Gummow, R. J.; Thackeray, M. M.; David, W. I. F.; Hull, S. Structure And Electrochemistry of Lithium Cobalt Oxide Synthesized At 400°C. *Mater. Res. Bull.*, **1992**, 27, 327.

Inaba, M.; Iriyama, Y.; Ogumi, Z.; Todzuka, Y.; Tasak, A. Raman study of layered rock-salt LiCoO_2 and its electrochemical lithium deintercalation. *J. Raman Spectrosc.*, **1997**, 28, 613-617.

Jiao, F.; Shaju, K. M.; Bruce, P. G. Synthesis of Nanowire and Mesoporous Low-Temperature LiCoO_2 by a Post-Templating Reaction. *Angew. Chem. Int. Ed.*, **2005**, 44, 6550-6553.

Jo, M.; Hong, Y.-S.; Choo, J.; Cho, J. Effect of LiCoO₂ Cathode Nanoparticle Size on High Rate Performance for Li-Ion Batteries. *Journal of The Electrochemical Society*, **2009**, 156(6), A430-A434.

Jung, Y. S.; Cavanagh, A. S.; Dillion, A. C.; Groner, M. D.; George, S. M.; Lee, S.-H. Enhanced Stability of LiCoO₂ Cathodes in Lithium-Ion Batteries Using Surface Modification by Atomic Layer Deposition. *Journal of The Electrochemical Society*, **2010**, 157, A75-A81.

Kosova, N. V.; Devyatkina, E. T. A New Approach to Prepare Nanosized Cathode Materials. *ECS Transactions*, **2010**, 25, 19-25.

Lu, C. – H.; Yeh, P. –Y. Surfactant effects on the microstructure and electrochemical properties of emulsion-derived lithium cobalt oxide powders. *Materials Science and Engineering*, **2001**, B84, 243-247.

Lundblad, A.; Bergman, B. Synthesis of LiCoO₂ starting from carbonate precursors I. The reaction mechanisms. *Solid State Ionics*. **1997**, 96, 173-181.

Mosa, J.; Velez, J.F.; Lorite, I.; Arconada, N.; Aparicio, M. Film-shaped sol-gel Li₄Ti₅O₁₂ electrode for lithium-ion microbatteries. *J. Power Sources*. **2012**, 205, 491-494.

Myung, S. -T.; Kumagai, N.; Komaba, S.; Chung, H.-T. Preparation and electrochemical characterization of LiCoO_2 by the emulsion drying method. *J. Appl. Electrochem.*, **2000**, 30, 1081-1085.

Nazri, G-A.; Pistoia, G. *Lithium Batteries: Science and Technology*; Kluwer Academic Publishers: Massachusetts, 2004; pp 3-4.

Okubo, M.; Hosono, E.; Kim, J.; Enomoto, M.; Kojima, N.; Kudo, T.; Zhou, H.; Honma, I. Nanosize effect on high-rate Li-ion intercalation in LiCoO_2 electrode. *J. Am. Chem. Soc.*, **2007**, 129(23), 7447.

Scott, I. D.; Jung, Y. S.; Cavanagh, A. S.; Yan, Y.; Dillon, A. C.; George, S. M.; Lee, S. -H. Ultrathin coatings on Nano- LiCoO_2 for Li-ion Vehicular Applications. *Nano Lett.* **2011**, 11, 414-418.

Sekizawa, O.; Hasegawa, T.; Kitamura, N.; Idemoto, Y. Crystal and electronic structure change determined by various method for delithiation process of $\text{Li}_x(\text{Ni,Mn})\text{O}_2$ -based cathode material. *J. Power Sources.* **2011**, 196, 6651-6656.

Song, S. -W.; Hong, S. -J.; Park, H. Y.; Lim, Y. C.; Lee, K. C. Cycling-Driven Structural Changes in a Thin-Film Lithium Battery on Flexible Substrate. *Electrochem. & Solid State Lett.*, **2009**, 12, A159-A162.

Wu, H.; Chan, G.; Choi, J.W.; Ryu, I.; Yao, Y.; McDowell, M.T.; Lee, S. W.; Jackson, A.; Yang, Y.; Hu, L.; Cui, Y. Stable cycling of double-walled silicon nanotube battery anodes through solid-electrolyte interphase control. *Nature Nanotechnology*, **2012**, 7, 310-315.

Yilmaz, M.; Aydin, S.; Turgut, G.; Dilber, R.; Ertugrul, M. Preparation of LiCoO_2 and $\text{LiNi}_x\text{Co}_{1-x}\text{O}_2$ by Solid State Reaction Technique. *Progress in Nanotechnology and Nanomaterials*. **2012**, 1, 5-8.

Yuan, X., Liu, H.; Zhang, J. *Lithium-Ion Batteries: Advanced Materials and Technologies*; CRC Press: Florida, 2012; pp 26-27.

Zhao, Y.; Xia, D.; Li, Y.; Yu, C. Investigation of High-Rate Spherical LiCoO_2 with Mesoporous Structure via Self-Assembly in Microemulsion. *Electrochem. & Solid State Lett.*, **2008**, 11, A30-A33.

Zheng, H., Liu, G., Crawford, S.; Battaglia, V. S., *Berkeley Electrochemistry for Storage, Transportation and Renewables*
<http://bestar.lbl.gov/vbattaglia/files/2010/12/CoinCellFabSOPrev1.pdf>, **2010**.

CHAPTER 9. CONCLUSION AND FUTURE OUTLOOK

Various aspects of the energy story concerning energy generation and storage were covered in this thesis. Using the two central characters – transition metal oxides and nanostructuring - important conclusions were drawn from studying various aspects of the respective fields. Chapters 2 to 4 explained the physics behind thermoelectrics in general, lithium-ion batteries, and oxide-based thermoelectrics. Chapters 3 and 4 dealt with introducing and explaining the exciting physics present in transition metal oxides that allow it to be used for energy generation and storage applications, and an interesting topic to research.

In Chapter 5, key parameters were covered in determining the most effective thermoelectric materials for production in the near future and for some time to come. The ZT value is the most important parameter that is mentioned in literature when trying to determine the most effective thermoelectric material as materials with a high ZT have the highest thermoelectric efficiency. A need was established to study other parameters apart from ZT . Cost and abundance were considered when choosing the appropriate thermoelectric material. A roadmap was laid out to determine the appropriate thermoelectric material. Maximum ZT values were considered at three temperature ranges. Material cost and abundance were visually demonstrated to improve ease of interpretation. Another parameter termed

efficiency ratio was calculated to give a better understanding into the feasibility of these materials. Using the aforementioned parameters, a conclusion was reached to finding the best material for the different temperature ranges. For low, moderate and high temperature applications, BiSb, β -Zn₄Sb₃ and Al_{0.02}Zn_{0.98}O were the best materials respectively. This chapter established the need to study oxide thermoelectrics for high temperature application.

Chapter 6 dealt with studying a traditionally good oxide thermoelectric, strontium titanate (SrTiO₃), through nanostructuring. The large thermal conductivity of bulk complex metal oxides such as SrTiO₃ had set a barrier for the improvement of ZT and the applications of these materials in high temperature ($\geq 1000\text{K}$) thermoelectric energy harvesting and solid-state cooling. A self-templated synthesis approach to grow ultrathin SrTiO₃ nanowires with an average diameter of 6 nm in large quantity was demonstrated. The thermal conductivity of the bulk pellet made by compressing nanowire powder using spark plasma sintering showed a 64% reduction in thermal conductivity at 1000 K and agreed well with theoretical modelling.

Chapter 7 dealt with studying a new phase of calcium cobalt oxide (Ca₉Co₁₂O₂₈) as a possible high temperature thermoelectric material and as an anode in lithium-ion batteries through nanostructuring. For the first time synthesis of one dimensional porous nanowires of Ca₉Co₁₂O₂₈ through a novel single source precursor based technique was demonstrated. Improved thermoelectric properties were observed, where the thermal conductivity was 1.06 W/mK and Seebeck coefficient was 213.3 $\mu\text{V/K}$ at 700K, which are the lowest and highest values, respectively vis-à-vis those reported in literature. Also, electrochemical characteristics

of $\text{Ca}_9\text{Co}_{12}\text{O}_{28}$ nanowires with lithium metal were evaluated and found to exhibit unique behavior. A first cycle discharge capacity of around 540mAh/g was observed at 100(0.1C)mA/g cycling, followed by rapid fade during the initial cycles, but in subsequent cycles exhibited excellent rate capability and increasing discharge capacity. Through a unique single source precursor based technique, porous nanowire structures of $\text{Ca}_9\text{Co}_{12}\text{O}_{28}$ were synthesized much lower temperature than conventional solid state techniques.

Chapter 8 was motivated by the successful synthesis of porous nanowires of complex metal oxide materials demonstrated in Chapter 7. For the first time, the use of a microemulsion reaction to synthesize different nanostructures of LiCoO_2 cathode material was demonstrated. Through varying the annealing temperature and time, porous nanowires and nanoparticles of LiCoO_2 were obtained. The electrochemical performances of these different nanostructures obtained at the respective annealing conditions were evaluated. It was shown that nanoparticles formed at annealing condition of 700°C, 1.5h performed the best, delivering an initial capacity of around 135mAh/g and exhibiting a capacity of retention of around 93% by 100 cycles at 0.1C. It was shown that for good electrochemical properties, a right balance between nanostructuring, annealing conditions and crystallinity was essential for materials to reach their true potential.

APPENDICES

Appendix A: Spark Plasma Sintering

Spark plasma sintering (SPS) is one of the newest methods of pressure-sintering techniques available. It is a process where pressure and electric current are directly applied on a sample. The application of electric current creates Joule heating that has enough energy to form dense materials at low temperatures and short sintering times.

A SPS consists of a uniaxial pressure device, in which two electrodes are used as the pressing punch. The electrodes are connected to an electric pulse generator that sends pulsed direct current (dc) through the electrodes into the sample. The sample is usually placed in a die, which is kept in a chamber between the electrodes. The chamber can be in vacuum or filled with inert gases like nitrogen or argon.

The application of the dc current generates the Joule heating effect on the sample and the die. This allows elevating the temperature of the sample at higher temperature at lower heating rates. The individual grains in the sample form a neck that connects to the other grains due to the high temperature at the surface of the grains. The rapid sintering of SPS creates a densifying mechanism where grain boundary and volume diffusion are predominant.

The main advantage of using a spark plasma sintering is the rapidity of the process compared to conventional techniques. The short processing times and the rapid

densification limit the grain growth during the sintering conditions that allow maintaining the nanostructuring characteristics of a nanomaterial.

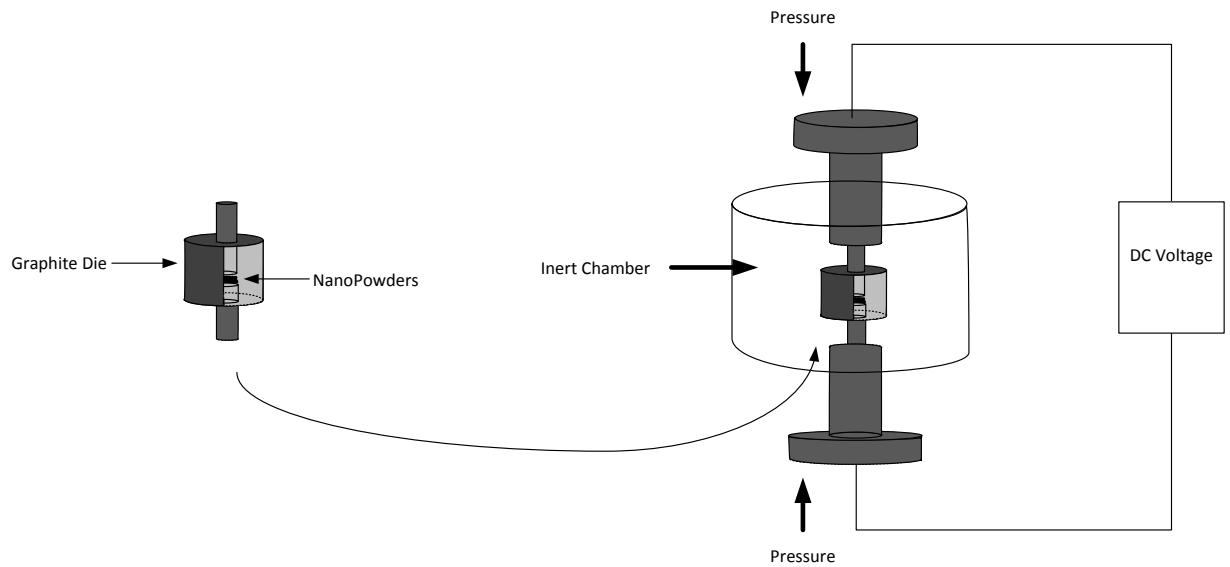


Figure A.1. Spark Plasma Sintering Process (Illustration by Gautam G. Yadav).

A.1. References

Hungria, T.; Galy, J.; Castro, A. Spark Plasma Sintering as a Useful Technique to the Nanostructuring of Piezo-Ferroelectric Materials. *Adv. Eng. Mater.*, **2009**, 11, 615-631.

Appendix B: Coin Cell Assembly

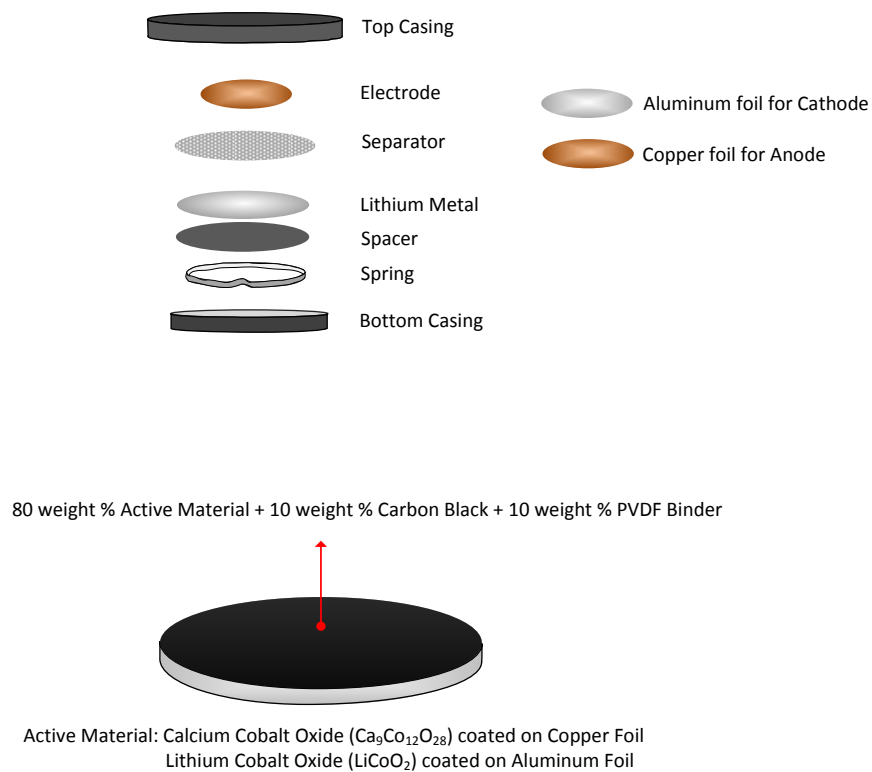


Figure B.1. Coin Cell Assembly Diagram. (Illustration by Gautam G. Yadav)

The electrochemical measurements reported for the respective materials in Chapter 7 and 8 were made on batteries made of coin cells. The coin cell assembly procedure is quite trivial and is shown in Figure B.1 to assist the reader in visualizing the assembly process. Briefly, the spring and spacer are used to tighten the coin cells during the crimping process. This allows in maintaining good contact with the two electrodes. The lithium metal reference electrode is polished till a bright shiny surface appears on the surface.

Appendix C: Doping of Strontium Titanate with Lanthanum: Tweaking of Hydrothermal Method to Produce New Nanowire Morphology

Strontium titanate is quite popular in the field of metal oxide field effect transistors. One of the major requirements is to use nanowires of larger diameters to assist in transistor fabrication, and preferably doped with lanthanum (La) to enhance the SrTiO_3 electrical properties. The hydrothermal method described in Chapter 6 proved inadequate to provide the two main requirements. Therefore, the procedure had to be tweaked to achieve the necessary requirements.

The new synthesis procedure is very similar to the old method. The reaction procedure remains unchanged, except for the reactants and an additional cation exchange step being added. The first step involves the creation of alkali titanate nanowires followed by reaction with 0.1M hydrochloric acid(HCl). The reaction with HCl facilitates the cation exchange between the alkali ion and hydrogen ion to create hydrogen titanate nanowires. The alkali agent used is sodium hydroxide (NaOH) because sodium is easily exchanged with hydrogen. In the final step, the hydrogen titanate nanowires react with a new strontium precursor, strontium hydroxide, which creates nanowires of the required diameter and length to be used in transistors.

C.1. Formation of Sodium Titanate Nanowires

0.2167g of commercially available titanium oxide (TiO_2) nanoparticles less than 25 nanometers in size are added to a glass vial containing 4.0320g of NaOH dissolved in 10ml of deionised (DI) water. The mixture is then thoroughly mixed and sonicated for around 10-20mins. The contents are then poured into a Teflon liner. The Teflon liner is placed inside an autoclave and heated at 200°C at atmospheric pressure for 1 day to transform all the particles into nanowires. After the reaction has ended, the autoclave is allowed to cool down to room temperature and the contents from the Teflon lined cylinder are transferred to a plastic tube where they are thoroughly washed with DI water to remove any sodium salts present.

C.2. Formation of Hydrogen Titanate Nanowires

The sodium titanate nanowires are then transferred to beaker containing 200ml 0.1M HCl. The contents are allowed to facilitate cation exchange for around 3 hours. The supernatant is drawn from the beaker and disposed appropriately in a waste container. The remaining powder is then washed with DI water 5 times to remove any presence of residue HCl and sodium salt. The washed powder is then dried at around 70°C overnight.

C.3. Formation of Strontium Titanate Nanowires

The hydrogen titanate nanowires from the previous step are then added to a glass vial containing with 0.6639g of strontium hydroxide octahydrate ($\text{Sr}(\text{OH})_2 \cdot 8\text{H}_2\text{O}$) dissolved in 10ml DI water. The contents are thoroughly mixed and sonicated for 10-20mins. The

contents are then poured into a Teflon liner and placed inside an autoclave. The autoclave is heated at 200°C at atmospheric pressure for 1 day to transform the hydrogen titanate nanowires to strontium titanate nanowires. After the reaction has ended, the autoclave is allowed to cool down to room temperature and the contents from the Teflon lined cylinder are transferred to a plastic tube where they are thoroughly washed with 0.1M HCl and DI water at least 3 times each, in that order, respectively.

C.4. Results

X-Ray diffraction (XRD) was performed on the intermediate products as well as final product to check for phase purity and it confirms the full conversion to SrTiO₃. The XRD analysis (Figure C.1a) showed the transformation from sodium titanate (1) to hydrogen titanate (2) and finally to strontium titanate nanowires(3). It is hard to index sodium and hydrogen titanate nanowires to one particular phase as it seems to be a mixture of different phases. However, a clear trend of cation exchange is observed. The transmission electron microscope (TEM) analysis (Figure C.1b,c,d) confirmed the formation of the nanowires with a very narrow diameter distribution. The average diameter for sodium, hydrogen and strontium titanate nanowires were 74, 113 and 240 nm. Moreover, the TEM image of SrTiO₃ reveals that the wires are formed by continuous attachment of individual particles. It is an interesting morphology that provides the required diameter and length to be used in fabrication of transistors. The Fast Fourier Transform (FFT) image additionally confirms the formation of pure SrTiO₃ nanowires.

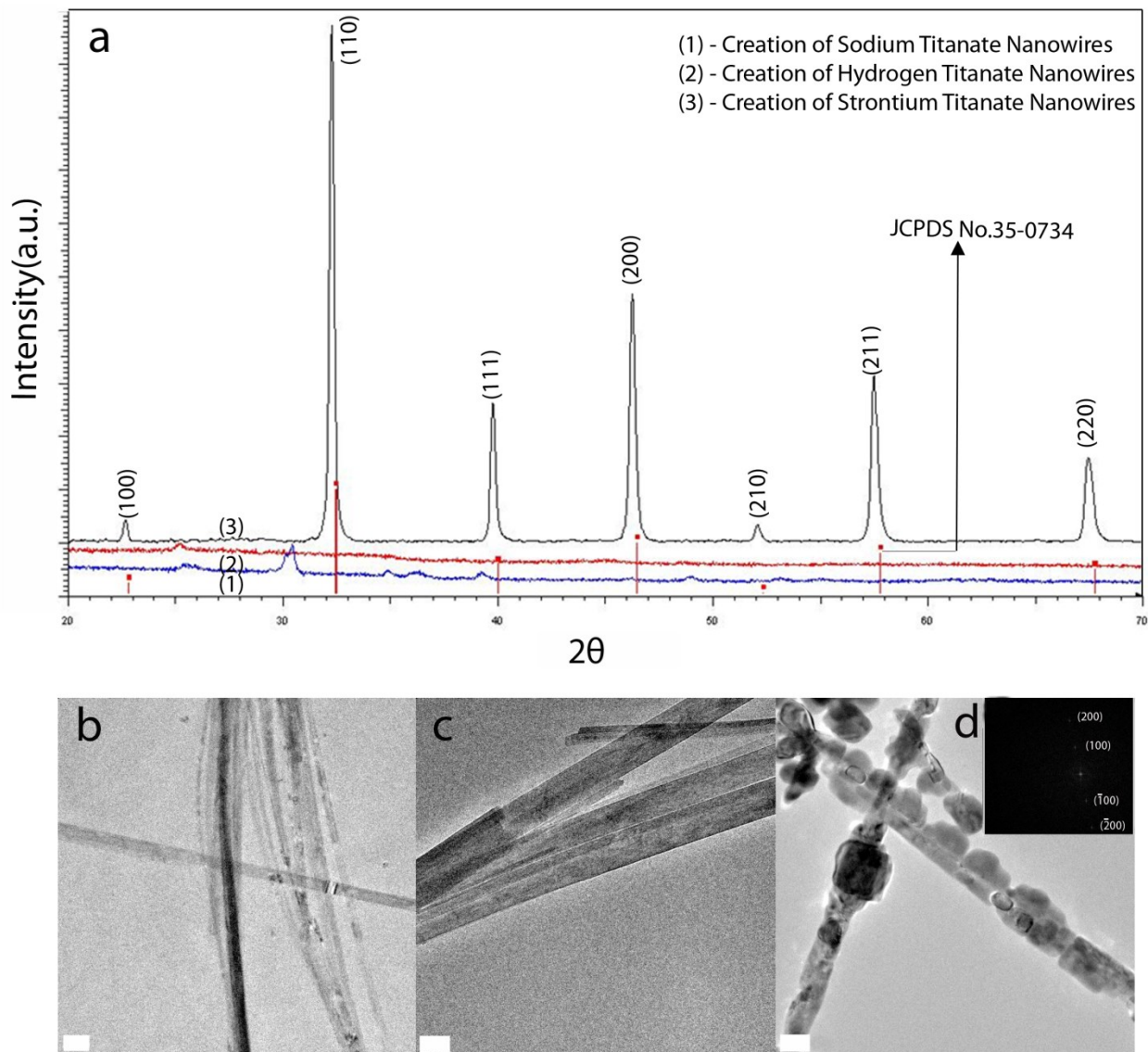


Figure C.1. (a) XRD patterns of SrTiO₃, hydrogen titanate and sodium titanate nanowires, respectively. (b) TEM image of sodium titanate (scale bar, 0.2 μm). (c) TEM image of hydrogen titanate nanowires (scale bar, 0.5 μm). (d) TEM image of SrTiO₃ nanowires (scale bar, 0.1 μm), inset at the top corner is a FFT image of a SrTiO₃ nanowire.

C.5. Doping Reactions with Lanthanum precursors

SrTiO_3 is electrically insulating, but its electronic properties can be substantially improved when doped with Lanthanum(La) or Niobium(Nb). However, it has been a challenge to dope the oxide nanowires with the formerly mentioned elements. Doping reactions are sometimes carried out by mixing the nanowire powder with the respective doping element precursor and annealing at high temperatures where the doped element enters into the lattice. This is a highly unwanted step as at high temperatures the nanowires could lose its morphology. We have overcome this drawback in the new synthesis procedure; where in the last step of the reaction, lanthanum(III) hydroxide and strontium hydroxide octahydrate are mixed with hydrogen titanate nanowires to give lanthanum doped strontium titanate nanowires. The concentration of lanthanum(III) hydroxide determines the amount of lanthanum doped inside the strontium titanate lattice.

C.6. Results

Two doping conditions were tried and they are presented in Table C.1. As stated before, concentration of lanthanum(III) hydroxide determines the final product being formed. It is clear from the XRD spectrums(Figure C.2 and C.3) that La is inside the lattice of SrTiO_3 . In Case 1, a different separate phase of lanthanum strontium titanate is formed; while in Case 2, a proper doping reaction is achieved where a small percent of La is inside the lattice. In Figure C.3, magnified images of the respective angles are presented to prove that

$\text{La}_{0.1}\text{Sr}_{0.9}\text{TiO}_3$ is the probable final product being formed. At high angles it is noticeable that the peaks correspond to $\text{La}_{0.1}\text{Sr}_{0.9}\text{TiO}_3$.

Table C.1. Relationship between doping reactant amounts and final product formation.

Doping Name	Amount of Strontium hydroxide octahydrate	Amount of Lanthanum(III) hydroxide	Product Formed
Case 1	0.6639g	0.0297g	$\text{La}_{0.6}\text{Sr}_{0.4}\text{TiO}_3$
Case 2	0.6639g	0.0087g	$\text{La}_{0.1}\text{Sr}_{0.9}\text{TiO}_3$

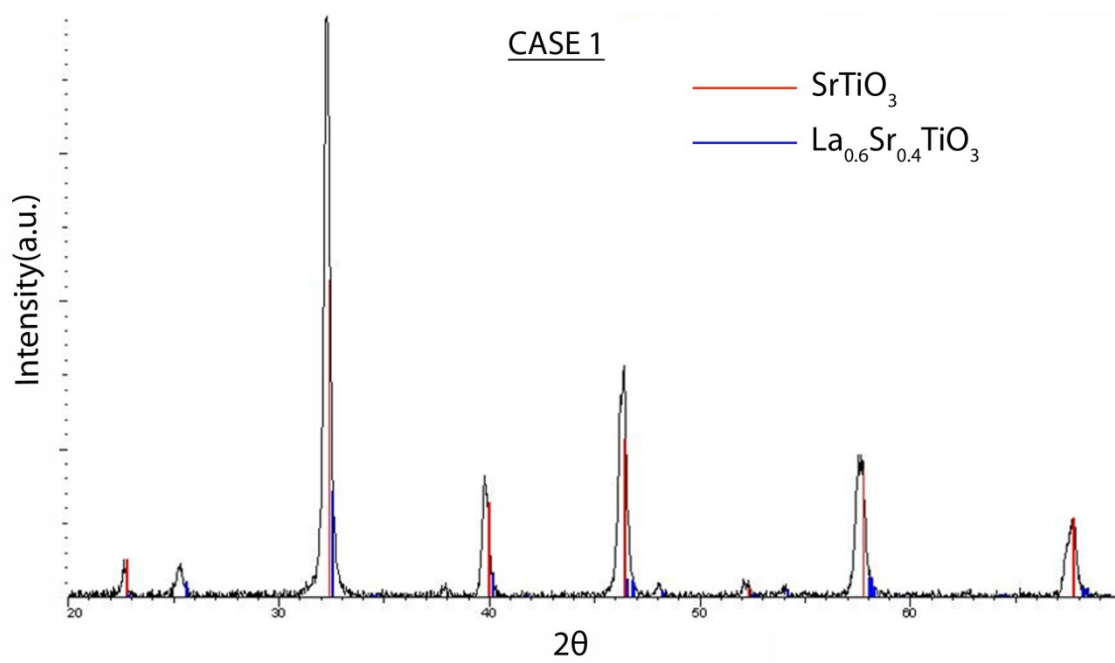


Figure C.2. XRD Spectrum of Case 1 where $\text{La}_{0.6}\text{Sr}_{0.4}\text{TiO}_3$ is formed.

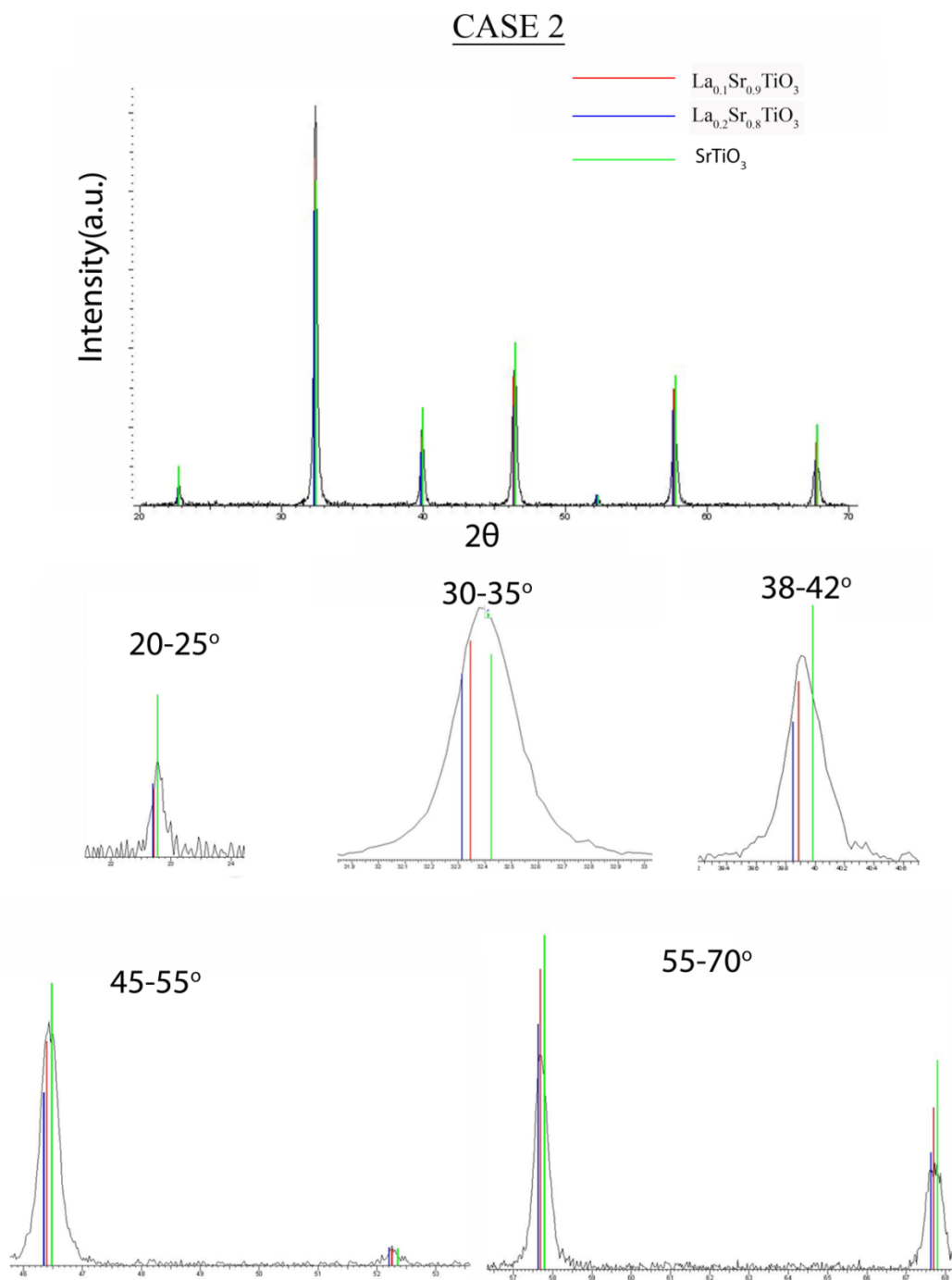


Figure C.3. XRD Spectrum of Case 2 where it is proved that $\text{La}_{0.1}\text{Sr}_{0.9}\text{TiO}_3$ is formed.

Magnified images of the respective angles are shown below the main XRD spectrum.

C.7. Conclusion

A new synthesis method has been developed to overcome the drawbacks of the previously developed method. The new reaction method cuts down reaction time drastically and is able to achieve the preferred diameter and length of the SrTiO₃ nanowires for transistor fabrication. Doping reactions have also been conducted with promising initial results. XRD indicates that doping of La inside the SrTiO₃ lattice is successful.

**Appendix D: Synthesizing of Microplates of Calcium Cobalt Oxide ($\text{Ca}_3\text{Co}_4\text{O}_9$)
by Molten Salt Method**

This method was developed to synthesize the traditional good thermoelectric material, calcium cobalt oxide ($\text{Ca}_3\text{Co}_4\text{O}_9$). Calcium cobalt oxide ($\text{Ca}_3\text{Co}_4\text{O}_9$) was synthesized using molten salt synthesis system. Molten salt synthesis is based on the principle that when salts are heated to their melting points and transformed into the ionic liquid state, a faster reaction between the two solids ensues. Accordingly, molten salt synthesis methodology using 0.617g of cobalt oxide nanoparticles (Co_3O_4), 1.2g of calcium chloride dihydrate ($\text{CaCl}_2 \cdot 2\text{H}_2\text{O}$) and 1.8g of calcium carbonate (CaCO_3) was performed. Here, the melting point of CaCl_2 is first reached, following which the reaction between Co_3O_4 and CaCO_3 is initiated. To perform the reaction, the powders were finely ground in a mortar using a ceramic pestle until a homogenous powdered mixture had formed, following which the mixture was placed inside an alumina crucible and heated inside a tube furnace according to a very specific temperature profile indicated below. Completion of the thermal processing results in formation of pure $\text{Ca}_3\text{Co}_4\text{O}_9$.

Table D.1. Annealing ramp rates

Temperature (°C)	Time(hours)
20 – 250	1.5
250-900	18

900	10
900-20	Immediately

Initial runs indicated that the mixture must be heated to 250°C to remove any moisture present in the samples. The temperature then needed to be steadily increased to 900°C whereat the powders reached their softening points. At 900°C, CaCl₂ then became a molten salt and initiated the reaction.



Figure D.1. Scanning electron image (SEM) of Calcium Cobalt Oxide (Ca₃Co₄O₉).

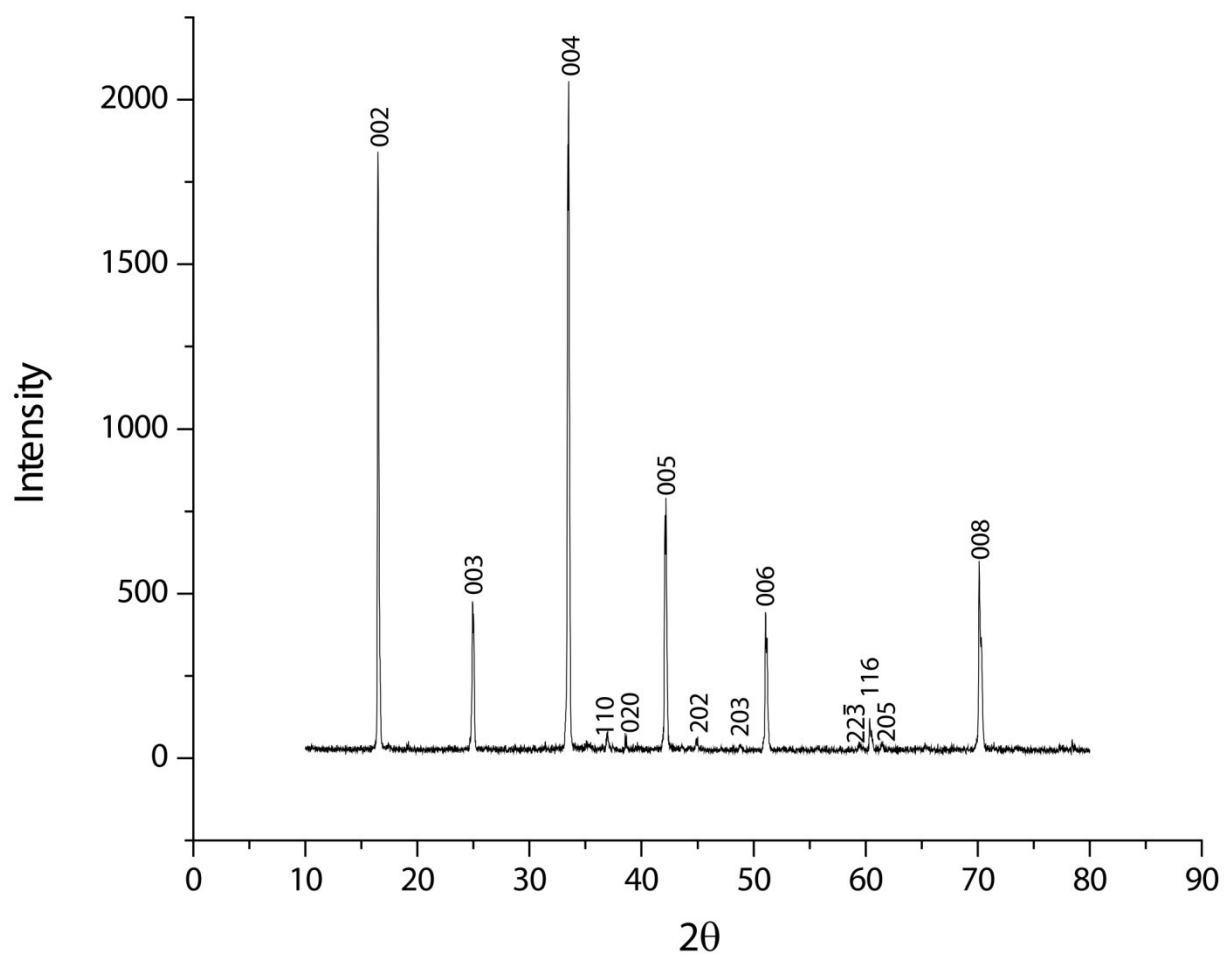


Figure D.2. X-ray Diffraction spectrum of Calcium Cobalt Oxide(Ca₃Co₄O₉).

Appendix E: Growth of Vertically Aligned Cobalt Oxide Nanowires

The synthesis method used in this procedure is not new; it has been used in literature to grow nanowires of different oxides. The goal of this project was to grow free standing cobalt oxide nanowires and subsequently infuse calcium, to make calcium cobalt oxide nanowires. The nanowires of cobalt oxide were successfully synthesized on titanium foil (Ti), silicon wafers and glass slides. However, infusing calcium into cobalt oxide proved to be difficult due to the high annealing temperature required to make this happen. The substrates were not stable at high temperatures and loss in nanowire morphology was seen in some cases. Nonetheless, this method involved using creative means to create a support to hold the substrates in position above a certain distance from the reaction solvents to grow the nanowire vertically. The method is described in detail below.

Titanium (Ti) foil was used as a substrate onto which freestanding Co_3O_4 nanowires were grown. 10 mmols of cobalt nitrate hexahydrate was first dissolved in 10ml of DI water and stirred for around 2 minutes. 40 ml of 28wt% of ammonia was then slowly added to the dissolved mixture and then stirred for approximately 30 minutes.

The reaction was carried out in a petri dish. For the nanowires to be freestanding on the Ti foil, the foil had to be approximately 1-2mm above the bottom of the petri dish. Initially, maintaining this distance proved to be an enormous challenge since the foil would float away when the ammoniated liquid was added to the dish. This problem was eventually addressed

through the design and fabrication of a glass-based foil suspension system (Figure E.1). The suspension system can accommodate maximum of 4 Ti foils.

After the Ti foils were placed within the suspension system and the solution of cobalt nitrate and ammonia was added to the dish, the dish was heated at 90°C for around 14 hours. During this procedure, the dish was kept covered to prevent any ammonia from escaping during the reaction.

After the reaction was complete, the Ti foils were recovered from the petri dish and washed in DI water. The washed Ti foils revealed a dark surface that is indicative of nanostructure growth. The Ti foils are then dried at room temperature, after which they are heated inside the tube furnace at 250°C using a thermal progression rate of 60°C/hour for 4 hours.

SEM images indicate that freestanding nanowires have formed on the Ti substrate. (Figure E.2). The nanowires have an average diameter of 530 nm and are fairly elongated.

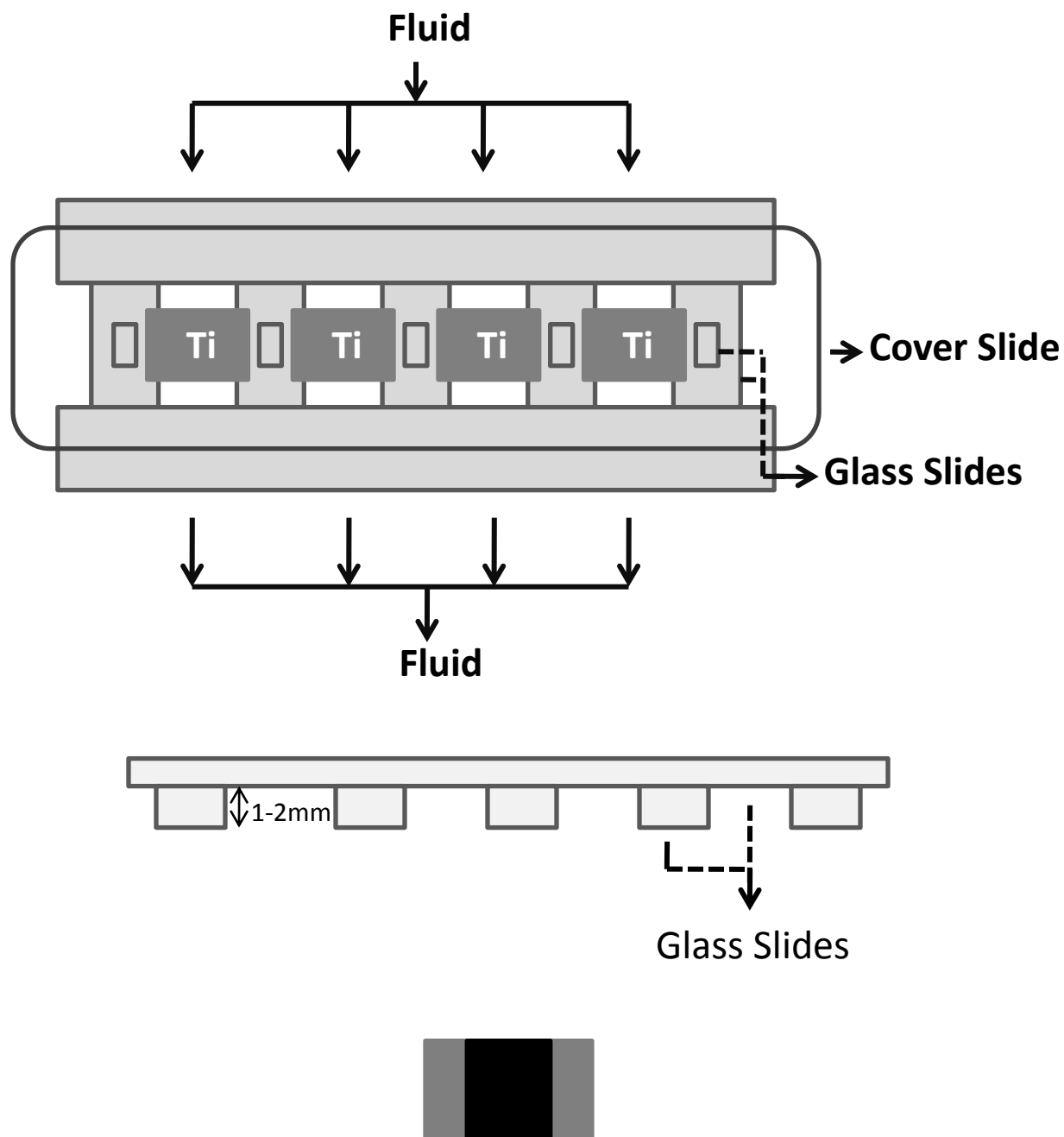


Figure E.1. (Top and Middle Image) Design of the glass system which allowed the Ti foil to be suspended 1-2mm above the bottom of the petri dish. (Bottom Image) The black part indicates the Co_3O_4 grown on the Ti foil after annealing it for 4 hours at 250°C .

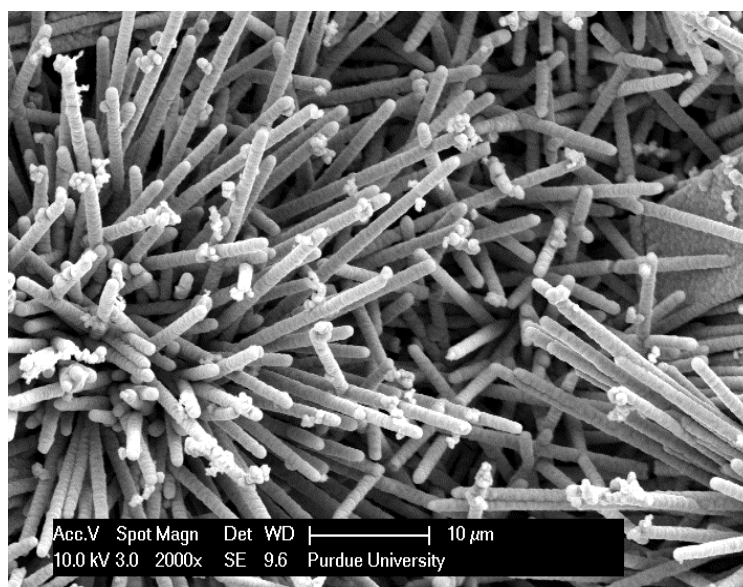
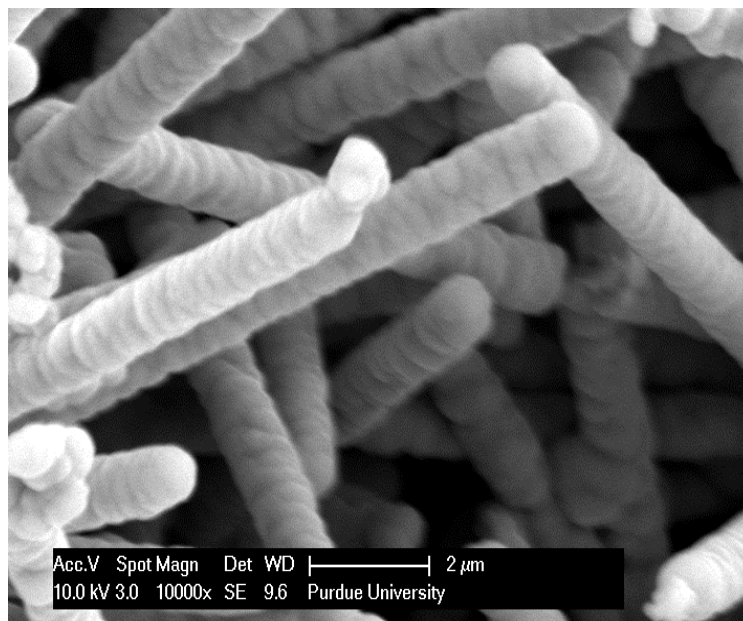


Figure E.2. Scanning electron images of cobalt oxide (Co_3O_4) nanowires grown on Ti foil.

VITA

VITA

Gautam Ganapati Yadav is an accomplished engineer and material scientist whose experience spans different fields. The highlights of his educational qualifications and achievements are listed below:

Education

Ph.D., Chemical Engineering

2013

Purdue University, West Lafayette, IN

- Thesis title: Design & Assembly of Nanostructured Complex Metal Oxide Materials for the Construction of Batteries & Thermoelectric Devices
- Thesis supervisor: Prof. Yue Wu
- Investigated the sustainability of a variety of complex metal oxides for large-scale deployment as energy harvesting and storage materials
- Developed novel synthetic approaches to produce nanostructured metal oxides for constructing thermoelectric devices and batteries
- Research has led to high-impact publications in the journal *Nanoscale* and *Journal of Materials Chemistry*.
- Gained experience setting up a laboratory for a first time advisor

B.Eng.Sc. in Chemical and Biochemical Engineering**2009****University of Western Ontario (Now Western University), London, ON, Canada**

- Inducted to the Faculty of Engineering's Dean's Honor List
- Third-place finish in the senior-year capstone project for work on the design of a soybean oil production plant
- Represented the University of Western Ontario at the Canada-wide EcoVentures business plan competition for emerging technologies in sustainable technologies, and placed fifth in the nation

Experience**Purdue University, Department of Chemical Engineering, West Lafayette, IN****2010 – 2011****Instructor**

- Taught fluid mechanics and heat & mass transfer to an undergraduate class of around 190 students
- Awarded the Magoon Award for Excellence in Teaching

University of Western Ontario, Dept. of Chemical Engineering, London, Canada

2008 – 2009

Research Assistant

Project Supervisor: Prof. Anand Prakash

- Investigated several technologies and feedstocks for biodiesel production from oleogenic crops such as soybean
- Designed several variations of the process implementing permutations and combinations of the available unit operations and conducted detailed techno-economic studies of the process designs
- Constructed and tested the design at laboratory-scale and drafted the final process & instrumentation diagrams for the at-scale process
- Project awarded the third prize in the senior-year capstone Engineering Design Competition

University of Western Ontario, Sustainable Technologies Team, London, ON

2008 – 2009

Chief Engineer & Team Leader

- Leader of a highly motivated and tight-knit group that pursued the development of sustainable energy solutions for rural communities in Canada
- Team successfully designed a waste collection, transport and biogas production system

- Design was submitted to EcoVentures, a Canada-wide business plan competition for green and sustainable technologies, and the venture placed fifth in the nation

Awards & Accomplishments

- Poster Presentation Awardee, Shell Energy Day (2012)
- Best Poster, Purdue University-Industry Symposia (2012 and 2011)
- Magoon Award for Excellence in Teaching, Purdue University (2011)
- Third place, Engineering Design Competition, University of Western Ontario (2009)
- Leader of the team that placed fifth in Canada in the EcoVentures business plan competition for green and sustainable technologies (2008)

Publications

- [1] **G. G. Yadav**, J. A. Susoreny, G. Zhang, H. Yang and Y. Wu, “ Nanostructure-based thermoelectric conversion: An insight into the feasibility and sustainability for large-scale deployment”, *Nanoscale*, 3, 3555-3562 (2011); ***also selected as the edition’s featured article***
- [2] **G. G. Yadav**, G. Zhang, B. Qiu, J. A. Susoreny, X. Ruan and Y. Wu, “Self-templated synthesis and thermal conductivity investigation for ultrathin perovskite oxide nanowires”, *Nanoscale*, 3, 4078-4081 (2011)

- [3] G. Zhang, S. Finefrock, D. Liang, **G. G. Yadav**, H. Yang, H. Fang, Y. Wu, “Semiconductor nanostructure based photovoltaic solar cells”, *Nanoscale*, 3, 2430 (2011);
Invited review
- [4] **G. G. Yadav**, A. David, T. Favaloro, H. Yang, A. Shakouri, J. Caruthers and Y. Wu, “Synthesis and the Investigation of Thermoelectric and Electrochemical Properties of Porous $\text{Ca}_9\text{Co}_{12}\text{O}_{28}$ Nanowires”, *Journal of Materials Chemistry*, 1, 11901-11908(2013)
- [5] **G. G. Yadav**, A. David, H. Zhu, J. Caruthers and Y. Wu, “Microemulsion-based synthesis and electrochemical evaluation of different nanostructures of LiCoO_2 prepared through sacrificial nanowire templates”, *Submitted to Chemistry of Materials*

Presentations

- [1] **G. G. Yadav** & Y. Wu, “Complex metal oxide nanowires for thermoelectric and battery applications” at the Materials Research Society (MRS) conference (2013)
- [2] **G. G. Yadav** & Y. Wu, “Complex metal oxide nanowires for thermoelectric and battery applications” at the American Chemical Society (ACS) conference (2013)
- [3] **G. G. Yadav** & Y. Wu, “Design of Thermoelectric Nanostructured Materials For Power Generation” at the Shell Energy Day, Purdue (2012)

- [4] **G. G. Yadav** & Y. Wu, “Design and assembly of nanostructured materials for the construction of batteries & thermoelectric devices” at the Purdue University-Industry Symposium (2012)
- [5] **G. G. Yadav** & Y. Wu, ”Design of Thermoelectric Nanostructured Materials” at the Purdue University-Industry Symposium (2011)